Safety in Mines Research Advisory Committee

Final Project Report

Develop guidelines for the design of pillar systems for shallow and intermediate depth, tabular, hard rock mines and provide a methodology for assessing hangingwall stability and support requirements for the panels between pillars

G. York, I. Canbulat, K.K. Kabeya, K. Le Bron, B.P. Watson, S.B. Williams

Research agency: CSIR Mining Technology

Project number: GAP 334

Date: December 1998

Executive Summary

The design of hard rock pillars, in shallow to intermediate depth hard rock mines, has been redefined as the determination of the pillar system load bearing capacity. This entails the ability to *design* each of the components of the pillar system:

1) the panel span
2) the pillar
3) the foundation.

Design charts have been produced that allow the assessment of stability for a particular set of geotechnical and geometric inputs, for each component. Design flowcharts have been produced to show the simple and practical use of the charts within an overall design process for each of the components of the pillar system.

Worked examples have been provided for each of the listed components of the pillar system, to facilitate technology transfer. The worked examples follow the logic of the design flowcharts.

In the design of a pillar system, the *load* as well as the *capacity* of the system must be determined. The load on an in-panel pillar system is not trivial to determine. The mechanisms of load transfer, and the influence of various variables (such as stope and panel spans, pillar width) on the loading of pillars have been investigated. Several important principles have been highlighted.

Some of the more significant results of the project are discussed in the following paragraphs.

It has been shown that the ¼ depth rule is probably conservative for hard rock mines. Underground experience, together with numerical modelling results, suggest that ratios of regional span to depths up to ½ may be safely used. In the presence of regional pillars, pillar loading is always less, in some cases significantly less, than the theoretical tributary area load. In back analysis, this may cause pillar strength to be overestimated, with negative safety implications. In-panel pillars reduce the load on the regional pillars. In the case of elastic pillars, this reduction is significant. The role of in-panel pillars in reducing the tensile zone has been shown.

In the development of an empirical Critical Panel Span Design Chart (the maximum panel span as a function of the rock mass rating), it was found that none of the 13 collapsed panels could be attributed to jointing alone. Most occurred as a result of major pre-existing discontinuities, such as faults. This implies that, in the absence of major discontinuities, panels with good rock mass ratings in the Bushveld Complex may be stable at large spans (in excess of 50 m). Nevertheless, a good relation has been developed between the rock mass rating system and the Critical Panel Span. This work showed that pillars should be laid out to prevent collapses on the weak side of persistent joints and faults which strike in the mining direction. This has implications not only to safety but also to the economics of mining. The mining direction relative to joint orientation is an important factor in the stability of panel hangingwalls.

Self-supporting and supportable spans have been defined as a function of geotechnical rock mass parameters, also by means of numerical modelling. A finding of this work was that pre-stressed elongate support could significantly reduce the potential for falls of ground.

A simplified methodology to determine *in situ* joint friction angles has been developed, based on Barton's methodology. This should aid rock mechanics practitioners a great deal in the determination of rock mass stability.

The new approach in the design of pillars involves an engineering understanding of the main factors that affect pillar strength. This engineering understanding has allowed the effect of these factors to be incorporated into a new rationale and process for pillar design.

The foundation bearing capacity and the footwall heave of panels have been described as a function of a number of geotechnical parameters. A yielding support design optimisation methodology has been produced to take the footwall heave into account.

These various outputs have been integrated into an overall pillar system design approach.

Acknowledgements

This project has been funded by the Safety in Mines Research Advisory Committee. CSIR Miningtek extends grateful acknowledgement to the management and staff of a number of mines for their co-operation and allowing us to use their mines for *in situ* observations, in particular Union Section, Lonrho Western Platinum, Western Chrome Mine, and Eastern Chrome Mine.

CSIR Miningtek extends grateful acknowledgement to the management and staff of the following mines for allowing *in situ* experiments at their mines: RPM Amandelbult Section, Lebowa Platinum Mine, Impala Platinum Mine, and Vaal River Operations Tau Lekoa Shaft.

Table of Contents

Executive Summary 2

Acknowledgements 4

List of contracted Enabling Outputs 13

List of Figures 14

List of Tables 22

List of Examples 24

Glossary 25

1 A short review of SIMRAC projects GAP024 and GAP027, and the formulation of future research strategy 29

2 The loading environment in shallow to intermediate depth mines 31

2.1 Introduction 31

2.2 Research methodology 32

2.3 Results 33

2.3.1 Finite vs. infinite depth modelling and the effect of the extent of the free surface modelled 33

2.3.2 Beam bending 34
2.3.3 The applicability of the ¼ depth rule 38
2.3.4 Effect of mining geometry 42
2.3.5 Effect of depth 42
2.3.6 The effect of the k-ratio 43
2.3.7 The effect of span on the in-panel tensile zone and on local support design 44
2.4 A review of the backbreak problem at Cooke Section, Randfontein Estates 44
2.4.1 Introduction 44
2.4.2 Support system used before 1980 45
2.4.3 Instrumentation and observations 45
2.4.4 Revised stope support system 47
2.4.5 Crush pillar design requirements 47
2.4.6 Residual pillar strength 47
2.5 Conclusions 49
2.6 References 50
3 Determination of the influence of rock mass parameters on the stability of panels between pillars 51
3.1 Introduction 51
3.2 The development of the Critical Panel Span Design Chart 51
3.2.1 Introduction 51
3.2.2 Methodology 52
3.2.3 The Critical Panel Span Design Chart 53
3.3 Worked example using the "Critical Panel Span Design Chart" 54

3.3.1 Introduction 54
3.3.2 Method 55
3.4 Description and discussion of instrumented and collapsed sites studied 56
3.4.1 Introduction 56
3.4.2 Installation methodology 57
3.4.3 Union-1 57
3.4.4 Amandel-1 57
3.4.5 Lebowa-1 58
3.4.6 Amandel-5 58
3.4.7 Impala-1 58
3.4.8 Impala 1 shaft 60
3.4.9 Lebowa-1 62
3.4.10 Amandel-2 62
3.4.11 Amandel-3 63
3.4.12 Lebowa-2 63
3.4.13 Lebowa-4 64
3.4.14 Lebowa-5 65
3.4.15 Vaal River Operations Tau Lekoa Shaft 66
3.4.16 Union Section open pit 68
3.5 Laboratory work 68
3.5.1 Introduction 68
3.5.2 Results 68
3.5.2.1 Union 68
3.5.2.2 Amandel-1 70
3.5.2.2.1 Results of the uniaxial and triaxial tests 70
3.5.2.2.2 Point load results 71
3.5.2.2.3 Results of the FLAC analysis program 72
3.5.2.3 Lebowa-1 73
3.5.3 Discussion 74

3.5.3.1 Footwall 74
3.5.3.2 Reef 74
3.5.3.3 Hangingwall 75
3.5.3.4 Point load tests 75
3.5.3.5 General observations 75
3.5.4 Conclusions 76
3.6 Analyses performed on wedge failures 77
3.6.1 Introduction 77
3.6.2 Results 77
3.6.3 Discussion 77
3.7 Influence of internal panel support systems on the stability of the panel hangingwall 77
3.7.1 Introduction 77
3.7.2 Description of Union-1 78
3.7.3 Instrumentation results 78
3.7.3.1 Extensometers 78
3.7.3.2 Closure meters 78
3.7.3.3 Timber prop results 81
3.7.4 Discussion 81
3.8 Conclusions 84
3.9 References 87
4 The stability of panels between pillars 88
4.1 Introduction 88
4.2 Definition of UDEC numerical model 89
4.3 Failure modes in numerical model 89
4.4 Applicability of the methodology based on UDEC model 89

4.5 Methodology for support design taking geotechnical parameters into account 90

4.6 Definition of unsupportable, supportable and self supporting panel spans 90

4.7 Supportable spans 92

4.8 The design of elongate support 93

4.9 Influence of pre-stressed support 95

4.10 Correlation between the numerical modelling and empirical results 96

4.10.1 Introduction 96

4.10.2 Method 96

4.10.3 Discussion 96

4.11 A methodology for the determination of the joint friction angle. 98

4.11.1 Determination of the joint roughness coefficient 99

4.11.2 Determination of Joint Wall Compression Strength, JCS 100

4.11.2.1 Schmidt Hammer Index test. 101

4.11.2.1.1 Influence of orientation of Schmidt Hammer test 101

4.11.2.1.2 Sample dimensions 101

4.11.3 Determination of Basic Friction Angle (ϕ_b) and Residual Friction Angle (ϕ_r) 102

4.11.4 Scale Effect 103

4.11.5 Influence of normal stress on the effective friction angle 103

4.12 Examples 104

4.13 Conclusions 109

4.14 References 110

5 The design of pillars 111

5.1 Introduction 111

5.2 Literature review 111

5.3 Research methodology: a new approach to pillar design 114

5.4 Results 115

5.4.1 The critical rock mass strength 115

5.4.1.1 The derivation of the critical rock mass strength from laboratory tests 115

5.4.1.2 Discussion 116

5.4.2 A comparison of the performance of the power and linear formulae 117

5.4.2.1 Scope of laboratory testing and testing methodology 117

5.4.2.2 Results of testing programme 118

5.4.3 The effect of w/h on pillar strength and the effect of the contact friction angle 119

5.4.4 An approximate method to determine the critical rock mass strength (Θ_c) 124

5.4.5 The effect of jointing on pillar strength 125

5.5 A methodology for the design of pillars 126

5.6 A preliminary methodology for the design of crush pillars 128

5.7 *In situ* crush pillar monitoring 130

5.7.1 Introduction 130

5.7.2 Site description and mining sequence 131

5.7.3 Results 133

5.7.3.1 Underground instrumentation 133

5.7.3.2 Laboratory rock test results 137

5.7.4 Discussion 137

5.7.5 Conclusions 141

5.8 Back analysis of pillar performance at Impala Platinum Mine . 141

5.9 Examples 142

5.10 Conclusions 146

5.11 References 146

6 A design methodology for the bearing capacity and the yielding of foundations of hard rock pillar systems ... 148

6.1 Introduction 148

6.2 Literature review 148

6.3 Research Methodology 150

6.3.1 Pillar foundation geometry 150

6.3.2 Bearing capacity determination 151

6.4 Results 152

6.4.1 Discussion of failure mechanisms 152

6.4.2 Pillar foundation design methodology 154

6.4.2.1 Implications of closure for support design 154

6.4.2.2 Bearing capacity and closure design charts 155

6.4.2.3 Influence of the pillar vertical stress profile 158

6.4.2.4 Examples: bearing capacity and closure 159

6.5 Case Study 159

6.6 Optimisation of the design methodology using closure for the design of yielding elongate support 159

6.6.1 Design methodology 159

6.6.2 Examples: Optimisation of foundation design to account for elongate support yield capacity 161

6.7 Laboratory testing of foundation yielding 162

6.8 Summary and conclusions 166

6.9 References 166

7 Integration of system design components into a pillar system design methodology for shallow to intermediate depth hard rock mines 7-1

7.1 Introduction 7-1

7.2 The pillar system design flowchart 7-1

7.3 The loading system 7-2

7.4 Panel span design component 7-4

7.4.1 The empirical approach 7-4

7.4.2 The numerical modelling approach 7-5

7.5 Influence of internal panel support systems on the stability of the panel hangingwall 7-8

7.6 Pillar design 7-8

7.7 Stability of the pillar foundation and panel footwall 7-11

7.8 Development of Windows™ based software for implementation of results and recommendations to industry.. 7-13

7.9 Conclusions 7-13

List of contracted Enabling Outputs

NO.	ENABLING OUTPUT
1	Review of current pillar project progress and formulation of future research strategy.
2	Determination of pillar performance requirements for the rock mass environment and pillar loading conditions.
3	Determination of the requirement for regional support and definition of design parameters.
4	Determination of parameters critical to the design of hard rock pillars and design recommendations for pillars.
5	Determination of the influence of rock mass parameters on the stability of panels between pillars.
6	Influence of internal panel support systems on the stability of the panel hangingwall.
7	Methodology for support design taking geotechnical parameters into account
8	Develop guidelines for the stability of the foundations of pillars and the inelastic deformation of the footwall of the panels between pillars.
9	Integration of system design components into a pillar system design methodology for shallow to intermediate depth hard rock mines
10	Development of Windows™ based software for implementation of results and recommendations to industry.

List of Figures

Figure 1-1 An ideal pillar system design flowchart. 30

Figure 2-1 According to Tributary Area Theory, each pillar carries an equal share of the overburden weight. 32

Figure 2-2 Effect of free surface size. 34

Figure 2-3 Two dimensional geometry of the DIGS model. 34

Figure 2-4 Distribution of vertical stress (from the vertical centre line to the edge of the pillar) across pillars under the same virgin stress values, but with the surface modelled at 100 m, and in infinite depth conditions. 35

Figure 2-5 Beam bending analogy 35

Figure 2-6 Horizontal stress distribution in the hangingwall for the stope at 3000 m depth. The diagram is a cross-section looking in the dip direction, in a window 240 m wide and 166 m high, with the right hand abutment at the bottom right hand corner. 36

Figure 2-7 Horizontal stress distribution in the hangingwall for the stope at a depth of 166 m. The diagram is a cross-section looking in the dip direction, in a window 240 m wide and 166 m high, with the right hand abutment at the bottom right hand corner. 37

Figure 2-8 Displacement in the hangingwall and on surface compared to the theoretical displacement. The depth was 140 m and the dip span of 300 m was constant. The strike span was increased according to the ratio on the x-axis. 37

Figure 2-9 Surface subsidence (S) normalised to seam thickness (t), plotted against the ratio of span (Width) to depth (after Cummins and Given, 1973). 38

Figure 2-10 The effect of depth on the surface subsidence and hangingwall convergence. The values plotted correspond to the mid-span of the excavation. 39

Figure 2-11 The interaction between regional pillars and in-panel pillars: (a) only regional pillars (b) regional pillars with in-panel pillars. 41

Figure 2-12 Effect of regional and in-panel pillars on regional pillar loading. 41

Figure 2-13 The APS as a proportion of the theoretical tributary area load, from numerical modelling of various mining geometries and pillar sizes at 200 m depth. 42

Figure 2-14 The difference in APS as calculated by Tributary Area Theory and from numerical modelling for various depths for 9 in-panel pillars and varying panel spans 43

Figure 2-15 The effect of the k-ratio. 43

Figure 2-16 Effect of span between pillars on the height of the tensile zone at a depth of 200 m. 44

Figure 2-17 A schematic strike section diagram showing instrumentation above stope hangingwall. 46

Figure 2-18 Schematic representation of trends of results from a 40 m borehole extensometer in the centre gully (A) and the corresponding closure (B). 46

Figure 2-19 Load-deformation laboratory results from rock specimen. Regions A-B, B-C, C-D represent pre-peak, post-peak, residual strength respectively and, after D, strain hardening respectively. 48

Figure 2-20 A comparison of backfill, grout pack, timber pack and crush pillar support systems showing support resistance as a function of the distance behind the stope face (after Özbay and Roberts, 1988). 48

Figure 3-1 A typical stratigraphic column above Merensky Reef. 52

Figure 3-2 Comparison between the rock mass rating systems 53

Figure 3-3 Proposed design chart for determining unstable spans (based on the Impala system). 54

Figure 3-4 Horizontal stress distribution in the strike direction in the hangingwall in the 9/87 stope at Impala 59

Figure 3-5 Extrapolation of the two measurements at the greatest depth, to estimate the tensile stress that could have developed, assuming plate bending. 60

Figure 3-6 Horizontal field stress measurements in the hangingwall of a panel at Impala 1 shaft. 61

Figure 3-7 MINSIM-W simulation showing horizontal stress in the hangingwall of a panel at Impala 1 shaft. 62

Figure 3-8 Sketch showing section through panel collapse at Amandel-2. 63

Figure 3-9 Sketch showing section through FOG's on curved joints at Amandel-3. 63

Figure 3-10 Cross-section on strike, showing the panel collapse at Lebowa-2. 64

Figure 3-11 Cross section showing the collapse mechanism at Lebowa-4. 65

Figure 3-12 Photograph taken at the lower end of the collapse at Lebowa-5..... 65

Figure 3-13 Photograph showing a high degree of stress fracturing in the hangingwall..... 66

Figure 3-14 Photograph showing the edge of the collapse at Tau Lekoa. 66

Figure 3-15 Photograph showing the plates that had fallen as a result of horizontal stress fracturing in the hangingwall. 67

Figure 3-16 Horizontal fracture plane in the hangingwall at the top end of the collapse..... 67

Figure 3-17 Vertical joints above the Merensky Reef, in the open pit at Union Section..... 68

Figure 3-18 Stress-strain curves of the triaxial tests performed on the Merensky Reef and immediate footwall and hangingwall. 71

Figure 3-19 Results of the triaxial tests and the FLAC analysis performed on the pyroxenite hangingwall. 73

Figure 3-20 Stope sheet of the instrumentation site at Union-1. 79

Figure 3-21 Hangingwall extensometer results from Union-1 80

Figure 3-22 Closure results from Union-1..... 80

Figure 3-23 Stick performance and closure relating to face advance..... 81

Figure 3-24 Initial hangingwall extensometer results from Union-1..... 82

Figure 3-25 Load deformation curve for a grout pack at Amandel-5. 83

Figure 3-26 Load deformation curve for a stick at Union-1. 83

Figure 3-27 Load deformation curve for a stick at Amandel-1 83

Figure 4-1 UDEC model. 89

Figure 4-2 Proposed methodology for support design. 90

Figure 4-3 Unsupportable hangingwall. 91

Figure 4-4 Supportable hangingwall. 91

Figure 4-5 Relationship between friction angle and panel span for the 0°/(85°-90°) joint orientations (0° is the orientation of the horizontal joint and the 85°-90° refers to the orientation of the other joint set). 92

Figure 4-6 Influence of joint orientation and friction angle on the panel span for a single stope. 92

Figure 4-7 Influence of joint orientation and friction angle on the panel span for multiple stopes. 93

Figure 4-8 Load deformation curves of elongate support used in modelling. 94

Figure 4-9 Percentage instability as a function of support spacing and joint spacing for 0°/(85°-90°) joint orientations with 5° friction angle for a 20 m panel span. 94

Figure 4-10 Percentage instability as a function of support spacing and joint spacing for 0°/(85°-90°) joint orientations with 10° friction angle for a 20 m panel span. 95

Figure 4-11 Model showing instability in hangingwall beam and influence of support for the 0°/(85°-90°) joint orientations for a 5 m support spacing. 95

Figure 4-12 Impala rating used to assess the influence of friction for various joint conditions. 97

Figure 4-13 Critical spans based on the influence of joint friction on panel span for various joint conditions, assessed from the chart. 97

Figure 4-14 a) Joint with infilling; b) Joint without infilling 98

Figure 4-15 Proposed methodology for determination of joint friction angle 99

Figure 4-16 Joint roughness profile chart, after Barton (1978) 100

Figure 4-17 Correlation chart for Schmidt (L) hammer, relating rock density, compressive strength and rebound number, after Miller (1965). 101

Figure 4-18 Influence of normal stress on effective friction angle. 103

Figure 4-19 Average roughness profile of the joints in the panel. 104

Figure 4-20 Relationship between stable panel span and joint friction angle for the 0°/(45°-60°) joint orientation. 105

Figure 4-21 Elongate support relative hazard chart for 0°/(45°-60°). 105

Figure 4-22 Roughness profile of the joints. 106

Figure 4-23 Joint with clay infilling. 106

Figure 4-24 Relationship between stable panel span and joint friction angle for the 0°/(60°-70°) joint orientation. 107

Figure 4-25 Elongate support relative hazard chart for 0°/(60°-70°). 108

Figure 5-1 The effect of dip angle and frequency of jointing on pillar strength, for pillar w/h = 3 (after Esterhuizen, 1997). 112

Figure 5-2 The strength size relation for a) coal (after Bieniawski, 1968a) and b) norite (after Bieniawski, 1968b). 113

Figure 5-3 The strength – size relation for Merensky Reef from Amandelbult Platinum Mine. 116

Figure 5-4 The strength – size relation for Merensky Reef from Amandelbult and Impala Platinum Mines. 116

Figure 5-5 The strength – w/h relationship for Merensky Reef from Amandelbult Platinum Mine, for cylinders of diameter = 248 mm. 120

Figure 5-6 The values of the w/h strengthening parameter, as a function of size (mm), for various data sets (coal data after York and Canbulat, 1998). 121

Figure 5-7 The values of the w/h strengthening parameter, as a function of size (mm), for the data sets including coal data (coal data after York and Canbulat, 1998) 122

Figure 5-8 A conceptual diagram of the effect of frictional end restraint on the confinement of a sample, depending on its w/h. 122

Figure 5-9 Geometry of FLAC model to test the effect of the contact friction angle on the strength of laboratory model pillars 123

Figure 5-10 The effect of the contact friction angle on the w/h effect, on the basis of numerical modelling. 123

Figure 5-11 The w/h strengthening parameter, 1-a, as a function of the contact friction angle, according to numerical modelling. The values derived from laboratory testing on coal and Merensky Reef are also shown. 124

Figure 5-12 UDEC model geometry and boundary conditions to determine the effect of jointing on coal pillar strength (after Esterhuizen, 1997). 126

Figure 5-13 A pillar design flowchart. 127

Figure 5-14 Preliminary chart for the design of crush pillars. 130

Figure 5-15 Stope sheet showing mining sequence at the "Crush pillar instrumentation site". 132

Figure 5-16 Dip section showing positions of instrumentation in the pillar and cubby. 133

Figure 5-17 View of pillar from gully showing positions of instrumentation 133

Figure 5-18 Total field stress measured by doorstopper P2 at 0,77 m above the pillar. 135

Figure 5-19 Stress change measured by vibrating wire stress cells at 0,17 m above the pillar. 136

Figure 5-20 Vertical field stress measured by the Zafer load cell at 0,36 m above the pillar. 136

Figure 5-21 Pillar dilation measured by an extensometer. 137

Figure 5-22 Geological section into the hangingwall at the position of the E2 extensometer. 138

Figure 5-23 Field stresses measured by doorstopper P2, reduced to reflect average pillar stress. 140

Figure 5-24 Pillar dilation measured up to the date of pillar failure 141

Figure 5-25 The basis of the calculation of tributary area theory load. 143

Figure 6-1 Failure mechanism of rock under stamp load (after Wagner and Schümann, 1971) 149

Figure 6-2 Tabular excavation ore body. 150

Figure 6-3 Model geometry: two dimensional cross section of pillar and panel geometry (after Kabeya et al, 1997). 151

Figure 6-4 Stress-displacement curve. 152

Figure 6-5 Failure mechanisms. 153

Figure 6-6 Failure mechanisms as shown by FLAC plots of velocity vectors. 154

Figure 6-7 APS versus closure: yield point. 155

Figure 6-8 Typical bearing capacity design chart (h=1). 156

Figure 6-9 Typical closure chart (h=1) at foundation yield point. 157

Figure 6-10: Typical maximum closure chart A (h=1) at full load. 157

Figure 6-11: Typical maximum closure chart B (h=1) at full load. 158

Figure 6-12 Optimisation design flow chart for closure of the footwall to aid in the design of yielding support. 161

Figure 6-13 Closure: standard case (no parting). 162

Figure 6-14 Geometry of sample (shown on left), with plan views of the square pillar geometry on the right. 163

Figure 6-15 The APS and axial displacement at the yield stress for the quartzite samples. 165

Figure 6-16 The APS and axial displacement at the yield stress for the norite samples. 166

Figure 7-1 The pillar system design flowchart. 7-1

Figure 7-2 The APS as a proportion of the theoretical tributary area load, from numerical modelling of various mining geometries and pillar sizes at 200 m depth. 7-2

Figure 7-3 The difference in APS as calculated by Tributary Area Theory and from numerical modelling for various depths for 9 in-panel pillars, and varying panel spans 7-3

Figure 7-4 Surface subsidence (S) normalised to seam thickness (t), plotted against the ratio of span (Width) to depth (after Cummins and Given, 1973). 7-3

Figure 7-5 Effect of regional and in-panel pillars on regional pillar loading. 7-4

Figure 7-6 The Critical Panel Span Design Chart for the Merensky Reef. 7-5

Figure 7-7 An example of a panel span design chart defined by the use of numerical modelling, for joint sets orientated at 0° and 85° to 90°. 7-6

Figure 7-8 Elongate support relative hazard chart for the 0°/(60°-70°) joint sets. 7-7

Figure 7-9 Proposed methodology to determine the joint friction angle. 7-7

Figure 7-10 Proposed methodology for panel span and support design. 7-8

Figure 7-11 The effect of w/h on pillar strength. Laboratory samples are Merensky Reef of diameter = 248 mm. 7-9

Figure 7-12 The w/h strengthening parameter, 1-a, as a function of the contact friction angle, according to numerical modelling. The values derived from laboratory testing on coal and Merensky Reef are also shown. 7-9

Figure 7-13 The effect of jointing on pillar strength as a function of the joint set dip angle, for a pillar of w/h = 3. A different curve is drawn for different joint frequencies. 7-10

Figure 7-14 A pillar design flowchart. 7-10

Figure 7-15 Design chart for the bearing capacity of foundations, for a 1 m deep parting in the footwall. 7-12

Figure 7-16 Design chart for the maximum heave (after full load transfer to the pillar / foundation system), for a 1 m deep parting in the footwall. 7-12

Figure 7-17 Optimisation design flow chart for closure of the footwall to aid in the design of yielding support. 7-13

List of Tables

Table 3-1 Impala adaptation of the "NGI Tunnelling Quality Index" 53

Table 3-2 Impala rock mass rating system (after Barton and Grimstad, 1994). 55

Table 3-3 Typical example of a panel on the Merensky Reef. 56

Table 3-4 Relationship between offsets and joint roughness (J_r) (after Barton, 1997) 56

Table 3-5 Horizontal stress change measurements made in the hangingwall at the "crush pillar" site 58

Table 3-6 Results of the direct tensile tests performed on hangingwall material from Union-1. 69

Table 3-7 Average uniaxial and triaxial compressive strength values of lithological units at Union-1. 69

Table 3-8 Average Brazilian test results from the hangingwall at Union-1. 70

Table 3-9 Average uniaxial compressive strength and effect of confinement factor (Kc) values for each lithological unit of borehole 9/38W/4. 70

Table 3-10 Tensile strengths calculated from point load tests. 71

Table 3-11 Average anisotropy ratios, calculated from the corrected axial and radial point load strengths. 72

Table 3-12 Average uniaxial compressive strength and Kc values for each lithological unit at Lebowa-1 74

Table 3-13 Summary of the laboratory derived rock properties of the immediate hangingwall rock types. 76

Table 3-14 Comparison between the calculated tensile stress at the top of the cantilever and the strength of the material. 77

Table 3-15 Description of the site. 78

Table 4-1: Corrections for Reduced Measured Schmidt Hammer Rebound number (R) when the hammer is not used vertically downwards (after Barton, 1978). 102

Table 4-2 Basic friction angles of various unweathered rocks (after Barton, 1978). 102

Table 4-3 Results of in-situ tilt tests. 107

Table 4-4 Updated Q-system parameter ratings (after Barton,1993) 108

Table 5-1 Number of samples tested for the range of w/h's and diameters in the testing programme 118

Table 5-2 Results of laboratory testing on Merensky Reef from Amandelbult Platinum Mine. 119

Table 5-3 Results of a regression fit of a power formula to the laboratory data. 119

Table 5-4 Results of straight line fits to original data of in situ compression tests on coal pillars and SIMRAC project COL021 laboratory data (after York and Canbulat, 1998) 121

Table 5-5 Details of the modelling parameters used by Esterhuizen (1997). 126

Table 5-6 Instrumentation installed at the site. 134

Table 5-7 Diary of major events recorded around the pillar. 135

Table 5-8 Results of the geomechanical test. 137

Table 5-9 Input data for pillar design problem – good rock mass condition 142

Table 6-1 Input parameters. 150

Table 6-2 Material properties 152

Table 6-3 Design chart colour – point marker scheme 156

Table 6-4 The scope and results of the tests in the testing programme 164

Table 7-1 The parameters modelled and the range covered in the parametric study 7-11

List of Examples

Example 3-1The use of the empirical Critical Panel Span Design Chart..... 55

Example 4-1 Panel span design, using the numerical modelling approach, with rough joints dipping at 55°..... 104

Example 4-2 Panel span design, using the numerical modelling approach, with smooth joints dipping at 55°..... 105

Example 4-3 Panel span design, using the numerical modelling approach, with smooth joints dipping at 85°..... 106

Example 4-4 Panel span design, using the numerical modelling approach, with infilled joints dipping at 85°..... 106

Example 4-5 Panel span design, using the numerical modelling approach, with smooth joints dipping at 65°..... 107

Example 5-1 Elastic pillar design – good rock mass conditions..... 142

Example 5-2 Elastic pillar design – poor rock mass conditions..... 144

Example 5-3 Crush pillar design..... 145

Example 6-1 Footwall stability: decision on the requirement for yielding support..... 159

Example 6-2 Footwall design optimisation to cater for yielding support capacities: footwall with no partings..... 161

Example 6-3 Footwall design optimisation to cater for yielding support capacities: footwall with a major parting..... 162

Glossary

Abbreviations

2D	two dimensional
3D	three dimensional
APS	average pillar stress
ASG	advance strike gully.
FOG	fall of ground
RQD	rock quality designation, usually determined by accumulating all pieces of core greater than 100 mm in a borehole and expressing the value as a percentage of the length of hole or portion of the hole
UCS	uniaxial compressive strength
w/h	ratio of the width to the height of a pillar, or model pillar

Symbols and technical terms

Θ	the strength of a pillar or model pillar of w/h=1
ρ	the density of rock
σ_1	in rock testing, commonly the axial stress
σ_1, σ_2 and σ_3	major, intermediate and minor principal stress
σ_3	in rock testing, commonly the confining stress
1-a	the slope of the linear pillar strength function normalised to Θ
a	the intercept of the linear pillar strength function normalised to Θ
abutment	the solid area at the edge of a mined out stope
anisotropy ratios	ratio of strengths in different directions
basic friction angle (ϕ_b)	the friction angle of an unweathered joint surface
breast mining	mining in a strike direction
brittle failure	failure with fracture development
core	cylindrical shaped rock retrieved from a borehole
"crush" pillar	a pillar that is designed to failed, such that the residual strength supports the hangingwall
D	depth of mining
discontinuity	geological or mining induced breaks in the rock mass
dog-earing	stress fracturing within a borehole, appears as pointed ears in a direction perpendicular to the major principal stress, in a two dimensional plane
domes	curved, anticline shaped joints
doorstoppers	strain gauges used to measure strain at the end of a hole and converted to stress by using the elastic properties of the rock material

elongate or stick	wooden poles used as support elements
extension fracturing	tensile fractures that develop parallel to σ_1 in the absence of confining stress
extensometer	measures deformation within the rock mass by means of anchors placed within a borehole
extraction ratio	the ratio of mined to unmined ground
face	the end of a panel which is advanced during mining
f_c	the factor applied to convert the strength at w/h = 1 for a 50 mm sample to the critical rock mass strength
f_j	pillar strength reduction factor accounting for the dip and strike joint sets; $f_j = f_{jd} \times f_{js}$
f_{jd}	pillar strength reduction factor accounting for the dip joint set
f_{js}	pillar strength reduction factor accounting for the strike joint set
flat jacks	hydraulic jacks used to measure pressure
footwall	the rock mass below the excavation
fracturing	discontinuities forming as a result of mining
f_{UCS}	the factor applied to convert the UCS strength to the strength of a w/h = 1 sample; $f_{UCS} = \frac{1}{1-(0,6)(1-a)}$
geomechanical testing	test to determine the physical properties of a geological material
geotechnical condition	an evaluation of the nature and condition of the geological discontinuities and rock material contained in a rock mass
Glotzl cell	hydraulic jack cemented in a borehole, operating by means of a set of valves, measuring stress change
gully	on reef tunnel mined either with a panel, usually slightly ahead, or excavated prior to mining a panel
h	depth of parting
hangingwall	the rock mass above the excavation
hard inclusion load cell	metallic load cell used to measure load as a result of borehole deformation, which is converted to stress change
holing	ventilation gaps between pillars
ISRM standards	international standards for rock mechanics tests set by the International Society of Rock Mechanics
joint	geological discontinuity
joint alteration number (J_a)	measure of the influence of infilling on joint shear strength
joint compressive strength (JCS)	the uniaxial compressive strength of a joint wall measured in MPa
joint dilation angle	measure of waviness of joint
joint orientation/dip angle of joint	the angle between the plane of the joint and the horizontal plane
joint roughness coefficient	measure of the roughness of a joint without infilling

(JRC)	
joint roughness number(J_r)	measure of the roughness of a joint surface
(joint) shear strength	the resistance of a joint to shear displacement
k	k-ratio
k, α, β	the constants in the Salamon and Munro pillar design formula
Kc	the factor describing the effect of an increase of σ_3 on the axial strength (maximum value of σ_1) in a linear relation between σ_1 and σ_3
k-ratio	the ratio between the horizontal and vertical stress
ledging	approximately 5 m face advance on either side of a centre gully to enable support installation
panel	slot mined out between pillars
panel collapse	FOG greater than 3 m thickness, for the purposed of the Critical Panel Span Design Chart
panel span	the mined out span between two adjacent lines of pillars or abutments
phi (N)	friction angle
plastic behaviour	flow within the crystal lattice
Poisson's ratio	lateral strain divided by axial strain, lateral strain being the result of an axial stress
pothole	syncline shaped basin, usually oval in shape, where the lithological units changed elevation to form a basin
q	yield stress or bearing capacity
rebound number (R) of Schmidt Hammer test	rebound on unweathered rock surface
rebound number (r) of Schmidt Hammer test	rebound on weathered rock surface
residual Friction angle (ϕ_r)	the friction angle of a weathered joint surface
residual strength	post failure strength of a material
S	expected pillar strength based on laboratory testing
s/w	ratio of span to pillar width
S_a	expected pillar strength taking contact conditions, the critical rock mass strength and jointing into account
S_c	expected pillar strength taking the contact conditions and the critical rock mass strength into account
Schmidt Hammer Index test	test used to measure JCS which is used to calculate the friction angle of a joint
serpentinization	geological alteration of pyroxenite, weakening the rock mass
spalling	slabs that develop as a result of stress fracturing
span	the shortest distance between in-panel pillars or faces
stope sheet	on reef plan showing face and pillar positions
stress shadow	region within the influence of a feature, which reduces the

	effective stress level
tensile zone	a tensile stress field that develops above a panel as a result of mining
vibrating wire load cells	measures deformation of a borehole, which can be converted to a stress change
virgin vertical stress	the value of the vertical stress at some depth before mining has taken place
Y_a^*	allowable closure, based on support capacity
Y_m	maximum closure, after full load transfer to pillar
Y_m'	new value of maximum closure after a trial in the optimisation of panel span design to account for footwall deformation
Young's modulus (E)	stress divided by the strain resulting from the stress

1 A short review of SIMRAC projects GAP024 and GAP027, and the formulation of future research strategy

This chapter addresses Enabling Output number 1 (see page 13).

The results from the previous SIMRAC projects were mainly focused on exploratory work, which detailed the mining and geological environment in the Bushveld Complex and the rock mechanics problems faced in the Bushveld Complex. A comprehensive geological assessment of the Bushveld Complex was performed, showing the variance in the stratigraphic column throughout the Bushveld Complex.

Important initial laboratory tests were performed to highlight the mechanical behaviour of model pillars of Merensky Reef. Important data regarding the scale effect and the effect of the pillar width to height ratio (w/h) was obtained.

In situ experimental work was performed at Impala Platinum Mine, to determine the pillar performance characteristics. It was found that significant footwall heave occurred as a result of the "Footwall 4" mud-parting, some 3 to 4 m into the footwall.

The modes of *in situ* hangingwall failure were observed and listed. An extensive monitoring programme was undertaken in a panel at Union Section. This panel failed in an unravelling mechanism.

A review of existing pillar design procedures was performed. A review of failed and stable pillar systems was also performed.

The following main conclusions were made:
1) pillar footwall punching formed an important mode of deformation in pillar systems
2) hangingwall deformation was limited, at two *in situ* sites observed, to 4,5 m into the hangingwall
3) laboratory-based model pillar behaviour allowed important insights into pillar behaviour
4) variability is an important parameter in the design of pillar systems
5) characteristic modes of hangingwall keyblock failure were identified
6) geotechnical mapping of stope pre-development can identify unstable structures prior to mining.

A number of comments were made regarding pillar system design. Variability, geotechnical structure, the loading system, and the stability of the footwall were all identified as important in the determination of the system strength (or pillar system bearing capacity).

The Final Project Reports of GAP024 and GAP027 highlighted the need for a rational approach to the design of pillar systems.

In the course of this project, GAP334, after intensive workshops, a flowchart of an ideal pillar design process was therefore produced. The workshops were guided by two elements:
1) the results discussed above
2) the structure of the proposed work in GAP334.

The flowchart shown in Figure 1-1 combines the two elements. This flowchart formed the basis, or blueprint, for the subsequent work in GAP334.

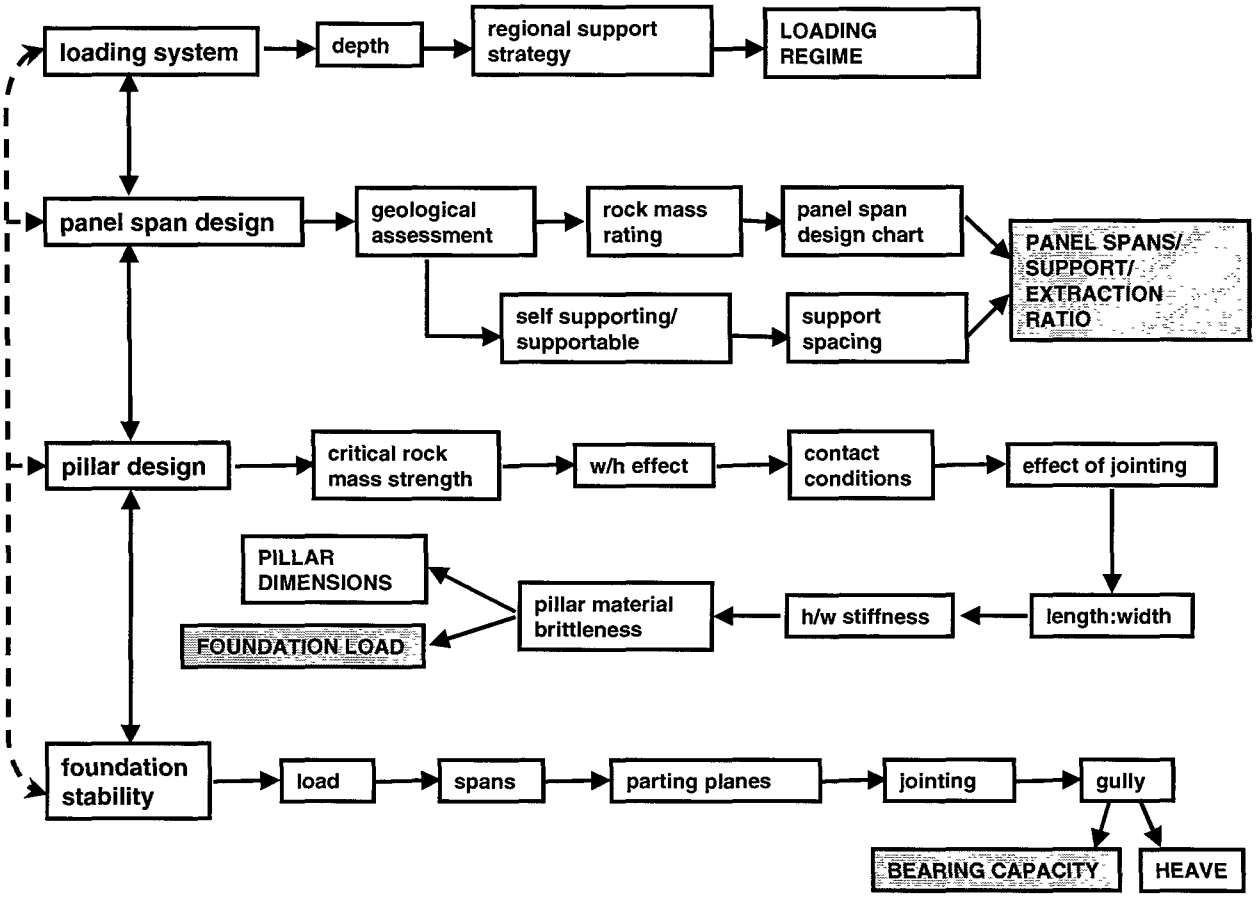

Figure 1-1 An ideal pillar system design flowchart.

2 The loading environment in shallow to intermediate depth mines

2.1 Introduction

This chapter addresses Enabling Output numbers 2 and 3 (see page 13).

The purpose of leaving pillars underground is to stabilise the hangingwall strata. This can only be achieved if the pillars are stable themselves. If they are too large, the extraction ratio will be unnecessarily decreased.

Pillar strength is one component which has to be determined when evaluating the stability of a pillar. The other main factor is the load acting on the pillar. The fundamental assumption for the determination of the load on a pillar is that each pillar in a large mined area carries an equal share of the overburden load (Tributary Area Theory), given a regular pillar-panel layout, Figure 2-1. The theory is strictly speaking only valid for those cases where the stope span is greater than the mining depth and the mining layout is regular. Regional pillars will affect the load on pillars depending on the stope span. The average pillar stress (APS), according to Tributary Area Theory, is calculated as follows:

$$APS = \frac{\rho g D}{1 - e} \qquad \textit{Equation 2-1}$$

where
- ρ = density (kg/m^3)
- g = gravitational acceleration (m/s^2)
- D = depth below surface (m)
- e = extraction ratio.

From this equation, the factors which influence pillar load are:
1) depth (the deeper the mining, the higher the load),
2) pillar width (the smaller the pillar, the higher the load), and
3) span (the wider the span, the higher the load).

Of these three factors, the pillar width and span can be controlled, while the mining depth cannot.

While this formula assumes that the full overburden load is carried by pillars, the effect of the overburden loading characteristics is not considered. Therefore, the effects of beam bending and stress arching, in shallow to intermediate depth environments, on the loading conditions of a pillar were investigated using numerical modelling.

In this chapter the load acting on pillars (stress) will be dealt with in detail and the results obtained from the numerical modelling will be presented. Due to the many variables which influence the loading conditions at shallow to intermediate depth, design charts to encapsulate the results are impractical. However, many questions relating to the loading system have been answered.

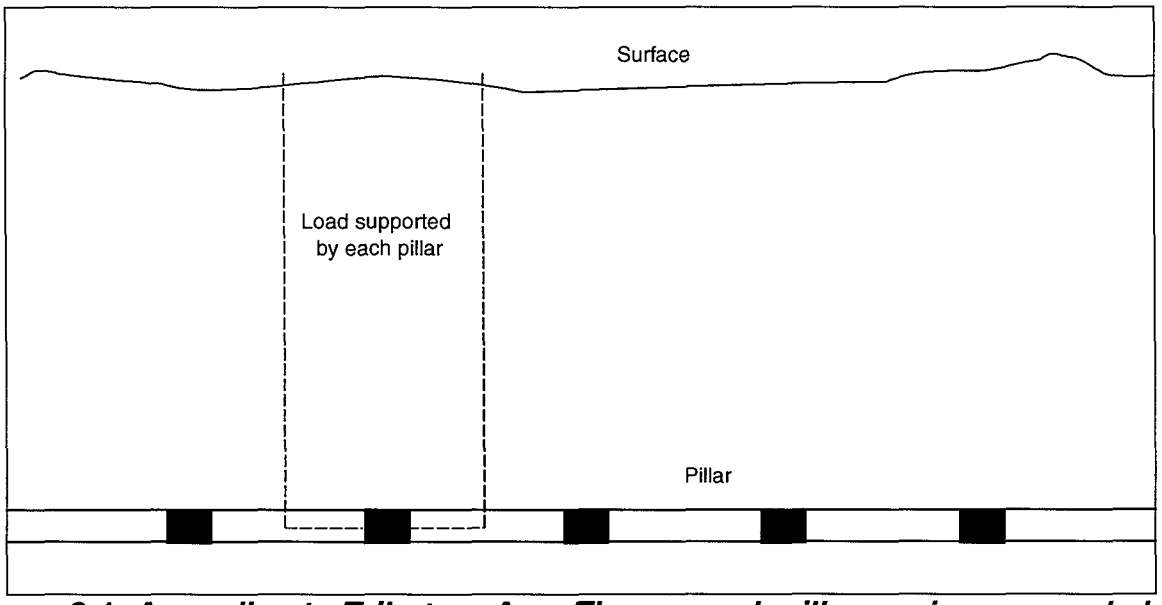

Figure 2-1 According to Tributary Area Theory, each pillar carries an equal share of the overburden weight.

Backbreaks were a significant problem at Cooke Section, Randfontein Estates Gold Mine before crush pillars were introduced (Roberts, 1998). This is a classic example of a backbreak due to large tensile zones in the hangingwall. The *in situ* monitoring and the solution has been reported in this Chapter.

2.2 Research methodology

In these analyses two dimensional (2D) and three dimensional (3D) boundary element models, namely DIGS and MAP3D, were used to calculate average pillar stresses and displacements. During these runs, due to modelling very large layouts and surfaces, some problems were experienced. This reduced the precision of the results and caused long running times. However, using different boundary element programs, it was possible to obtain acceptable accuracy. Therefore, 2D and 3D boundary element models were used together where it was appropriate.

An attempt was also made to use finite difference codes such as FLAC and UDEC and the finite element code ELFEN. However, using these programs resulted in long running times, due to the need to mesh all the geometry and surrounding strata. Therefore, it was decided to use boundary element programs. MINSIM, DIGS 2D and MAP3D were compared in terms of running times and accuracy. The latter two were found to be the most appropriate codes for this modelling programme.

Both the rock mass and pillars were limited to elastic behaviour in all the modelling. The elastic constants employed were: Young's modulus of 70 GPa and Poisson's ratio of 0,2.

At shallow depths, the following factors are considered to have an important effect on pillar loading:

1) the extent of the free surface modelled
2) beam bending and the presence of the free surface
3) mining geometry
4) depth
5) k-ratio
6) span, as it affects the shape and size of the in-panel tensile zone and local support design.

In addition, the applicability of the ¼ depth rule was investigated.

2.3 Results

2.3.1 Finite vs. infinite depth modelling and the effect of the extent of the free surface modelled

If excavations are close to the surface, the loading system is different to that found at great depth. The nature of the loading system is determined by the ratio of the stope span to mining depth. The stope span is defined as the span between abutments, or between regional pillars, where the regional pillars may be considered to properly compartmentalise regional spans. This implies that the regional pillars are able carry the full overburden load, and that regional spans do not "see" the adjacent spans.

As will be shown in Sections 2.3.2 and 2.3.3, the minimum ratio of stope span to depth at which the surface begins to effect the loading system is 0,25. At ratios of stope span to depth less than 0,25, the surface need not be modelled. The loading conditions may then be termed "infinite depth" loading. At ratios greater than 0,25, the surface must be explicitly modelled. The loading conditions are then termed "finite depth". Under these conditions, the rock mass undergoes beam bending, and the tensile zone must be taken into account. These phenomena will be discussed in the following sections.

This section will focus on the required extent of the modelled free surface, so as to properly approximately the effect of the real free surface. This is only relevant under "finite depth" conditions.

The 2D boundary element model DIGS was used in this investigation. The model geometry was nine 5 m wide pillars (10 panels), with 40 m panel spans. The results are shown in Figure 2-2.

As seen from this figure, if the free surface length modelled is at least five times larger than the span of the workings, then the effect of the free surface will be modelled correctly at any depth. This is important when numerical modelling is performed for the purposes of mine design. The ratio of depth/span at which the surface has no effect is dealt with in detail in the next section. All models in this chapter report have been modelled with a free surface 20 times bigger than the overall extent of mining.

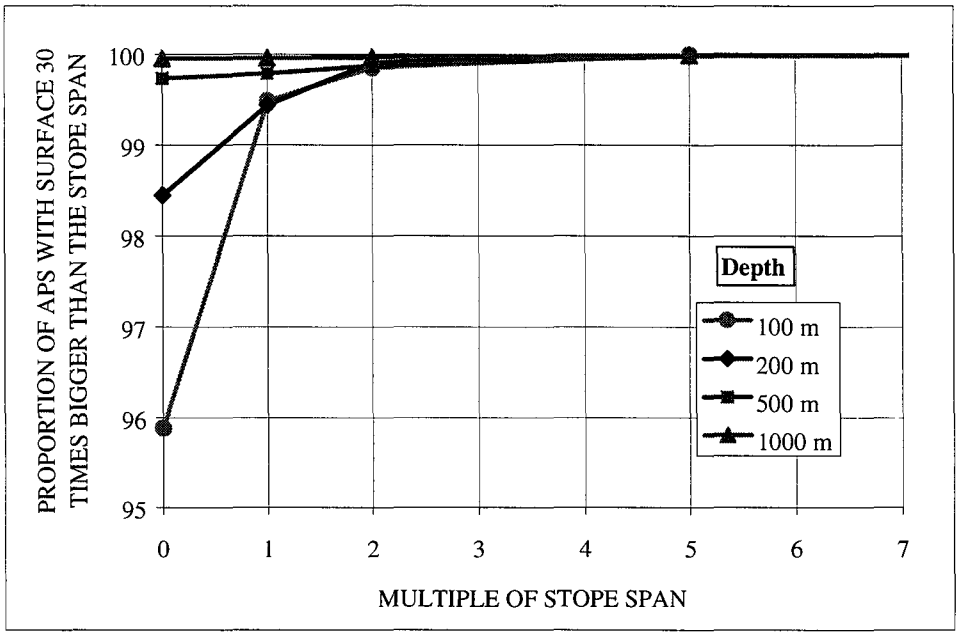

Figure 2-2 Effect of free surface size.

2.3.2 Beam bending

At shallow to intermediate depths, the hangingwall strata to surface may behave as a beam, depending on the ratio of stope span to depth.

To investigate the difference in deformation and APS when the surface is accounted for or not, two numerical models were analysed using DIGS. A virgin stress condition corresponding to a depth of approximately 100 m (vertical stress = 3 MPa) and a k-ratio of 0,5 was used. In the first model, the surface was simulated 100 m above the excavation. In the second model, infinite depth conditions were assumed, with a constant 3 MPa vertical stress field at all depths. In this case, no surface is modelled. These latter conditions correspond to Salamon's assumptions for his solutions of two dimensional problems at great depth.

The model geometry is shown in Figure 2-3. The pillar width was 10 m with two spans of 118 m. The strike length was modelled as infinite. The pillar stress distributions are shown in Figure 2-4. There is a 35 per cent increase in average pillar stress (APS) when the surface is modelled.

In the infinite depth case, the horizontal centre line of the pillar undergoes zero vertical displacement. In the case where the surface is modelled, the pillar centre line, and the stope as a whole moves vertically downwards. If the overall movement is subtracted, then the displacement profiles of the pillar contacts are symmetrical at the hanging-and footwall contacts. The average convergence, and therefore the average strain, is 41 per cent higher in the case where the surface is modelled. This corresponds, approximately, to the 35 per cent increase in APS. The difference is ascribed to the different loading system in the presence of the surface.

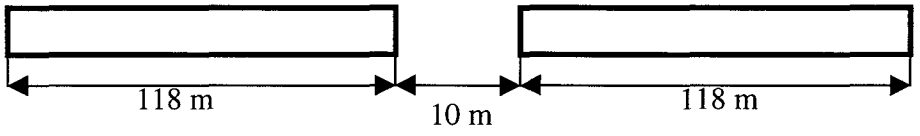

Figure 2-3 Two dimensional geometry of the DIGS model.

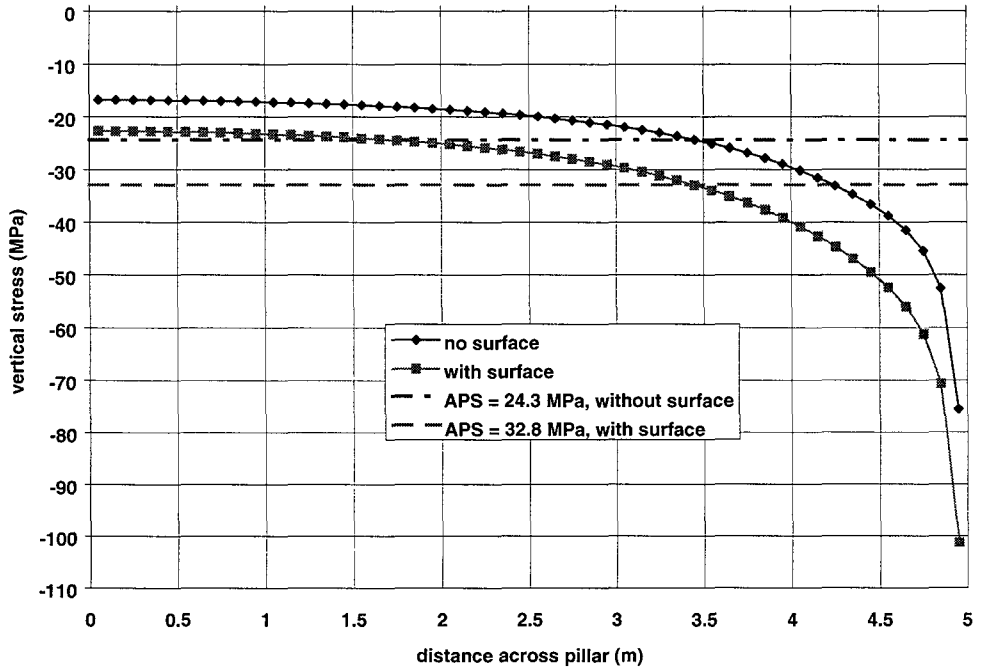

Figure 2-4 Distribution of vertical stress (from the vertical centre line to the edge of the pillar) across pillars under the same virgin stress values, but with the surface modelled at 100 m, and in infinite depth conditions.

The nominal Young's modulus of the country rock was taken as 100 GPa. The resultant moduli of the pillars were found to be 151 and 145 GPa for the infinite depth and finite depth cases respectively. The modelled width to height ratio of the pillars was 10:1. The difference in effective modulus of the pillars and country rock indicates that pillars of increasing width to height ratio could be increasingly stiff. The difference between the two moduli for the two modelling conditions (4 per cent) is not thought to be significant.

The mode of deformation at great depth changes from beam bending at more shallow depths, as shown in Figure 2-5, to the elastic relaxation of a rock mass into an opening. The "T" and the "C" refer to zones of tension and compression.

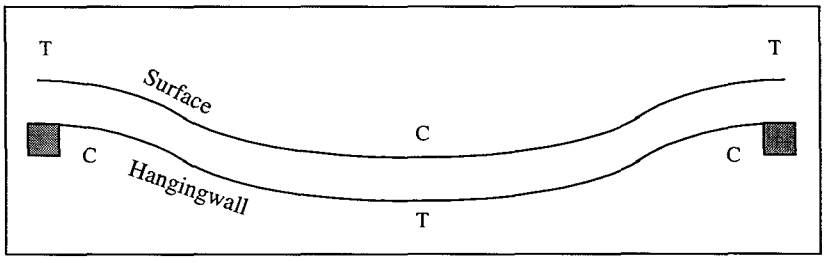

Figure 2-5 Beam bending analogy.

This is shown in Figure 2-6 and Figure 2-7 by examining the shape and size of the tensile zone under the two conditions. In these figures, 240 m wide by 166 m high windows in the hangingwall above the right hand edge of the stope are shown (the left edge is 1020 m away on strike). At a depth of 3000 m (Figure 2-6), the tensile zone is above the stope only. At the shallow depth of 166 m (Figure 2-7), the tensile zone extends over the solid abutment. The top of Figure 2-7 is at the surface. Therefore, the horizontal tensile zones extend to the surface above the abutment. Above the stope, the surface is in compression, while the immediate hangingwall is in tension. This is similar to the stress condition shown in Figure 2-5.

This mechanism is further illustrated in Figure 2-8 by comparing the theoretical hangingwall convergence for a geometry assuming infinite depth to the displacement obtained when the surface is modelled, using MAP3D. The depth modelled was 140 m. The dip span was 300 m, and was therefore more than twice the depth. The hangingwall displacement at the middle of the excavation is plotted in Figure 2-8. The surface plot is that of the point on the surface directly above this point. In this case, the hangingwall displacement far exceeds the theoretical hangingwall convergence. The surface displacement almost matches that of the hangingwall displacement. The entire 140 m thick hangingwall is moving down as a single unit, as shown conceptually in Figure 2-5.

In conclusion, the presence of the free surface has a significant effect on APS and the deformation characteristics, which must be taken into account in pillar system design.

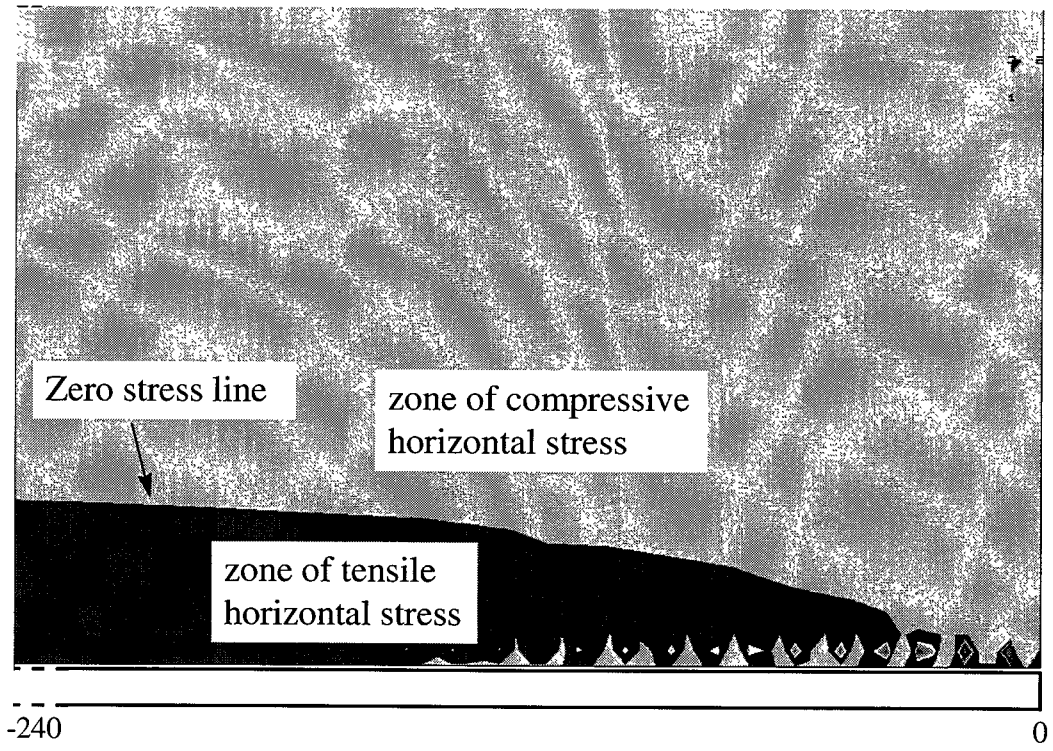

Figure 2-6 Horizontal stress distribution in the hangingwall for the stope at 3000 m depth. The diagram is a cross-section looking in the dip direction, in a window 240 m wide and 166 m high, with the right hand abutment at the bottom right hand corner.

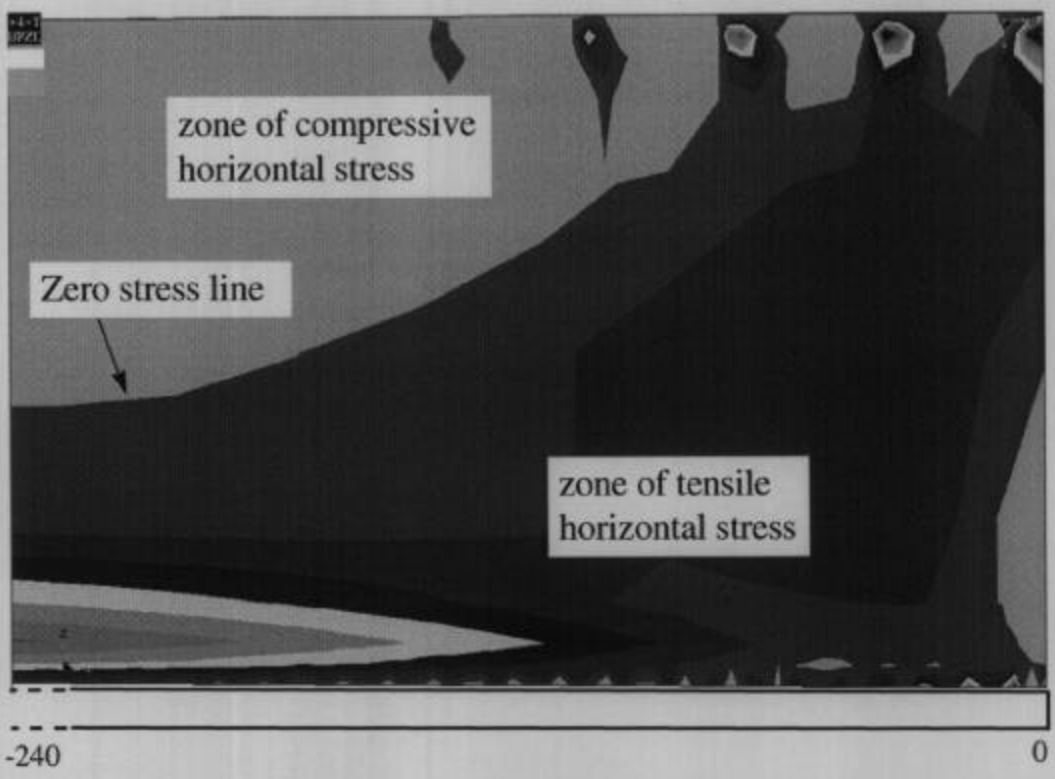

Figure 2-7 Horizontal stress distribution in the hangingwall for the stope at a depth of 166 m. The diagram is a cross-section looking in the dip direction, in a window 240 m wide and 166 m high, with the right hand abutment at the bottom right hand corner.

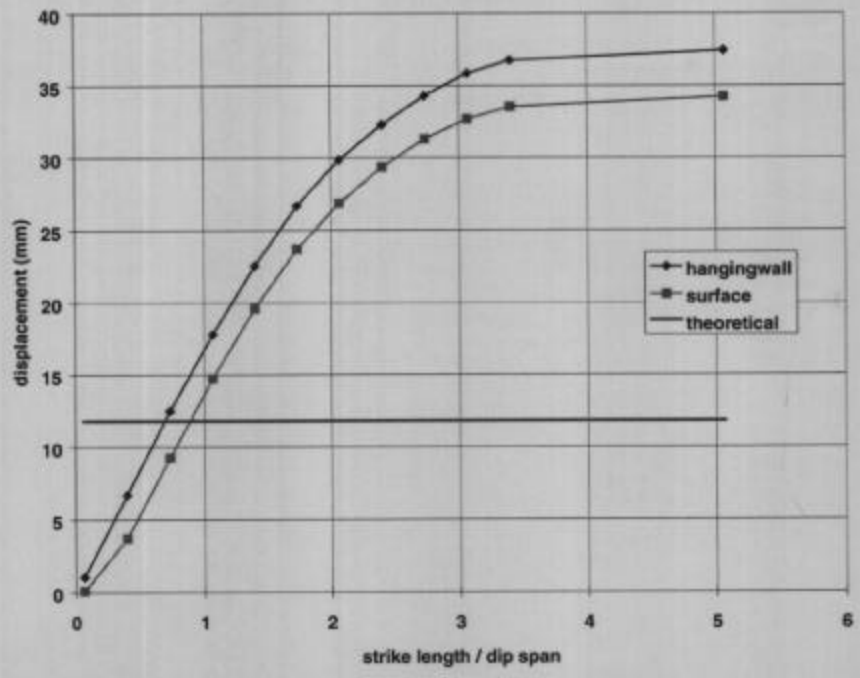

Figure 2-8 Displacement in the hangingwall and on surface compared to the theoretical displacement. The depth was 140 m and the dip span of 300 m was constant. The strike span was increased according to the ratio on the x-axis.

2.3.3 The applicability of the ¼ depth rule

This work examined the rule of thumb that suggests that the maximum span of a stope should be less than a ¼ of the depth before regional support is required. The ¼ depth rule implies that once the ratio of mining span to depth exceeds 0,25 the likelihood of instabilities, including backbreaks, is increased. Empirical evidence for this has been presented by Cummins and Given (1973). They plotted data from over 157 longwall coal mines in Britain. In Figure 2-9, it can be seen that subsidence accelerates at about a width (span) to depth ratio of about 0,25.

MAP3D was used to model the surface displacement for a given geometry as the depth decreased. The rock mass was assumed to be purely elastic. The dip span was 300 m, while the strike span was 1020 m. Thus the depth at which the surface displacement may be expected to accelerate according to the ¼ depth rule is 1200 m.

The results are shown in Figure 2-10. The hangingwall convergence can be seen to begin to deviate from the analytic straight line between 1000 and 1200 m. This agrees with the rule of thumb mentioned above. However this deviation is negligible at 1200 m; the significant deviation is found to be at approximately 600 m, where the span to depth ratio is 0,5.

Thus the trend shown in Figure 2-9 is confirmed. The accelerated closure rate is lower for the elastic medium (Figure 2-10) than for the empirical data (Figure 2-9). The greater acceleration shown in Figure 2-9 must be due to inelastic behaviour of the rock mass at the abutments.

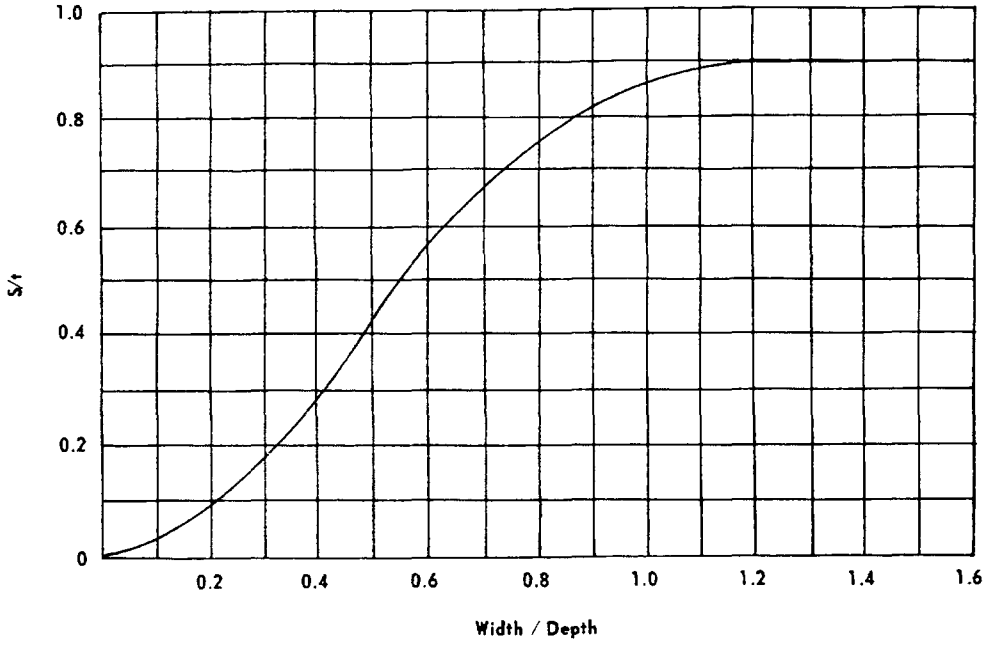

Figure 2-9 Surface subsidence (S) normalised to seam thickness (t), plotted against the ratio of span (Width) to depth (after Cummins and Given, 1973).

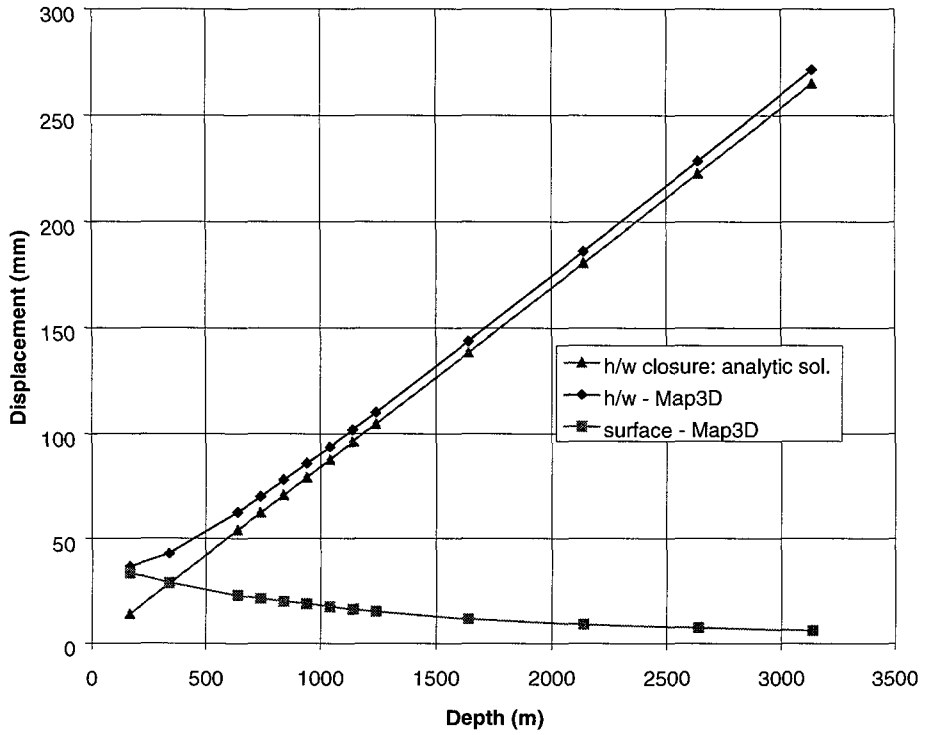

Figure 2-10 The effect of depth on the surface subsidence and hangingwall convergence. The values plotted correspond to the mid-span of the excavation.

In laboratory testing, the platens on the testing machine continue to apply load or displacement to a specimen as it compresses. In the mining environment, the situation is not so simple. The roof strata is not necessarily able to move down and continue to fully load a pillar as it compresses. This can arise when stiffer pillars (regional pillars) surround the pillar of interest. These regional pillars can be stiffer because they have a high width to height ratio. Whatever the reason for their higher stiffness, they provide greater resistance to the weight of the overburden and prevent the roof strata from displacing downwards and continuing to fully load the softer in-panel pillars. Some of the load that would otherwise act on the softer pillar is transferred onto the stiffer surrounding pillars.

The roof strata may be very competent and rigid and therefore not continue to deflect as the pillar compresses. Instead, the roof strata bridges across the in-panel pillars and transfers some of the load onto the panel abutments. In these situations, very large mining spans may be required before the stiffness of the roof strata is reduced to the point where full dead-weight load acts on the pillar. (Hangingwall strata stiffness decreases with increasing excavation width, and decreasing depth.)

In-panel pillars also play an important role in decreasing the height of the tensile zone above the stopes by creating a compression zone above themselves.

In order to investigate the interaction between regional and in-panel pillars, a series of runs was conducted using DIGS.

The results are shown in Figure 2-11. In these runs, three regional spans with two regional pillars were modelled. Figure 2-11 (a) represents the central 234 m wide stope with no in-panel pillars and Figure 2-11 (b) represents the same stope with six 4 m wide in-panel pillars, and seven 30 m panels. The depth was 500 m. In this figure, the black coloured areas in the hangingwall are the zones of vertical tension. If there are no in-panel pillars, the height of the tensile zone is almost 60 m above the panel. In the presence of in-panel pillars, the height of the tensile zone above the panel is very small, as arching between adjacent pillars occurs. This tensile zone is of limited height into the roof.

Also seen in Figure 2-11(a) is that, while there was a tensile zone 60 m above the stope, regional pillars create a compression zone extending to surface above themselves, thus limiting any major failure, possibly induced by large geological structures, to the region between regional pillars.

Figure 2-12 shows the interaction between regional pillars and in-panel pillars. The geometry of the model is the same as that shown in Figure 2-11. Figure 2-12(a) shows the load calculated on a 15 m wide regional pillar with no in-panel pillars. Figure 2-12(b) represents the same regional pillar with six 4 m wide in-panel pillars with spans of 30 m. The average stress on the regional pillars with in-panel pillars is reduced by a factor of four compared to the stress on the regional pillars with no in-panel pillars. In the presence of in-panel pillars, the full overburden load is not transferred to the regional pillars; a significant proportion of the load is carried by the in-panel pillars.

Thus, in shallow mining, down to a depth of about four times the span, the mechanism of hangingwall movement is fundamentally different to that found in deep level conditions. This refers only to the behaviour of an elastic rock mass. Inelastic beam effects at shallow depths and large scale inelastic shear deformations in deep level mines have been neglected in this study. Such phenomena in shallow depths would very likely lead to an increase in the rate of subsidence.

The results shown in Figure 2-9 and Figure 2-10 are for spans with no in-panel pillars. The results shown in Figure 2-11 and Figure 2-12 are for spans with in-panel pillars. A comparison of the two cases implies that the ¼ depth rule need only apply to situations where no in-panel pillars are used. The above results indicate that regional pillars may not be necessary at all in the presence of elastic pillars. However this conclusion is based upon theoretical numerical modelling considerations. In the light of this, it is suggested that regional pillars should be maintained as "barriers", even in the presence of elastic pillars. In the presence of elastic pillars, the ¼ depth rule is conservative. Ratios of span to depths up to ½ are commonly used with no occurrences of backbreaks. This experience, together with the numerical modelling results, suggest that ratios of regional span to depths up to ½ may be safely used.

The above statement that regional pillars may not be necessary at all in the presence of elastic pillars needs to be confirmed by further research and controlled experimentation. This could lead to greater extraction ratios.

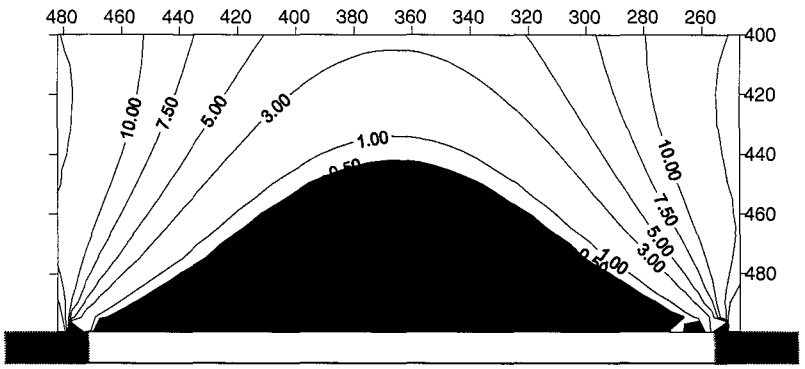

(a)

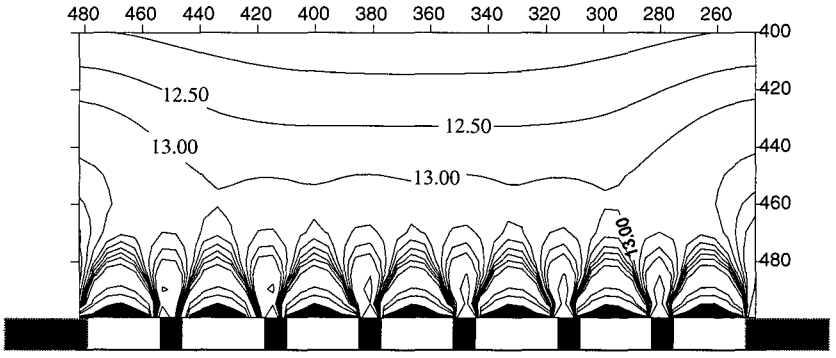

(b)

Figure 2-11 The interaction between regional pillars and in-panel pillars: (a) only regional pillars (b) regional pillars with in-panel pillars.

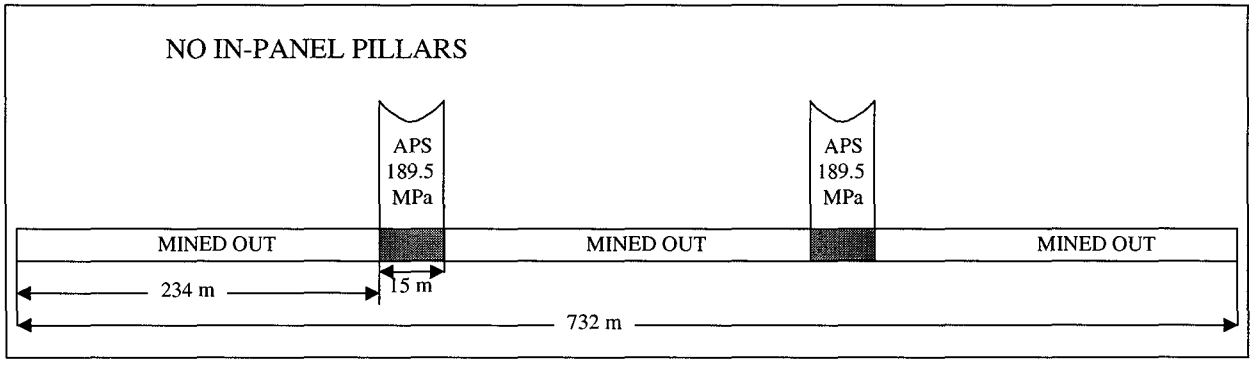

(a)

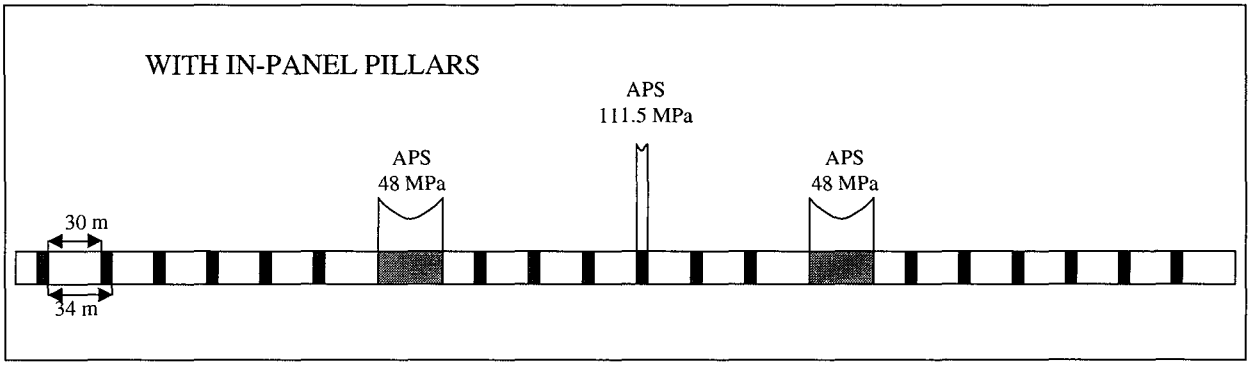

(b)

Figure 2-12 Effect of regional and in-panel pillars on regional pillar loading.

2.3.4 Effect of mining geometry

One of the simplifications often made in pillar design is that of considering the loading on pillars to be that calculated from Tributary Area Theory. In this section this assumption is investigated.

Probably the most critical parameter in the loading system is the geometry, which is the pillar width, panel span and stope span. In order to investigate the effect of geometry, DIGS was used to model different geometries at 200 m depth. The number of in-panel pillars ranged from three to nine. The panel spans ranged from 15 m to 50 m. This resulted in stope spans ranging from 80 m to 600 m. The APS on the middle pillar was calculated.

Figure 2-13 shows the results obtained from this analysis. The figure shows that the percentage difference between the Tributary Area load and that obtained from numerical modelling increased with smaller pillar widths, and with smaller stope spans.

For example, with five rows of 3 m wide pillars spaced at 20 m intervals, i.e. a stope span of 135 m, the central pillar sees only 82 per cent of the Tributary Area load. The pillars closer to the abutments will be loaded even less. This is an important finding, because crush pillars will not crush if the design load acting on them is calculated from Tributary Area Theory. Crush pillar design is discussed in Section 5.6.

From this it can be concluded that the load will be overestimated and that pillars will be over-designed if Tributary Area Theory is used in pillar design, and therefore extraction ratios, especially in deeper stopes, could be compromised. Bigger pillars are stiffer and therefore take relatively higher loads. Smaller pillars are less stiff, take less load, and transfer a greater proportion of the load onto the abutments.

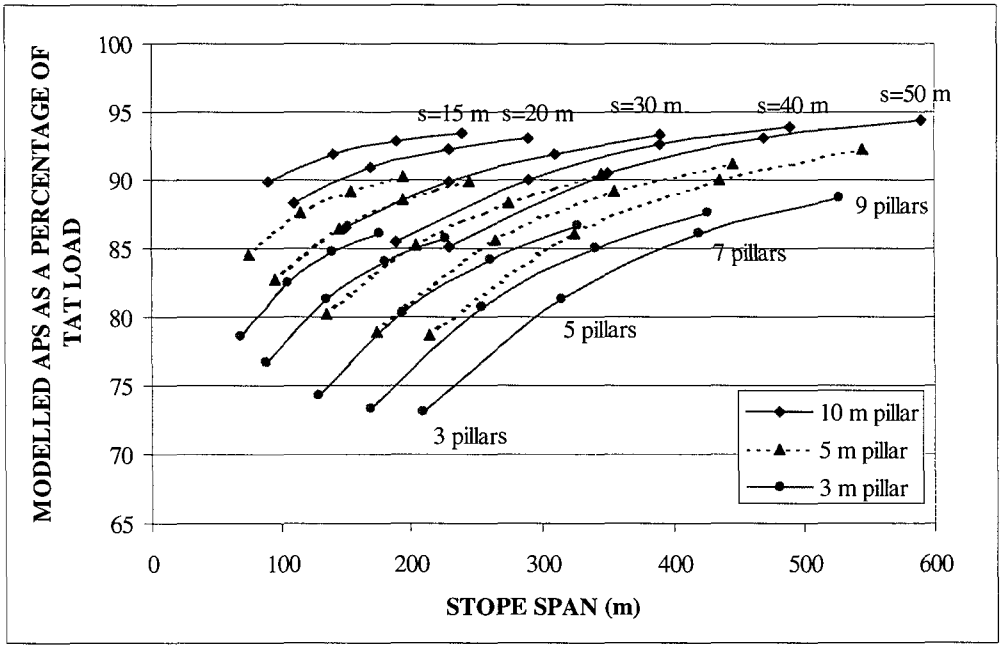

Figure 2-13 The APS as a proportion of the theoretical tributary area load, from numerical modelling of various mining geometries and pillar sizes at 200 m depth.

2.3.5 Effect of depth

In order to investigate the effect of depth on APS as calculated by Tributary Area Theory and numerical modelling, nine 5 m wide pillars (10 panels) were modelled at different depths and panel spans. The results are shown in Figure 2-14. This figure shows that there is a slight

increase between 100 m and 400 m for spans less than 30 m, but at greater depth the change in the proportion of Tributary Area Theory load is negligible.

Thus the results shown in Figure 2-13 remain valid at the range of depths shown in Figure 2-14, although the small variation as depth increases in Figure 2-14 should be noted.

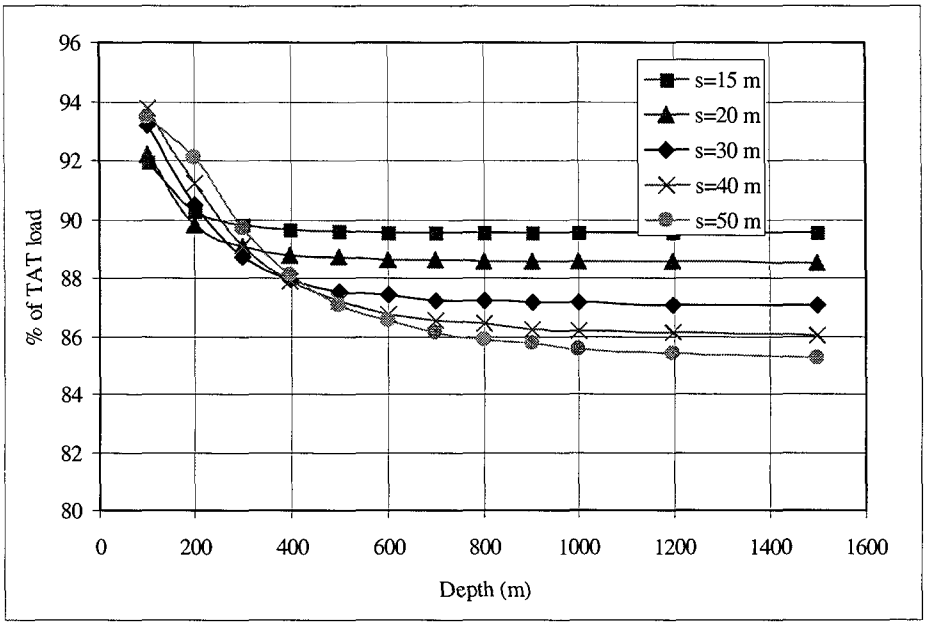

Figure 2-14 The difference in APS as calculated by Tributary Area Theory and from numerical modelling for various depths for 9 in-panel pillars and varying panel spans.

2.3.6 The effect of the k-ratio

The effect of k-ratio on the loading has also been investigated for two depths: 200 m and 500 m. Nine pillars of 5 m width with 20 m panel spans were modelled. The values of k-ratio ranged from 0,5 to 3. Changes in the k-ratio resulted in no difference in the modelled pillar loading (Figure 2-15).

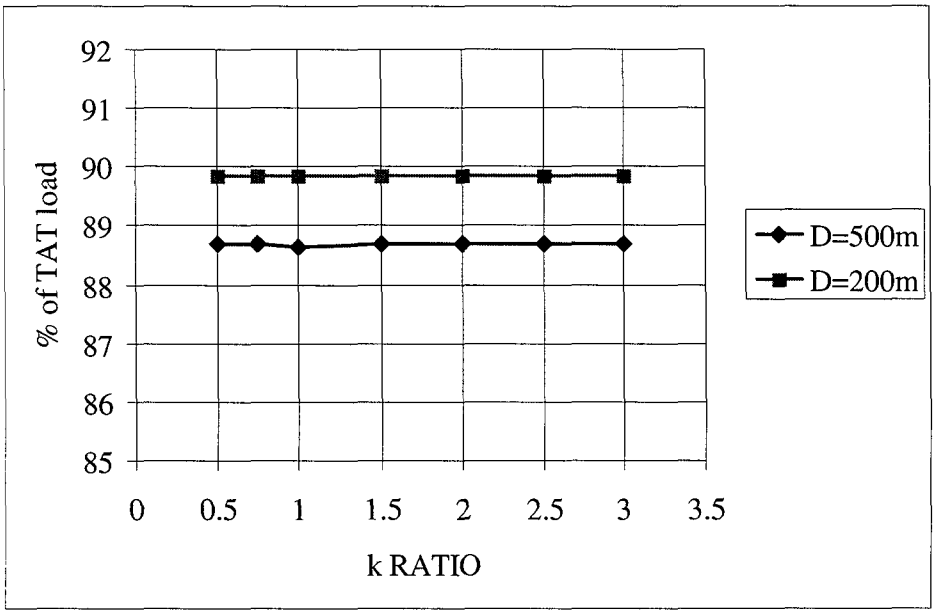

Figure 2-15 The effect of the k-ratio.

2.3.7 The effect of span on the in-panel tensile zone and on local support design

The results from Sections 2.3.5 and 2.3.6 show that the most critical parameter in the loading system is geometry. Pillar width, span and regional spans are important parameters in calculating the load. However, increasing the spans, in the light of pillar loads smaller than Tributary Area Theory loads, might result in unsafe environments due to unstable hangingwalls. The depth of the tensile vertical stress zone as a function of panel span was investigated. In these models, a k-ratio of 2 and depth of 200 m were used with nine 5 m wide pillars in the stope. Figure 2-16 shows the maximum depth of the vertical tensile zones obtained from numerical modelling. At a span of 15 m, the depth of the tensile zone is negligible. The depth of the tensile zone increases to 0,6 m at a span of 30 m. However, the height of the tensile zone increases substantially at spans above 30 m and reaches 3,5 and 5,8 m into the hangingwall for spans of 40 m and 50 m spans respectively. Those thicknesses of strata if defined by partings cannot be supported practically by most types of support.

This indicates that the panel span is a critical parameter in determining the stability of the hangingwall, and hence support requirements as well as the pillar load.

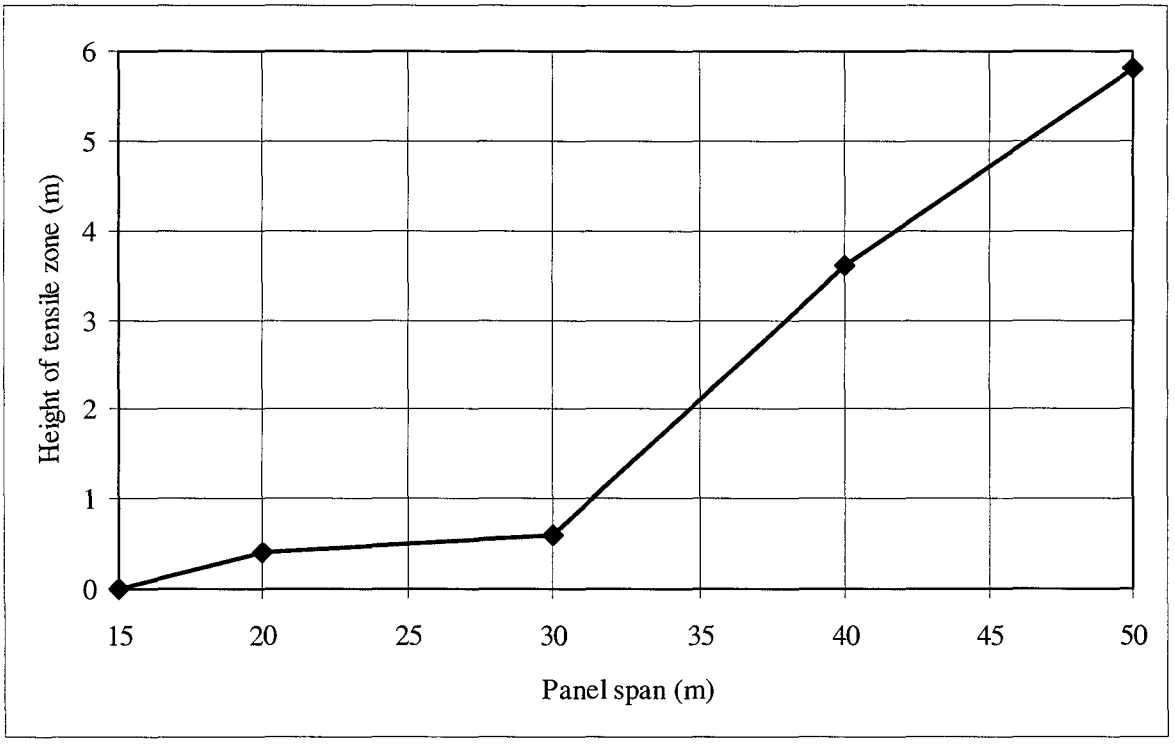

Figure 2-16 Effect of span between pillars on the height of the tensile zone at a depth of 200 m.

2.4 A review of the backbreak problem at Cooke Section, Randfontein Estates

2.4.1 Introduction

Backbreaks are the most catastrophic strata control problem encountered in South African shallow mines. They result in an increased risk of fatalities and huge collapses which destroy

the stope support, and can extend over mined areas well in excess of 20 000 square metres. Early indications of the potential backbreak sequence can be identified through simple monitoring and observations and changes can be made timeously to prevent the full backbreak.

The use of pillars in shallow mining as a component of the stope support system goes back many years when mining was started on the Witwatersrand. In any mining situation it is important to attain safe working conditions and increased productivity. Therefore the design of such pillar support systems needs to be optimised, both for safety and increased extraction. For the purpose of this section, shallow mining is considered to be at depths less than 1 000 metres.

To understand support requirements and rock mass behaviour at shallow depths, it is important to understand the mechanism of the backbreak sequence. An understanding of the backbreak sequence would allow a better assessment of the conditions under which backbreaks are likely to occur and allow informed decisions on the type of pillar support system necessary.

This section is based on observations of operations over the period 1981-1984 on the Cooke Section of the Randfontein Estates Gold Mining Company (Roberts, 1998). At the Cooke Section there are known water-bearing zones in the dolomites, which are separated from the workings horizons by approximately 300 m of lava and quartzite. A number of post Transvaal dykes and faults are intersected in the workings and in the majority of cases these features tap a water bearing horizon located in the dolomites. Therefore, it is also important for the stope support system not only to prevent collapse but to clamp the water bearing features and ensure the integrity of the rock mass in their vicinity. An evaluation of the support systems used will be presented. The backbreak mechanism will be described on the basis of instrumentation observations and the changes that were made to the support system.

2.4.2 Support system used before 1980

The support system previously used on the mine was based on continuous regional stability pillars, left approximately 350 m apart. Stoping operations took place in discrete blocks bounded by strike oriented regional pillars. At this time the internal support system was based on Mark 1 grout packs. These packs consisted of a wooden skeleton surrounding a grout filled sack. The packs had some difficulties associated with them, the more important of these being:

1) Lack of flexibility. A blast every four days had to be planned to accommodate the installation of the packs, thus to break the required tonnage an increased amount of face length had to be worked.
2) High cost of grout based packs.
3) Dangerous practice of having to blast down ore passes which had hang-ups, due to being blocked by grout.
4) Lack of sufficient stiffness of the installed packs for conditions that existed in Cooke Section.

In spite of the robust grout pack stope support, the UEIA reef suffered stope collapses or backbreaks. This reef is characterised by a massive hangingwall and very high strength quartzite.

The collapses which destroyed the stope support extended over mined areas well in excess of 20 000 square metres. In most cases, the problem was exacerbated by the fact that the Randfontein Estates Gold Mine is overlain by water bearing dolomites. In the past, stope collapses have in some cases led to free water inflow into the caved areas, particularly where collapses occurred next to a water-bearing feature.

2.4.3 Instrumentation and observations

Extensometers were installed in the centre gully in a 40 m hangingwall borehole to monitor the hangingwall behaviour as shown in Figure 2-17. Anchors were installed at different intervals in

the borehole to monitor movement in the hangingwall. Closure meters were installed at each extensometer site.

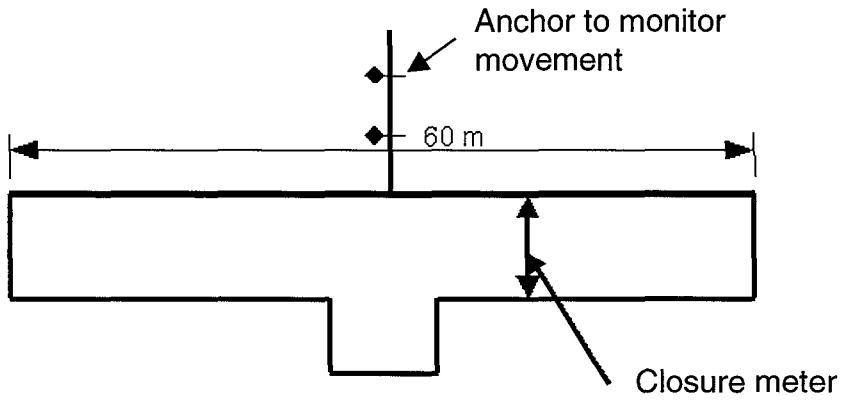

Figure 2-17 A schematic strike section diagram showing instrumentation above stope hangingwall.

Figure 2-18A shows a schematic representation of trends of results from extensometer versus mining span. The extensometer instrumentation was installed after mining spans of 60 m. The corresponding elastic closure along the centre gully is shown in Figure 2-18B.

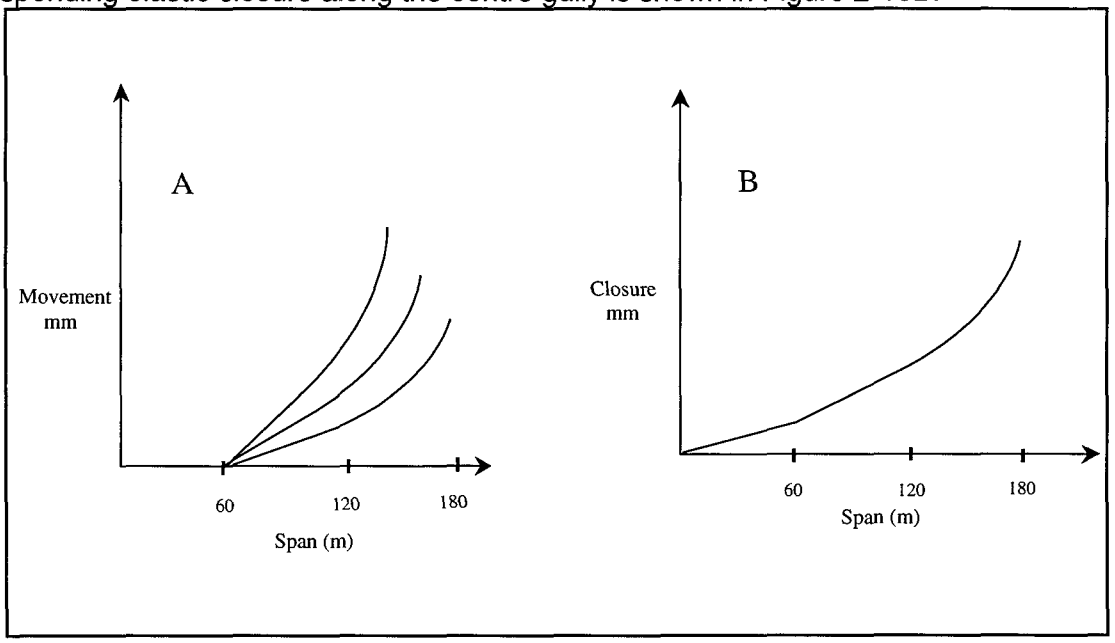

Figure 2-18 Schematic representation of trends of results from a 40 m borehole extensometer in the centre gully (A) and the corresponding closure (B).

At mining spans between 60 m and 120 m, the extensometer detected openings of bedding planes between the anchors, as shown in Figure 2-18A. Bedding planes opened up between 6 m and 40 m into the stope hangingwall, loading the grout pack stope support system. Figure 2-18B shows the increase in closure rates between the mining spans of 60 m to 120 m. The closure was still mostly elastic between the mining spans of 60 m to 120 m.

When the stope span increased from 120 m to 180 m, inelastic deformation in the form of open tensile fractures took place up to 40 m into the hangingwall. Fractures, inclined at 30º, developed on the face, dog earring of drill holes occurred and observed closures were in excess of the expected (elastic) convergence. Once the stope collapse (backbreak) began, closures of 2 m within 24 hrs were recorded. Another prominent precursor to the stope collapses was the development of large open steep dipping fractures in the stope hangingwall, close to the middle of the span. These were often accompanied by a seismic event. Fractures extending up to 12 m

into the stope hangingwall were observed. The fracture length could exceed 100 m and on occasions allowed water inflow into the stope.

At Cooke 1 Shaft, a return airway had been developed in the hangingwall of the reef and then undermined. Using extensometers and information from the conveniently situated hangingwall haulage, it was found that the stope hangingwall collapses migrated 40 m up into the hangingwall.

Further investigation into the cause of these collapses revealed that there was no common span at which collapse occurred. In fact stopes that had collapsed in this way had spans varying from 75 m to 250 m. It was recognised that the conventional stope support systems were not able to support the beams and dead weight evolved. Once the backbreak problem had been more clearly understood with the help of instrumentation, a solution could be found.

2.4.4 Revised stope support system

In order to prevent stope collapses and backbreaks, resistance was required to support the 40 m thick hangingwall beam. The grout pack support was discontinued and replaced by a crush pillar and stick support system. After the introduction of the crush pillar system, extensometers showed that no openings of bedding planes occurred and that the large hangingwall beams were stabilised. The post failure or residual strength of the crush pillars provided the required support resistance to the stope hangingwall. The design of the crush pillars requires that the pillars are fractured when cut and formed at their residual strength.

The depth at which elastic pillars can be replaced by crush pillars varies. This depth has been defined as the transition zone by Özbay and Roberts (1988). The transition zone was defined as a range, rather than a single depth, to account for uncertainties in load and pillar strength, and practical difficulties in cutting pillars of the correct dimensions.

The revised regional support system consisted of discontinuous regional pillars at 150 m spacing. The internal support consisted of strike pillars and sticks. The strike pillars were located 1,5 m on the down dip side of the strike gullies, which were approximately 30 m apart on dip. At a mining height of 1,0 –1,8 m, the pillars were 9 m in length (on strike) with a dip dimension to yield an approximate width to height ratio of 2:1. This was found to be correct and the pillars crushed close to or on the face when subjected to stope closure of about 9 millimetres, equivalent to about six millistrains.

2.4.5 Crush pillar design requirements

The design of the crush pillar is very critical to the success of the system, and is dependent on the width to height ratio. It has been found from experience underground that, at mining heights of between 1,0 m and 1,8 m, the pillar width to height ratio should not exceed 2:1. At greater width to height ratios, the pillar does not initially fracture in the stope face and dangerous pillar bursting can occur. At width to height ratios less than 2:1, the pillar can be cut but accurate cutting is required. Pillar length can be varied but because of ventilation and geometric limitations, this contributes only a small change to extraction ratios. For the pillar layout used, an extraction ratio of about 92 per cent was attained.

2.4.6 Residual pillar strength

The performance of the crush pillars allowed a back analysis to be undertaken to determine the minimum residual stress in the crush pillars, such that no bed separation occurred up to 40 m above the stope. Using this information, and with the given mining layout, Özbay and Roberts (1988) showed, by back analysis of many collapsed and non-collapsed stopes, that the pillars maintained a residual strength of 13 MPa at a strain of 0,4 (see Figure 2-19 below). The

stabilisation of the 40 m thick mass of hangingwall required a support resistance of 1,1 MPa over the whole stope, which translates to a minimum pillar residual strength of 13 MPa.

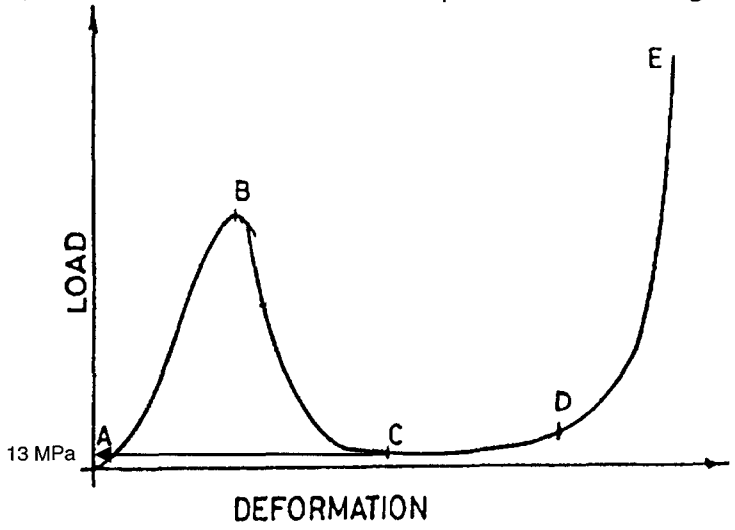

Figure 2-19 Load-deformation laboratory results from rock specimen. Regions A-B, B-C, C-D represent pre-peak, post-peak, residual strength respectively and, after D, strain hardening respectively.

The support resistance (1,1 MN/m^2) of the crush pillar system is significantly higher than that can be achieved by any conventional support system, excluding backfill. Figure 2-20 shows a comparison of a pillar system with other support systems.

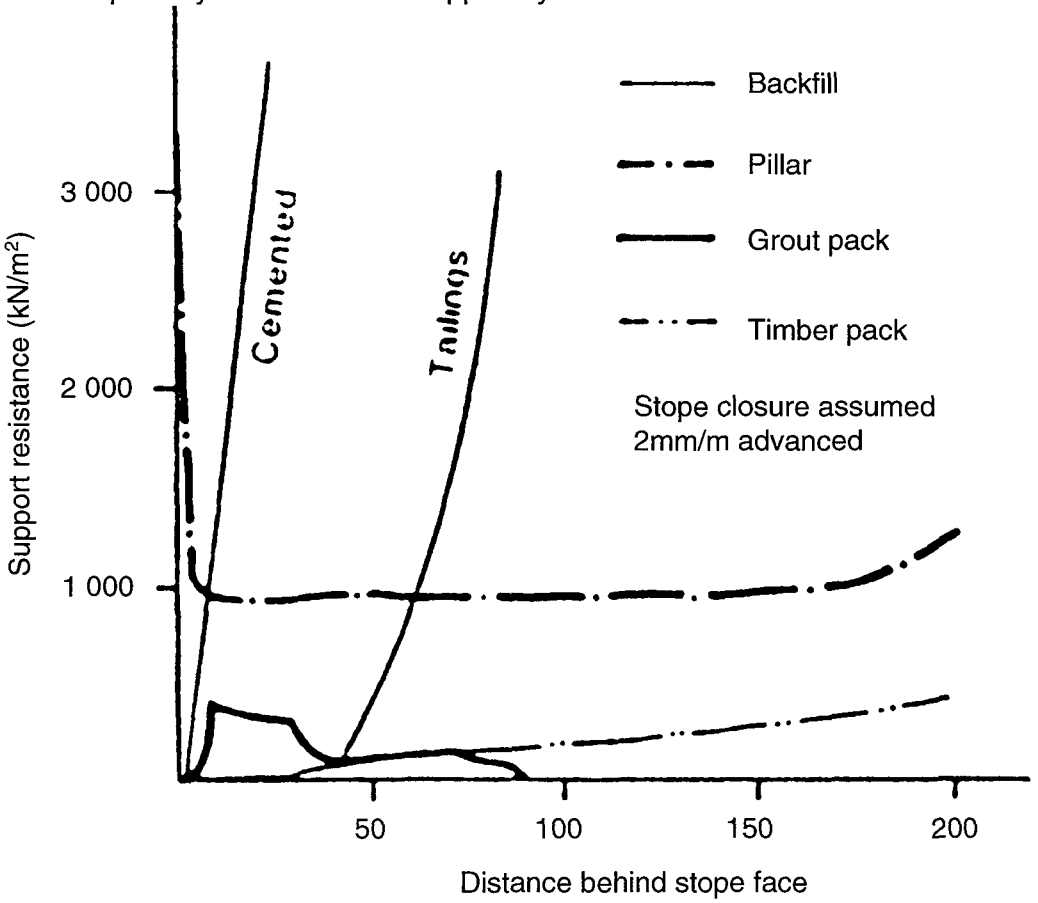

Figure 2-20 A comparison of backfill, grout pack, timber pack and crush pillar support systems showing support resistance as a function of the distance behind the stope face (after Özbay and Roberts, 1988).

2.5 Conclusions

Extensive numerical modelling has shown that there are many parameters affecting the loading system in shallow to intermediate depth mines. However, the most critical parameter is the geometry as defined by pillar width, panel span and stope span.

While depth and k-ratio have a negligible effect on the calculated load, the free surface has a major influence on the calculated APS, which can increase the APS on a pillar by 35 per cent. Therefore it is necessary that modelling for shallow mine layouts (< 1 000 m) should be done using the finite depth approach, where the length of surface modelled should be at least five times the mining span. A more general guide is that where the ratio of regional spans to mining depth exceeds 0,25, the surface should be modelled. Where the ratio of regional spans to mining depth is smaller than 0,25, the surface need not be modelled.

The various figures in this chapter have included the elastic effects of surface and beam bending. In shallow mining, the mechanism of hangingwall movement is fundamentally different to that found in deep level conditions. This refers only to the behaviour of an elastic rock mass. At shallow depths, the hangingwall strata to surface behaves as a beam, depending on the ratio of stope span to depth (up to a maximum of 0,25), whereas at greater depths the elastic response of the rock mass is relaxation into the excavation together with inelastic effects.

In-panel pillars play an important role in reducing the tensile zone above the stopes. In the presence of in-panel pillars, elastic theoretical numerical modelling shows that the ¼ depth rule is not applicable. Ratios of span to depths up to ½ are commonly used with no occurrences of backbreaks. This experience, together with the numerical modelling results, suggest that ratios of regional span to depths up to ½ may be safely used. In the presence of in-panel pillars, the overburden load is not fully transferred to regional pillars. This can result in four times less load on the regional pillars, depending on the geometry.

The above statement that regional pillars may not be necessary at all in the presence of elastic pillars needs to be confirmed by further research and controlled experimentation. This could lead to greater extraction ratios.

Tributary Area Theory can overestimate the load acting on pillars by over 30 per cent for a geometry comprising three rows of 3 m pillars in a 200 m stope span, and by 25 per cent for a geometry of five 30 m panels supported by 3 m wide pillars. The Tributary Area loading assumption therefore can lead to the over-design of pillars. However, the opposite effect could be obtained when carrying out back analyses, where non-failed pillars are assumed to carry the Tributary Area Theory calculated load, with negative safety implications.

Stope span and regional pillars are also important factors which can be modified to reduce the tensile or unstable zone above the stopes and influence the strata stiffness.

The height of the tensile zone should also be considered in the design of local support. The results showed that with in-panel pillars the tensile zone increases significantly when the span exceeds 30 m. At spans greater than 40 m, it would difficult to provide sufficient support with practical spacings of conventional elongate support units. This is ameliorated by high k-ratios.

In the study of the backbreak phenomenon at Randfontein Estates, it has been shown that backbreaks can cause massive stope collapses that will affect safety as well as productivity in the mines. Conventional support systems (grout packs) are unable to support the dead weight of the beams caused by bed separation in the hangingwall and, as a result, stopes suffered backbreaks causing loss of panels and increased fatality and injury risks.

The backbreak mechanism sequence could be monitored from an early stage and changes made to the support system, on the basis of data obtained from proper instrumentation. The

crush pillar support system was able to bear the full thickness of the hangingwall up to the discontinuities (40 m) with no bed separation. Furthermore, the pillars were able to assist in the control of water into the mine workings.

2.6 References

Cummins, A. B. & Given, I. A. 1973. SME Mining Engineering Handbook, Soc. of Min. Eng. of The American Inst. of Min., Met. and Pet. Eng., Inc. New York.

Roberts, M. K. C. 1998. Personal communication on the backbreak problem at Cooke Section, Randfontein Gold Mine. CSIR Miningtek, PO Box 91230, Auckland Park, 2006, South Africa.

Özbay, M. U. and Roberts, M. K. C. 1988. Yield pillars in stope support *SANGORM symposium : Rock Mechanics in Africa*. Swaziland.

3 Determination of the influence of rock mass parameters on the stability of panels between pillars

3.1 Introduction

This chapter addresses Enabling Output numbers 5 and 6 (see page 13).

Generally very little geotechnical monitoring has been carried out on the platinum mines. The current panel spans (defined as the distance between in-panel pillars) and support configurations are often based on what worked in the past. This approach can result in a lower than necessary extraction ratio or in some cases dangerous mining conditions. Much of the shallow reserves have been mined out and rock engineers require a suitable guide, based on a fundamental understanding of the rock behaviour allied to experience, for the mining of these deeper reserves under different geotechnical conditions. Initially, an approach of predicting stable panel spans based solely on a rock mass rating of discontinuities was adopted. A "Critical Panel Span Design Chart" (chart) was developed empirically, based on an analysis of collapsed and stable panels on the Merensky Reef. The system appears to have been generally successful but it is doubtful if the rating system was sufficiently comprehensive. The development of the chart, *in situ* instrumentation and laboratory work is described below.

3.2 The development of the Critical Panel Span Design Chart

3.2.1 Introduction

Only panels mined on the Merensky Reef were considered for this chart. Between 10 m and 30 m above the Merensky Reef (depending on the locality), there is a distinct discontinuity, located at the base of the Bastard Reef (see Figure 3-1). It is suspected to be a plane of weakness along which a parting could take place. Pillars are currently being designed (using equations derived from coal pillars) to support the material up to this discontinuity. The panel spans between these pillars are restricted by the capabilities of conventional support, such as elongates or packs, to prevent parting within the tensile zone and resultant collapse of the hangingwall. The stability of these panels would depend, in part, on the strength of the rock mass. The rock mass strength is largely dependent on discontinuities (frequency, dip, orientation persistence and filling), serpentinization (both of joints and rock mass) and "domes" (curved, anticline shaped joints). The immediate hangingwall rock type is mostly pyroxenite and does not vary significantly over the Bushveld Complex. Serpentinization of the rock mass only appears to be prevalent in highly jointed areas. The strength variation could therefore be considered proportional to a discontinuity index. This chapter attempts to give a guide for ensuring stable panel spans based on an evaluation of discontinuities, using a geomechanical rock mass rating system. However, dome structures occur randomly and vary in size from 1 m - 30 m. These are difficult to control and comprise a separate study.

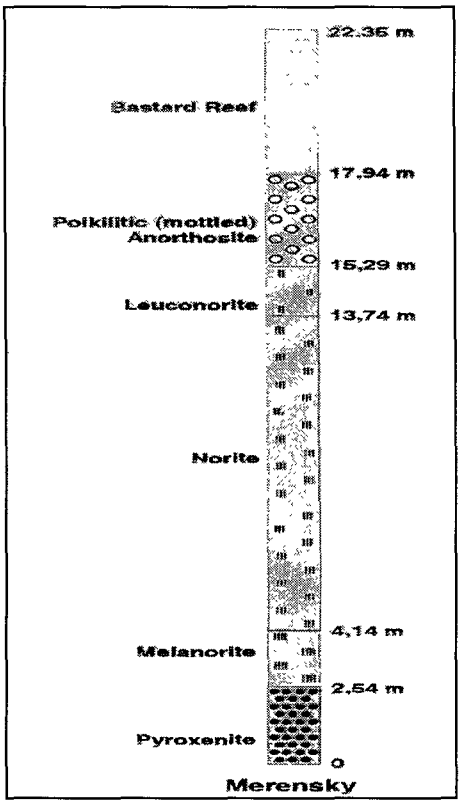

Figure 3-1 A typical stratigraphic column above Merensky Reef.

3.2.2 Methodology

Twelve panels were evaluated in terms of discontinuities using different rating systems. The chart was developed considering timber or grout packs as support, where an unsupportable thickness of rock in a fall of ground (FOG) would be anything greater than 3 m. Therefore, a collapse was considered to be a FOG greater than 3 m thick.

Descriptions of the sites included in the chart are given in CSIR Miningtek Technical Report 98/0440.

The joint survey data was evaluated using four rock mass classification methods (see CSIR Miningtek Technical Report 98/0440). Rock quality designation (RQD) values for most of the evaluated sites were estimated using Equation 3-1 (Afrouz, 1992). In the case of the instrumentation sites, RQD values were calculated from borehole core up to 10 m into the hangingwall.

Generally the parameters described in Table 3-1 (Impala system) provided what was considered the most accurate description of actual observed conditions and therefore this system was adopted for the chart. The analysis required a joint survey down the centre gully, and the discontinuities were assessed using Table 3-2. A "Q" value was determined using Equation 3-2. Figure 3-2 shows that the Impala system was more sensitive to shallow dipping discontinuities than the NGI system. However, this tool does not predict the aspect of stress influences or discontinuity orientation and persistence.

$$RQD = 115 - (3{,}3 \times J_t) \qquad \textit{Equation 3-1}$$

Where J_t is the number of joints per cubic metre.

$$Q = (RQD/J_n) \times (J_r/J_a) \times (J_w/Srf) \qquad \textit{Equation 3-2}$$

Where RQD = Rock quality designation

J_n = Number of joint sets
J_r = Joint roughness
J_a = Joint alteration
J_w = Joint water
Srf = Stress reduction factor.

Table 3-1 Impala adaptation of the "NGI Tunnelling Quality Index".

PARAMETER	UNION-1 RATING	AMANDEL-1 RATING	LEBOWA-1 RATING	AMANDEL-2 RATING	AMANDEL-3 RATING	AMANDEL-4 RATING	LEBOWA-2 RATING
RQD	44	57	82	100	89	98	100
Jn	6	6	12	6	12	6	12
Jr	0,5	1,0	1,0	1,0	1,0	1,0	1,5
Ja	8	4	4	2,5	4	4	4
Jw	1	0,66	1,0	1,0	1,0	1,0	1,0
SRF	5	0,5	5	2,5	7,5	0,5	5
Q	0,09	3,14	0,34	2,66	0,25	8,17	0,62
	Very poor	Fair	Very poor	Fair	Very poor	Fair	Very poor

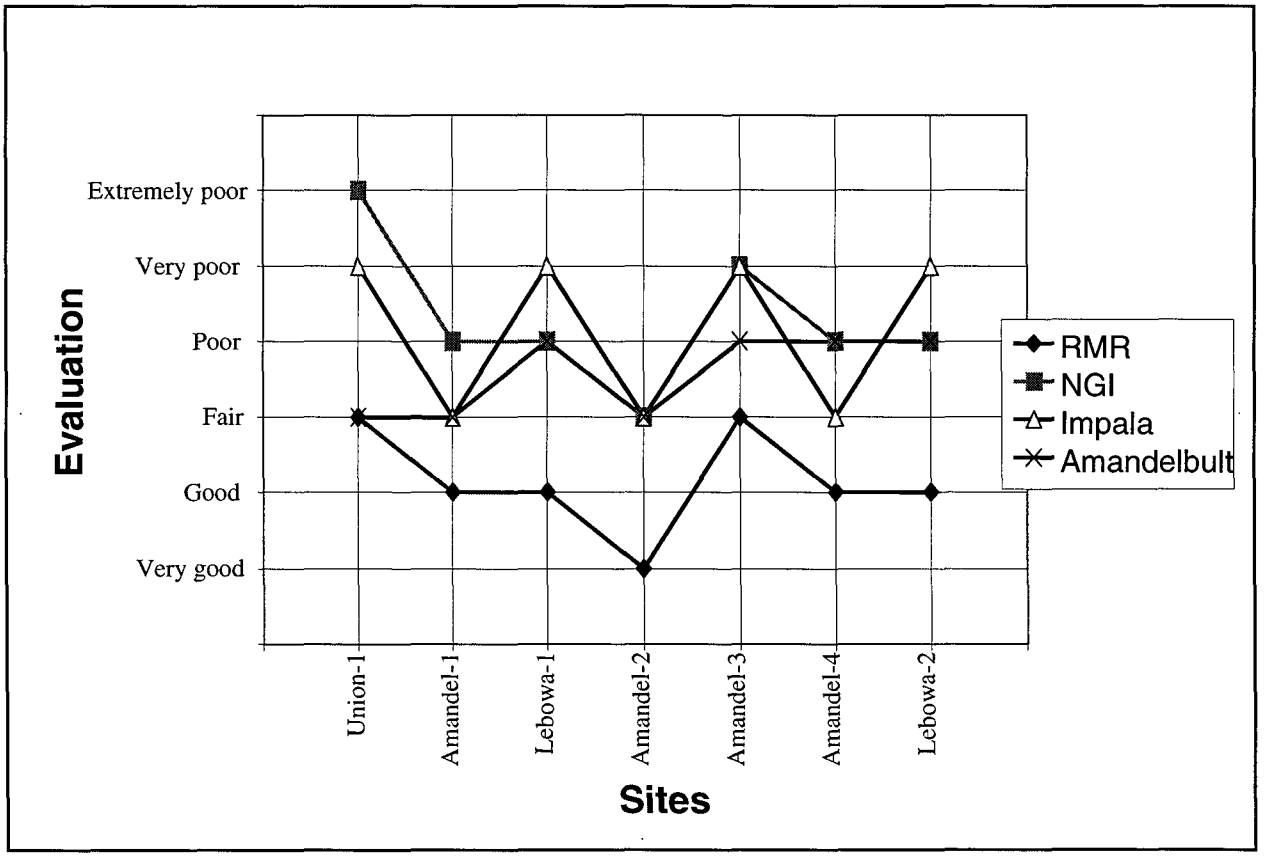

Figure 3-2 Comparison between the rock mass rating systems.

3.2.3 The Critical Panel Span Design Chart

Figure 3-3 defines stable and unstable spans using the results of Equation 3-2. The sites where a collapse occurred are circled. The regression fit was performed on the collapsed cases, except Lebowas-5 case. This defined the "critical line", with stable panel above the line, and unstable panel below the line.

Amandel-2 contained a fault. In Figure 3-3, Amandel-2 has been plotted twice since it was obvious that if the fault had not been there it would have been a stable panel. The point that is indicated by the arrow is the value attributed to this site assuming no fault. By excluding the fault in the analysis, there is a five times increase in the rock mass rating value. This result indicated that major discontinuities should be considered and supported separately.

The position of Amandel-1 indicates that the span could have been greater, and, therefore, if the chart had been used, the extraction ratios could have been increased. The Amandel-3 panel started at a span of 17 m with good mining conditions. When the span was increased to 30 m, conditions deteriorated dramatically without there being a change in rating. This site shows that a change in span can affect mining conditions. Lebowa-5 collapsed on horizontal fracture planes, which appeared to have formed due to high horizontal stress. This site plotted well below the predicted critical span, highlighting the need to include stress in the rating assessment.

Another anomaly was found at Impala-1, where a large stable panel span of 77 m plotted just above the critical line. Stress measurements performed at this site (Figure 3-4) indicated no tensile stresses in the hangingwall. This site is discussed in more detail in Section 3.4.7.

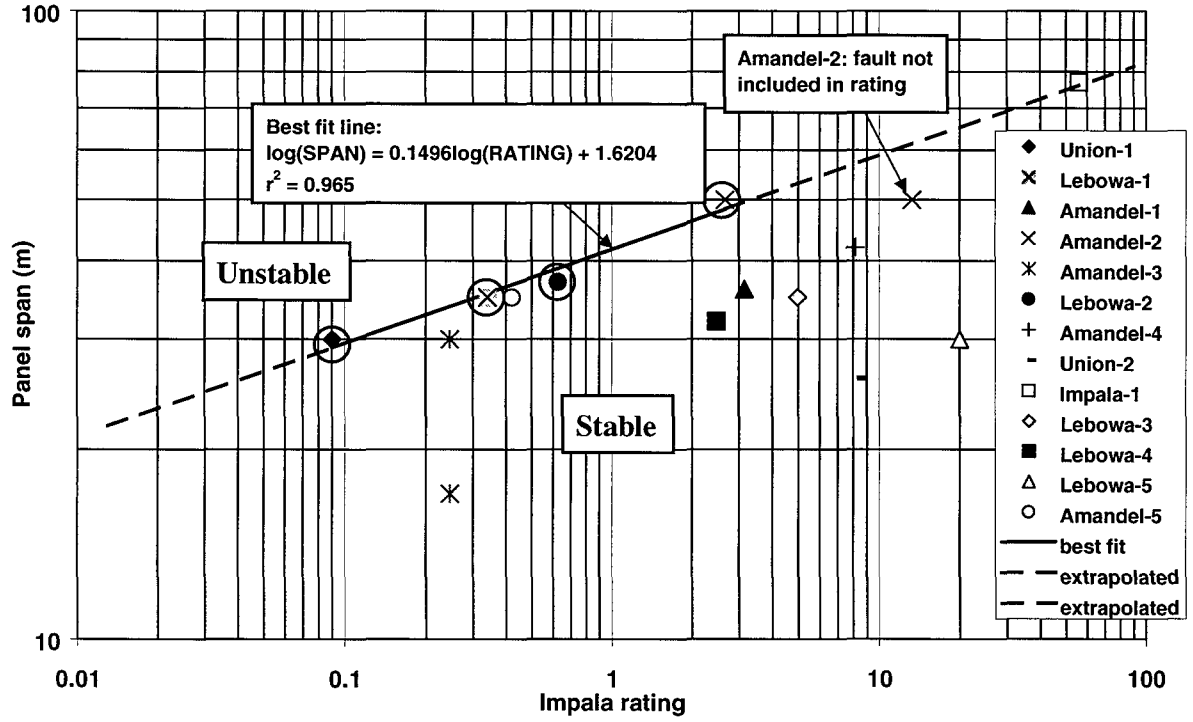

Figure 3-3 Proposed design chart for determining unstable spans (based on the Impala system).

3.3 Worked example using the "Critical Panel Span Design Chart"

3.3.1 Introduction

In this section the methodology behind the rock mass rating is explained. It is envisaged that an assessment could be made during the ledging stage and therefore the panel spans decided before planning the positions of the advanced strike gullies (ASG's).

3.3.2 Method

A joint survey would be performed down the whole length of the centre-raise of the panels that are to be assessed. The assessment should be repeated at several sites in a strike direction, i.e. from face to face. It is important to note the dip angle and strike of the joints in order to identify sets. The total number of joints in each set should be counted so that a fair assessment of the RQD can be made. In the chart, RQD was generally assessed from vertical borehole core, but it can also be calculated from Equation 3-1. The number of joints in a cubic metre can be assessed by calculating the average distance between joints in a set, and including the orientations and dips of each set. . The evaluation of the joints should be performed on the most dangerous set. Joint roughness should be assessed by using offsets from a metre ruler (see Table 3-4). Joint filling thickness, type and whether there has been any shearing (slickensided), as well as the presence of water, should be noted. The results should be analysed in terms of Table 3-2, Table 3-4 and Equation 3-2. The resulting Impala "Q" value would be applied to the chart (Figure 3-3). The panel span would be chosen such that it should be below the critical curve. Therefore, a span just less than the measurement on the curve could be used.

Table 3-2 Impala rock mass rating system (after Barton and Grimstad, 1994).

Description	Value	Description	Value
1) RQD		**4) Joint alteration**	**J_a**
a) Very poor	0 - 25	a) Tightly healed, hard impermeable filling	0,75
b) Poor	25 - 50	b) Joint wall stained only	1
c) Fair	50 - 75	c) Slight in fill, joint walls coated	2,5
d) Good	75 – 90	d) Soft serpentinite, clay in filling	4
e) Excellent	90 - 100	e) Zones of shear – thick bands of serpentinite.	8
2) Joint set number	**J_n**	**5) Joint water**	**J_w**
a) No joints	1	a) Dry	1
b) One joint set	2	b) Dripping water	0,5
c) One joint set + random	3		
d) Two joint sets	4	**6) Stress reduction factor**	Srf
e) Two joint sets + random	6	a) No shear, fault, dyke – good rock	0,5
f) Three joint sets	9	b) Single shear, fault, dyke less than 1 m wide	2,5
g) Three joint sets + random	12	c) Flat or curved joints, competent surrounds	5
h) Four joint sets or more	15	d) Flat or curved joints, incompetent surrounds	7,5
i) Sheared rock	20	e) Multiple shear, faults, dykes, incompetent sur.	7,5
		f) Wide shear zone, more than 5 m.	10
3) Joint roughness	**J_r**		
See Table 3-4			

Example 3-1The use of the empirical Critical Panel Span Design Chart.

A typical panel on the Merensky Reef could have the discontinuity properties shown in Table 3-3. These values are evaluated according to Table 3-2 and Table 3-4 and accumulated in the right hand column of Table 3-3 to obtain the example rating of 8,1. The chart (Figure 3-3) indicates a maximum span of about 57 m for a Q-value of 8,1. The collapsed sites plotted within

10 per cent of the critical line on the chart (excluding Lebowa-5, which was stress induced). Therefore, a safety factor of 1,1 should be applied to ensure a safe span of about 52 m.

Table 3-3 Typical example of a panel on the Merensky Reef.

Description	Value
1) RQD – Two joint sets spaced at about 0,5 m each and random joints, giving a maximum of 5 joints in a cubic metre.	98
2) J_n – Two joint sets + random	6
3) J_r – Smooth planar	1
4) J_a – Soft serpentinite filling in at least one of the sets	4
5) J_w – Joints dry	1
6) Srf – No shear, fault, dyke – competent surrounds	0,5
Rock mass rating (modified Q-value)	**8,1**

Table 3-4 Relationship between offsets and joint roughness (J_r) (after Barton, 1997).

Joint description		Off-set	J_r
Stepped	Rough	11	4
	Smooth	9	3
	Slickensided	8	2
Undulating	Rough	9	3
	Smooth	8	2
	Slickensided	6	1,5
Planar	Rough	2,3	1,5
	Smooth	0,9	1,0
	Slickensided	0,4	0,5

3.4 Description and discussion of instrumented and collapsed sites studied

3.4.1 Introduction

Several panels were instrumented across the Bushveld Complex at various depths to gain an understanding of the rock mass behaviour and to see if stable panel spans could be assessed

by discontinuities only. In addition to some, as yet, unexplained phenomena, several interesting facts were discovered.

Some sites were simply investigated after a collapse, or large FOG, had occurred. These sites were not instrumented. These collapses were carefully analysed to identify the mechanisms of failure.

More detailed site descriptions and analyses are supplied in CSIR Miningtek Technical Report 98/0440.

3.4.2 Installation methodology

For the sites that were instrumented, rock mass movement was initially monitored using extensometers, closure-ride meters and crack meters. Support behaviour was also monitored and correlated with the closure. After having visited many collapsed and stable sites, as described in Section 3.2, several questions arose concerning the stress-state of the hangingwall before and after mining, and the effect of the face and pillars on horizontal stress. Stress measurements were carried out at three different sites to answer these questions.

3.4.3 Union-1

Numerical modelling with MINSIM-W showed an expected closure of approximately 35 mm, which was about one tenth of the measured closure of 340 mm. Most of the movement occurred in the footwall with approximately 65 mm inelastic movement in the hangingwall. A borehole camera survey indicated that most of the hangingwall movement occurred in the immediate 4,5 m. Many more low angle joints/fractures were observed in this 4,5 m zone than when the hole was originally geotechnically logged (before mining had begun), indicating that horizontal stress fracturing had taken place up to this height. A back analysis performed using MINSIM-W and assuming a tensile zone of 4,5 m, indicated a k-ratio of 0,5. However, it is doubtful if the observed fractures resulted from a tensile stress. It is more likely that high horizontal stresses caused extension fracturing to develop when the confinement was removed by extracting the reef below and therefore the k-ratio could not have been that low. At a span of 30 m a significant increase in closure rate occurred, indicating that the panel had reached the critical span, which resulted from the combination of inherent geological discontinuities and the stress fracturing.

3.4.4 Amandel-1

Very little, if any, movement was indicated by either the extensometer or the borehole camera at the Bastard Reef contact. This demonstrates that the span between the pillars was stable for the assumed plate thickness of 18 m. However, visual observation indicated that these pillars, designed to be 4 m x 4 m "crush" pillars, had not failed. A partial explanation for this is discussed below.

Large amounts of inelastic movement were measured by the footwall extensometer, indicating footwall heave and therefore pillar punching by the "crush" pillars. This phenomenon was confirmed by the closure results, where the greatest closure was measured close to the pillars. A borehole camera survey, performed after mining had been completed, showed numerous open joints and fractures below the footwall contact. Observations of steep shear zones near the "crush" pillars also indicated that the pillars were punching into the footwall.

Conditions in the panel indicated that the span could have been greater. The span for the rock mass rating at the site fell below the critical span curve in the chart (Figure 3-3).

3.4.5 Lebowa-1

The total amount of closure was small and the instrumentation did not indicate a pending collapse. Nevertheless a sudden collapse, preceded by a few minor falls well behind the face, occurred. The extensometer indicated the thickness of the collapse to be 1 m into the hangingwall at the edge of the collapse. The closure observed on packs, towards the centre of the collapsed area, indicated that the collapse thickness was more than 5 m. The hole drilled before mining commenced, for geotechnical assessment, showed low angle discontinuities between 3 m and 6 m into the hangingwall. The collapse appeared to be the result of high horizontal stress associated with a pothole, which was mined through.

3.4.6 Amandel-5

The site was located at a depth of 550 m in very poor geotechnical conditions, just below the critical span (0,42 – Impala rating). Both the up dip and down dip panels were about 35 m. Unfortunately the pillar chosen for the stress measurements was in an iron replacement zone which meant that it was much stronger (UCS 276 MPa) than the other pillars in the vicinity (UCS 133 MPa). This resulted in the pillar attracting a much higher than usual stress and eventually failing violently. Therefore, the horizontal stresses induced in the hangingwall could also have been higher than usual.

Horizontal stress changes were measured at several depths into the hangingwall as shown in Table 3-5. These stresses would act to clamp any high angle dipping joints but displace wedges defined by low angle joints. It appears that shallow dipping stress fracturing occurred just above 0,5 m, which caused the block in which one of the doorstoppers was located to fall out. No computer modelling was performed to verify the measurements shown in Table 3-5.

Table 3-5 Horizontal stress change measurements made in the hangingwall at the "crush pillar" site.

Distance from pillar (m)	Depth into hangingwall (m)	Maximum stress change (MPa)
2,5	0,5	44
2,5	1,0	108
3,6	4,5	75
4,0	15	>113

3.4.7 Impala-1

A large panel span of 77 m x 100 m was rated and plotted on the chart (Figure 3-3). The original in panel pillars had been mined out some time previously and the hangingwall was stable. The chart predicted that the panel should have collapsed, thus indicating that either the chart under estimates the critical span for very good rock mass ratings or some other mechanisms, apart from unravelling due to jointing, also need to be considered. Therefore, stress measurements in a horizontal plane, by the doorstopper method, were made at various depths into the hangingwall in the centre of the panel (see Figure 3-4) to investigate whether the stress state could indicate the mechanism.

The stress profile plotted in Figure 3-4 has a number of features:

1) Of the first four measurements (marked A, to D), A and D are close to zero, while C is 0,65 MPa. Taking the relative location of B into account, it is therefore surmised that measurement B may have been a localised stress concentration. Thus, the stress is likely to have been close to zero for up to 2 m into the hangingwall.
2) The elastic stress profile determined from MINSIM-W runs was approximately 0,37 MPa horizontal stress per metre up into the hangingwall for a solid hangingwall, after elastic

relaxation into the stope. The stress gradient is 5,9 MPa/m for the measured stress values between points F and G in Figure 3-4. This is an order of magnitude difference.

3) The tensile value at point E was 5,7 MPa. This is much more tensile than expected from MINSIM-W runs.

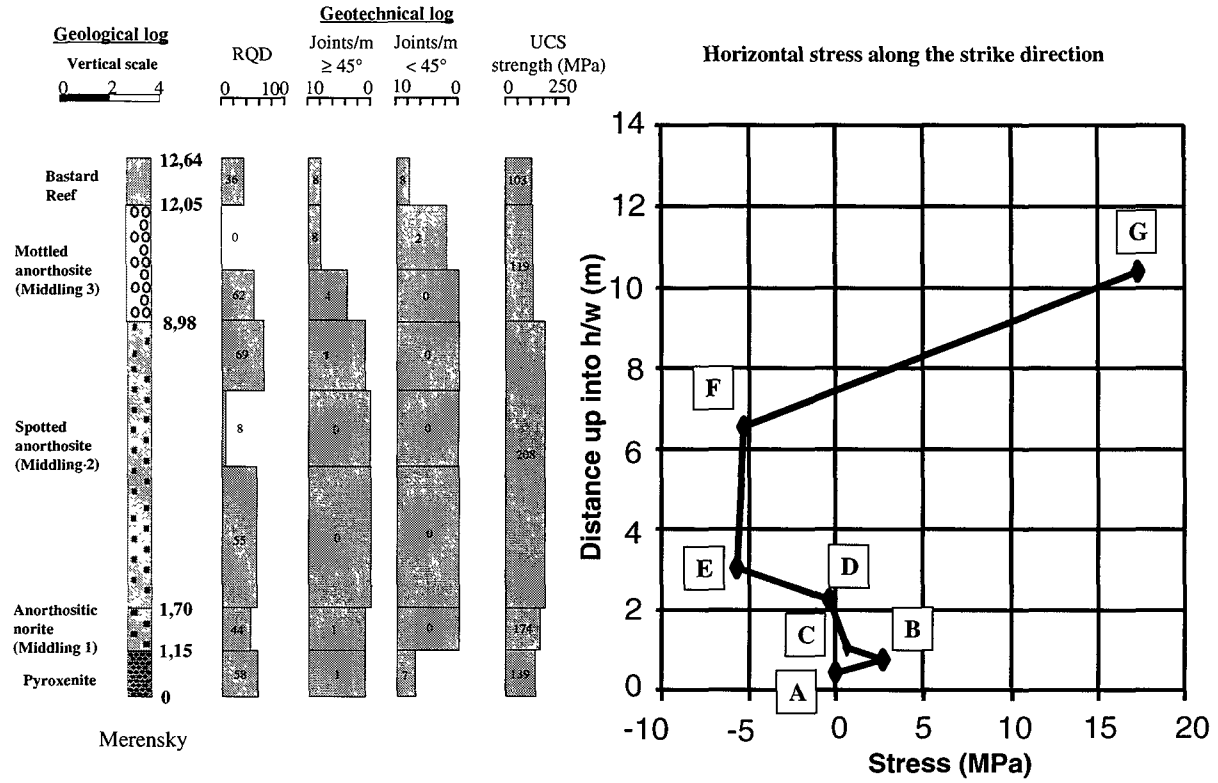

Figure 3-4 Horizontal stress distribution in the strike direction in the hangingwall in the 9/87 stope at Impala.

Taking the above into account, it is not possible to arrive at this stress distribution from elastic displacements of a solid hangingwall rockmass. From points 2) and 3) above, and by visual observation of the stress profile, it is hypothesised that the hangingwall deformed as a large, thick plate, some 15 m thick (the zero stress value indicates the centre of the plate in an elastic beam / plate bending, and is at approximately 7,5 m into the hangingwall).

If this is the case, a linear extrapolation of points F and G to the stope horizon results in a potential tensile stress of 44 MPa (Figure 3-5). This is the stress distribution that is expected if elastic plate bending has occurred, and if the measurements at points F and G are assumed to be correct (the self consistency of these readings indicated high reliability). From Figure 3-5 it can be seen that from point E downwards to point A, the stress profile has been "bent", to arrive at the almost zero stress conditions in the first 2 m of the hangingwall discussed above.

The question therefore arises: if plate bending has occurred, why are the horizontal stresses in the immediate hangingwall close to zero?

Two partial solutions are hypothesised:

1) The pyroxenite hangingwall underwent creep, so as to relieve the tensile horizontal stresses in the immediate hangingwall. The joints in the panel are discontinuous. An initial tensile stress of the order of 44 MPa need not have caused pre-existing cracks (joints) to grow and lengthen, as long as the pyroxenite hangingwall underwent creep.
2) The joints may nevertheless have opened by very small amounts (fractions of millimetres), resulting in a partial relief of the horizontal tensile stresses.

These two phenomena may have combined in such a way as to result in the stress profile seen in Figure 3-4.

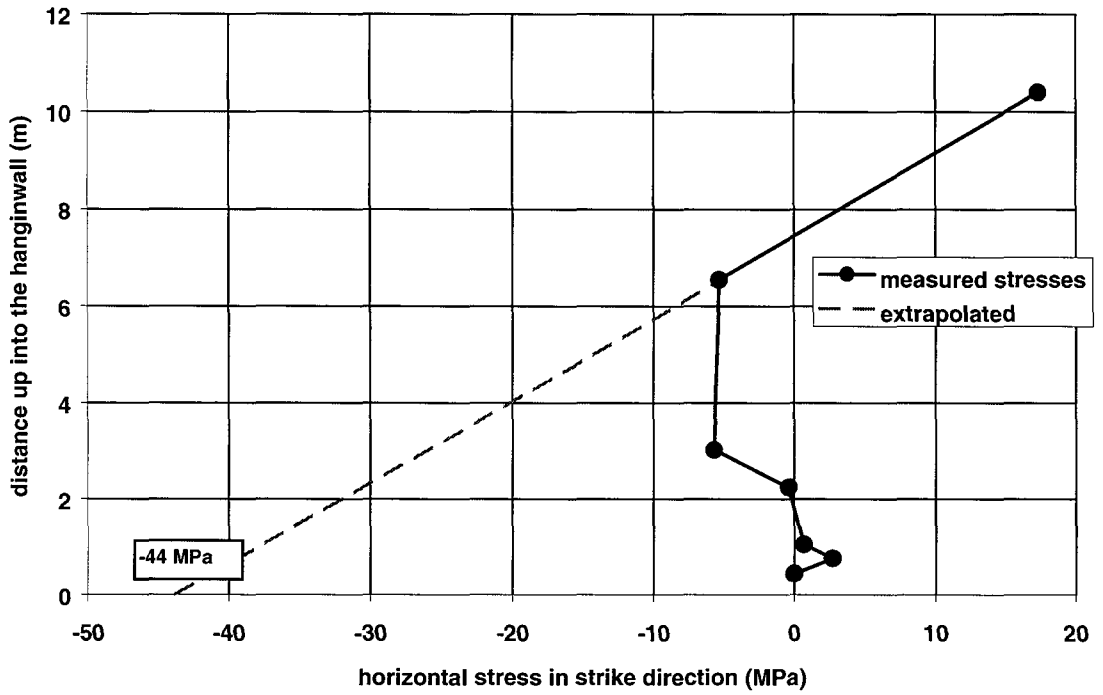

Figure 3-5 Extrapolation of the two measurements at the greatest depth, to estimate the tensile stress that could have developed, assuming plate bending.

A parting plane was modelled in MINSIM-W at 12 m into the hangingwall (corresponding to the depth of the Bastard Reef). It was found that the horizontal stress gradient did not change significantly from the value of 0,37 MPa/m (obtained for a solid hangingwall, after elastic relaxation into the stope). The predicted deformation was almost the same as that predicted for no parting. From other numerical modelling problems encountered, it is suspected that MINSIM-W does not model the bending mechanism well.

Simple beam bending calculations were performed for a 15 m thick beam, with the following assumptions and input parameters:

1) span = 77 m; density = 3000 kg/m^3; beam thickness = 15 m
2) the length of the panel was long enough to assume a two dimensional case (i.e. beam is 1 m thick into the page)
3) the beam is fixed-ended.

All the above assumptions are only roughly true. However, the calculations were merely performed to obtain very rough numbers. Using standard beam bending equations, the maximum tensile horizontal stress is 228 MPa. The hangingwall deflection is expected to be about 10 mm. If a 12 m thick beam is assumed (to coincide with the Bastard Reef contact), then a parting of approximately 9 mm is expected. Borehole camera observations in the centre of the panel indicated extremely small dislocations (less than one millimetre), that may well have been due to the drilling.

3.4.8 Impala 1 shaft

An investigation was conducted to understand the interaction of the support on the rock mass and to observe the effect of mining on horizontal stress. Field stress measurements were performed at several depths into the hangingwall, near to the face, in the middle of a panel, when the panel was at the ledging stage. Permanent instruments were installed in the same holes, to measure stress change as mining progressed. At the present time the face has not advanced and therefore only the field stress measurements are available for the report. MINSIM-W was used with a k-ratio of 1,3 (Coetzer, Spencer and de Maar, 1993) to simulate the

results. The modelling results (Figure 3-7) correlated well with the measured results (Figure 3-6).

Assuming a normal panel span of about 35 m, MINSIM-W was used to simulate the horizontal stresses once the panel had been mined out (Figure 3-7). The stresses reduced by about 30 per cent and the gradient relating stress to depth (into the hangingwall) also reduced. However, the stresses were still significantly compressive and able to clamp steeply dipping joints.

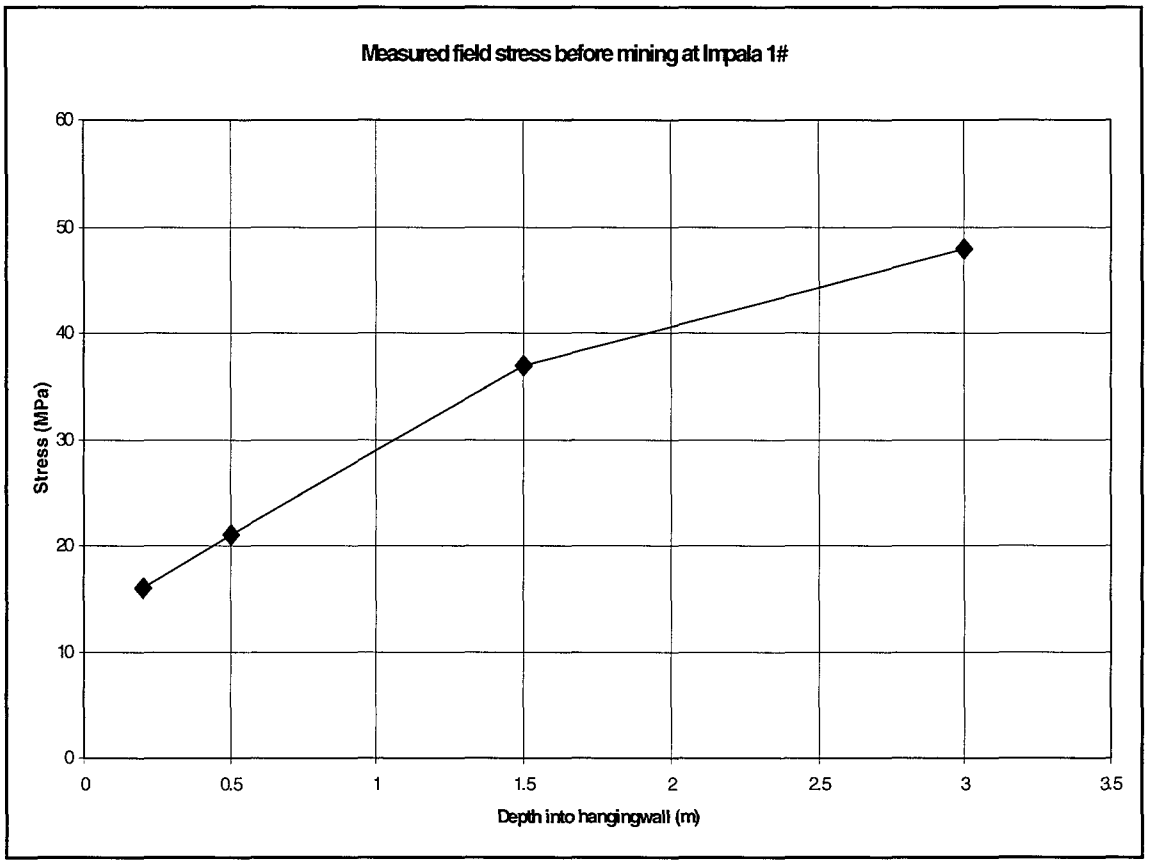

Figure 3-6 Horizontal field stress measurements in the hangingwall of a panel at Impala 1 shaft.

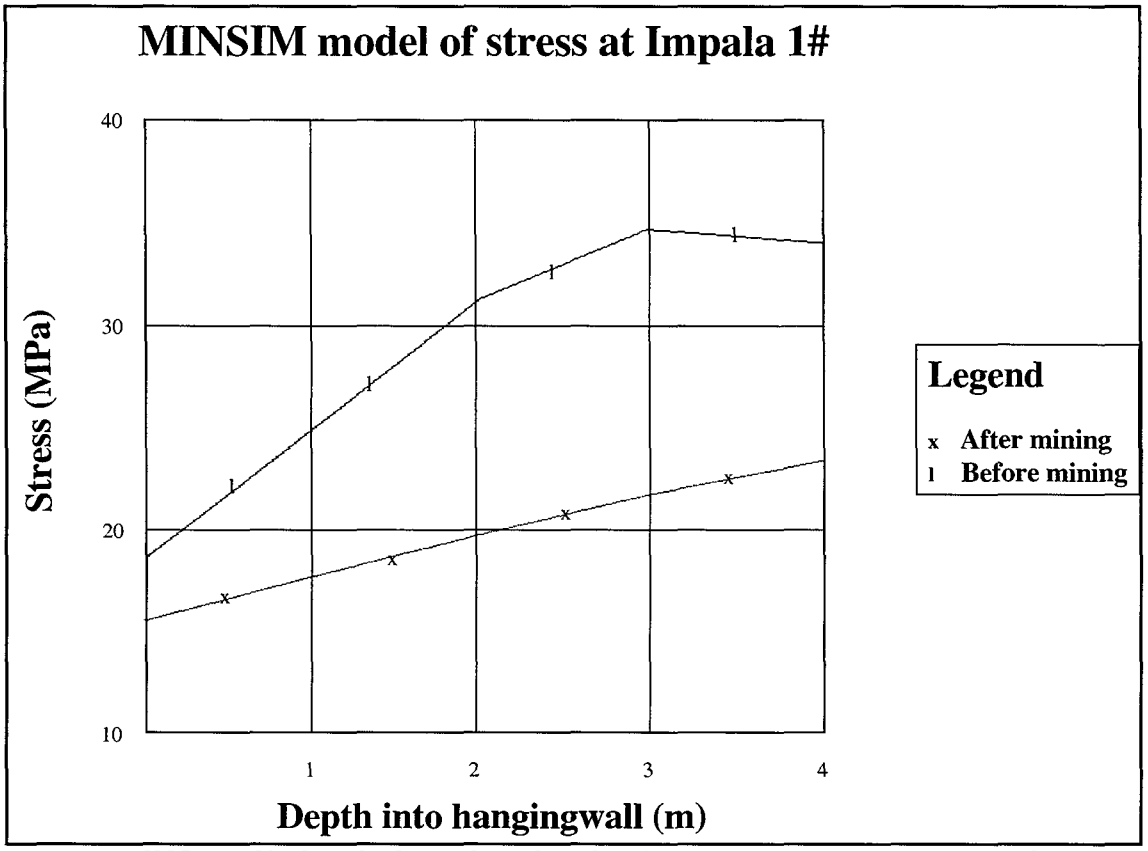

Figure 3-7 MINSIM-W simulation showing horizontal stress in the hangingwall of a panel at Impala 1 shaft.

High horizontal stress in the hangingwall would act to clamp steeply dipping joints but destabilise those with a shallow angle. Therefore, stability cannot be accounted for merely with a joint analysis. The results of this investigation highlight the need for the effects of horizontal stress to be included in the analysis affecting the chart (Figure 3-3).

3.4.9 Lebowa-1

During a sudden collapse, the hangingwall at this site dropped as an intact block. Only the rock at the edges of the collapse was fragmented. The collapse did not result in total closure in this region and the pack support elements were able to carry the load, allowing the thickness of the collapse to be calculated. From support resistance calculations, the height of collapse was estimated to be about 6,6 m. The collapse was preceded by a few minor falls, well behind the face.

Large-scale footwall heave, and hangingwall fragmentation, occurred on the edge of a pothole, which was mined out. The rock type in the pothole region was different to the rest of the hangingwall, being much more brittle. The stress fracturing indicated high horizontal stress in the pothole. The collapse appeared to have initiated from this point and the plane from which parting took place appears to have been a fracture.

3.4.10 Amandel-2

At this site it appears that the collapse was associated with an under supported fault. The fault was located about 2 m up dip and orientated parallel to the "crush" pillars at the base of the panel. As a result a large, intact cantilever appears to have failed on the upper solid abutment causing complete closure to take place (see Figure 3-8). The thickness of the collapse was estimated to be greater than 5 m.

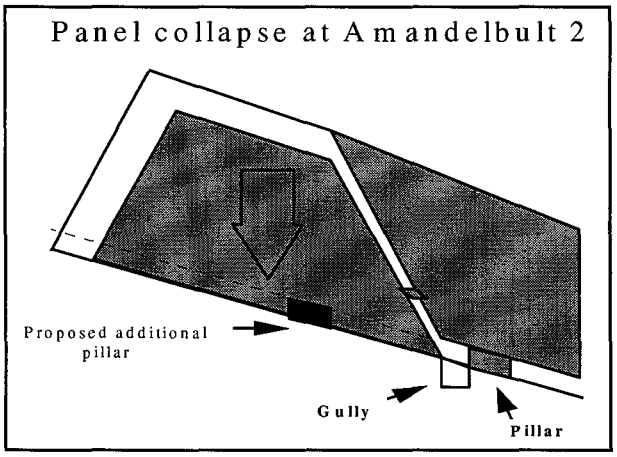

Figure 3-8 Sketch showing section through panel collapse at Amandel-2.

The large block that fell was almost intact. Only a few joints were open towards the upper and lower boundaries, obviously resulting from the fall. It appears that if the fault had not been there, the collapse would not have occurred. Excluding the fault from the rock mass rating analysis, positioned the site below the critical line in the chart, confirming observations. This site shows that adversely orientated, and positioned, major geological structures, should be identified separately and supported appropriately and the chart should be used in areas between major features.

3.4.11 Amandel-3

This panel did not experience a collapse, but there was a change in panel span and a corresponding change in hangingwall conditions. In a region of the panel where there was a 30 m span, 1,5 m high FOG's occurred on curved joints. The FOG's varied in width between 1 m and 1,8 m and there were definite signs of hangingwall loosening. Where the panel span was 17 m, with the same geotechnical rating and support, the hangingwall conditions were much more stable.

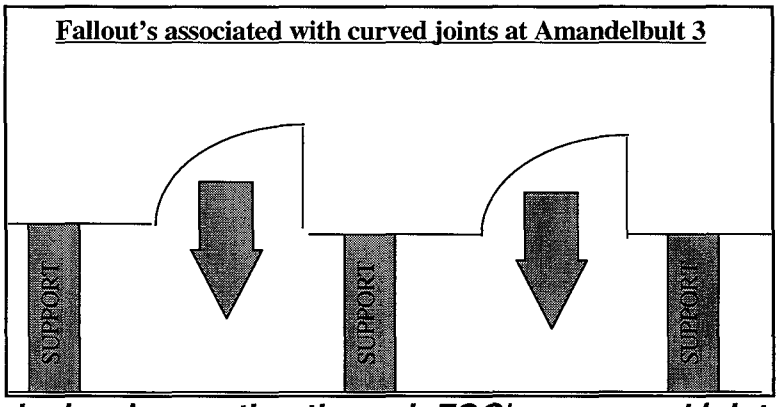

Figure 3-9 Sketch showing section through FOG's on curved joints at Amandel-3.

This site shows that reducing panel spans can improve hangingwall conditions, thus showing that the concept of the chart is credible.

3.4.12 Lebowa-2

Figure 3-10 is a sketch drawn from observations made in the strike gully at the bottom of the panel. Definite signs of footwall heave were observed in the region of the dyke. Complete closure took place at 15 m from the centre gully and persisted to 10 m from the face.

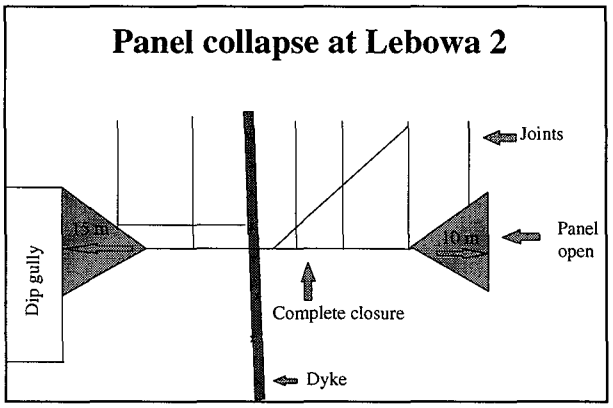

Figure 3-10 Cross-section on strike, showing the panel collapse at Lebowa-2.

The joint surveys performed in the strike and dip gullies indicated relatively few joints, however there was a high frequency of dangerous, low angle joints, especially in the lower half of the panel. The testimony of those people present when the FOG initiated confirmed that initially there was a FOG on a persistent shallow dipping discontinuity at the bottom corner of the panel.

It appears that where the panel was restricted to about 30 m, by the stabilising pillar at the top of the panel, the damage was also restricted. This was confirmed by the relatively low closure estimated by the compression of the packs along the centre gully edge. The 2 m x 2 m "crush" pillars at the bottom of the panel effectively stopped the collapse from "running" into the adjacent panel. Footwall heave could have been a result of pillar punching which may have reduced stresses on these pillars slightly.

Similar geological features and mechanisms were observed at both Lebowa-2 and Lebowa-1 indicating some association of high horizontal stress to potholes and dykes. Especially potholes have often been associated with high horizontal stress. It would appear that a dip span of 30 m would have created a stable environment indicating a relationship between stability and span.

3.4.13 Lebowa-4

The FOG occurred on a fissure, which was between 0,5 m to 1 m in the hangingwall. Failure appears to have initiated on a fault striking parallel to the face. The hangingwall fell out as a cantilever, pushing the stick support over without failing the elements (as shown in Figure 3-11). Since the panel was at a shallow depth below surface, there was not enough closure to generate sufficient support reaction on the stick support elements to clamp the fissure. Clamping the fissure would have reduced the lateral movement, thus reducing the risk of pushing the elements over. The closely spaced packs located between the face and the fault did not prevent parting along the fissure but could not be pushed over, thereby maintaining the integrity of the hangingwall. The randomly scattered, small pillars appear to have generated a high enough stress to cause movement on adjacent steeply dipping joints. Therefore, the fall was able to extend to the edge of the pillars on the loosened joints. In some cases, where the stress on the pillars was high enough, punching into the material between the fissure and the hangingwall could have occurred.

This site highlights the importance of accounting for the effect of low angle dipping discontinuities to a greater degree in the chart analysis. A discontinuity orientated parallel to the reef plane is particularly dangerous because its existence is often not known until a FOG or collapse occurs. In this case the FOG could easily have been avoided if the correct support was installed.

The chart could not have predicted a collapse in these conditions without prior knowledge of conditions in the vertical direction. Therefore, this site shows that a fundamental understanding of the rock mass is required.

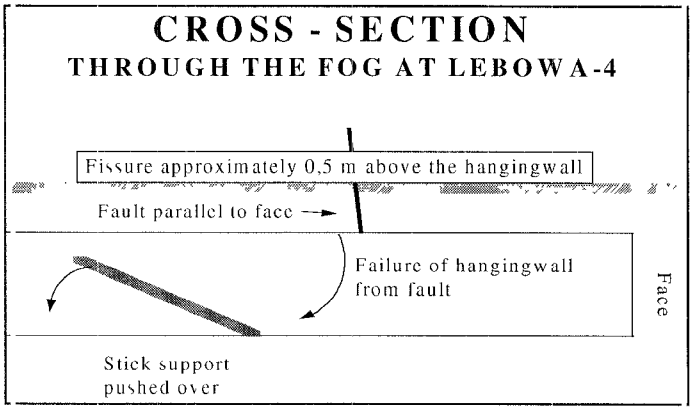

Figure 3-11 Cross section showing the collapse mechanism at Lebowa-4.

3.4.14 Lebowa-5

The collapse occurred between the strike pillars on either side of the centre raise. There were at least three potholes, two at the top and one at the bottom of the panel. The panel collapsed up to the face, which was a strike distance of about 37 m, and the whole dip span, which was about 30 m. The thickness of the collapse appeared to be about 2,5 m and fell as one massive block. The stick support elements had brushed over and ridden out, some of which were pushed into the strike gully. A photograph of the collapse looking down the ASG at the bottom of the panel is shown in Figure 3-12.

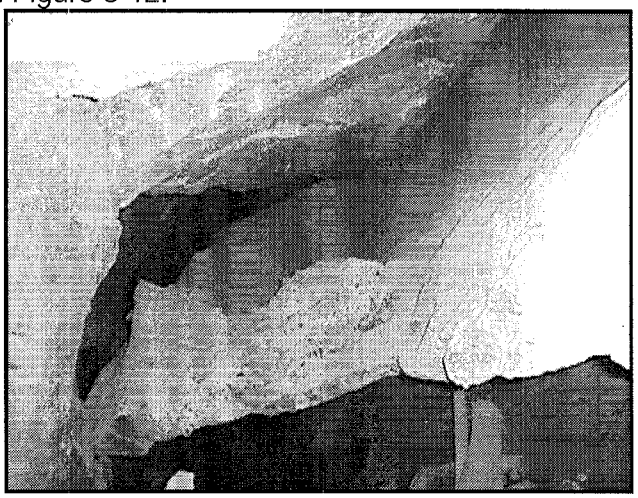

Figure 3-12 Photograph taken at the lower end of the collapse at Lebowa-5.

There was no doubt that the mechanism involved with this collapse was high horizontal stress, causing extension fractures which were the release planes from which the fall occurred (see Figure 3-12). It appeared that the fall initiated from the fractures emanating from the lower pillar and broke off on steep fractures forming blocky ground just below the down dip edge of the pillars at the top of the panel. There was a high degree of horizontal stress fracturing in the hangingwall at the bottom of the adjacent panel (immediately up dip of the collapse), see Figure 3-13.

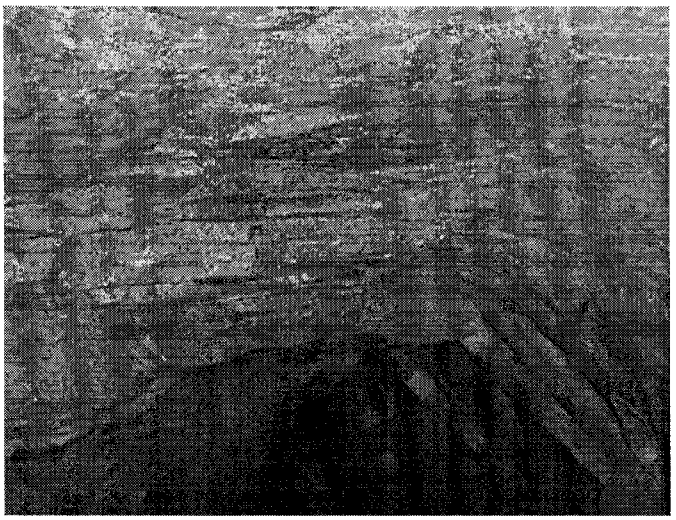

Figure 3-13 Photograph showing a high degree of stress fracturing in the hangingwall.

It appears that the localised high horizontal stress was associated with the potholes. The rock mass rating was good and the joints obviously had little to do with the collapse as shown in the chart (Figure 3-3).

This collapse shows that chart needs to take the affect of high horizontal stress into account.

3.4.15 Vaal River Operations Tau Lekoa Shaft

It appears that the hangingwall failure initiated on a steeply dipping, persistent discontinuity (quartz vein), which was striking about 40^0 to the reef strike (Figure 3-14), and which, subsequently developed into a sub-horizontal fracture. A large portion of the collapse appears to have occurred on the fracture. Striations in the hangingwall indicated that movement took place in a direction towards the discontinuity (see Figure 3-14).

A pile of thin plates on the top of the FOG (Figure 3-15), indicated that there had been horizontal stress fracturing in the hangingwall and therefore high horizontal stress.

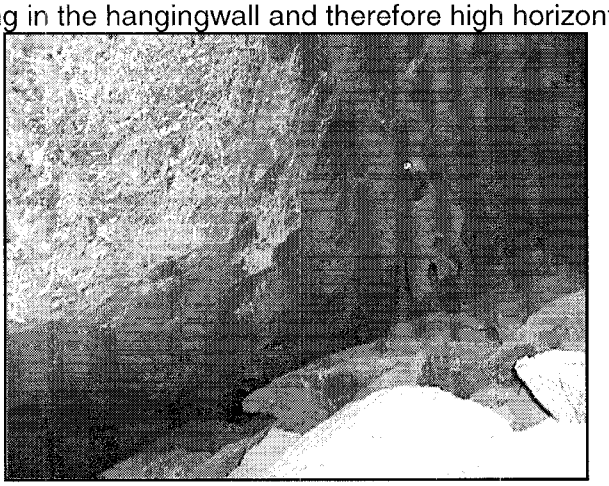

Figure 3-14 Photograph showing the edge of the collapse at Tau Lekoa.

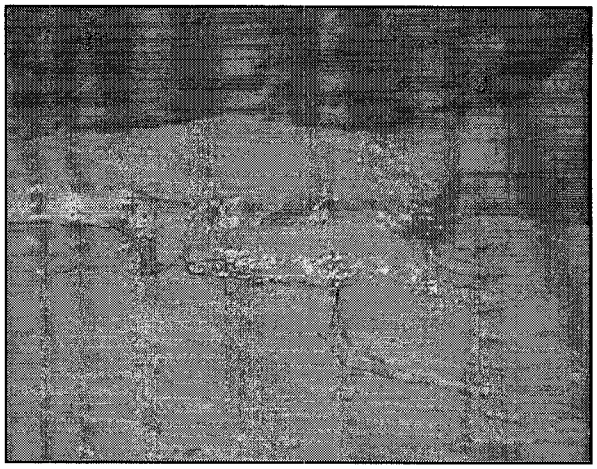

Figure 3-15 Photograph showing the plates that had fallen as a result of horizontal stress fracturing in the hangingwall.

The upper boundary of the collapse appears to have been a brow cut slightly into the hangingwall. The collapse included the whole panel, terminating as a curved fracture against the abutment. Figure 3-16 shows the surface of the fracture along which the parting took place, indicating that the collapse involved high horizontal stresses.

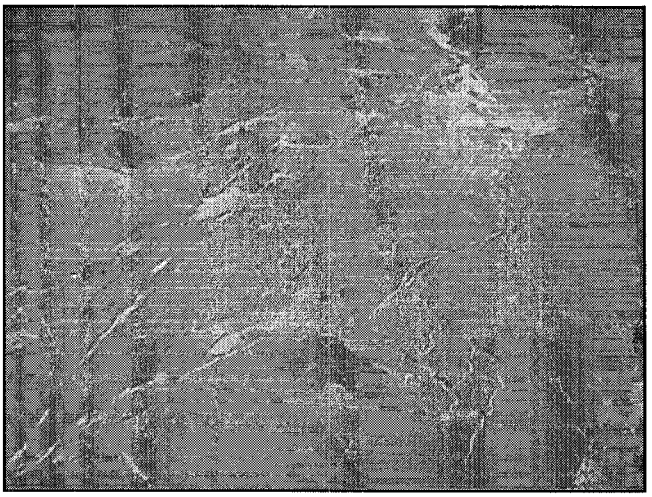

Figure 3-16 Horizontal fracture plane in the hangingwall at the top end of the collapse.

It appears that there are two possible mechanisms that could have been involved in the collapse. The first suggestion is that the span between the in panel pillars was too great and therefore the tensile zone between the pillars was higher than the top of the roof-bolts. This theory indicates that the panel was insufficiently supported. The pillar spacing, to ensure stable panel spans, was derived empirically using statistics from previous collapses on the mine. It appears that on this mine the unstable zone in the hangingwall is rarely more than 0,11 times the span between pillars, and therefore the 13 m distance between the pillars involved in the collapse should not have created hangingwall instabilities to a depth greater than 1,4 m. The average FOG thickness was greater than 2 m. If the collapse occurred because of an unusual stress condition, then the empirically based calculations would underestimate the collapse height, indicating that the collapse would probably have occurred even if the pillar spacing were correct.

3.4.16 Union Section open pit

Observations were made in the open caste high wall at Union Section to identify the vertical persistence of joints in the hangingwall. Figure 3-17 shows that generally the vertical extent of the jointing was about 2 m, with a few extending to 3 m.

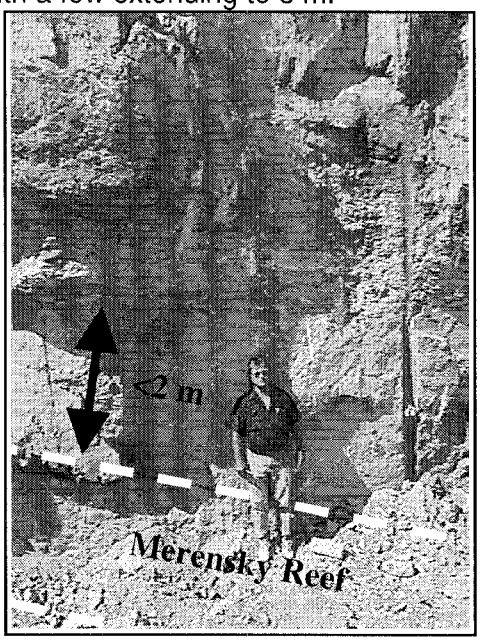

Figure 3-17 Vertical joints above the Merensky Reef, in the open pit at Union Section.

3.5 Laboratory work

3.5.1 Introduction

Comprehensive geomechanical laboratory testing was carried out on core from the instrumentation sites to establish the geomechanical properties of the Merensky Reef and the various lithological units in the immediate footwall and hangingwall of the reef.

3.5.2 Results

3.5.2.1 Union

It is unclear whether the limiting factor for the failure zone in the hangingwall of this site was the result of a change in rock strength, the presence of unusual bands or "laminae", as discovered in the tensile tests, or confinement. It appears that the fracture zone extended up to the base of the norite, which was significantly stronger than the melanorite host (see Table 3-7).

Unfortunately, the borehole drilled into the footwall was drilled after mining had been completed, which means that fracturing had already taken place in the rock mass. No samples large enough for testing were available from the borehole core in the Course Pseudo, which was located in the immediate footwall. This suggests that the rock mass was weak in this region, which could either be because of an unusual high intensity of adversely orientated discontinuities or that the uniaxial compressive strength of the material was low. It appears that this zone facilitated the observed pillar punching.

Brazilian tests give an indication of the tensile strength in a direction perpendicular to the core. The results of Table 3-8, therefore, show the tensile strength in a horizontal direction, and direct tensile tests were performed to determine geomechanical properties in the vertical direction (Table 3-6). Since the jointing was mainly vertical in this region, it is suspected that parting would take place on one of these before actual failure of the rock.

Table 3-6 Results of the direct tensile tests performed on hangingwall material from Union-1.

Specimen no.	Rock type	Depth (m)	Strength (MPa)	Young's Modulus (GPa)	Density
DTM-01	Pyroxenite	0,75	4,45	94.6	3218
DTM-02	Pyroxenite	2,70	8,89	132,3	3231
DTM-03	Melanorite	3,70	4,66	30,0	3140
DTM-04	Melanorite	5,55	3,27	30,6	3026
DTM-05	Leuconorite	8,55	6,30	40,2	2890

Table 3-7 Average uniaxial and triaxial compressive strength values of lithological units at Union-1.

Rock Type	Calculated Uniaxial Compres. Strength (MPa)	Average Uniaxial Compres. Strength (MPa)	Cohesion at Failure (MPa)	Average Young's Modulus (GPa)	Average Poisson's Ratio	Kc
Hanging						
Bastard	167	167	30.6	104	0.21	7.45
Mottled Anorthosite	196	196	40.2	80	0.20	5.96
Spotted Anorthosite	179	180	29.5	74	0.23	9.20
Leuconorite	202	189	34.3	81	0.23	8.62
Norite		209		96		
Melanorite	145	137	25.6	74	0.23	8.01
Merensky	132	133	29.7	104	0.20	4.79
Footwall						
Tarentaal		218				
Pyroxenite	167	167	34.8			5.74
Harzburgite		Approx. 170				
UG2		38				
Upper Pyroxenite		101				
Lower Pyroxenite	187	187	50.2			2.59

Kc: is the confinement factor, describing the effect of confinement on σ_1.

Table 3-8 Average Brazilian test results from the hangingwall at Union-1.

Tensile Strength (MPa)	Rock type
6,3	pyroxenite
8,2	melanorite
4,6	norite
9,2	leuconorite

3.5.2.2 Amandel-1

Uniaxial and triaxial compressive tests were performed on cores from the Merensky Reef, the immediate footwall and hangingwall of the reef. Radial point loads were performed every 100 mm, where possible, along the length of the core. These point loads were used to determine if any abnormalities existed and to identify variation of strength within a rock type. A comparison between the average uniaxial compressive strength and the point loads for each rock type was made. Axial point loads were performed less frequently and used as a comparison with some of the radial point loads, in an attempt to determine the anisotropy ratios of the various rock types. The test results were compared to observations made in the Merensky Reef panel.

3.5.2.2.1 Results of the uniaxial and triaxial tests

Table 3-9 summarises the average results of the uniaxial and triaxial testing, and Figure 3-18 shows the stress-strain curves of some of the triaxial testing. The strength parameters shown in Table 3-9 were derived from straight line fit regression analyses, relating the axial stress at failure to the confining stress. The results of individual tests and a graphical representation of the regression analyses are presented in the technical document.

Table 3-9 Average uniaxial compressive strength and effect of confinement factor (Kc) values for each lithological unit of borehole 9/38W/4.

Rock Type	Calculated Uniaxial Compres. Strength (MPa)	Average Uniaxial Compres. Strength (MPa)	Cohesion at Failure (MPa)	Average Young's modulus (GPa)	Average Poisson's ratio	Kc
Footwall						
Leuconorite		235		82		
Poikilitic anorthosite		290		90		
Harzburgite (P2)		106		72		
Pegmatoidal harzburgite						
Melanorite		153		103		
Norite						
Poikilitic anorthosite		247		87		
Norite		201		86		
Poikilitic anorthosite	236	227	41,1	90	0,22	8,26
Merensky Reef	123	123	31,4	74	0,18	3,84
Hangingwall						
Poikilitic pyroxenite	133	130	26,7	115	0,15	6,22
Melanorite	174	163	34,9	104	0,20	6,25
Norite	188	195	38,4	92	0,23	5,98
Leuconorite		179		85		
Poikilitic anorthosite	170	187	26,8	90	0,25	9,24
Bastard Reef	136	122	26,4	112	0,17	6,58

Kc: is the effect of confinement factor, illustrating what effect confinement has on the major principal stress (σ_1).

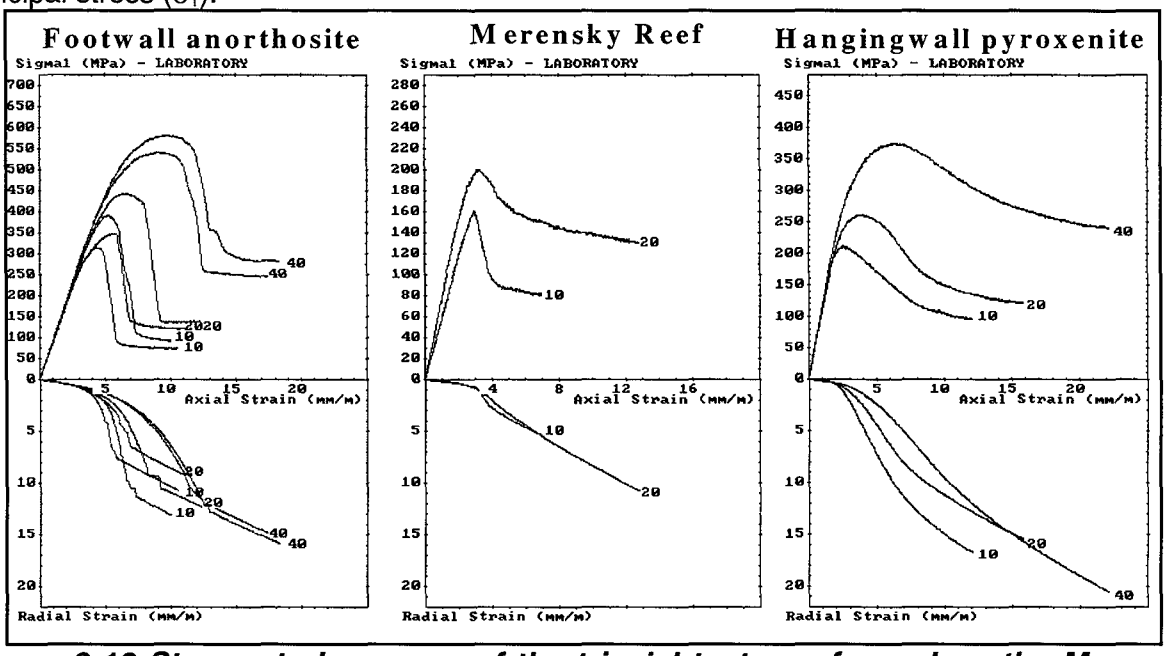

Figure 3-18 Stress-strain curves of the triaxial tests performed on the Merensky Reef and immediate footwall and hangingwall.

3.5.2.2.2 Point load results

Detailed analyses and the results of the individual point load tests are shown in the technical document. Two different methods of evaluation have been applied; hence there are two results for each test i.e. the standard ISRM evaluation, which was developed to calculate uniaxial compressive strength values and a concept developed by Butenuth (1997) to provide uniaxial tensile strength values (Table 3-10). The anisotropy ratios calculated using the standard ISRM evaluation are shown in Table 3-11.

Table 3-10 Tensile strengths calculated from point load tests.

DEPTH	TENSILE STRENGTH (MPa)	ROCK TYPE
27,92 – 22,36	10,6	Leuconorite
22,36 - 20,81	13,1	Poikilitic anorthosite
20,81 – 16,81	6,3	Harzburgite
16,81 – 16,66	4,8	Pegmatoidal harzburgite
16,66 – 15,17	11,9	Melanorite
15,17 – 11,44	12,8	Norite
11,44 – 10,93	13,9	Poikilitic anorthosite
10,93 – 5,16	12,1	Norite
5,16 – 0	12,6	Poikilitic anorthosite
	6,5	Merensky Reef
0 – 2,54	13,3	Poikilitic pyroxenite
2,54 – 4,14	12,4	Melanorite
4,14 – 13,74	11,9	Norite
13,74 – 15,29	11,4	Leuconorite
15,29 – 17,94	13,6	Poikilitic anorthosite
17,94 – 22,35	16,2	Bastard Reef

Table 3-11 Average anisotropy ratios, calculated from the corrected axial and radial point load strengths.

Depth into Borehole (m)	Depth into Footwall or Hangingwall (m)	Anisotropy ratio	Rock Type
0 - 5,56	27,92 - 22,36	1,44	Leuconorite
5,56 - 7,11	22,36 - 20,81	1,02	Poikilitic anorthosite
7,11 - 11,11	20,81 - 16,81	-	Harzburgite (P2)
11,11 - 11,26	16,81 - 16,66	3,23	Pegmatoidal harzburgite
11,26 - 12,75	16,66 - 15,17	1,04	Melanorite
12,75 - 16,48	15,17 - 11,44	-	Norite
16,48 - 16,99	11,44 - 10,93	-	Poikilitic anorthosite
16,99 - 22,76	10,93 - 5,16	1,10	Norite
22,76 - 27.92	5,16 - 0	1,07	Poikilitic anorthosite
27,92 - 29,56		2,42	Merensky Reef
29,56 - 32,10	0 - 2,54	0,64	Poikilitic pyroxenite
32,10 - 33,70	2,54 - 4,14	-	Melanorite
33,70 - 43,30	4,14 - 13,74	1,28	Norite
43,30 - 44,85	13,74 - 15,29	0,55	Leuconorite
44,85 - 47,50	15,29 - 17,94	1,03	Poikilitic anorthosite
47,50 - 51,91	17,94 - 22,35	0,80	Bastard Reef

3.5.2.2.3 Results of the FLAC analysis program

The results of the FLAC analysis performed on pyroxenite from the Merensky Reef hangingwall are shown in Figure 3-19. FLAC analyses for the other rock types where relevant rock tests have been performed are in the technical document. The FLAC analysis program attempts to fit various input data, which is required for FLAC modelling. The left-hand curves of Figure 3-19 are the plots of the actual test data and the right hand side represents curves derived from the analysis. The graphs below the triaxial test results (Figure 3-19) provides the analysis used to simulate these results. The vertical lines shown on the cohesion curves are error bars. The length of the bars indicates the magnitude of the error associated with the fitted data.

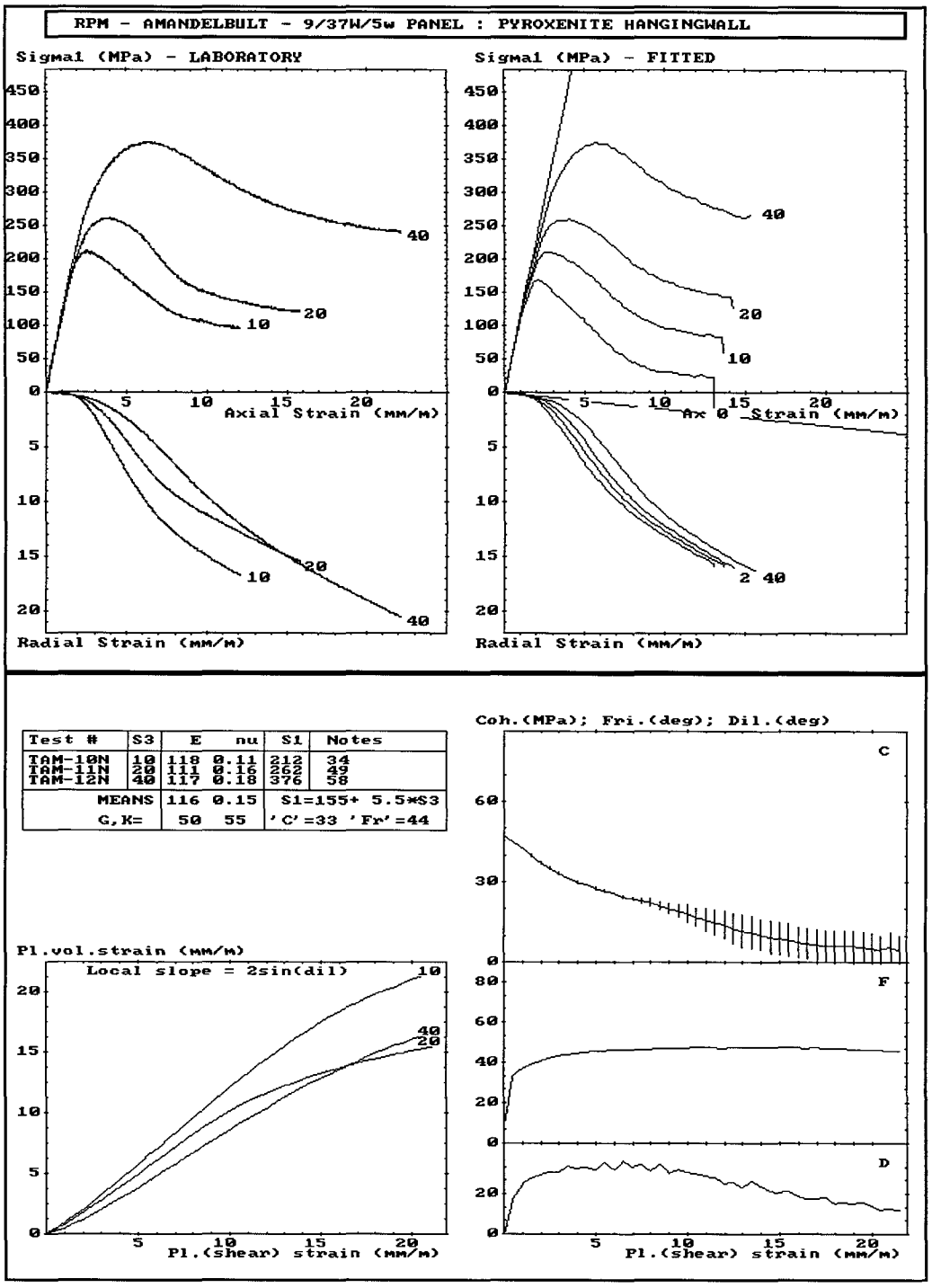

Figure 3-19 Results of the triaxial tests and the FLAC analysis performed on the pyroxenite hangingwall.

3.5.2.3 Lebowa-1

Table 3-12 summarises the average results of the uniaxial and triaxial testing performed on core from borehole GH 67. The strength parameters were derived from straight line fit regression analyses, relating the axial stress at failure to the confining stress.

Table 3-12 Average uniaxial compressive strength and Kc values for each lithological unit at Lebowa-1.

Rock Type	Depth (m)	Calculated Uniaxial Compres. Strength (MPa)	Average Uniaxial Compres. Strength (MPa)	Cohesion at Failure (MPa)	Average Young's modulus (GPa)	Average Poisson's ratio	Kc	Density
Leuconorite	0,30 - 1,80	119	118	22,6	71	0,26	6,91	2962
Spotted anorthosite	1,80 – 5,90	179	169	30,5	73	0,25	8,63	2782
Mottled anorthosite	5,90 – 14,10	167	186	31,2	75	0,25	7,17	2758
Bastard Reef	14,10 – 17,50 (EOH)	111	100	26,2	110	0,17	4,47	3200

Kc: is the effect of confinement factor, illustrating what effect confinement has on σ_1.

3.5.3 Discussion

3.5.3.1 Footwall

The uniaxial compressive tests performed in the immediate footwall of the Merensky Reef at Amandel-1 indicated that it is stronger than the immediate hangingwall. However, the radial point loads, calculated using the standard ISRM method, indicated the opposite to be true. The reason for this discrepancy is proposed in Section 3.5.3.5. The uniaxial compressive tests are assumed to give a more accurate intact rock strength than the point load tests and therefore the point load tests have not been used in the determination of intact rock strength. The Young's modulus of the immediate Merensky Reef footwall was lower, and the Poisson's ratio higher, than the immediate hangingwall. This indicates that more dilation should take place in the footwall than the hangingwall for the same stress and could therefore be a contributing factor to the observed footwall heave.

3.5.3.2 Reef

The intact strength of the Merensky Reef was lower than either the footwall or hangingwall. The "Kc" value indicated that confinement also had a smaller effect on strength than in either the footwall or hangingwall, therefore pillar punching should not occur. A relatively high residual strength observed after failure at the 20 MPa confinement level indicated that the specimen was approaching the brittle / ductile transition. Any confinement at or above the brittle / ductile transition level causes plastic flow to occur within the specimen and brittle failure cannot occur. It is possible that high confinement levels are generated within a pillar, and may be the reason why some "crush" pillars do not appear to fail.

The high degree of plasticity observed on the stress / strain curves before failure, indicates that more deformation should be observed on Merensky pillars than expected if a comparison were made with similar panels on the Witwatersrand gold mines. The comparatively controlled manner in which samples failed (Section 3.5.3.5) is an indication that pillars should also fail in a more controlled way than experienced, for the same loading conditions, on the Witwatersrand gold mines, if they fail at all.

The comparatively high degree of non-linear behaviour observed at the beginning of the test indicates that more deformation will take place at very low stresses or shallow depths for a given load increment than expected from the modulus. Unfortunately, the non-linear behaviour

observed at the beginning of the test was not recorded on the stress / strain curves (Figure 3-18).

3.5.3.3 Hangingwall

The strength of the poikilitic pyroxenite, located in the immediate hangingwall of the Merensky Reef, was relatively weak at 130 MPa and was the same as measured at Union-1 (Table 3-13). Above the poikilitic pyroxenite there was a thick plate of melanorite and norite, which were considerably stronger that the poikilitic pyroxenite. The relatively high Poisson's ratio of the thick plate could potentially provide stabilising horizontal stresses, being induced by the high vertical stresses generated on the pillars and the face. However, the horizontal stresses could also be a mechanism of hangingwall instability if the angle between the dip of the discontinuities and the dip of the reef is less than 45°, because the horizontal stresses could cause shearing, thus enabling loosening of hangingwall blocks

The percentage stress drop between failure and residual strength, of the immediate pyroxenite hangingwall, was greater than the reef specimens but were still relatively low. The brittle/ductile transition appears to be at a relatively low confinement (see Figure 3-19) which, if achieved horizontally above a pillar, could prevent brittle failure. There was also a high degree of plastic behaviour displayed at failure indicating that brittle stress fracturing and blast damage would probably be less than in a more brittle rock, such as the immediate footwall.

3.5.3.4 Point load tests

A direct comparison between the corrected radial point load tests and the uniaxial compressive tests, using the standard ISRM method of evaluation, indicated that each rock type in the borehole required a different correction factor in order to determine the uniaxial compressive strength from the radial point load tests. Butenuth (1997) suggested that the point load test gave an indication of the tensile strength rather than compressive strength, without a correction factor. If point load tests are an indication of tensile strength, then the horizontal tensile strength of the immediate hangingwall of the Merensky Reef was slightly greater than the footwall.

The point loads indicated that there was, in some cases, significant variation of properties within a rock type.

The anisotropy ratios shown in Table 3-11 indicated a considerable degree of anisotropy within the rock types. The Merensky Reef and the P2 marker are materials with large crystals and the results could vary depending on the position of the crystals in relation to the points of the tester.

3.5.3.5 General observations

The following observations were made during the uniaxial and triaxial testing:

1) Generally the samples failed in a more controlled manner than in tests performed on the Witwatersrand rock types, even though the Young's Moduli were similar, or higher.
2) A high degree of non-linear, plastic behaviour was observed both at the beginning of the test and above the yield point. This was particularly noticeable in the triaxial tests.

The high degree of plasticity, shown by the relatively high Kc values (Table 3-9) of the hangingwall and footwall rocks of the Merensky Reef, is an indication that a large amount of plastic flow would occur before brittle failure (Figure 3-18).

A polynomial equation gives a better fit than a straight-line regression when comparing the failure stress (σ_1) to confinement (σ_3), for the poikilitic pyroxenite in the Bastard Reef at Amandel-1. To a lesser degree, the polynomial equation also gives a better fit for the poikilitic pyroxenite located in the immediate hangingwall of the Merensky Reef. The polynomial equation indicates that for low levels of confinement, the effect of confinement on σ_1 is more than at higher confinements.

There was a large variation in strength parameters within lithological units across the Bushveld Complex.

The tests performed on material from Amandel-1 showed that, while inelastic radial dilation initiated at low strains in the reef and hangingwall pyroxenite, the radial dilation was greater in the footwall anorthosite for any given axial strain. Similarly, the footwall anorthosite had a larger radial strain than the hangingwall pyroxenite, for any given level of stress. This could account for some of the footwall heave, but not the observed fracturing. At failure, the footwall material experienced a sudden loss of load on fracture planes, which was not observed in either the hangingwall or reef tests (Figure 3-18), indicating that the footwall was more brittle. The difference between the residual strength and the failure stress was substantially greater in the footwall than either the hangingwall or reef, indicating that the brittle-ductile transition would require a greater confinement in the footwall than either the reef or hangingwall. Therefore, the confinement at the centre of the pillars could be great enough to cause plastic deformation without brittle failure, which could have torn the footwall apart. The geomechanical behaviour of the footwall material indicates that the footwall could be more susceptible to blast damage or to being split apart by the dilating pillar than either the reef or hangingwall. The point load tests indicated that the tensile strength of the footwall, in a horizontal direction, was relatively low which could have enabled extension fractures to develop in a high horizontal stress environment. These findings indicate that anorthositic hangingwalls could also be more susceptible to stress fracturing and brittle failure than pyroxenite.

The average laboratory results for the geomechanical tests performed on the immediate hangingwall at some of the instrumentation sites have been summarised in Table 3-13.

Table 3-13 Summary of the laboratory derived rock properties of the immediate hangingwall rock types.

Mine	Rock Type	Thickness of the lithological unit (m)	UCS (MPa)	Cohesion at Failure (MPa)	E (GPa)	<	Axial tensile strength (MPa)	Radial tensile strength (MPa)
Union-1	Pyroxenite	3,00	133	29,7	104	0,20	6,7	6,3
Amandel-1	Pyroxenite	2,54	130	26,7	115	0,15	9,6	13,3
Lebowa-1	Leuconorite	1,50	118	22,6	71	0,26		

The equation used to calculate point load strengths was taken from Butenuth (1997)

3.5.4 Conclusions

The uniaxial compressive tests performed at Amandel-1 showed that the pillar material was weaker than either the footwall or the hangingwall and that the footwall material was the strongest. Therefore, punching into the footwall should not occur. However, the geomechanical behaviour observed in the laboratory tests indicated that the footwall material could be more susceptible to blast damage or to being split apart by the dilating pillar than either the reef or hangingwall. The point load tests indicated that the tensile strength of the footwall, in a horizontal direction, was relatively low which could have enabled extension fractures to develop in a high horizontal stress environment. The footwall anorthosite had a larger radial strain than the pyroxenite for any given level of stress. These findings indicate that anorthositic hangingwalls could also be more susceptible to stress fracturing and brittle failure than pyroxenite. Anisotropy ratios indicate large strength variations for different directions.

There was a large variation in strength parameters within lithological units across the Bushveld Complex.

3.6 Analyses performed on wedge failures

3.6.1 Introduction

Two additional sites that were visited involved large wedge failures, where the one plane was a fault and the other appeared to be a tensile fracture. It appears that the fractures developed as a result of tensile stresses at the top of the cantilevers, which gave an opportunity to calculate the tensile stresses that caused the fractures to develop. The rock type at the Tau Lekoa site was Ventersdorp Lava and at the Lebowa site was melanorite.

3.6.2 Results

The tensile stresses that would have developed at the top of the wedge as a result of the weight of the material was calculated assuming that the cohesion on the fault plane was zero (see technical document 98-0434). The results of the calculations are shown in Table 3-14.

Table 3-14 Comparison between the calculated tensile stress at the top of the cantilever and the strength of the material.

Rock Type	Calculated tensile stress (MPa)	Tensile strengths from laboratory testing (MPa)
Ventersdorp Lava	-0,6	~ -20 (10 % of UCS)
melanorite	-1,7	-8,2

3.6.3 Discussion

The calculated stresses in Table 3-14 were much lower than the laboratory determined strength indicating that failure should not have occurred. However, there were joints within the fracture plane in the Ventersdorp lava (Tau Lekoa) which could have weakened the plane along which the failure initiated. Two conclusions can be made from the results:

1) the tensile strength of the rock mass is much weaker than the laboratory results
2) there was a horizontal driving force, which pushed the wedges out.

Direct tensile strength tests performed on melanorite, perpendicular to the reef plane indicated a very much lower tensile strength (2,6 MPa) than the Brazilian tests, parallel to the reef plane. Either there was a high degree of anisotropy or the Brazilian test over estimated the tensile strength. If the Brazilian result is correct, then it is unlikely that the wedge fell out under the force of gravity and it is assumed that there was a horizontal driving force.

3.7 Influence of internal panel support systems on the stability of the panel hangingwall

3.7.1 Introduction

Instrumentation was installed to observe the effect of panel support on the hangingwall at several sites, on the Merensky Reef, across the Bushveld Complex. Only the site at Union Section (Union-1) showed any influence of the support on the stability of the hangingwall. The results of Union-1 are discussed in the report.

3.7.2 Description of Union-1

Table 3-15 describes the geotechnical conditions of the site. A stope sheet of Union-1 is shown in Figure 3-20, the instrumentation site highlighted by the dashed area. The positions of the closure-ride meter stations in Figure 3-22 are also shown in Figure 3-20. The extensometer (Figure 3-21) position was near to the centre of the panel, in the centre gully (see Figure 3-20).

Table 3-15 Description of the site.

DEPTH (m)	SPAN (m)	Stoping width (m)	MAJOR JOINT ORIENTATION	OBSERVED PANEL CONDITIONS
1200	35	1,2	Perpendicular to face	Ultimately dangerous mining conditions with many falls of ground and a high closure rate.

The raise and strike gullies were pre-developed for a down-dip mining configuration. However the initial mining in the connection was carried out in panels "Stope 3" and "Stope 4" (see Figure 3-20) which were mined on breast configuration to a maximum span of 35 m. In this case the significance of having crush pillars was removed, as there were large solid abutments on either side of the panels.

The support pattern consisted of a line of grout packs spaced 2 m apart on dip, alternating with a line of sticks, also spaced 2 m apart. The spacing between lines was 2 m skin to skin.

3.7.3 Instrumentation results

3.7.3.1 Extensometers

The borehole for the extensometer (Figure 3-21) was drilled into the Merensky hangingwall, intersecting the base of the Bastard Reef at 25,2 m. No movement was detected on this contact and only 10 mm between the Bastard Reef and 7,5 m above the Merensky Reef. Approximately 60 mm of deformation occurred below 7,5 m during a face advance of 35 m. Deformation amounting to about 12 mm continued in those strata after the panel had stopped mining (see Figure 3-21). No deformation was measured below 1 m until a span of 7 m had been mined. Once the panel had exceeded 19 m, no further deformation was recorded below 1 m (see Figure 3-21).

3.7.3.2 Closure meters

Over 120 closure meters were installed in the stope. The results of those highlighted in Figure 3-20 are plotted in Figure 3-22. Initially the closure rate was about 9 mm/m of face advance. At a span of approximately 15 m, it reduced to 6 mm/m. However at about 30 m it increased to 14 mm/m. This was associated with a large fall of ground near the centre of the panel, indicating an approach to unstable conditions. Closure of 60 mm was recorded after mining on panels "Stope 3" and "stope 4" had stopped.

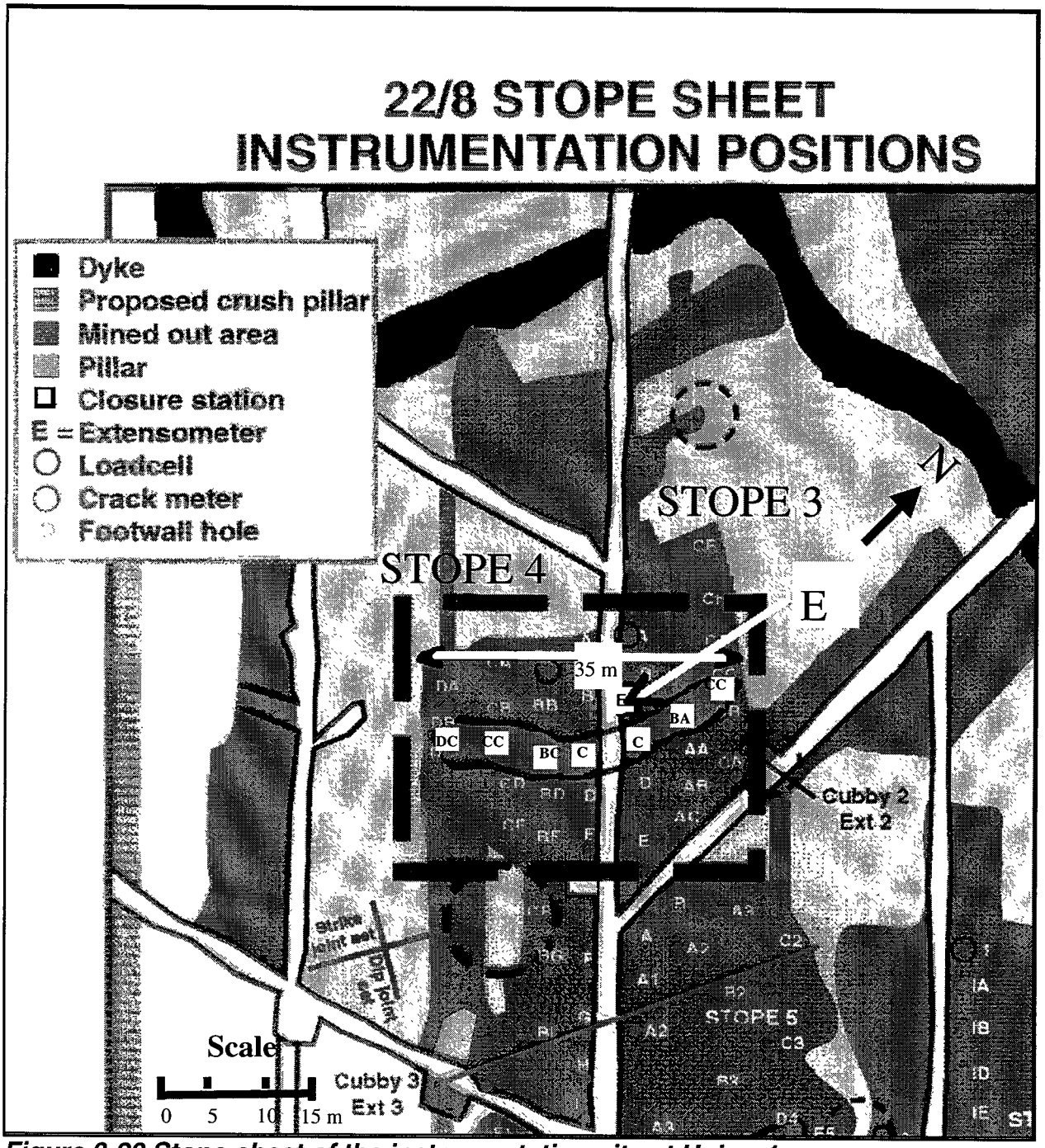

Figure 3-20 Stope sheet of the instrumentation site at Union-1.

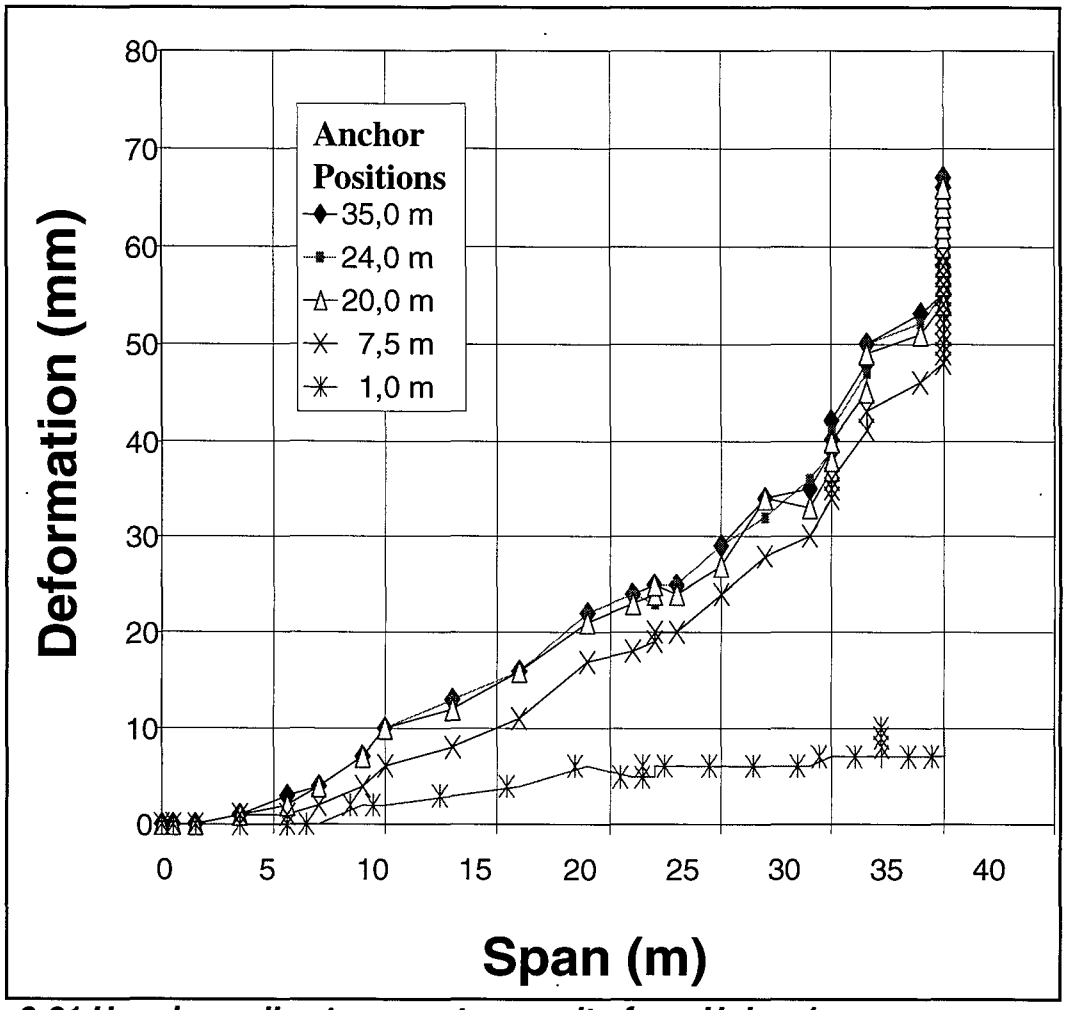

Figure 3-21 Hangingwall extensometer results from Union-1

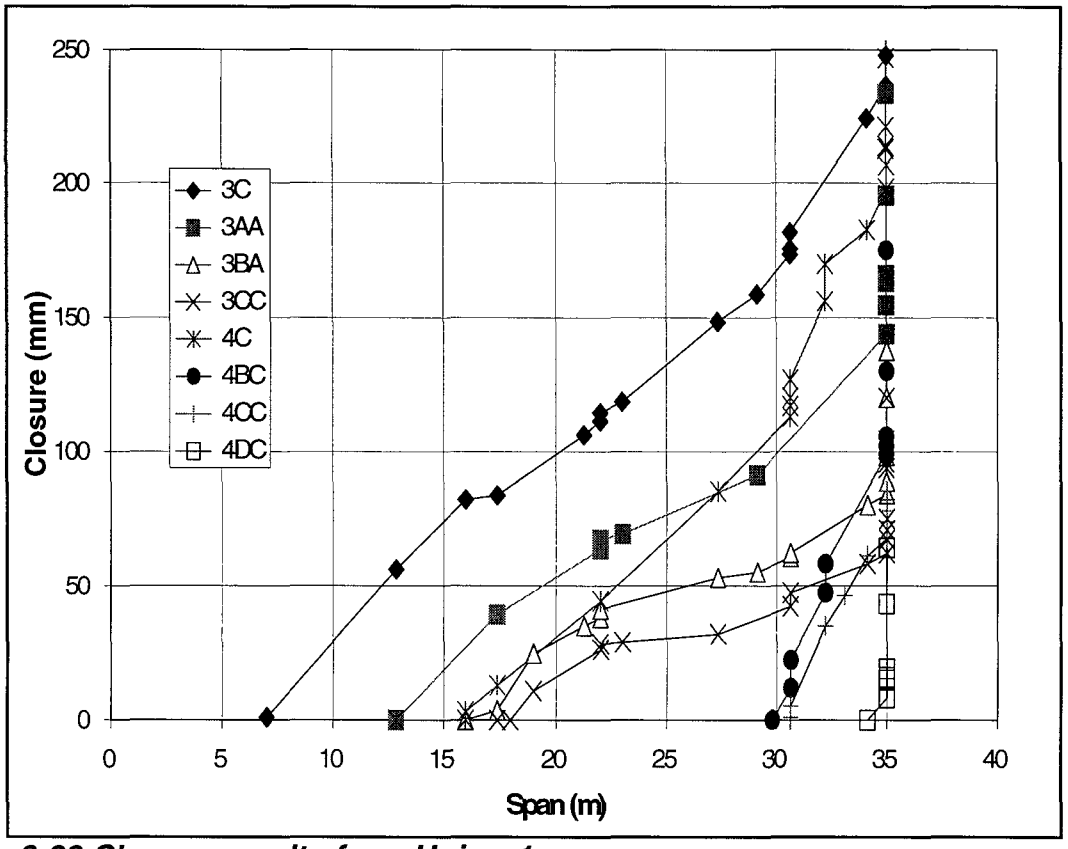

Figure 3-22 Closure results from Union-1.

3.7.3.3 Timber prop results

Figure 3-23 is a typical example of the load versus deformation and distance to face curves for the 200 mm diameter mine poles used at Union-1. The mine poles were installed at 3 m from the face and begun failing after about a 2 m face advance, i.e. 5 m behind the face (see Figure 3-23). At this position the next row of permanent support was installed. Grout packs were installed between the sticks in every second row, usually at 3 m from the face but the first row was installed at 5m from the face (in line with the extensometer). Closure measured at the load-cell positions indicated that the poles were stiff, attaining 200 kN after 4 mm compression, but reached peak load and started failing at 20 mm compression.

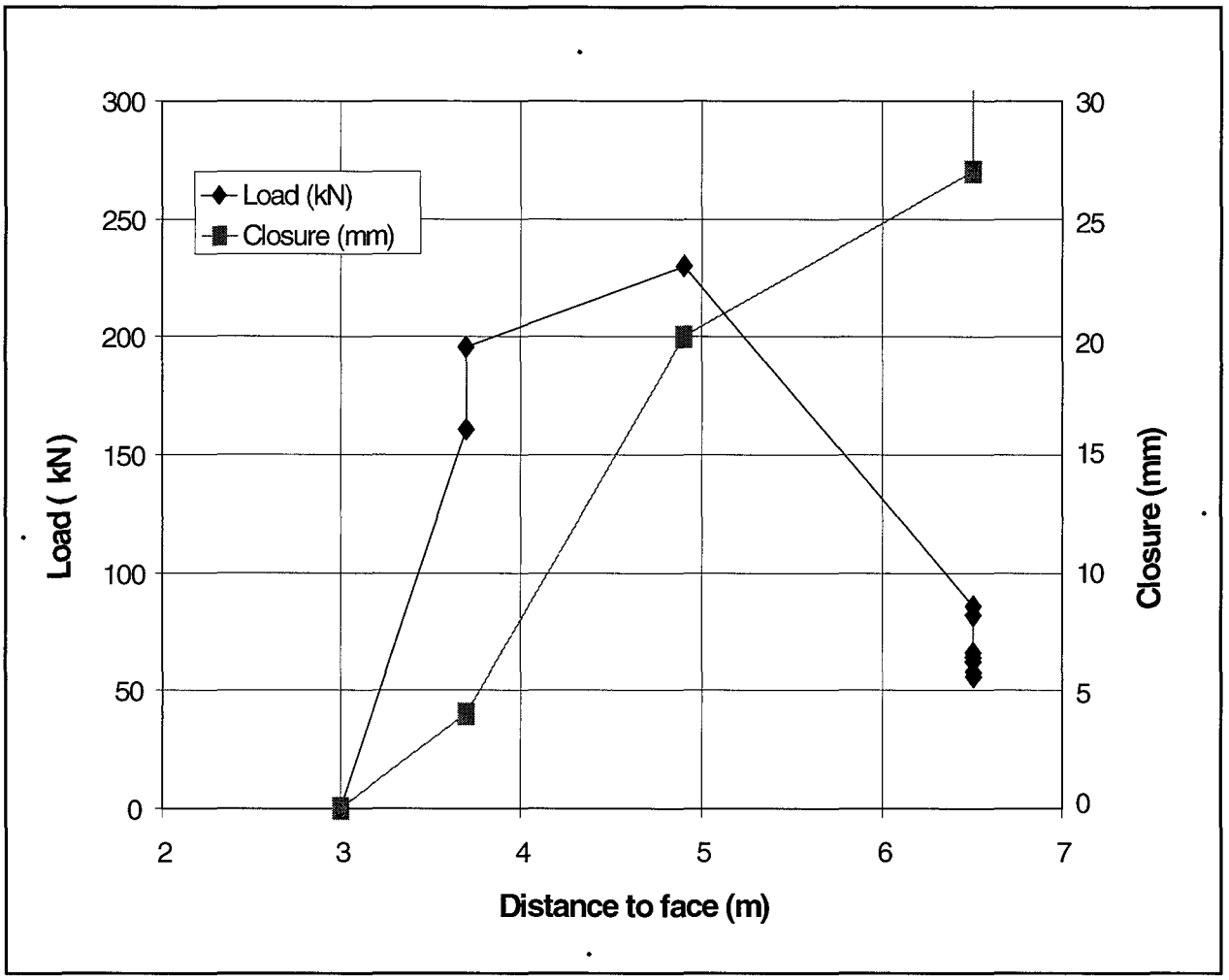

Figure 3-23 Stick performance and closure relating to face advance.

3.7.4 Discussion

Approximately 65 mm inelastic movement occurred in the hangingwall. The horizontal extension fractures, observed in a borehole camera survey at the end of the mining, indicated that most of the hangingwall movement occurred in the immediate 4,5 m. It appears that a high horizontal stress could have caused the extension fractures to develop parallel to σ_1, when the vertical confinement was reduced during mining.

A comparison between the geotechnical log performed prior to mining and the borehole camera survey, showed that many fractures had developed in the immediate 4,5 m during mining. The mine poles failed after about a 5 m face advance (see Figure 3-23), which created a situation where parting or loosening of the hangingwall could take place. The 5 m face advance formed a span of about 7 m (including the centre gully). Figure 3-24 showed that inelastic deformation initiated in the immediate 1 m of hangingwall when the stick failed. It therefore appears that

inelastic deformation was prohibited, to a depth of about 1 m into the hangingwall, until the sticks failed. Based on the theory that the extension fractures developed when the confinement was removed, it appears that the load reaction generated by the sticks was sufficient to stop stress fracturing for at least one metre into the hangingwall. The first line of packs was installed between the sticks at 5 m from the face. Four sticks were installed inside the metal rings used to contain the grout, which increased the post failure load carrying capacity of the sticks and enabled the pack to generate a load reaction quickly. However, the packs were not all installed correctly and generally required about 30 mm closure before the grout started to generate a load reaction. By the time the grout pack started generating a load reaction, the sticks within the grout pack and in the adjacent row had started to fail. However, the packs were stiff, generating about 10 x more load than the sticks after 20 mm deformation (see Figure 3-23 and Figure 3-25).

Figure 3-22 showed a reduction in closure rate at a span of about 16 m and Figure 3-21 showed that inelastic deformation stabilised in the immediate 1 m of hangingwall at a span of 18 m (a span of 18 m was achieved when the panel to the north of the extensometer had been mined out to 15 m and the south face was 3 m from the extensometer). Therefore, it appears that the packs started to generate sufficient reaction to support the fractured zone after about a span of 16 m - 18 m had been mined. The borehole camera survey indicated that this fracture zone extended to a depth of 4,5 m. The closure that would have occurred on the packs near the extensometer at a span of 17 m was 84 mm (see 3c in Figure 3-22). However, the packs generally required about 30 mm closure before the grout started to generate a load reaction. Therefore, the effective deformation was about 54 mm. The load deformation characteristics of a grout pack measured at Amandelbult Section (Figure 3-25), showed that a load of about 5,7 MN per pack could have been generated at 54 mm. The packs did not appear to be failing at the span of 17 m, and therefore could have reached 5,7 MN. Each pack supported about 8 m^2, indicating that a support resistance of 712 kN/m^2 was required to stabilise the fracture zone in the hangingwall (to a depth of 4,5 m). The weight of the material up to 4,5 m would have generated a load of 140 kN/m^2, indicating that there was a horizontal driving force enabling the observed inelastic deformation to occur. The high degree of fracturing observed in the zone up to 4,5m appeared to confirm this hypothesis.

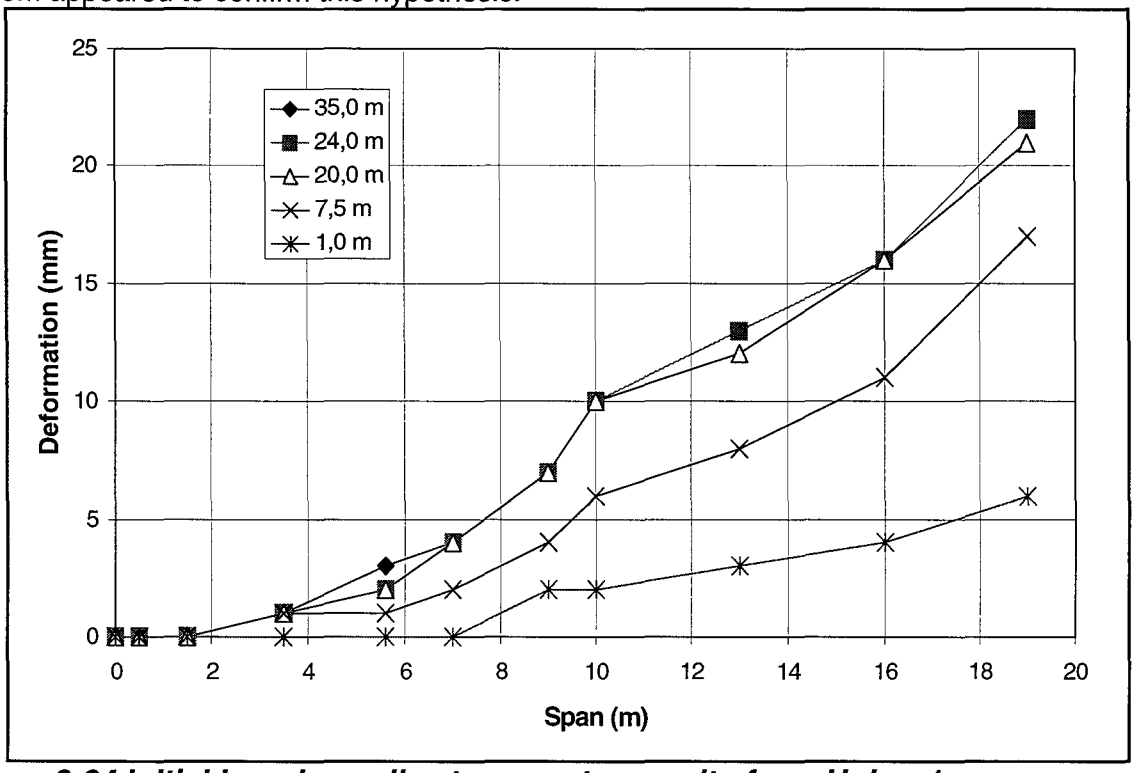

Figure 3-24 Initial hangingwall extensometer results from Union-1.

Inelastic deformation occurred, between 1 m and 7,5 m into the hangingwall, from the first blast, i.e. from a span of 1,8 m (Figure 3-24), indicating the need to install support as close to the face as possible. After a span of 4 m - 6 m had been mined (Figure 3-24) inelastic deformation occurred above 7,5 m into the hangingwall, indicating that the abutments supported the hangingwall above 7,5 m up to these spans. Therefore, it appears that the face supported an arc of about 50^0 - 75^0 over the immediate hangingwall. Face support requirements should therefore be designed ignoring the face capacity.

The in situ load deformation characteristics of timber props varied significantly at different loading rates, as shown in Figure 3-26 and Figure 3-27. The loading rate at Union-1 was 9 mm/m face advance and at Amandelbult 1,4 mm/m face advance. These results indicate that timber props are less stiff if the closure rate reduces, and therefore, the engineer should design panel spans using the timber characteristics suited to the closure rates on his mine.

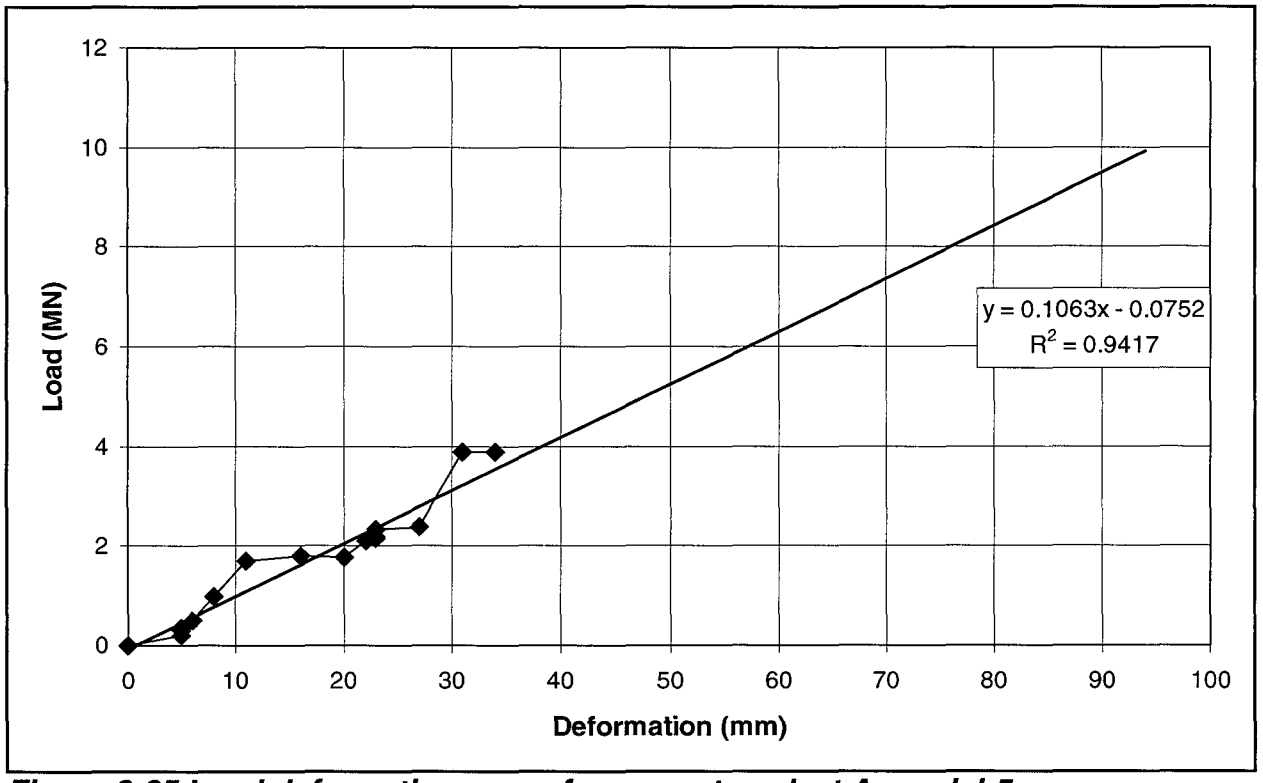

Figure 3-25 Load deformation curve for a grout pack at Amandel-5.

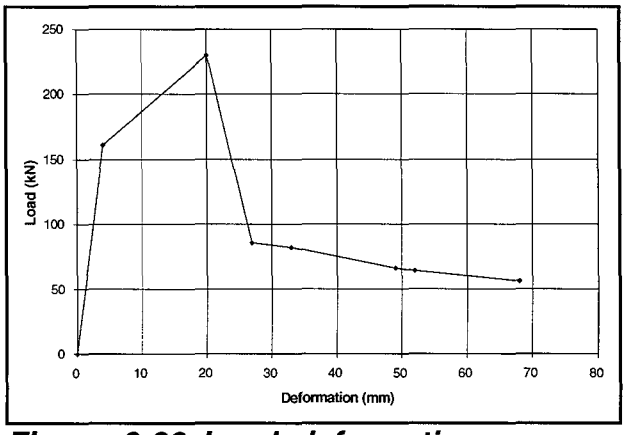

Figure 3-26 Load deformation curve for a stick at Union-1.

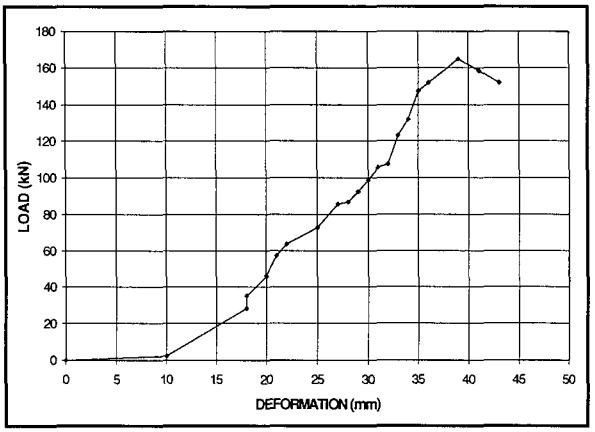

Figure 3-27 Load deformation curve for a stick at Amandel-1

3.8 Conclusions

A comparison of the various geotechnical rock mass classification systems shows that the Impala modification of the "NGI Tunnelling Quality Index" system provides the most accurate description of actual observed conditions. Figure 3-3 is an attempt to define stable and unstable spans by using this system.

Generally collapses could be related to a critical span using this rating (see Figure 3-3). However, there were some exceptions, which highlighted the fact that a greater understanding of the rock mass is required. Of the four points through which the straight line has been drawn (see Figure 3-3), one panel failed in an "unravelling" manner, with a poor rock mass rating, while the other three failed on major geological discontinuities. Despite the different failure mechanisms between these four sites, a straight line, with a high r^2 of 0,965, was fitted.

Stress measurements, observations and even stratigraphy, have shown that the virgin "k-ratio" varies from area to area, implying that greater emphasis should be allocated to stress determination, especially in areas where unusual stress conditions are suspected.

The chart, at this stage of its development, cannot adequately take unusual stress conditions into account and requires some modification to account for discontinuity persistency and orientation. This implies that the rock mass rating system, requires some modifications to account for stress and discontinuity orientation and persistence. This is despite the finding that the Impala rock mass rating system best described the prevailing *in situ* conditions.

Joint surveys should be carried out along the whole length of the raise to be assessed and a rating determined for the time being from the Impala system. The rating could be compared to the chart to determine safe panel spans.

The site at Union Section indicated that high horizontal stresses could have been responsible for the fracturing observed at 4,5 m depth into the hangingwall. An increase in closure rate appears to have signalled a pending collapse and therefore the critical span. The Amandel-1 site plotted well below the critical line in the chart (Figure 3-3), indicating that it could have been mined at a greater span. Observed conditions in the panel confirmed this postulation. The Lebowa Plats site indicated that at shallow depths there is very little, if any, warning of a collapse. This highlights the importance of having a reliable method to determine safe spans, particularly at shallow depths.

In all three of the above sites the "crush" pillars punched into the footwall, causing footwall heave. The effect of footwall punching on "crush" pillar design confirming the need for this to be investigated in detail. Very little stress fracturing was observed either on the pillars or on the face, indicating that an elastic model should correlate well with actual measurements. Extensometers did not measure parting on the Bastard Reef, nor was any significant parting observed at any of the instrumentation sites. However, the MINSIM-W model of the 77 m wide panel at Impala indicated that, even with a k-ratio of 0,5, only about 0,2 mm parting in a 12 m thick plate is predicted. This small deformation could not have been detected with a wire extensometer.

Two of the three sites, where stress measurements were conducted, measured relatively high horizontal stresses in the hangingwall, indicating that compressive horizontal stress may be common. These stresses would act to clamp steeply dipping discontinuities and destabilise those with a low angle dip, and therefore could not be accounted for merely with a joint analysis.

Stress measurements at Impala 8 shaft show that some form of inelastic deformation must have occurred to result in the measured distribution of horizontal stresses. The indications are that a plate bending deformation mechanism occurred. Despite this, the horizontal stresses in the first

two metres of hangingwall are close to zero. It is hypothesised that creep and slight opening of discontinuous joints may explain this phenomenon.

Stress measurements should be made in every geotechnical area and the results included in the analysis of collapsed and stable panels. This could lead to improvements in the Critical Panel Span Design Chart.

All but one of the collapsed sites either occurred on a major geological discontinuity, such as a fault, dyke or persistent horizontal joint, or as a result of high horizontal stress. Observations indicated that high horizontal stresses probably also played a part in most of the discontinuity collapses. Horizontal stress fracturing indicated high k-ratios in many of the collapses. Generally, the jointing above the Merensky Reef was almost vertical, with an extent of less than 3 m. It appears that horizontal stresses acted to clamp the almost vertical joints in most panels but destabilised discontinuities with a low angle dip. The findings of the investigation suggest that:

1) High horizontal stresses in the hangingwall are often associated with potholes.
2) The effects of stress should be included in the chart rating.
3) A change in span often results in a corresponding change in conditions.

A search was made on the mines to identify a panel collapse resulting only from a joint / panel span relationship. Only the Union-1 collapse could be attributed to jointing alone. Most of the observed collapses occurred on major, pre-existing discontinuities such as faults or persistent shallow dipping discontinuities or as the result of abnormally high horizontal stresses.

A collapse resulting from an adversely orientated fault could have occurred at almost any span, provided that there was a suitably orientated vertical joint to form a wedge. Conversely if the position or orientation of the collapsed panels had been different the collapse would probably not have occurred. Therefore, the collapses may not have been span related. However, there was evidence that a change in span resulted in a corresponding change in hangingwall conditions. It appears that a change in the span has the greatest influence when there are shallow dipping discontinuities. There also appears to be a linear relationship for four out of five collapsed cases (Figure 3-3), suggesting again that there is a correlation between span and hangingwall jointing but that other geophysical conditions also need to be included in the analysis. A search was made on all the platinum mines and some gold mines, to see if a panel collapse could be identified which was not related to a major geological discontinuity, however only stress related mechanisms were found. Lebowa-5 confirmed that high horizontal stresses were involved in some collapses. The results of the wedge analysis also seemed to confirm horizontal driving forces, which pushed the wedges out. These findings indicate that the inclusion of a stress analysis in the design chart could improve span prediction. Other findings indicated that orientation and persistency of discontinuities are also an important consideration, which is not adequately included in the rating analysis. Modelling of these discontinuities could improve understanding of behaviour.

If high horizontal stresses were acting in a hangingwall then vertical joints would be insignificant and low angle joints more significant than currently rated in the chart. Joint densities could be less significant than the levels of stress (high horizontal stresses could clamp vertical joints that are orientated perpendicular to it). It was therefore important to carry out some stress measurements to observe:

1) If there is a tensile zone above a panel.
2) How high does it extend if it exists?
3) What are the horizontal stress levels above a panel?
4) How do horizontal stress levels vary with depth and span?

The variation in results of the three sites where stress measurements were performed was considerable. Stress measurements performed to determine k-ratio variation with depth showed a large scatter in the results (Coetzer *et al.*, 1993). It is therefore suggested that more measurements should be performed.

Generally, the jointing above the Merensky Reef is almost vertical, and usually has a vertical extent of less than 3 m. Instrumentation failed to measure any horizontal dilation across these joints, even at the centres of the panels. MINSIM-W predicted the elastic movement to be small, especially if the dilation was spread over all the joints as Impala-1 suggested. The Impala-1 site showed that panels can be stable in an horizontal tensile stress environment. The comparison between the UDEC model and analysis performed using the chart (Section 4.10) appears to confirm that collapses could occur at relatively small spans if there were low angle discontinuities in the hangingwall. The absence of low angle discontinuities in the hangingwall of the Merensky Reef could explain why the minimum span does not often need to be less than 30 m. In all three of the sites where rock mass movement was monitored, footwall heave was observed. The effect of footwall punching on crush pillar design needs to be investigated in detail.

The tests performed on material from Amandel-1 showed that the footwall material was significantly stronger than the hangingwall or reef. However, the instrumentation indicated that the hangingwall was relatively stable with most of the closure being attributed to footwall heave as a result of pillar punching. It should be noted that, while inelastic radial dilation initiated at lower strains in the reef and hangingwall pyroxenite, the footwall anorthosite had a larger radial strain, than the hangingwall pyroxenite, for any given level of stress. This could account for some of the footwall heave. Anorthosite also appears, from laboratory tests, to be more brittle than pyroxenite, failing violently whilst the pyroxenite failed in a controlled manner under the same loading conditions. Stress fractures have been more frequently observed in anorthosite than pyroxenite underground and collapses associated with stress also appeared to be more common in anorthosite than pyroxenite. The point load tests indicated that the tensile strength of the anorthosite footwall, in a horizontal direction, was relatively low which could have enabled extension fractures to develop under a high horizontal stress environment. These findings indicate that anorthositic hangingwalls could be more susceptible to stress related collapses than pyroxenite.

There was a large variation in strength parameters within lithological units across the Bushveld Complex.

The results of wedge analysis of large scale falls of ground that collapsed in a cantilever fashion, suggest that there were horizontal driving forces, which pushed the wedges out. This underlines the importance of an understanding of the stress environment, as well as the interaction between stress and the rock mass.

In terms of the influence of internal panel support systems, the load reaction generated by the sticks that were instrumented appears to have been sufficient to delay inelastic deformation for at least 1 m into the hangingwall. Inelastic deformation occurred from the first blast, indicating the need to install support as close to the face as possible. The effective stress trajectory from the face abutment into the hangingwall sufficient to prevent horizontal stress fracturing was at an angle of 60^0 - 75^0, indicating that face support design should not take the face capacity into account. It appears that the packs started to generate sufficient reaction to support the fractured zone, of 4,5 m, after about 84 mm of closure had occurred. A support resistance of 712 kN/m^2 could have been generated to stabilise the fracture zone, where the weight of the material would have generated a load of 140 kN/m^2. This finding indicates that there was a horizontal driving force enabling the observed inelastic deformation to occur.

Timber props increase their capacity to deform if the closure rate reduces, but are less stiff, therefore, the engineer should design using the timber characteristics best suited to the closure rates on his mine.

3.9 References

Afrouz, A.A. 1992. Practical handbook of rock mass classification systems and modes of ground failure. CRC Press. Bocaraton, 12

Barton, N. 1997. Rock mass characterisation workshop. *Workshop notes.*

Barton, N. & Grimstad, M. 1994. The Q-system following twenty years of application in NMT support selection. *Fachzeitschrift fur Ingenieurgeologie, Geomechanik, Projektierung und Bauausfuhrung,* 12 : 428 – 436.

Butenuth, C. 1997. Comparison of Tensile strength values of rocks determined by point load and direct tension tests. *Rock Mechanics and Rock Engineering,* 30 : 65 - 72.

Coetzer, S.J., Spencer, D. and de Maar W. 1993. Rock stress and mining: a case history. Rock engineering problems related to hard rock mining at shallow to intermediate depths. *Symposium proceedings*, 28 – 37

CSIR Miningtek. SS 1993. Strain softening analysis, providing input parameters for FLAC models from laboratory triaxial tests.

Hoek, E. and Brown, E.T. 1982. Underground Excavations in Rock, 14 - 35.

Itasca Consulting Group. 1993. Universal distinct element code, ver 2.0.

MINSIM-W. 1997 Boundary element code for calculating elastic stress and displacements.

Watson, B.P. 1998. A programme of underground instrumentation and laboratory tests, to understand the rock mass behaviour on the Merensky Reef, Bushveld Complex. *Advances in Rock Mechanics*, 38 – 47.

Watson, B.P. 1998. Assessment of large panel spans at Impala Platinum Bafokeng North mine 8 shaft. *Internal note 98 - 0219.*

Watson, B.P. 1998. Large fall of ground in the 3U20-3E panel at Lebowa Platinum Mine. *Internal note 98 - 0107.*

Watson, B.P. 1997. Collapse of the 6/5E/9E panel at Lebowa Platinum Mine. *Internal note RE 7/97.*

Watson, B.P. and Noble, K.R. 1997. Comparison between geotechnical areas on the Bushveld Complex platinum mines, to identify critical spans and suitable in-panel support. *SARES97 proceedings*, 440 – 451.

4 The stability of panels between pillars

4.1 Introduction

This chapter addresses Enabling Output numbers 5, 6 and 7 (see page 13).

A high percentage of accidents occur in various locations in stope panels. From this point of view, and the fact that most underground workers find themselves in stopes everyday, it is very important that these panels are made safe, or as safe as possible.

In this analysis, the influence of joint properties on the stability of a stope hangingwall at shallow to intermediate depths is investigated. The model was set up so that failure always occurred on joints and not of the rock itself.

The stability of panels depends on a number of factors such as the rock mass properties, the stress regime, the influence of pillars, and the span of panels. Rock masses consist of intact rock material which is cut by discontinuities. The strength of the discontinuity (weakness plane) has a large influence on the strength and stability of the rock mass.

The influence of the following factors on the stability of a stope hangingwall, were investigated:
1) joint orientation
2) joint friction angle
3) panel span
4) joint spacing
5) support spacing.

Other factors, such as the magnitude and direction of the principal stresses, joint cohesion, and joint dilation were not considered as variables in the analysis.

Failure of the hangingwall occurs due to different mechanisms. These mechanisms are functions of a combination of the different rock mass parameters. Some of the possible failure mechanisms are:
1) shear failure along existing discontinuities
2) dead weight fallout of individual blocks or keyblocks with unfavourable geometry
3) formation of tensile cracks in the hangingwall, or the opening of discontinuities under a tensile stress field
4) compression of hangingwall beam leading to buckling
5) pillar punching
6) a cantilever effect.

Apart from the bedding plane joint set, only one other set has been modelled, at various dips (see Figure 4-1). This is considered to be realistic, because two major joint sets with the same strike, or even similar strikes, are rarely encountered underground.

In addition, the results obtained from the empirical approach (the Critical Panel Span Design Chart in Chapter 3) and the numerical modelling approach presented in this chapter are compared.

4.2 Definition of UDEC numerical model

The universal distinct element program, UDEC (Itasca,1991), was used to analyse the stability of a jointed rock mass.

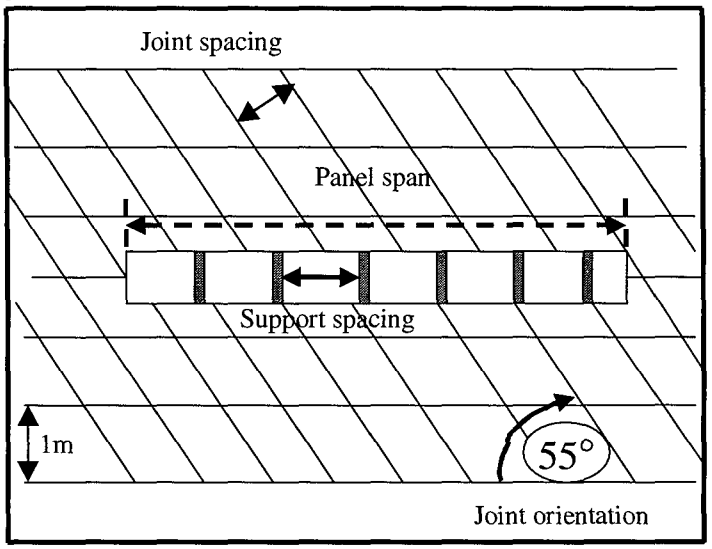

Figure 4-1 UDEC model.

In this analysis, a failure path is provided by creating two sets of discontinuities. The one set is always flat dipping (bedding planes), and the dip angle of the other set is varied from 5° to 90°. These joints are assumed to be cohesionless and to have a dilation angle of 2°. The friction angle of the joints was varied to produce either stable or unstable conditions. The horizontal joints were up to 4,5 m above and below the reef-hanging- and footwall contacts at a spacing of 1 m. Both joint sets were assigned the same properties. The influence of multiple stopes with pillars separating panels, and single stopes with abutments on either side of the panel, on the stability of different rock masses was investigated. This was done to ascertain the relative stability of stope hangingwalls for the two situations. The virgin vertical stress and the k-ratio were taken as 13,5 MPa and 2 respectively. The bottom boundary of the model was fixed. A pressure of 13,5 MPa was applied to the top, and 27 MPa was applied to each side, of the model. This corresponds to a depth of approximately 500 m, assuming the density of the rock mass is 2700 kg/m^3.

4.3 Failure modes in numerical model

Two types of hangingwall failure occurred in the modelling. In most cases failure occurred due to shear failure on the joints closest to the abutment. Due to the initial shear failure on the joints at the one abutment, systematic failure of the hangingwall occurred that propagated from the one side of the panel to the other side. The second type of failure was due to tensile stresses at the centre of the panel. Thus, due to the extent of the closure at the centre of the panel, beam failure occurred which propagated towards the abutments. This failure pattern was typical for the very steep dipping joint sets (greater than 75°).

4.4 Applicability of the methodology based on UDEC model

The analysis was done using a two dimensional program. This is a very simplified model of reality. Only two joint sets were used in the model. All joints are assumed to be continuous throughout the model. Joint sets, or the odd joint, in the plane of the model cannot be modelled. This is not necessarily a major limitation because the second major joint set is often very non-persistent.

Due to the above-mentioned limitations, the results must only be used for situations where similar conditions prevail in terms of the rock mass structure and properties. The results should not be used if a different failure mode is experienced. Examples of where this methodology is not applicable are:

1) triplets in UG2 reef, which fail by a plate bending mechanism
2) very good rock mass with very few joints
3) dilational movement in the hangingwall due to high stress at the face
4) the rock itself fails in shear or tension
5) two orthogonal major joint sets of very high persistence.

The results presented may be conservative under the following *in situ* conditions:

1) lack of reef parallel planes
2) only one major joint set that is non-persistent (apart from the bedding planes)
3) a second major joint set is present (more or less orthogonal to the modelled inclined joint set i.e. in the plane of the model) and both joint sets are non-persistent
4) any combination of the above.

4.5 Methodology for support design taking geotechnical parameters into account

The proposed methodology is presented in Figure 4-2 in a flow chart form. The contents of the chart are discussed in Sections 4.6, 4.7 and 4.8.

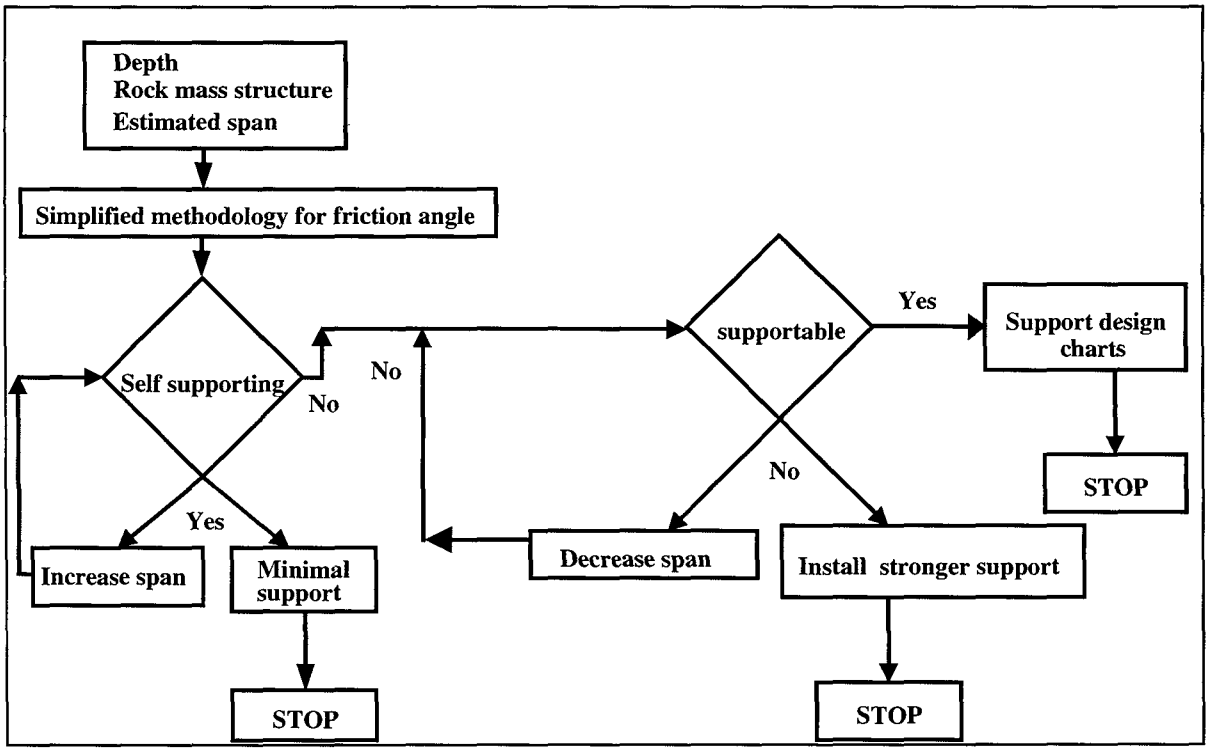

Figure 4-2 Proposed methodology for support design.

4.6 Definition of unsupportable, supportable and self supporting panel spans

If failure occurs on the horizontal joints up to 4,5 m, the situation is defined as unsupportable. This is shown in Figure 4-3. The vertical scale was changed to allow easy visual understanding. The stope width is 1 m.

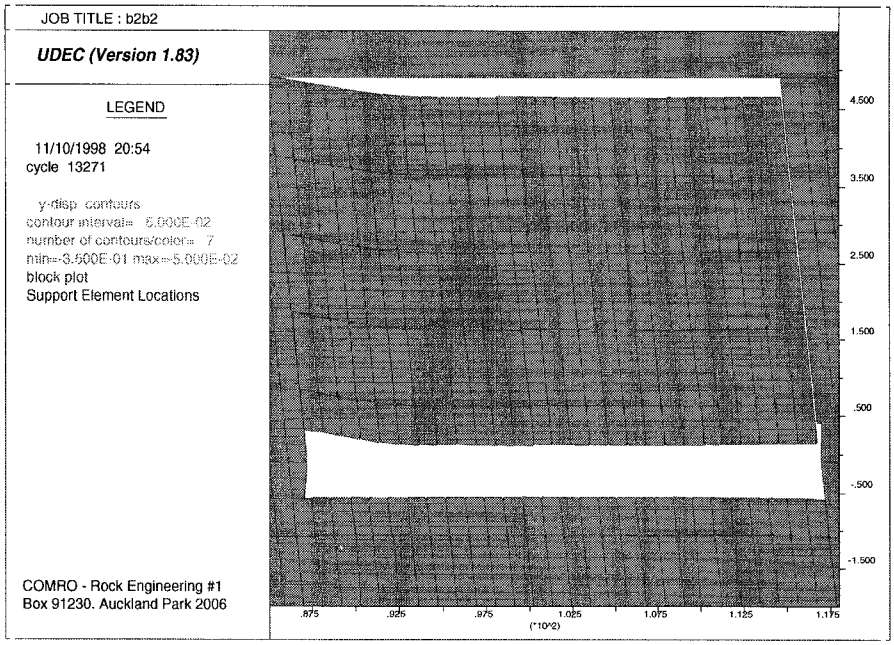

Figure 4-3 Unsupportable hangingwall.

If the failure occurs up to a maximum of 1,5 m above the reef-hangingwall contact, it is defined as supportable, with a support resistance requirement of at least 45 kN/m^2. This definition is based on the assumption of the support capabilities of an elongate based support system.

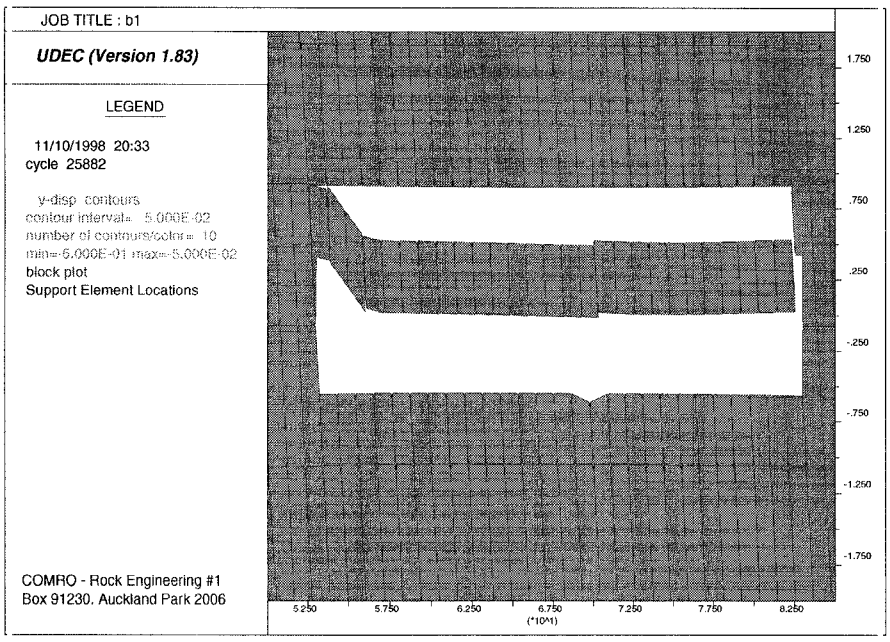

Figure 4-4 Supportable hangingwall.

If no failure of the hangingwall occurs, the configuration is defined as self-supporting. This does not imply that no support is needed in these panels, but only distinguishes between very stable and potentially unstable ground conditions.

Some of the joint orientations resulted in a stable configuration when the friction angles on these joints were sufficiently high. Under these conditions the rock mass was defined as self-supporting. An example of this analysis for steeply dipping joints is given in Figure 4-5 where the self-supporting zone is to the right of the second curve. Similar charts for all the joint set combinations are shown in Appendix A.

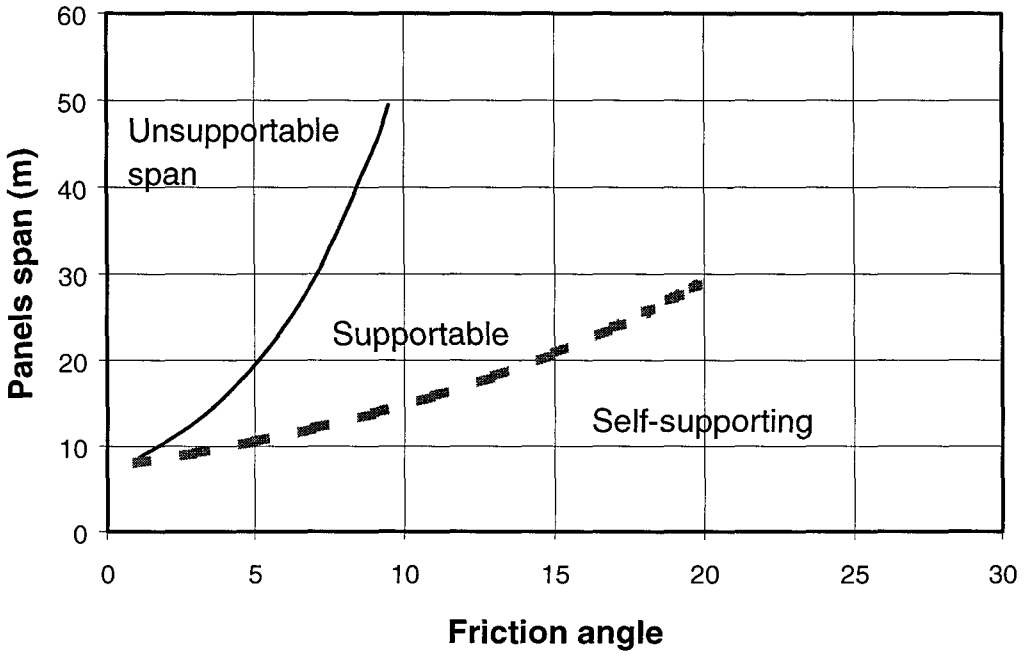

Figure 4-5 Relationship between friction angle and panel span for the 0°/(85°-90°) joint orientations (0° is the orientation of the horizontal joint and the 85°-90° refers to the orientation of the other joint set).

4.7 Supportable spans

The single stope models resulted in the graph shown in Figure 4-6. It was found that certain joint orientations exhibited similar behaviour. These joint orientations were categorised in 10° to 25° ranges as shown in Figure 4-6. The left of each curve in Figure 4-6 is referred to as unsupportable, whereas the right of each curve is referred to as the supportable zone for the particular range of joint sets.

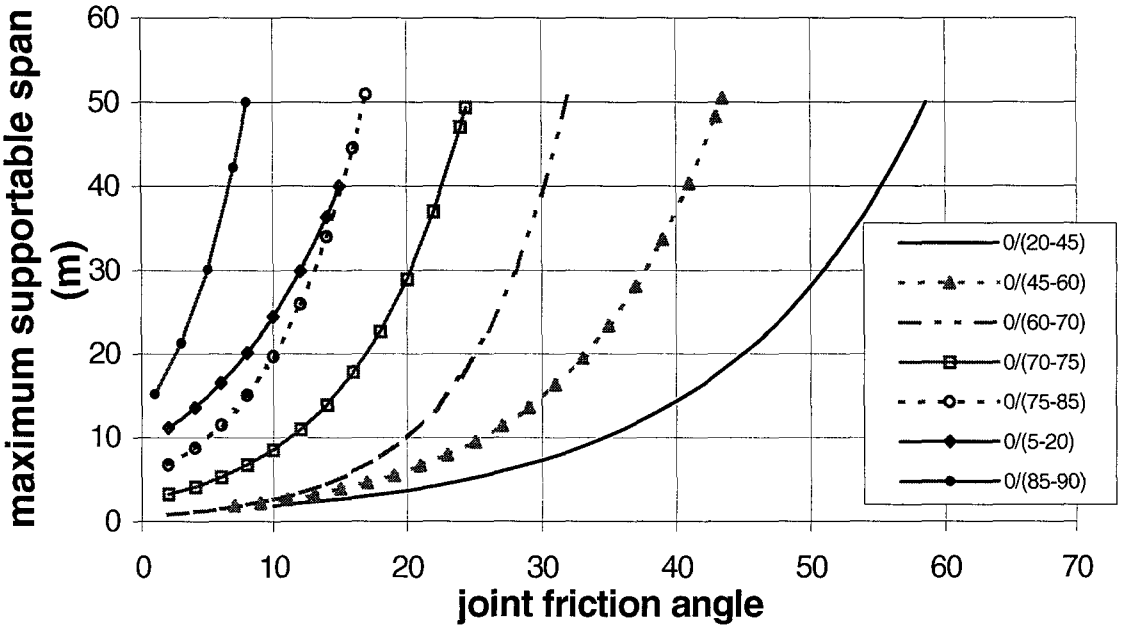

Figure 4-6 Influence of joint orientation and friction angle on the panel span for a single stope.

From the results it is clear that the 0°/(85°-90°) joint orientation is the most favourable for stable mining conditions. The 0°/(20°-45°) joint orientation is the most unstable because a larger joint friction angle is required for the stability of any given span compared to other joint orientations. The 0°/(5°-20°) joint orientation however requires a low friction angle for panel spans up to 30 metres. The explanation for this apparent anomaly is that the low angle joints form large blocks that are difficult to dislodge from the hangingwall.

The relationships between joint orientation, friction angle and panel span are shown in Figure 4-7, for multiple panel spans (6 panels, with 4 m wide pillars). The absence of the 0°/(20°-45°) curve in Figure 4-7 is because the hangingwall beam was unsupportable even at friction angles of 60°.

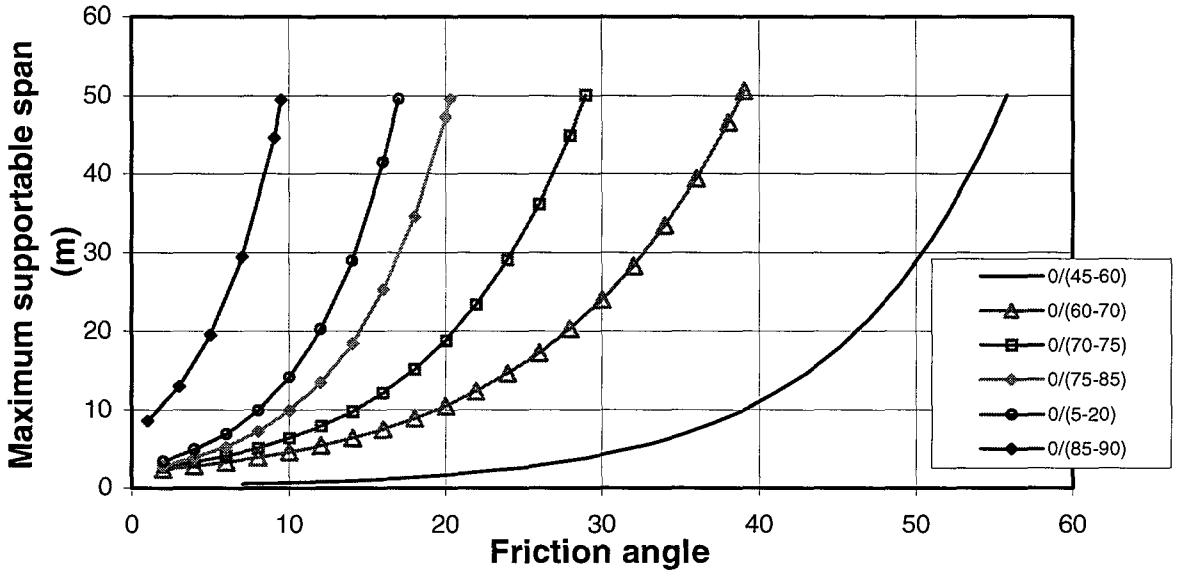

Figure 4-7 Influence of joint orientation and friction angle on the panel span for multiple stopes.

The supportable and self-supporting curves for the 0°/(85°-90°) joint orientations are presented in Figure 4-5. For all of the joint orientations that resulted in a self-supporting configuration, the maximum self-supporting panel span was 30 m, even at very high friction angles. Panel spans greater than 30 m required support in all cases. At low friction angles of less than 10°, supportable spans of over 20 m are only possible where the joints dip at over 85°.

4.8 The design of elongate support

For certain points in the supportable region, the influence of elongate support on the stability of the hangingwall beam was investigated. These points are defined in CSIR Miningtek Technical Report 98/0440. The load–deformation characteristics of the support is given in Figure 4-8.

The boundary conditions of the model are the same as before. Failure of the support will occur after 25 cm of deformation. Thus, the influence of the support after failure is zero and is not taken into account in further calculations. The support spacing was varied from 1 m to 5 m. For each model the number of blocks that dislodged between support units were expressed as a percentage of the total number of blocks in the hangingwall beam up to the first horizontal parting ("% instability" in subsequent figures). From these models, a relationship between the support spacing, the percentage instability and the joint spacing could be obtained. The percentage instability is a hazard indicator. The higher the percentage instability, the greater the hazard. For the 0°/(85°-90°) joint orientations, the percentage instability and the support spacing was determined for friction angles of 5° and 10°, for panel spans of 20 m and 30 m. The results for the 20 m panel span and friction angle of 5° are shown in Figure 4-9. For a support spacing

of 2 m, 40 per cent of the hangingwall beam is unstable for both the 1 m and the 2 m joint spacing. For this scenario, a support spacing of 1 m results in complete stability of the hangingwall beam.

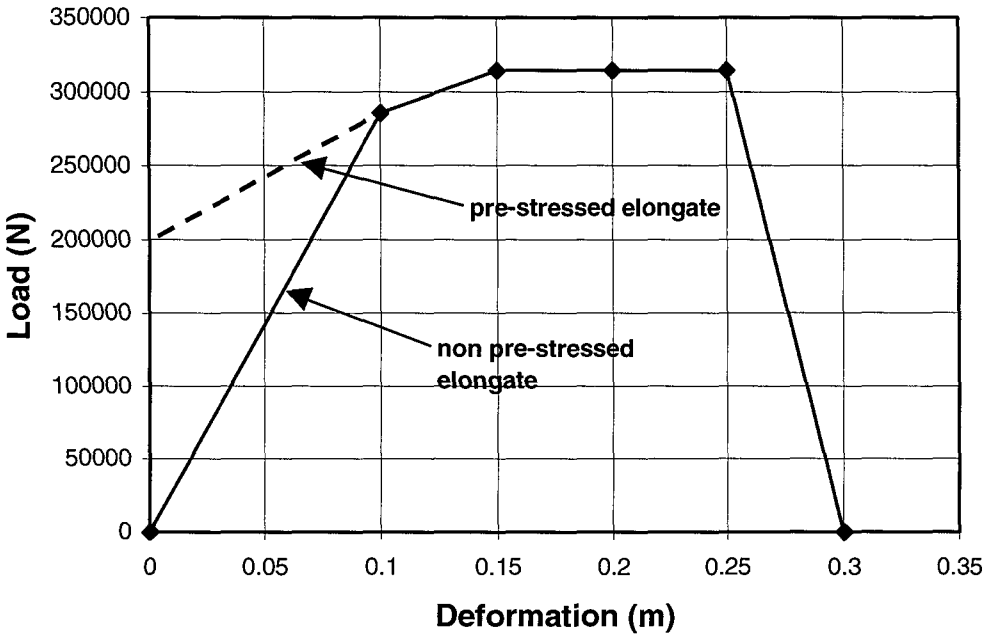

Figure 4-8 Load deformation curves of elongate support used in modelling.

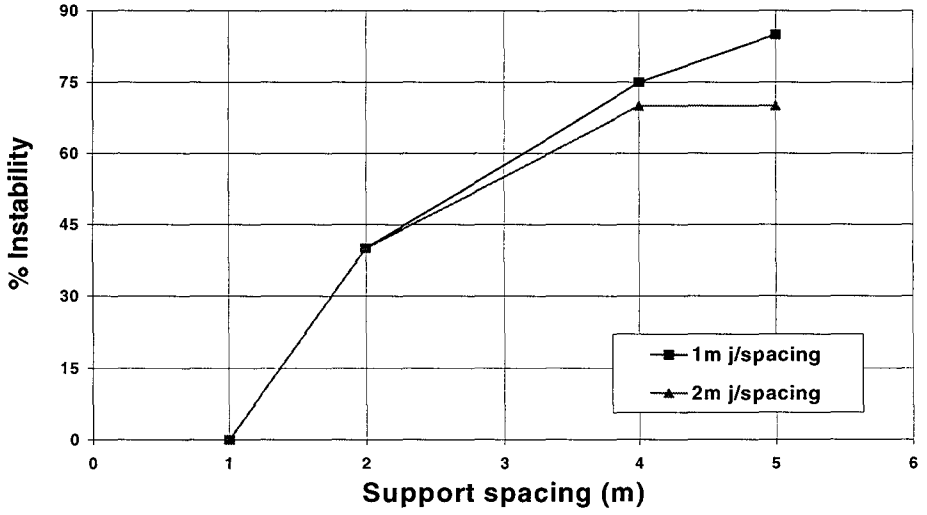

Figure 4-9 Percentage instability as a function of support spacing and joint spacing for 0°/(85°-90°) joint orientations with 5° friction angle for a 20 m panel span.

The results for the 20 m panel span and a friction angle of 10° are shown in Figure 4-10. The cross over in Figure 4-10 is because the same blocks were unstable for both accesses, but there are more blocks in the hangingwall for the 1 m joint spacing than for the 2 m joint spacing respectively. Similar charts for the design of elongate support for each joint set combination are provided in Appendix A.

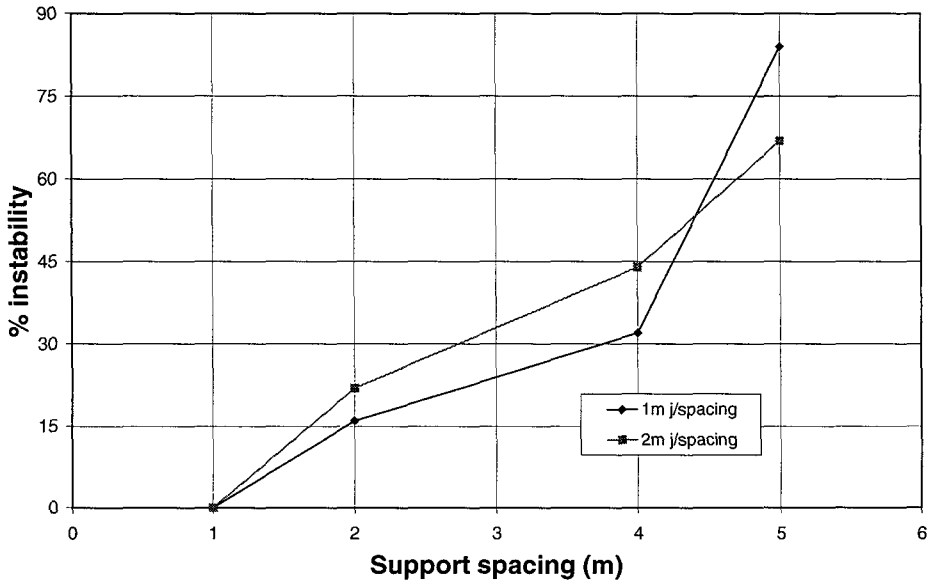

Figure 4-10 Percentage instability as a function of support spacing and joint spacing for 0°/(85°-90°) joint orientations with 10° friction angle for a 20 m panel span.

Although a friction angle of 10° results in less instability of the hangingwall, the optimum support spacing is still 1 m. The UDEC model for the 0°/(85°-90°) joint orientation with a friction angle of 10°, support spacing of 5 m and a joint spacing of 1 m, is shown in Figure 4-11.

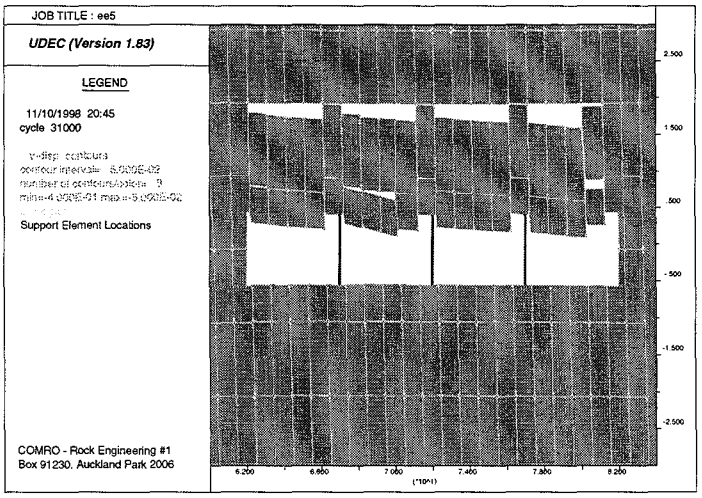

Figure 4-11 Model showing instability in hangingwall beam and influence of support for the 0°/(85°-90°) joint orientations for a 5 m support spacing.

It is emphasised that the support design charts should only be used as first approximations of relative hazard. More details concerning detailed support design can be found in the final project report on SIMRAC project GAP330, Design of Face Support Systems.

4.9 Influence of pre-stressed support

The influence of pre-stressed elongate support was investigated for the 0°/(85°-90°), 0°/(70°-75°) and 0°/(45°-60°) joint combinations. The support was pre-stressed to 200 kN as indicated by the dotted line in Figure 4-8. This was done for a 20 m panel span with the joint properties and boundary conditions the same as for non pre-stressed support. For all three cases a support spacing of 5 m was taken. Without the pre-stressed support, the percentage instability

for the 0°/(85°-90°) joint combination was 84 per cent and with the pre-stressed support, the percentage instability was 26 per cent. For the 0°/(70°-75°) joint combination the percentage instability reduced from 11 per cent to zero per cent when the pre-stressed support was introduced. Without pre-stressed support, the percentage instability for the 0°/(45°-60°) joint combination was 87 per cent and with the pre-stressed support, the percentage instability was 37 per cent. Since the percentage instability is viewed as a hazard indicator, it can be said that the pre-stressed support is more useful than conventional support in reducing the hazard of rock falls, in these particular cases, and under the modelling assumptions.

4.10 Correlation between the numerical modelling and empirical results

4.10.1 Introduction

The influence of joint dip and friction angle on stable panel spans has been modelled using UDEC programme. Figure 4-7 shows the results of the investigation, where each curve represents the maximum stable spans where combinations of joint sets have various coefficients of friction. Any value to the left of the curves would result in a collapse, i.e. not supportable. With a view to comparing the predictions based on the empirical methodology to that based on the numerical modelling approach, analyses performed on the Critical Panel Span Design Chart (Figure 3-3) were compared to the UDEC output.

4.10.2 Method

The rating system used for the empirical chart (Figure 3-3) did not estimate friction angles, and therefore the joint friction angles used in the models (Figure 4-12 and Figure 4-13), for the purposes of this comparison, were taken from Table 4-4. Most of the panels that were assessed had a thin filling on at least one of the joint sets, and therefore the sub-group (b) was used. The highest friction angle analysed was the intact value (the angle of internal friction), derived from laboratory tests. In this case a joint alteration number of 0,75 was considered to be intact. Six parameters were considered in the development of the empirical chart (as discussed in Section 3.2.2), whereas only two were considered in Figure 4-7. In the comparisons (Figure 4-12 and Figure 4-13), two discontinuity sets were assumed, i.e. the dip set and a set parallel to stratification. All joints were taken as smooth and planar with no water in the joints. Excellent conditions assumed an RQD of 100 per cent (i.e. all pieces of core in a 10 m vertical borehole were greater than 100 mm), with no observable movement having occurred on any discontinuity (competent surrounds). Good conditions assumed an RQD of 80 per cent with competent surrounds. Poor conditions assumed an RQD of 30 per cent with incompetent surrounds (see Table 3-2). Only the excellent joint conditions could be compared directly to the UDEC model, where the joint dip was between 85^0 and 90^0 and, therefore, only these conditions are considered in the discussion. A comparison between the good and poor conditions of Figure 4-13 and Figure 4-7 could only be made if it were assumed that shallow dipping joints would reduce the RQD.

4.10.3 Discussion

The trends shown in the model (Figure 4-7) and the results derived from the empirical chart (Figure 3-3) are the same but detailed correlation is not possible. One of the greatest differences was that the model predicted collapses at relatively small spans whereas the results of the empirical chart show that collapses should not occur at a span less than 30 m. Some possible reasons for the differences are:

1) Bedding parallel planes were seldomly observed within 10 m of the hangingwall, in any of the sites analysed in the chart.
2) In reality joints were rarely flat, but consisted of a micro friction angle and a macro wavelength, and only the micro friction angle was modelled.
3) The model is two dimensional and assumes 100 per cent persistency for all joints, which in reality can only be compared to faults and bedding planes.
4) The model does not take into account the affect of support.

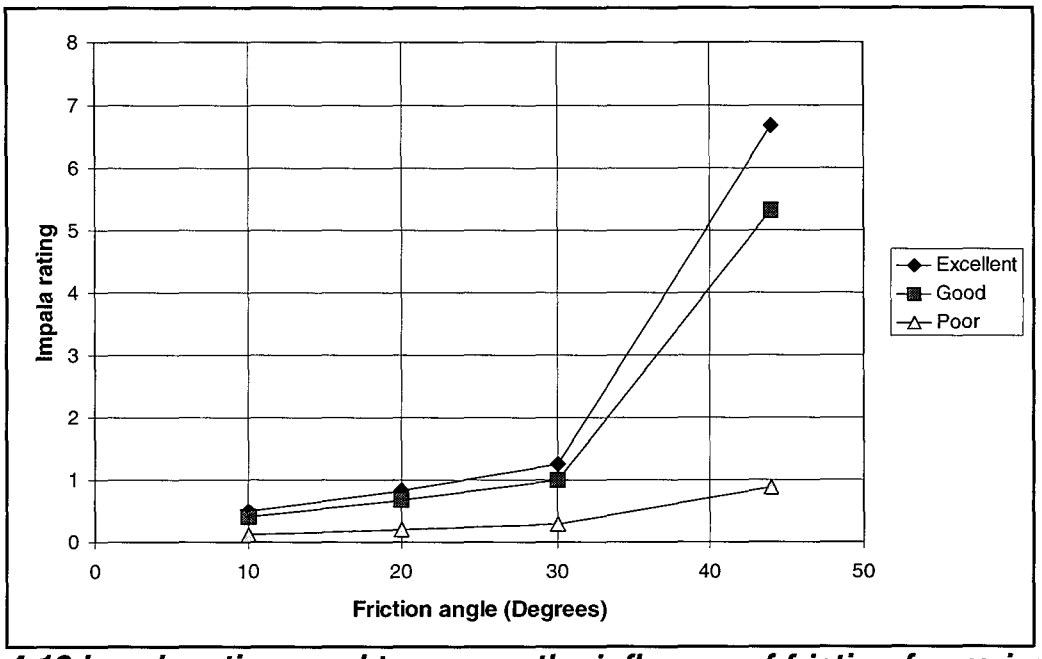

Figure 4-12 Impala rating used to assess the influence of friction for various joint conditions.

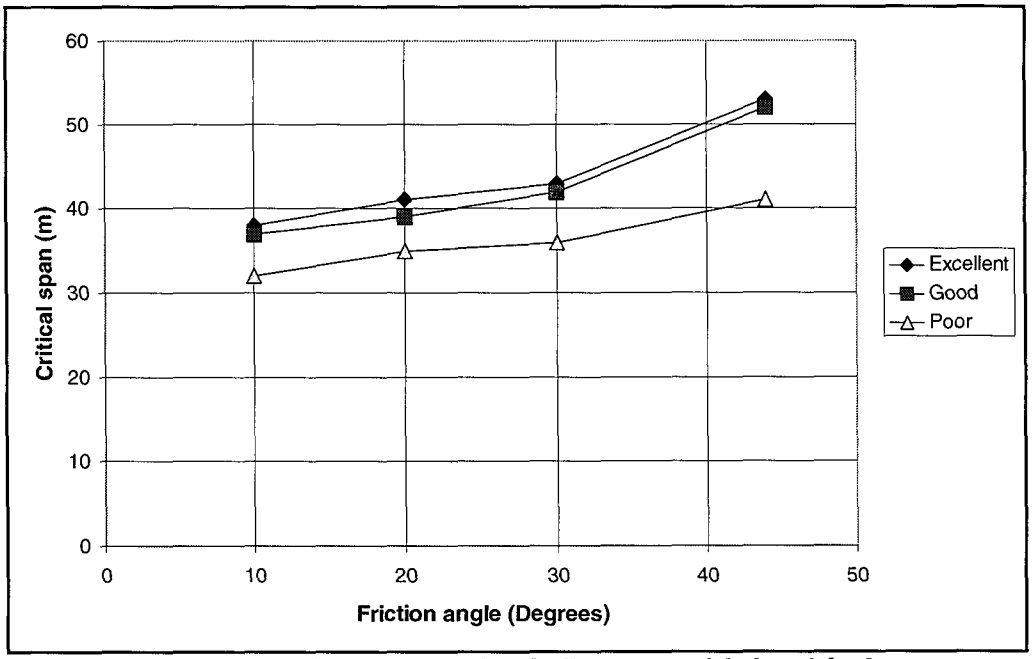

Figure 4-13 Critical spans based on the influence of joint friction on panel span for various joint conditions, assessed from the chart.

The lack of bedding planes, in reality, appears to have had the greatest influence in restricting the minimum span to 30 m (Figure 4-13). A span of 30 m is the generally accepted safe panel span on the Merensky Reef, and most mines use spans between 28 m and 35 m. It could therefore be inferred from Figure 4-13 that a safe panel span need only be less than 30 m

where there are persistent bedding parallel discontinuities. However, this analysis has only considered the effect of discontinuities and not stress.

Figure 4-13 has a similar trend to Figure 4-7, indicating that there could be a correlation between the model and reality if additional steeply dipping discontinuity sets are included in the model and the bedding planes removed. Figure 4-13 shows that there is a relationship between filling on joints (friction angle) and span. This finding could explain why some, apparently similar, panels behave differently and highlights the need for careful analysis of joint surfaces. The model has excluded other factors influencing stability and enabled the understanding of the effects of joint infill. These results highlight the potential of numerical models to provide a better understanding of discontinuity interaction.

4.11 A methodology for the determination of the joint friction angle.

The main difficulty with the methodology presented in this chapter is the identification of the correct *in situ* friction angle. This section aims to provide a simple methodology for the determination of the effective joint friction angle, for use in the design charts shown previously. The following is a summary of the methodology developed by Barton (1978) to determine the effective friction angle on joints.

The two cases that occur most frequently in hard rock mines are shown in Figure 4-14.

Figure 4-14 a) Joint with infilling; b) Joint without infilling.

The shear strength (τ) of the joint shown in Figure 4-14 a) is given by:

$$\tau = \sigma_n \tan (J_r/J_a) \qquad \textit{Equation 4-1}$$

where J_r = the joint roughness number
J_a = the joint alteration number
σ_n = the normal stress acting on the joint.

The parameter (J_r/J_a) is the effective friction angle of the joint. The values of these can be estimated from the Q-system parameter rating charts, Table 4-4. The shear strength of the joint shown in Figure 4-14 b) is given by:

$$\tau = \sigma n \tan [JRC \log10 (JCS/\sigma n) + Z] \qquad \textit{Equation 4-2}$$

where JRC = the joint roughness coefficient
(JCS/σ_n) = the joint wall compressive strength / normal stress
Z = residual friction angle for weathered joints (ϕ_r)
Z = basic friction angle for unweathered joints (ϕ_b).

The dilation angle of the joint is included in the term ($JRC \log_{10} (JCS/\sigma_n)$). The friction angle of weathered joints is defined as the residual friction angle and the friction angle of unweathered joints is defined as the basic friction angle.

The proposed methodology is shown in Figure 4-15. The methods to determine the unknowns will be shown in the following sections.

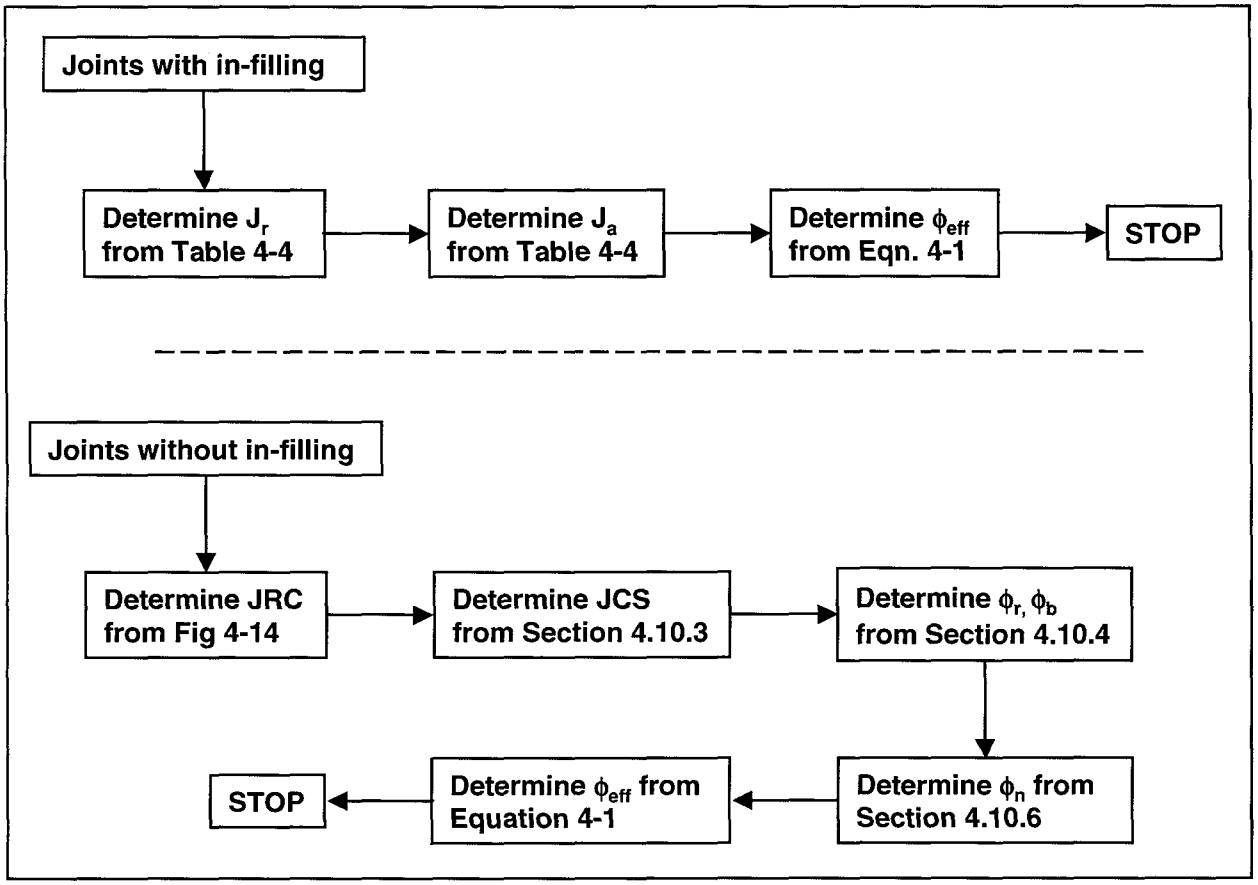

Figure 4-15 Proposed methodology for determination of joint friction angle.

4.11.1 Determination of the joint roughness coefficient

The JRC for any joint can be estimated from Figure 4-16.

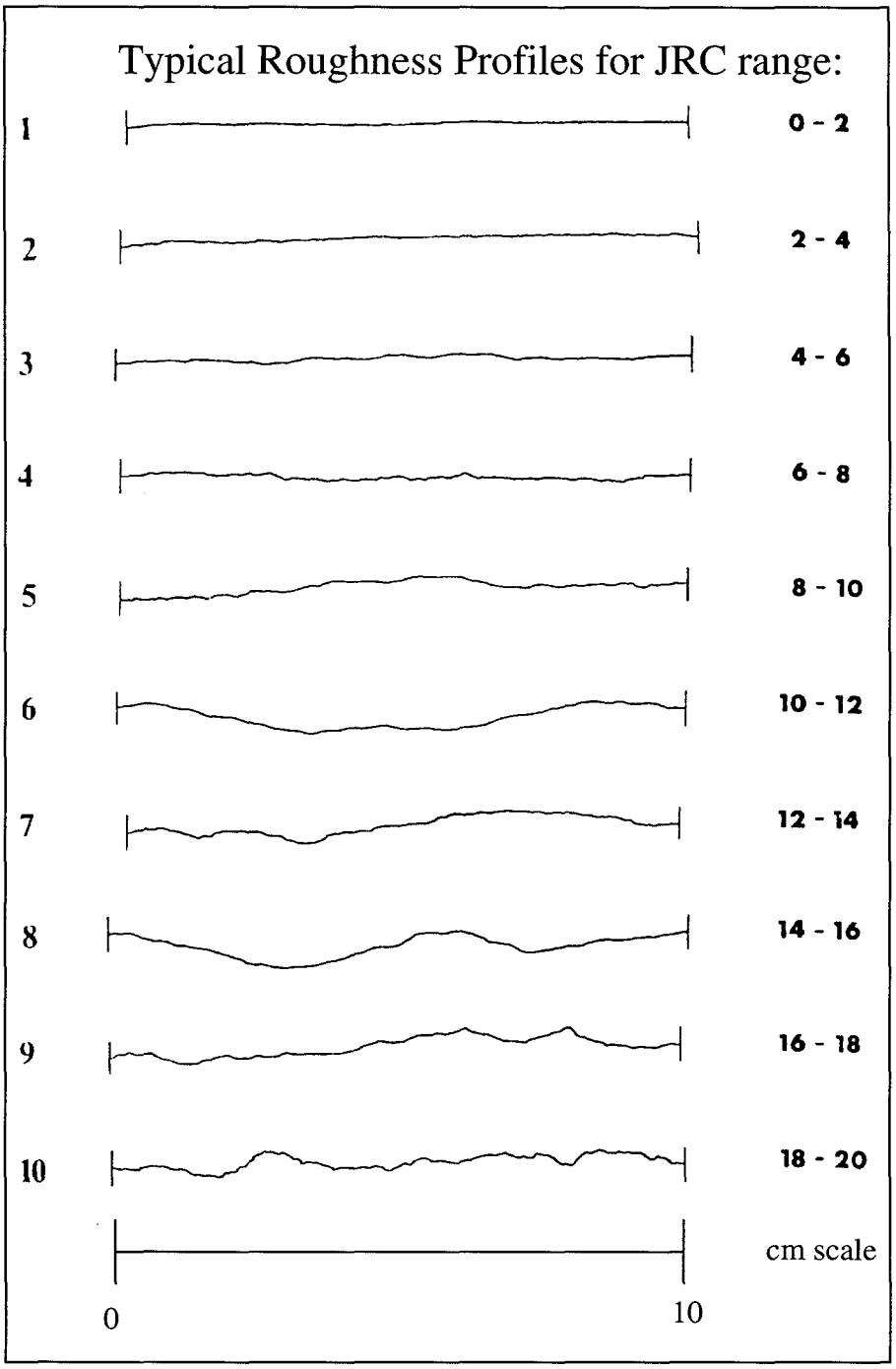

Figure 4-16 Joint roughness profile chart, after Barton (1978).

4.11.2 Determination of Joint Wall Compression Strength, JCS

The weathering process of a rock mass can be summarised as follows:

1) Formation of joint in intact rock; JCS value the same as σ_c (compressive strength of rock surface) since no weathering.
2) Slow reduction of joint wall strength if joints are water conducting; JCS becomes less than σ_c.
3) Common intermediate stage; weathered, water conducting joints, impermeable rock blocks; JCS some fraction of σ_c.
4) Advanced stage of weathering; more uniformly reduced σ_c finally drops to same level as JCS, rock mass permeable throughout.

The JCS values for stages 1) and 4) can be obtained by conventional unconfined compression tests on intact cylinders or from point load tests on rock core or irregular lumps. The JCS values

relevant to weathered, water conducting joints (stages 2 and 3) cannot be evaluated by standard rock mechanics tests. The following sections describe the tests and equations used to determine JCS for joints in stages 2 and 3.

4.11.2.1 Schmidt Hammer Index test.

Miller (1965) obtained a good estimation for the JCS when he multiplied the rebound number by the dry density of the rock.

$$Log_{10}(JCS) = 0.00088\,\rho\,R + 1.01 \qquad \textit{Equation 4-3}$$

where (JCS) = unconfined compression strength of joint surface (σc in Figure 4-17) (MPa)

ρ = dry density of rock (kN/m^3)

R = rebound number.

The above relationship and an approximate measure of the anticipated scatter are shown in Figure 4-17.

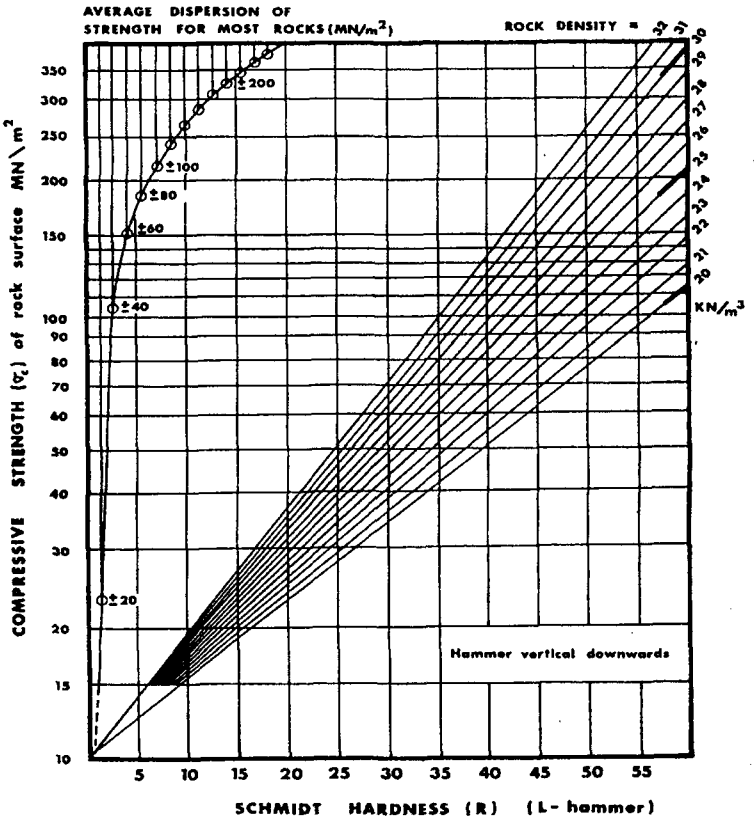

Figure 4-17 Correlation chart for Schmidt (L) hammer, relating rock density, compressive strength and rebound number, after Miller (1965).

4.11.2.1.1 Influence of orientation of Schmidt Hammer test

For a given surface the rebound number is at its minimum when the hammer is used vertically downwards (rebound against gravity) and its maximum when used on horizontal surfaces. The corrections given in the Table 4-1 should be applied when the hammer is used in other directions. The hammer should be applied perpendicular to the surface in question.

4.11.2.1.2 Sample dimensions

A correct rebound measurement will not be obtained if the impulse of the Schmidt hammer is sufficient to move the rock sample being tested. If small samples such as rock core or small blocks are to be tested, they should be firmly seated or clamped on a heavy base. Blocks extracted from rock slopes or tunnel walls that are to be tested unclamped should measure at least 20 cm in each direction.

Table 4-1: Corrections for Reduced Measured Schmidt Hammer Rebound number (R) when the hammer is not used vertically downwards (after Barton, 1978).

Rebound no. R	Downwards		Upwards		Horizontal
	$\alpha = -90°$	$\alpha = -45°$	$\alpha = +90°$	$\alpha = +45°$	$\alpha = 0°$
10	0	-0,8	---	---	-3,2
20	0	-0,9	-8,8	-6,9	-3,4
30	0	-0,8	-7,8	-6,2	-3,1
40	0	-0,7	-6,6	-5,3	-2,7
50	0	-0,6	-5,3	-4,3	-2,2
60	0	-0,4	-4,0	-3,3	-1,7

4.11.3 Determination of Basic Friction Angle (ϕ_b) and Residual Friction Angle (ϕ_r)

Basic friction angles of different rock types are given below.

Table 4-2 Basic friction angles of various unweathered rocks (after Barton, 1978).

Rock Type	Moisture Condition	Basic friction angle N_0	Reference
A. Sedimentary Rocks			
Sandstone	Dry	26 – 35	Patton, 1966
Sandstone	Wet	25 – 33	Patton, 1966
Sandstone	Wet	29	Ripley & Lee, 1962
Sandstone	Dry	31 – 33	Krsmanovi, 1967
Sandstone	Dry	32 – 34	Coulson, 1972
Sandstone	Wet	31 – 34	Coulson, 1972
Sandstone	Wet	33	Richards, 1975
Shale	Wet	27	Ripley & Lee, 1962
Siltstone	Wet	31	Ripley & Lee, 1962
Siltstone	Dry	31 – 33	Coulson, 1972
Siltstone	Wet	27 – 31	Coulson, 1972
Conglomerate	Dry	35	Krsmanovi , 1967
Chalk	Wet	30	Hutchinson, 1972
Limestone	Dry	31 – 37	Coulson, 1972
Limestone	Wet	27 – 35	Coulson, 1972
B. Igneous Rocks			
Basalt	Dry	35 – 38	Coulson, 1972
Basalt	Wet	31 – 36	Coulson, 1972
Fine-grained granite	Dry	31 – 35	Coulson, 1972
Fine-grained granite	Wet	29 – 31	Coulson, 1972
Coarse-grained granite	Dry	31 – 35	Coulson, 1972
Coarse grained granite	Wet	31 – 33	Coulson, 1972
Porphyry	Dry	31	Barton, 1971b
Porphyry	Dry	31	Barton, 1971b
Dolerite	Dry	36	Richards, 1975
Dolerite	Wet	32	Richards, 1975

C. Metamorphic Rocks

Amphibolite	Dry	32	Wallace et al., 1970
Gneiss	Dry	26 – 29	Coulson, 1972
Gneiss	Wet	23 – 26	Coulson, 1972
Slate	Dry	25 – 30	Barton, 1971b
Slate	Dry	30	Richards, 1975
Slate	Wet	21	Richards, 1975

The residual friction angle (applicable to weathered joint surfaces) can be estimated from the results of Schmidt Rebound tests. The following empirical relationship may be used:

$$\phi_r = 10° + r/R\,(\phi_b - 10°) \qquad \textit{Equation 4-4}$$

where r = rebound on weathered joint surface
R = rebound on unweathered rock surface.

4.11.4 Scale Effect

The basic friction angle is not affected by scale, but both the asperity and geometrical factors are. They decrease as the scale increases as described by the following equations.

$$JRC_n = JRC_o\,[\,L_n / L_o\,]^{-0.02\,JRC_o} \qquad \textit{Equation 4-5}$$

$$JCS_n = JCS_o\,[\,L_n / L_o\,]^{-0.03\,JCS_o} \qquad \textit{Equation 4-6}$$

JRC_0 and JCS_0 are appropriate values for the length of joint actually rated, L_0. L_n is the total length of the joint. If, for example, only 10 cm (L_0) of a joint can be measured and this joint extends 2 m (L_n) into the hangingwall, JRC_0 can be determined by rating the joint that is exposed and JRC_n can be calculated by using Equation 4-5. JCS_0 and JCS_n can be determined following the same procedure.

4.11.5 Influence of normal stress on the effective friction angle

In Equation 4-2, the determination of σ_n causes difficulties, as this implies a proper modelling of the jointed rock mass, which can be complex and time consuming. To provide some guidelines, a sensitivity analysis was done to show the influence of normal stress on the effective friction angle. This is shown in Figure 4-18.

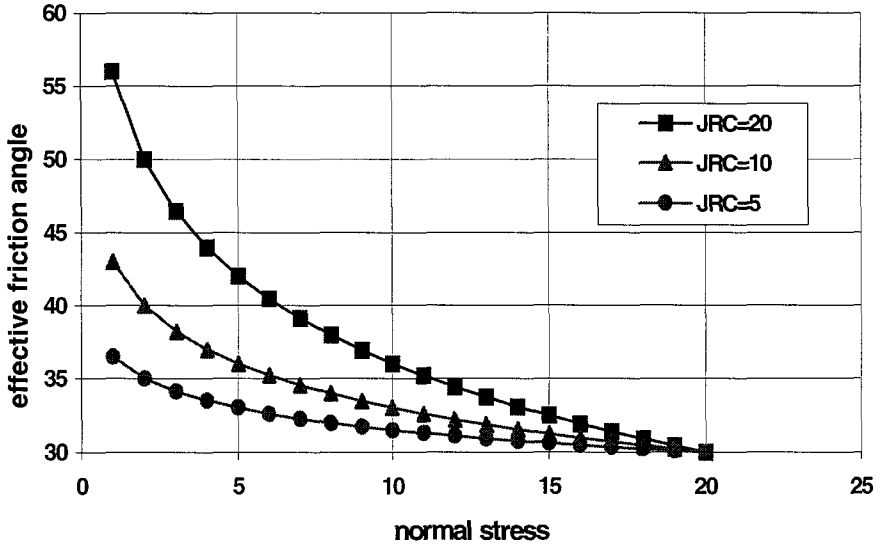

Figure 4-18 Influence of normal stress on effective friction angle.

A typical JCS value of 30 MPa and a basic friction angle of 20° were assumed. For low values of JRC, the influence of normal stress is very limited. For normal stresses above 5 MPa, the change in effective friction angle is negligible.

For high values of JRC, above 10, the influence of normal stress is more pronounced. A good estimation of the normal stress would give a more accurate value of the effective friction angle. Normal stress values lower than 5 MPa have a significant effect on the value of the effective friction angles in this range of values of JRC (i.e. rough to very rough)

4.12 Examples

The following examples will illustrate the use of the method developed by Barton for determining the effective joint friction angle, the use of the supportable, unsupportable, self-supporting span charts and the elongate support relative hazard charts.

Example 4-1 Panel span design, using the numerical modelling approach, with rough joints dipping at 55°.

Problem

A block of ground is to be mined with 30 m stope panel spans and in-panel pillars. The rock mass has two joint sets. One joint set dips at 55° towards the face and the other joint set is horizontal. The average joint spacing of both sets is approximately 1 m. The density of the rock is 27 kN/m^3 and the rebound number from the Schmidt hammer test was recorded at 11. No correction was made for orientation since the hammer was applied vertically downwards. The average joint roughness profiles of the joints is shown in Figure 4-19. The dry joint surface of the conglomerate rock type is unweathered.

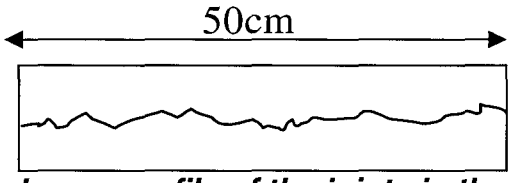

Figure 4-19 Average roughness profile of the joints in the panel.

Solution

From Figure 4-16, the JRC of these joints is estimated to be 20.
The normal stress on these joints was estimated to be 2 MPa (hangingwall stress behind the stope face).
From Figure 4-17, the JCS of the rock surface is 20 MPa.
The basic friction angle is 35° (Table 4-2). Thus, the effective friction angle of the joint (Equation 4-2) is:

$$\phi_{eff} = (JRC \log_{10} (JCS/\sigma_n) + \phi_b)$$
$$\phi_{eff} = (20 \log_{10} (20°/2) + 35)$$
$$\phi_{eff} = 55°$$

Figure 4-20 gives the relationship between stable panel span and joint friction angle for the 0°/(45°-60°) joint orientation combination.
The effective friction angle of the joints was calculated to be 55° and the planned panel span is 30 m. The combination of the friction angle and the panel span results in point A in Figure 4-20, which falls into the supportable area of the graph.

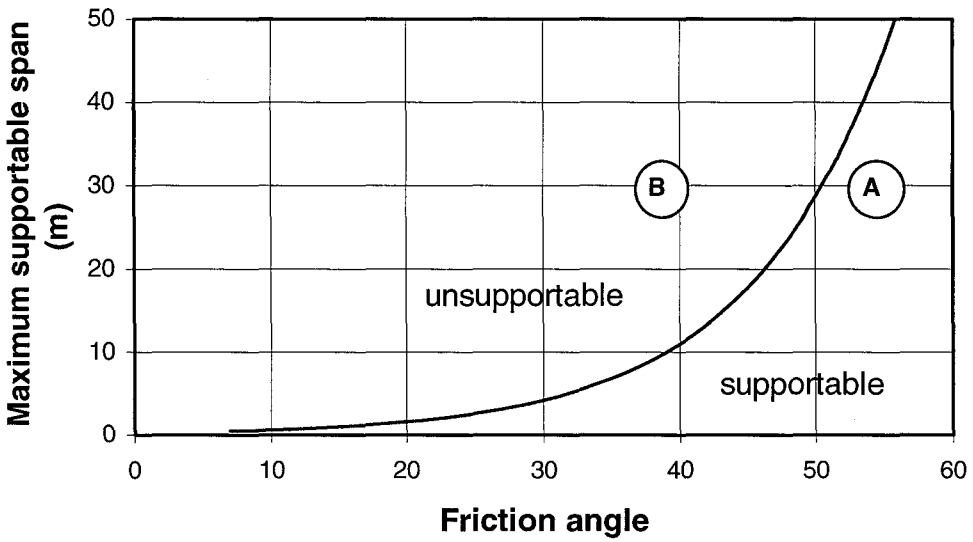

Figure 4-20 Relationship between stable panel span and joint friction angle for the 0°/(45°-60°) joint orientation.

Since the stope is supportable at a span of 30 m, the elongate support relative hazard chart in Figure 4-21 can be used to determine the average support spacing.

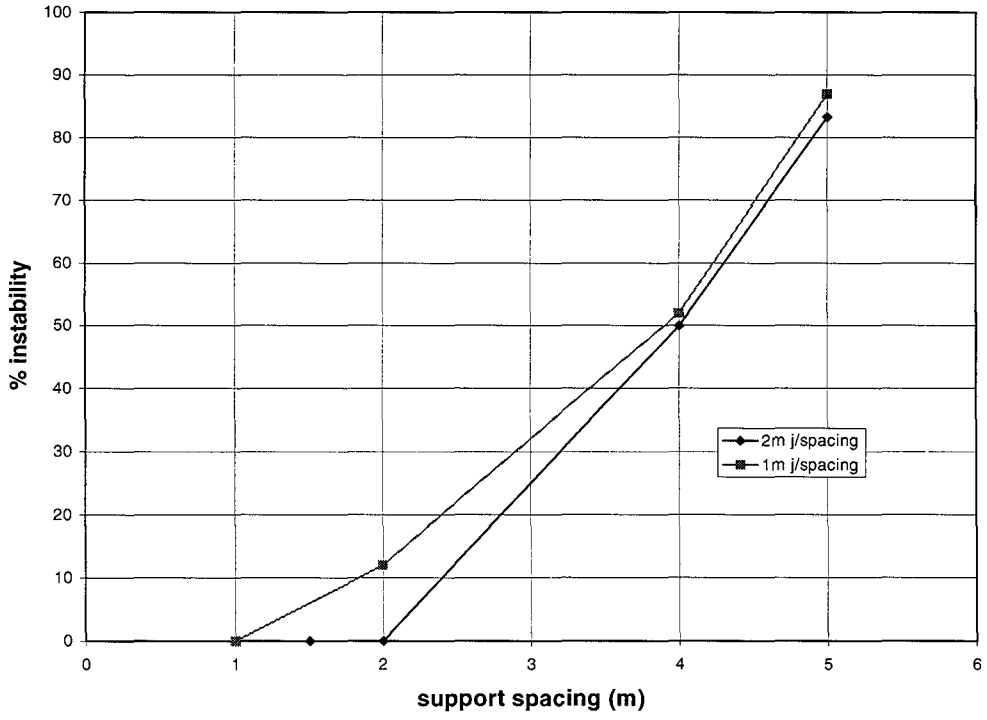

Figure 4-21 Elongate support relative hazard chart for 0°/(45°-60°).

For a joint spacing of 1 m, the optimum support spacing would be 1 m since 0 per cent of the blocks in the hangingwall would be unstable. However, for a support spacing of 2 m, only 12 per cent of the hangingwall rock is potentially unstable. Thus, a support spacing of 2 m can be implemented if areal support is used with the support units, i.e. headboards.

Example 4-2 Panel span design, using the numerical modelling approach, with smooth joints dipping at 55°.

Problem

For the conditions as stipulated in the previous example, determine whether the given panel

span would still be supportable if the joint roughness profile of the joints is that given in Figure 4-22, and the joints extend 2 m into the hangingwall.

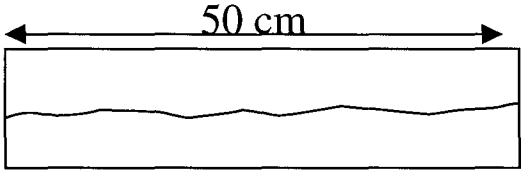

Figure 4-22 Roughness profile of the joints.

Solution

The JRC of the 50 cm joint is estimated as 5 from Figure 4-16. The value of L_n is 2 m, L_0 is 50 cm and JRC_0 is 5. Applying Equation 4-5, the value of JRC_n for the 2 m joint is 4,4. The JCS_0 value is 20 MPa, the L_n value is 2 m and the L_0 value is 50 cm. From Equation 4-6, the value of JCS_n is now 8,7. The effective friction angle is thus 38°. The panel span of 30 m and the effective friction angle on the joints result in point B in Figure 4-20, which falls into the unsupportable zone (see Figure 4-3). Thus, a supportable panel span would be 10 m or mid-panel pillars must be used. Another option is that stronger support must be used in these panels, such as grout packs.

Example 4-3 Panel span design, using the numerical modelling approach, with smooth joints dipping at 85°.

Problem

The rock mass consists of two joint sets. One dips at 85° and the other at 3° towards the stope face. The average spacing of these joints is 1 m. The planned panel spans are 25 m. The joints have the same properties as given in Example 4-2.

Solution

The effective friction angle is 38°. A panel span of 25 m and an effective friction angle of 38° result in the rock mass being self supporting, since it is to the right of the second curve in Figure 4-5. Thus, minimal support is required.

Example 4-4 Panel span design, using the numerical modelling approach, with infilled joints dipping at 85°.

Problem

For the same rock mass conditions as given in Example 4-3, determine whether the rock mass would be supportable if the joints have a sandy-clay infilling of less than 1 mm, as shown in Figure 4-23.

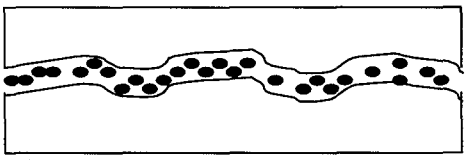

Figure 4-23 Joint with clay infilling.

The shear strength of this joint is given by Equation 4-1, repeated here for convenience:

$$\tau = \sigma_n \tan (J_r / J_a)$$

The joint wall can be described as rough, irregular and undulating.

Solution

The shear strength of this joint is given by Equation 4-1, repeated here for convenience:

$$\tau = \sigma_n \tan (J_r / J_a)$$

The joint wall can be described as rough, irregular and undulating. From Table 4-4, the value for J_r is 3. The value for J_a for the given joint is also 3. Thus, the effective friction angle of the joint is

1°. From Figure 4-5, the rock mass is unsupportable at 25 m panel span and 1° joint friction angle (see Figure 4-3).

Example 4-5 Panel span design, using the numerical modelling approach, with smooth joints dipping at 65°.

Problem

Tilt tests were done on joint surfaces underground and the results are presented in Table 4-3. The tilt test may be done by placing two rocks intersected by a joint on a horizontal plane, one on top of the other. The lower rock is then tilted (increasing the angle between the discontinuity and the horizontal). The angle at which sliding on the joint between the rocks is initiated represents the joint friction angle. The average effective friction angle from Table 4-3 is 32°. The rock mass consists of two joint sets. One dips at 65° and the other at 3° towards the stope face. The average spacing of these joints is 2 m. The planned panel spans are 20 m.

Table 4-3 Results of* in-situ *tilt tests.

Test	Friction angle
1	33°
2	28°
3	31°
4	35°
5	33°

Solution

Figure 4-24 shows the relationship between stable panel span and joint friction angle for the 0°/(60°-70°) joint orientation combination. The effective friction angle of the joints was calculated at 32° and the planned panel span is 20 m. The combination of the friction angle and the panel span results in point C in Figure 4-24, which falls into the supportable area of the graph.

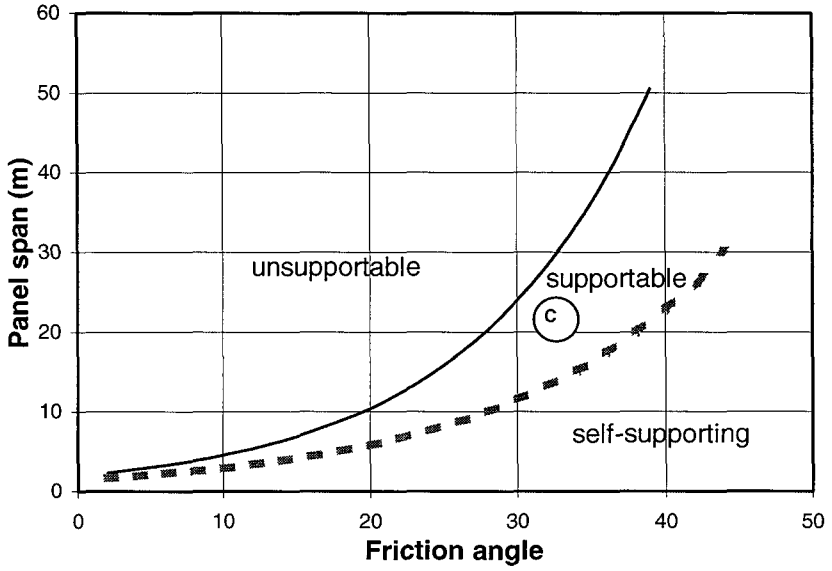

Figure 4-24 Relationship between stable panel span and joint friction angle for the 0°/(60°-70°) joint orientation.

The stope is supportable at a span of 20 m. From Figure 4-25, the optimum support spacing is clearly 2 m.

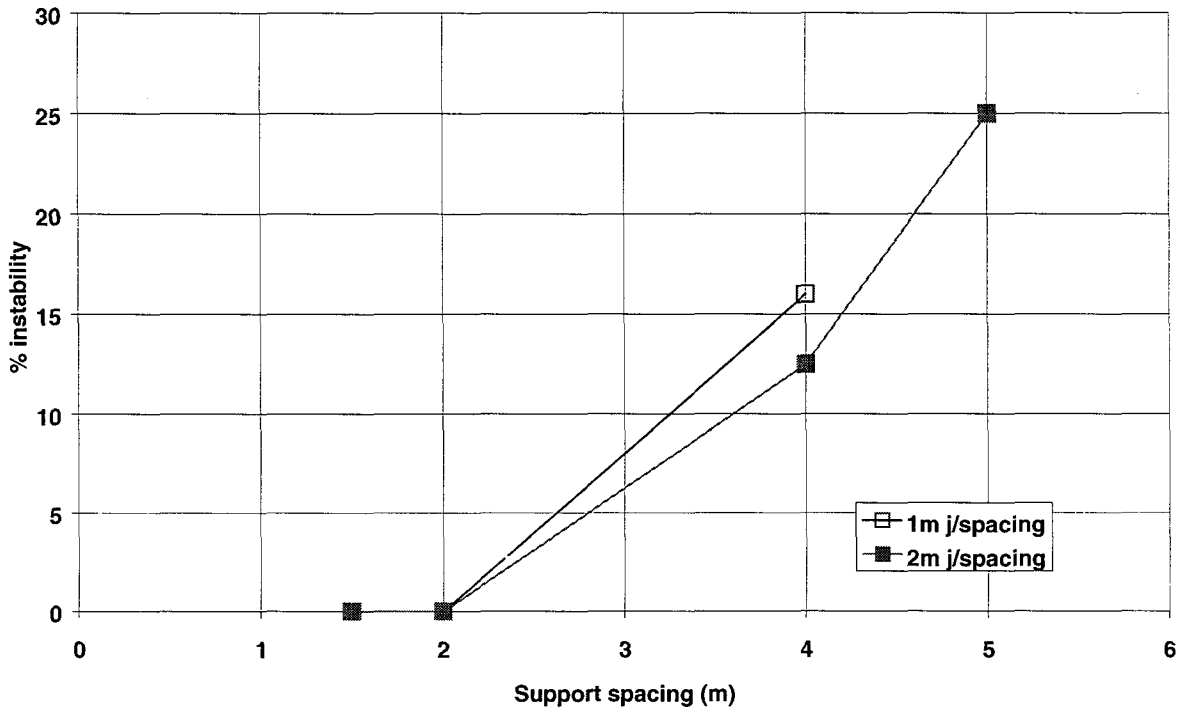

Figure 4-25 Elongate support relative hazard chart for 0°/(60°-70°).

Table 4-4 Updated Q-system parameter ratings (after Barton,1993)

1. Joint Roughness Number		J_r
a) Rock-wall contact, and b) rock-wall contact before 10 cm shear		
A	Discontinuous joints	4
B	Rough or irregular, undulating	3
C	Smooth, undulating	2
D	Slickensided, undulating	1.5
E	Rough or irregular, planar	1.5
F	Smooth, planar	1.0
G	Slickensided, planar	0.5
Note: i) Descriptions refer to small scale features and intermediate scale features, in that order.		
c) No rock-wall contact when sheared		
H	Zone containing clay minerals thick enough to prevent rock-wall contact	1.0
J	Sandy, gravelly or crushed zone thick enough to prevent rock-wall contact	1.0
Note: i) Add 1.0 if the mean spacing of the relevant joint set is greater than 3 m. ii) J_r = 0.5 can be used for planar slickensided joints having lineations, provided the lineations are oriented for minimum strength.		

2. Joint Alteration Number		ϕ_r approx.	J_a
a) Rock-wall contact (no mineral fillings, only coatings)			
A	Tightly healed, hard, non-softening, impermeable filling, i.e., quartz or epidote	-	0.75
B	Unaltered joint walls, surface staining only	25-35E	1.0
C	Slightly altered joint walls. Non-softening mineral coatings, sandy particles, clay-free disintegrated rock, etc.	25-30E	2.0
D	Silty- or sandy-clay coatings, small clay fraction (non-softening)	20-25E	3.0

E	Softening or low friction clay mineral coatings, i.e., kaolinite or mica. Also chlorite, talc, gypsum, graphite, etc., and small quantities of swelling clays	8-16E	4.0
b) No rock-wall contact before 10 cm shear (thin mineral fillings)			
F	Sandy particles, clay-free disintegrated clay mineral	25-30E	4.0
G	Strongly over-consolidated non-softening clay mineral fillings (continuous, but < 5 mm thickness)	16-24E	6.0
H	Medium or low over-consolidation, softening, clay mineral fillings (continuous, but < 5 mm thickness)	12-16E	8.0
J	Swelling-clay fillings, i.e., montmorillonite (continuous, but < 5 mm thickness). Value of J_a depends on per cent of swelling clay-size particles, and access to water, etc.	6-12E	8-12
c) No rock-wall contact when sheared (thick mineral fillings)			
KL M	Zones or bands of disintegrated or crushed rock and clay (see G, H, J for description of clay condition)	6-24E	6, 8, or 8-12
N	Zones or bands of silty- or sandy-clay, small clay fraction (non-softening)	-	5.0
O P R	Thick, continuous zones or bands of clay (see G, H, J for description of clay condition)	6-24E	10, 13, or 13-20

4.13 Conclusions

A two-dimensional UDEC model of single and multiple stopes was constructed for this analysis. The model consists of two joint sets of which the dip of one set was varied. The friction angle on the joints was varied as well as the panel span. The stress levels of the stopes were assumed to be similar to that at shallow depth. It was found that the multiple stopes were less stable than the single stopes. The results should be applied only to cases that are similar to the UDEC model and where similar failure mechanisms are expected to occur. The applications and limitations of the methodology have been discussed in detail.

A methodology for panel span and elongate support design has been presented. Any given panel (within the modelling assumptions) may be categorised as self-supporting, supportable or unsupportable. If the panel is supportable, elongate support relative hazard charts may be used.

The design charts presented in this report are of a preliminary nature as only two joint sets were modelled, one of which was kept horizontal while the other was varied from 5° to 90°. The results therefore can be used only as a guide. For a comprehensive set of charts which could be used on the mines for design purposes under most conditions, a substantial programme of further modelling is required. This would involve two sets of joints both with variable dips, with and without the hangingwall parallel discontinuity. In addition, the influence of strata dip on the results needs to be established.

Insight has been gained into failure mechanisms and the control that various joint parameters and panel spans have on the type and extent of failure. A simple methodology for estimating joint friction angles has been provided. This needs to be verified by a comprehensive laboratory testing programme for geotechnical areas of interest. The elongate support relative hazard charts were developed for support units with performance characteristics typical of common elongates and assess the support spacing requirements. For the same reasons as stated for the span design charts, these must be considered as preliminary. An important finding of this work has been the influence of pre-stressed support. Pre-stressed support has a major influence in the reduction of the percentage instability of the hangingwall, in the one case modelled. Thus, pre-stressed support may be more useful in reducing the hazard of rock falls. In the elongate support relative hazard charts, the percentage instability should be seen as a

hazard indicator and not in terms of the actual values. For high values of percentage instability, the stope hangingwall can be expected to be problematic. Readers are referred to the final report on SIMRAC project GAP 330 (Design of Face Support Systems) for detailed support design methodologies.

In the comparison between the empirical and numerical modelling approaches, Figure 4-13 shows that there is a relationship between joint fill properties and span, indicating the need to carefully analyse the joint surfaces during a survey. The correlation between the model (Figure 4-7) and the results of the chart (Figure 4-13) was not good but the trends were similar. It appears that the model could be useful in achieving an improved understanding of discontinuity interactions, if more realistic conditions were used, and by permitting the study of each joint property in isolation.

One of the major differences between the joint model (Figure 4-7) and the analysis performed on the chart (Figure 4-13) is that persistent horizontal planes were included in the model. The lack of such planes in the empirical data base explains the poor correlation between the two results. However, this result also shows that panel spans need only be less than 30 m where there are persistent bedding parallel discontinuities, stress related damage or the rock mass quality is particularly low. Data to populate this end of the empirical chart is required.

4.14 References

Barton, N. and Choubey, V. 1978. The Shear Strength of Rock Joints in Theory and Practice. *Norwegian Geotechnical Institute, Publication no. 119.*

Barton, N. 1995. The influence of joint properties in modelling jointed rock masses. *Eighth International congress on rock mechanics.*

Bandis, S., Lumsden, A. and Barton, N. 1981. Experimental studies of scale effects on the shear behaviour of rock joints. *International Journal of Rock Mechanics. Min. Sci. and Geomech. Pp. 1-21.*

Grimstad, E. and Barton, N. 1993. Updating of the Q-system for NMT. *Proceedings of the International Symposium on Sprayed Concrete - Modern Use of Wet Mix Sprayed Concrete for Underground Support, Norwegian Concrete Institute.*

ITASCA Consulting Group, Inc. 1991. *UDEC Universal Distinct Element Code, Version 1.7 Volume 1.*

Brady, B.H.G. and Brown, E.T. 1985. Rock Mechanics For Underground Mining. London: George Allen and Unwin.

5 The design of pillars

5.1 Introduction

This chapter addresses Enabling Output number 4 (see page 13).

The design of hard rock pillars in South Africa is based on empirical design equations. The two empirical equations in use are based on a wide survey of coal pillar collapses in one case, and, in the other, a back analysis of a limited data base of collapsed and intact pillars in a Canadian hard rock mine.

A general design methodology that is applicable to South African hard rock pillars is thus required. Such a methodology is presented in this chapter. It may be supposed that pillar strength would depend on a number of factors. Some of these may be:
1) the pillar dimensions, including stoping width (these lead to the w/h ratio)
2) strength of the pillar material
3) contact conditions between the pillar and the hanging- and footwall
4) horizontal weak layers or partings in the pillar
5) k-ratio (the ratio of virgin horizontal to vertical stresses)
6) the length : width ratio
7) different heights in the same pillar, due to one side being adjacent to a gully
8) jointing in the pillar
9) brittleness of pillar material
10) local loading system (relative stiffness of pillar and foundation)
11) creep and other time effects.

The first three factors have been deemed to be most influential to the strength of pillars. These have been investigated in the scope of the research, and form part of the pillar design methodology presented in Section 5.5.

5.2 Literature review

Pillars in underground mine workings are typically designed using an empirically derived strength formula. Typically, this may be the "power" formula, or a linear function of the ratio of the width to the height of the pillar (w/h).

The linear function is of the form:

$$S = c + m(w/h) \qquad \textit{Equation 5-1}$$

where S = the expected pillar strength
m = the slope of the linear function
c = the intercept of the linear function
w/h = the width to height ratio of the pillar.

The power formula is of the form:

$$S = kh^{\alpha}w^{\beta} \qquad \textit{Equation 5-2}$$

where S = the expected pillar strength
k, α and β are numerically back analysed constants
h = the height of the pillar
w = the width of the pillar.

The linear function as applied in coal pillar design was substantiated by Bieniawski and van Heerden (1975). The linear function proposed by Bieniawski and van Heerden was based on *in situ* tests, with the use of a concrete platen at the top of the specimen. The base of the specimen was in the natural state.

It has been found that laboratory test results of strength as a function of w/h ratio are well explained by a linear fit, for coal, sandstone, and hard rocks, such as Merensky Reef, norite and anorthosite.

The power formula has found wide, consistent and successful application in South Africa and Australia since the paper by Salamon and Munro (1967). Their paper constitutes the most complete back analysis of *in situ* collapsed and intact pillars in underground coal mine workings. In the work, several important principles regarding the linking of the Safety Factor concept with probability of failure were applied to the design of underground mine pillars. K, α and β were determined as 7,17 MPa, -0,66 and 0,46 respectively.

Above a certain value of w/h, the strength increases exponentially (the so-called "squat pillar" effect), with increasing w/h. The squat pillar formula is:

$$S = k\frac{R_0^b}{V^a}\left\{\frac{b}{\varepsilon}\left[\left(\frac{w/h}{R_0}\right)^{\varepsilon} - 1\right] + 1\right\} \qquad \textit{Equation 5-3}$$

where S = the expected pillar strength
R_0 = the critical w/h at which the squat pillar effect starts (commonly assumed to be 5)
ε = is the rate of strength increase
a = a constant = 0,0667
b = a constant = 0,5933
V = pillar volume.

Conventionally, the squat pillar effect is assumed to occur at w/h $\geq$ 5. In this range of w/h, equations (1) and (2) are invalid, and the "squat pillar" formula is often used (Wagner and Madden, 1984).

Esterhuizen (1997) has determined the effect of jointing on coal pillar strength through numerical modelling and back analysis of existing pillars in the coal fields of South Africa. An example is shown Figure 5-1, for pillars of w/h = 3. The y-axis shows the ratio of the strength of a pillar with jointing and a pillar with no jointing. The reduction in pillar strength is shown as a function of pillar joint dip angles and joint frequency, with separate curves drawn for different joint frequencies.

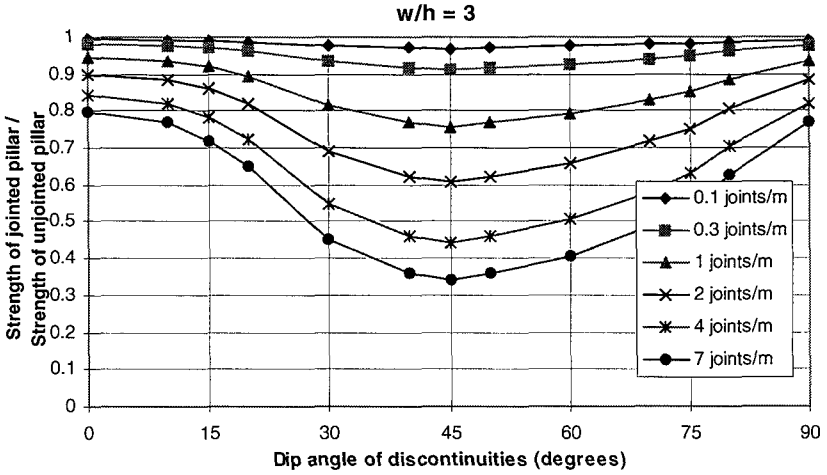

Figure 5-1 The effect of dip angle and frequency of jointing on pillar strength, for pillar w/h = 3 (after Esterhuizen, 1997).

The design of hard rock pillars in South Africa is often based on the Salamon and Munro coal pillar design formula. The value of k is often estimated by taking a proportion of the uniaxial compressive strength (UCS) of the pillar strength. This proportion typically varies from 0,3 to 0,5 of the UCS. Another method involves a material downgrading of laboratory strength according to the method of Hoek and Brown (1988).

Hedley and Grant (1972) proposed values of α and β of 0,5 and –0,75 respectively, from a back analysis of collapses in a Canadian hard rock mine. These values are widely applied in the Bushveld Complex. Unfortunately, their data base consisted of only three crushed pillars, two partially crushed, and 23 intact pillars in their database. Of these, only eight cases had w/h ratios above one, with a maximum w/h ratio of 2.5. Their k and α values were fixed; only β was allowed to float in the regression analysis. Due to the limitation in the data and the concomitant limitation in the analysis procedure, the applicability of their results to other hard rock mining environments is not well substantiated.

Evidence in the literature shows that, for design problems at mine pillar scale, the strength-size relation flattens out. This is illustrated for coal and norite in Figure 5-2. The size at which the curve flattens was termed the *critical size* by Bieniawski(1968a), and the corresponding strength, the *critical strength.*

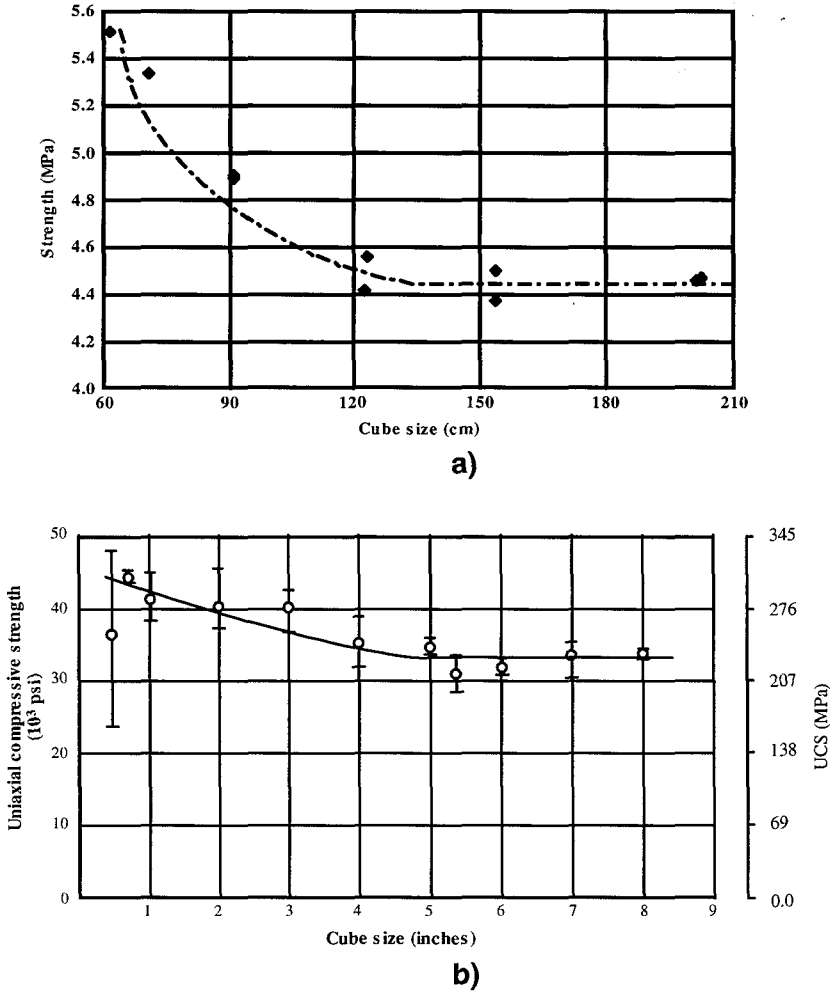

Figure 5-2 The strength size relation for a) coal (after Bieniawski, 1968a) and b) norite (after Bieniawski, 1968b).

5.3 Research methodology: a new approach to pillar design

Empirical formulae, such as those of Salamon and Munro (1967), Bieniawski (1968a) and Hedley and Grant (1972), have the limitation that they must be used with caution for design values that fall outside the empirical range. Empirical formulae should also not be used in geotechnical areas different from that in which the empirical data was obtained. There is another limitation that is not as often appreciated. This will be discussed in the following paragraphs.

The pillar formula that is most strongly based on *in situ* data is that of Salamon and Munro (1967). Their database was built as a result of replies to questionnaires sent to the industry. Cases of pillar collapses that could not be clearly attributed to the pillars themselves failing as the weakest element were rejected. For both collapsed and intact pillars, little information was collected regarding the above mentioned pillar system factors. The actual data that was used in their statistical analysis were the dimensions of the pillar, the mining height (stoping width) and the depth. Other data collected included rock type, surface effects and comments on mining activities at the time of failure and whether there were any early warning signs. The pillar system factors mentioned in the introduction above were not explicitly catered for in their analysis.

Therefore, Salamon and Munro's database contained an unknown combination of the above mentioned, and probably other, pillar system factors. The combination is unknown in two senses: it is not known which factors were present in each case, and what the relative importance and interdependence of the various factors were.

The power formula, involving two geometric variables, w and h, cannot explicitly cater for this unknown combination of factors. In addition, the values of k, α and β obtained are the maximum likelihood parameters for the particular data set, that is, for the particular combination of pillar system factors taken as a whole. The values obtained are thus unique to that data set and only applicable to situations of like conditions. Also, k, α and β are obtained as a result of one statistical process, and form an indivisible set of parameters that best fits the data set. K cannot be separated from α and/or β. K is therefore not a material strength parameter as is commonly assumed, but is merely a point on the strength-size curve; and α and β are not necessarily material constants that define the strength decay with volume.

The strength decay with volume is empirically true (weakly: the volume exponent, a, = -0.067, when Equation 5-2 is written as $S = kV^a(w/h)^b$); however, in the light of the evidence of a constant strength beyond a critical size (see Figure 5-2), as well as consideration of the pillar system factors mentioned, it is postulated that Salamon and Munro's empirically observed volume strength decay is a function of the pillar system factors, rather than a pillar material property. It is evident that Salamon and Munro's formula implicitly lumps together the particular set of pillar system factors that were present in their data set. These pillar system factors are expressed, or captured, in the derived coefficients, k, α and β. Taking this concept further, any particular pillar strength formula, whether derived from *in situ* tests, as Bieniawski did, or based on laboratory tests, will have the same essential feature: the prevailing pillar system factors are expressed in the derived coefficients or constants of the particular formula.

It is clear that seam strength alone is not a basis for design, because seam strength is just one of several factors that determine the overall pillar system strength. Mark and Barton (1996), in back analysis of a US Bureau of Mines database of more than 100 pillar collapse cases, found the factor of safety for *in situ* pillars to be almost meaningless when individual seam strengths based on laboratory tests were used. The factor of safety was a substantially more reliable indicator when a uniform, or average, seam strength was assumed. This shows that the other pillar system factors had a large influence on the strengths of the pillars, so much so as to overwhelm the effect of the different seam strengths. Equally, this shows that the particular pillar system factors present in laboratory testing on model pillars are different to those found

underground. This implies that a seam, or geotechnical-area-reef specific strength should not be the primary pillar design parameter.

The new approach, therefore, is to explicitly define the pillar system factors that influence the pillar system strength. Then the influence of each factor is investigated in turn. In the scope of this project, the most important pillar system factors have been deemed to be:
1) w/h
2) the effect of the contact conditions
3) strength of the pillar material
4) the effect of jointing.
The first three have been investigated in the scope of this project. The effect of jointing is accounted for according to the methodology presented by Esterhuizen (1997).

The new approach is an attempt to derive an engineering methodology based on a mechanistic understanding of the factors that influence pillar strength. This represents a major departure from the statistical approach used previously. It is envisaged that future work should include back analyses based on the engineering insights discussed in this chapter.

5.4 Results

5.4.1 The critical rock mass strength

As discussed in the previous section, evidence suggests that, for design problems of the scale of *in situ* pillars, the strength-size relation has flattened out. The strength obtained at this size may be termed the *critical rock mass strength*. Once this value has been obtained, no further significant changes in strength may be expected as a result of volume changes. For the purposes of pillar design, this strength should be adjusted to account for other factors that affect pillar strength, the main factors being w/h ratio effect, jointing and contact conditions. The power formula is therefore no longer necessary.

The next section deals with the laboratory determination of the critical rock mass strength. An approximate method to determine the critical rock mass strength from UCS strengths is shown in Section 5.4.4.

5.4.1.1 The derivation of the critical rock mass strength from laboratory tests

The form assumed for the strength - size curve is such that a term that decays with increasing size is added to a constant term:

S = [strength decay with size] + constant term.

If the form of the strength decay term is chosen such that it tends to zero with increasing size, the constant term becomes the critical rock mass strength, and the assumed asymptotes inferred from Figure 5-2 are replicated. The strength decay term tending to zero is consistent with the notion of a critical size / critical rock mass strength. With this in mind, and with observation of the decay of the strength data with increasing size, the decay term was chosen to be exponential (other forms were tried, but the exponential form provided the best fit to the data). The form of the function is therefore:

$$\Theta = A^{*}e^{(B^{*}size)} + C \qquad \textit{Equation 5-4}$$

where Θ = the strength of a sample of w/h = 1
size = the diameter of a cylinder or width of a cube
A, B and C are regression parameters.

The strength – size relation for Merensky Reef from Amandelbult Platinum Mine is shown in Figure 5-3. All the test samples were cylinders of w/h = 1. The diameter is plotted on the x-axis

in Figure 5-3. From the best fit regression curve, the critical rock mass strength is predicted to be 111 MPa. Details of the testing methodology are discussed in Section 5.4.2.1.

Similar tests were performed under SIMRAC project GAP024, but on Merensky Reef from Impala Platinum Mine. The number of w/h = 1 tests in this data set is too sparse to be analysed on its own, and is plotted together with the data from Amandelbult in Figure 5-4. The regression was then performed on the combined data. As may be seen in Figure 5-4, the fitted curve changes slightly, while the predicted critical rock mass strength is also slightly changed. This is despite the fact that data from two different mines in the Bushveld Complex were included in the regression analysis. The critical size for both curves (Figure 5-3 and Figure 5-4) is less than 150 mm. The scatter observed in the results is expected because of he large grain size in the pyroxenite rock type, which, on occasions is pegmatitic.

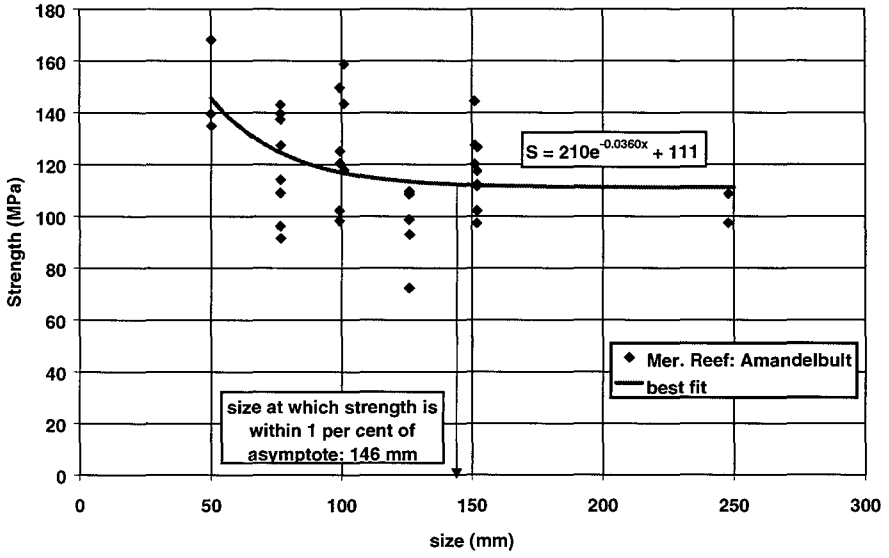

Figure 5-3 The strength – size relation for Merensky Reef from Amandelbult Platinum Mine.

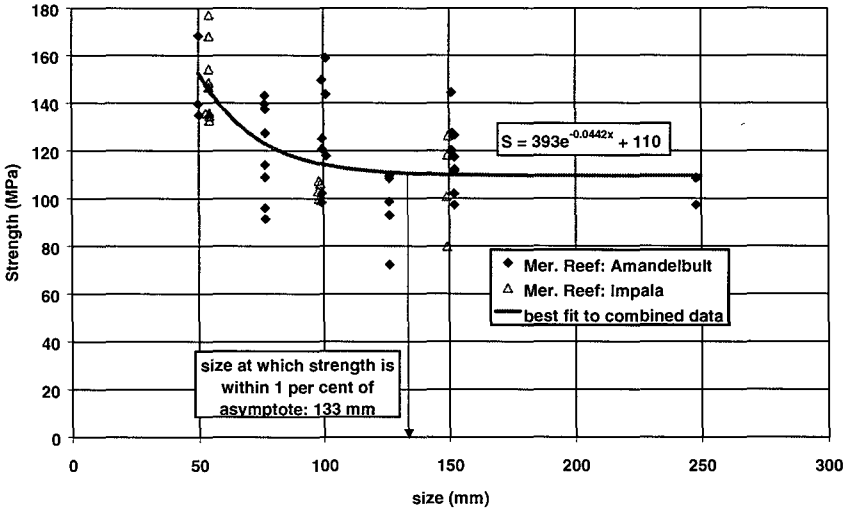

Figure 5-4 The strength – size relation for Merensky Reef from Amandelbult and Impala Platinum Mines.

5.4.1.2 Discussion

Coal, a soft rock, has a critical size of between 1 m and 1,5 m. Norite, a hard rock, has a critical size of about 125 mm (see Figure 5-1). Experimental evidence collected within the scope of this project indicates that Merensky Reef has a critical size between 100 mm and 150 mm. It is thus postulated that hard rocks, in general, may have a critical size of approximately 150 mm.

This has important implications for hard rock pillar design. Because no volume effect is expected above the critical size, it implies that hard rock pillar design need not be concerned with the volume effect. This implies that the power formula, which is relatively complex to derive, need not be used, rather, a simple linear function is applicable. Another factor is the limited number of well documented pillar collapse cases in hard rock mines.

York and Canbulat (1998) show that the strength of a rock specimen is a function of the end, or boundary, conditions, both with respect to frictional conditions and the relative material properties and geometry of the loading platen / end piece / hangingwall (assuming other conditions such as loading rate, temperature and moisture content are unchanged). Strength is therefore not a stand alone value, but is a value for a given set of boundary conditions. Thus, the critical rock mass strength should be quoted with a statement regarding the end conditions, the means of load control, loading rates, etc. It is suggested that, especially for model pillar studies, previous results have been presented with ill defined boundary conditions.

The typical size of uniaxial compressive strength test samples, as recommended by the ISRM, is about 50 mm in diameter. This is within the range of sizes that is affected by scale for a number of rock types. Therefore, the use of UCS tests, even as a comparative measure, can only be regarded as a first approximation. It is suggested that the use of the critical rock mass strength, as determined according to the methodology described in the preceding section, removes this ambiguity. The basis of comparison of different material strengths would then be the same.

The critical rock mass strength which is being proposed as one of the input parameters in pillar system design, must therefore be determined under clearly defined boundary conditions. Strength values so obtained may then be adjusted accordingly for the pillar system factors mentioned above, primarily for different boundary conditions.

5.4.2 A comparison of the performance of the power and linear formulae

If the linear function (Equation 5-1) is normalised to the strength of a sample or pillar of w/h=1, and if we define this strength to be Θ, then the result may be written as follows:

$$S/\Theta = a + (1-a)(w/h) \qquad \textit{Equation 5-5}$$

where S = the expected model pillar strength

Θ = the strength at w/h=1

= m + c (see Equation 5-1)

$1-a = m / \Theta$

$a = c / \Theta$.

The value c / Θ has been arbitrarily termed "a". Due to the fact that $c / \Theta + m / \Theta = 1$, and if c / Θ is termed a, then m / Θ may be termed 1-a.

In this case, S/Θ may be regarded as the strength normalised to the strength at w/h = 1. Alternatively, the following form is more convenient for pillar design (see Section 5.5), in which S_c denotes the strength taking contact conditions and the critical rock mass strength into account:

$$S_c = \Theta_c[a + (1-a)(w/h)] \qquad \textit{Equation 5-6.}$$

where Θ_c = the critical rock mass strength derived in Section 5.4.1.1 or Section 5.4.4.

5.4.2.1 Scope of laboratory testing and testing methodology

Drill core was obtained from Amandelbult Platinum Mine. The core was drilled perpendicularly to the reef and the specimens were prepared to the highest surface finish possible. (The smaller

sample diameters were prepared to better than ISRM surface finishing tolerances, but this was not always possible on the larger diameters.)

The tests were done on the 25 MN soft testing machine at CSIR Miningtek, Carlow Road. The machine was not servo-controlled. No post failure sample behaviour was examined, although some post failure behaviour was captured, and the residual loads were recorded. A displacement transducer was placed on opposite sides of each sample to record changes in sample length. Strain gauges were attached to all samples of w/h = 1 and to certain samples of other w/h's, within practical restraints. The strains recorded from the transducers were then correlated to the strains measured from the strain gauges, so that strains could be calculated for those samples not strain gauged. Cylindrical end pieces (platens) were used, which were made from EN30B steel and hardened to about 48 Rockwell C. The platens had diameters 5 mm larger than the sample diameters and each had a w/h = 1. This was to counter the effect of sample indentation into the platen and bending of the platen over the sample. Between each test the platens were reground to ensure that the friction angle between the sample and platen was the same for each test. Soft-board 15 mm thick was placed between the machine platen and the top sample loading platen to act as a spherical seat for each test.

Table 5-1 Number of samples tested for the range of w/h's and diameters in the testing programme.

w/h	Sample diameter (mm)						
	50	54	76,5	101	125	151	248
1	3	6	8	8	5	9	2
2			4				
3	2		6	2		2	2
4	2		6	2		2	2
5	2		4				
6			6	2		2	2
7			4				
8			4				
9			4				
10	2		6	1		2	2

5.4.2.2 Results of testing programme

Linear functions (Equation 5-1) were fitted to the data, for w/h $\leq$ 6. The results are shown in Table 5-2. A power formula (Equation 5-2) was also fitted to the data. The values of the regression parameters for the power formula are shown in Table 5-3.

The r^2 values indicate the proportion of the total variation in strength which is accounted for by the variation of the independent variable/s in the fitted functions. The r^2 values shown in Table 5-2 compare favourably with the r^2 value shown for the power formula in Table 5-3. It can be concluded that the linear function performs as well as the power formula.

In the above analysis, a separate linear function was fitted for each diameter, while the same power formula parameters were applied for all diameters. This demonstrates the ability of the power formula to handle volume. Conversely, it is demonstrated that the linear function is comparable to the power formula if the volume ratio is comparatively small. A similar result has been shown for coal laboratory and *in situ* data (York and Canbulat, 1998). Galvin *et al* (1996), in a statistical comparison between the power formula and the linear function on a set of Australian and South African coal pillar collapse cases, showed that the difference between the two formulae is not statistically significant.

Table 5-2 Results of laboratory testing on Merensky Reef from Amandelbult Platinum Mine.

Size (mm)	No. of samples	r^2	Linear function parameters		Normalised linear function parameters	
			m	c	Θ	1-a
50	9	0,80	45,1	99,64	145	0,31
77	17	0,59	32,37	87,65	120	0,27
101	14	0,90	44,28	77,22	121	0,36
151	13	0,95	27,01	90,40	117	0,23
248	8	0,91	25,60	79,34	105	0,24

Table 5-3 Results of a regression fit of a power formula to the laboratory data.

k	α	β	r^2
78,4041	-0,4605	0,2775	0,80

5.4.3 The effect of w/h on pillar strength and the effect of the contact friction angle

An example of the strength – w/h relation is shown in Figure 5-5, for samples of 248 mm diameter. The relation is clearly linear. The fitted parameters of Equation 5-1 are shown in the figure: m = 25,60 and c = 79,34. The increase in strength for each unit increase in w/h is 25,60 MPa. The strength at w/h = 1, termed Θ, is 104,94 MPa = m + c. The normalised strength effect of the w/h effect is therefore 25,60 ÷ 104,94 = 0,24 = 1-a. These values may be seen in Table 5-2, for each of the diameters tested.

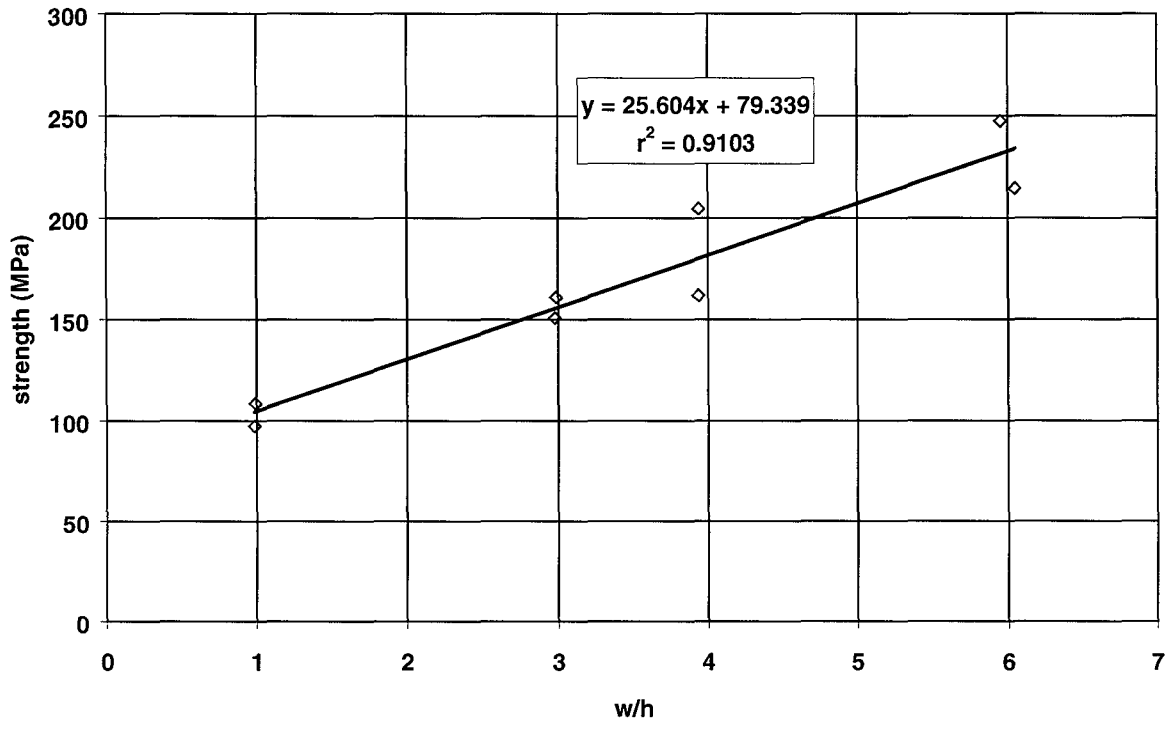

Figure 5-5 The strength – w/h relationship for Merensky Reef from Amandelbult Platinum Mine, for cylinders of diameter = 248 mm.

A similar analysis has been performed for coal data (York and Canbulat,1998), and on the w/h tests performed in the scope of SIMRAC project GAP024. The values of the parameter 1-a for all the laboratory data sets analysed are shown in Figure 5-6. As may be seen, the average values of 1-a are roughly the same for the coal and Merensky Reef data. This implies that the strengthening effect of w/h is similar for coal and Merensky Reef, under laboratory loading conditions.

A number of *in situ* pillar compression test results have been re-analysed, from the original data, to determine the *in situ* w/h strengthening parameter (York and Canbulat, 1998). The results are shown in Table 5-4, together with the COL021 laboratory data The *in situ* 1-a values in Table 5-4 are plotted in Figure 5-7, together with the results shown in Figure 5-6. The value of 1-a is shown to be scale independent for coal.

The strengthening effect of w/h is generally ascribed to the increased confinement in the sample as w/h increases. This is shown graphically in Figure 5-8. However, the level of confinement must depend on the shear resistance at the loading platen / rock sample interface. This shear resistance, in turn, depends on the friction angle at the platen / sample contact. Therefore, a slippery contact should result in weaker samples, while a rougher contact should result in a greater w/h effect.

To test the effect of the value of the contact friction angle, the laboratory tests shown in Table 5-2 and Figure 5-5 were numerically modelled using FLAC. The FLAC model geometry is shown in Figure 5-9. The contact between the strain softening rock material and the elastic steel platen was varied from 0° (perfectly slippery) to 30°. The value of w/h was varied for each contact friction angle. The results of this analysis are shown in Figure 5-10.

Table 5-4 Results of straight line fits to original data of* in situ *compression tests on coal pillars and SIMRAC project COL021 laboratory data (after York and Canbulat, 1998).

Source	Size (mm)	no. of samples	r^2	Fitted function	
				Θ	1-a
lab : COL021	25	226	0,63	50.8	0.25
lab : COL021	50	290	0,63	46.6	0.19
lab : COL021	100	242	0,59	34.2	0.22
lab : COL021	200	75	0,82	28.6	0.26
lab : COL021	300	91	0,84	20.8	0.38
Bieniawski 0.9 and 1.2 m	1050	11	0,72	4.86	0.38
van Heerden	1400	10	0,91	14.5	0.26
Bieniawski 1.5 and 2.0 m	1500	13	0,97	4.32	0.33
Wagner	1800	12	0,54	11.3	0.31
Salamon and Munro	7128	26	0,53	5.74	0.26

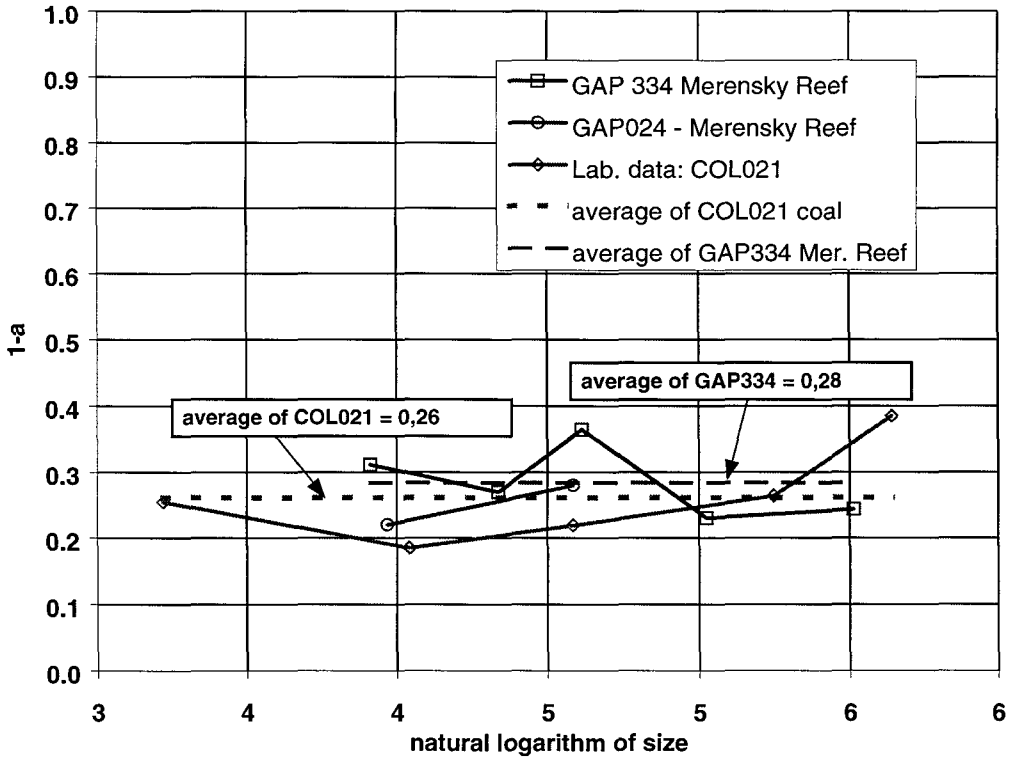

Figure 5-6 The values of the w/h strengthening parameter, as a function of size (mm), for various data sets (coal data after York and Canbulat, 1998).

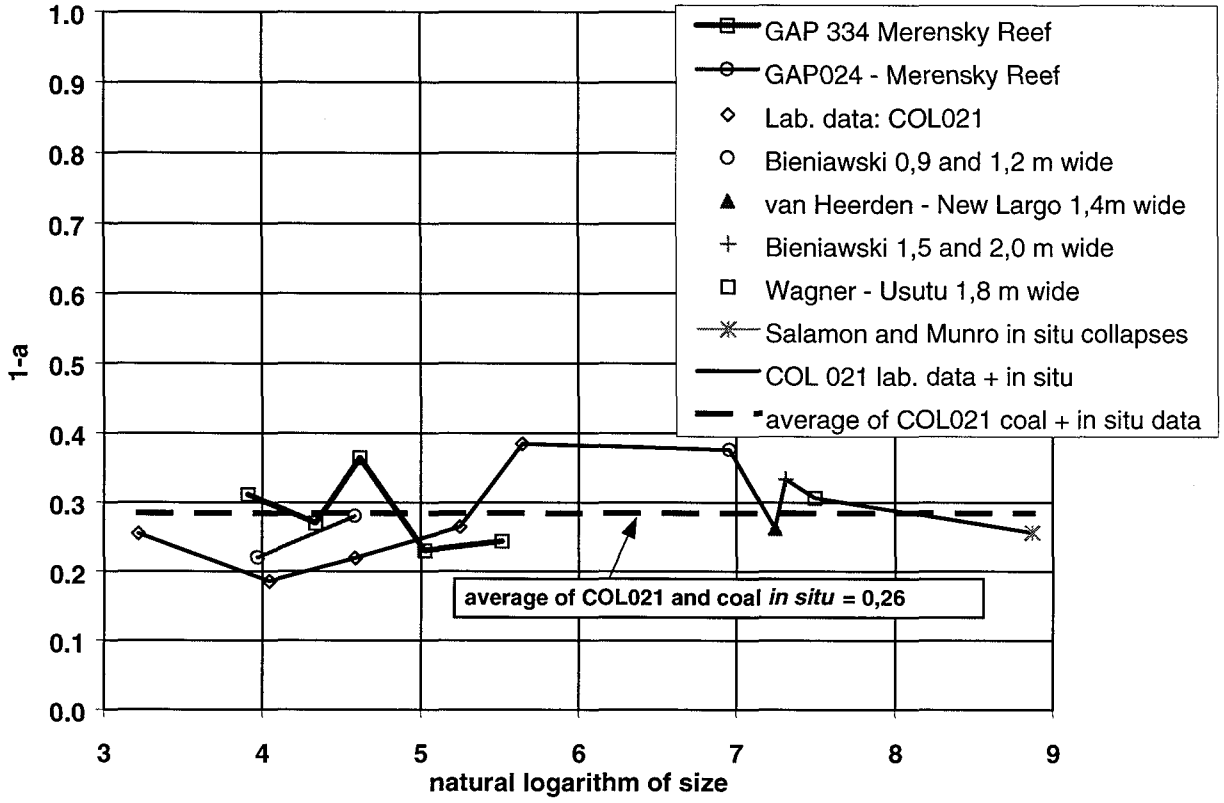

Figure 5-7 The values of the w/h strengthening parameter, as a function of size (mm), for the data sets including coal data (coal data after York and Canbulat, 1998).

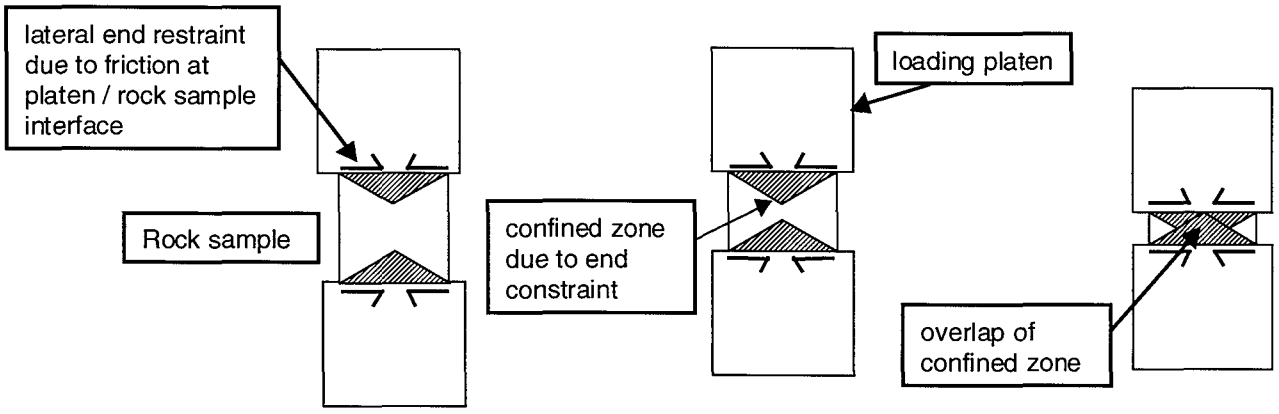

Figure 5-8 A conceptual diagram of the effect of frictional end restraint on the confinement of a sample, depending on its w/h.

The portion of each curve in Figure 5-10 before the squat pillar effect is effectively a plot of the linear function in the form as shown in Equation 5-5. The y-axis in Figure 5-10 is the term S/Θ. The slope of each curve is the term 1-a. As may be seen in Figure 5-10, the change in contact friction angle affects two parameters:

1) the w/h strengthening parameter 1-a, and
2) the w/h at which the squat pillar effect starts.

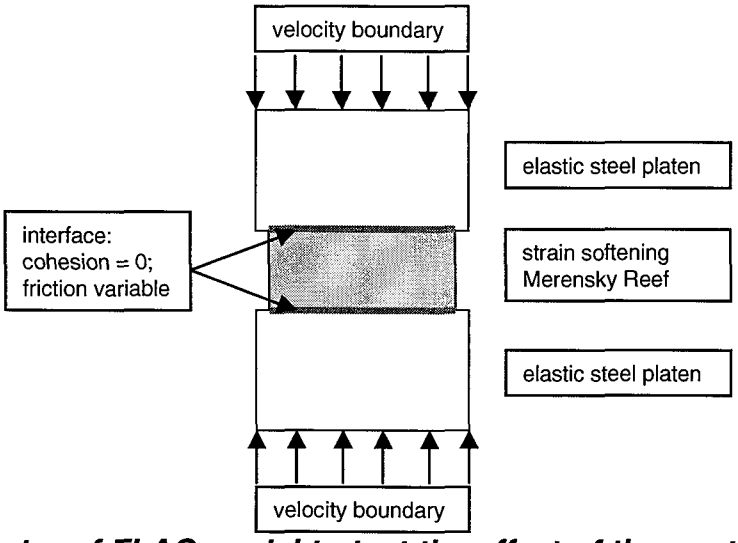

Figure 5-9 Geometry of FLAC model to test the effect of the contact friction angle on the strength of laboratory model pillars.

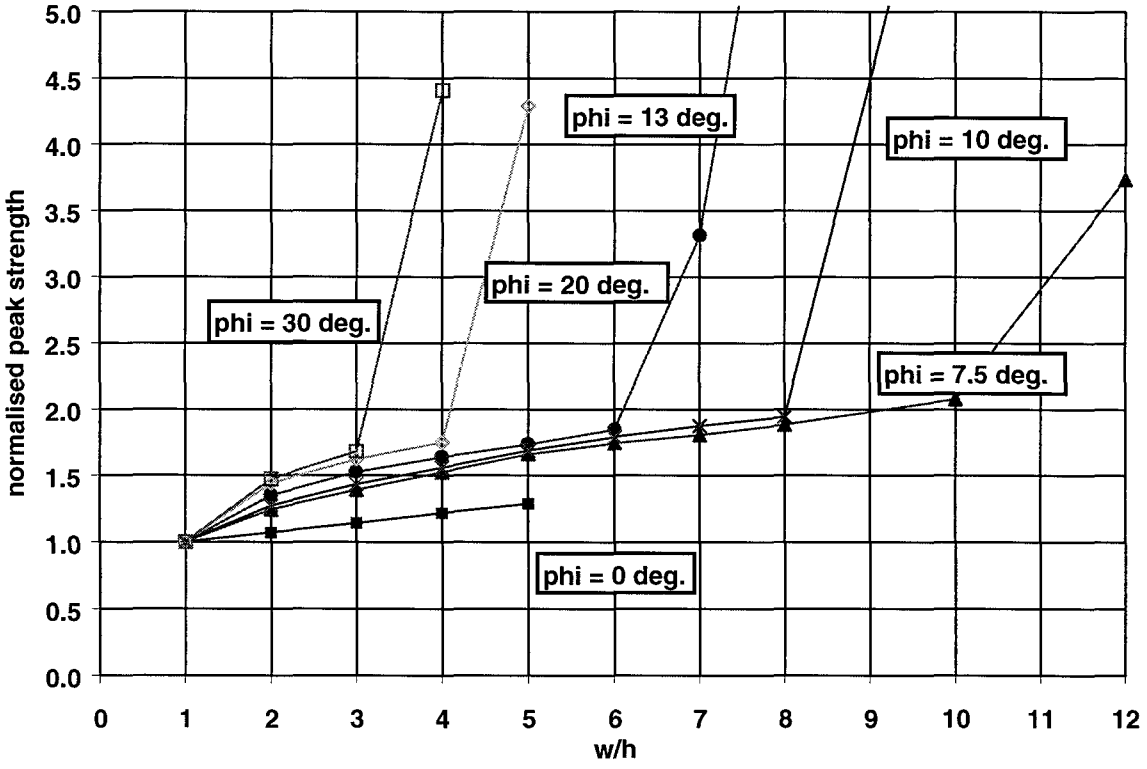

Figure 5-10 The effect of the contact friction angle on the w/h effect, on the basis of numerical modelling.

The slopes of the curves (before the squat pillar effect) in Figure 5-10 are plotted as a function of the contact friction angle in Figure 5-11. Three shear box tests were performed on the contact between Merensky Reef and steel platens. Both the Merensky Reef and the platens were surface finished to the normal standard required for rock testing. The average value of the contact friction angle was 13,7°. A series of tests was performed on a friction angle testing bed, resulting in friction angles ranging between 11° and 13°. A shear box test was performed on a specimen of coal. The contact friction angle was 12,7°. Both these results are plotted on Figure 5-11. The corresponding values of 1-a are as shown in Figure 5-7. The laboratory test data points plotted on Figure 5-11 lie close to the curve predicted by numerical modelling.

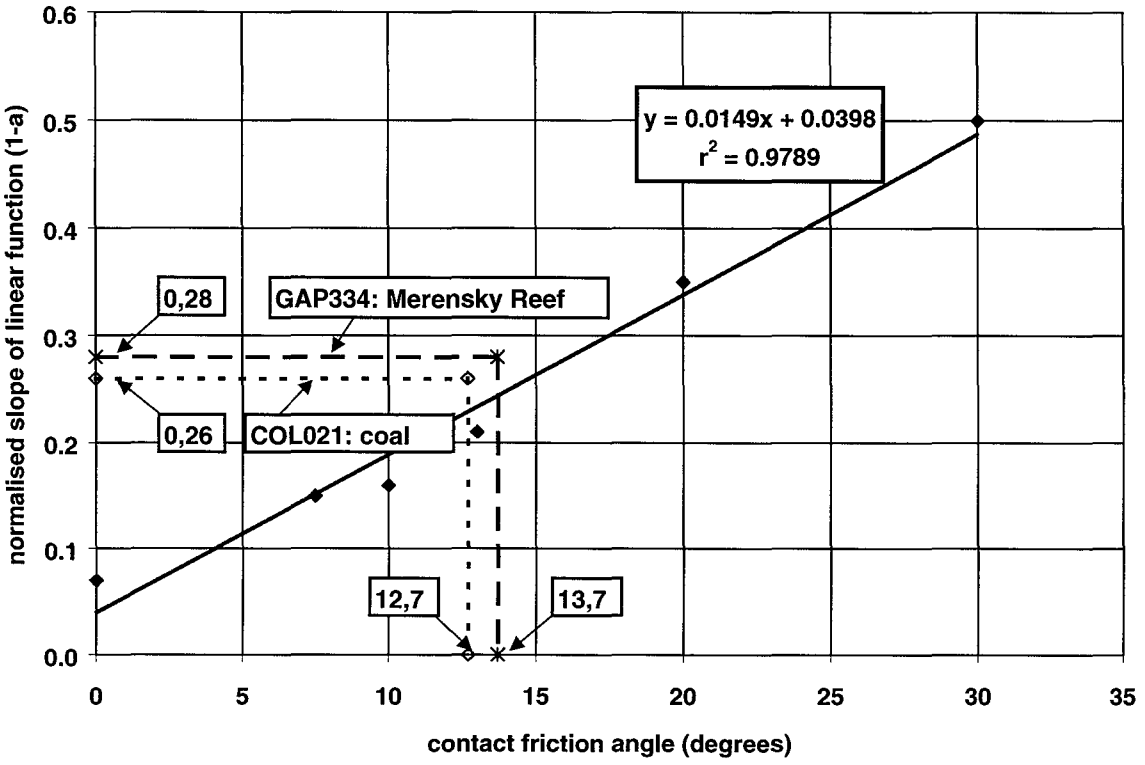

Figure 5-11 The w/h strengthening parameter, 1-a, as a function of the contact friction angle, according to numerical modelling. The values derived from laboratory testing on coal and Merensky Reef are also shown.

The agreement between the theoretically modelled curve in Figure 5-11 and the plotted points based on laboratory data provides some confirmation of the notion that the w/h strengthening parameter (1-a) is strongly influenced by the contact friction angle.

5.4.4 An approximate method to determine the critical rock mass strength (Θ_c)

While the best method of determining the critical rock mass strength is to derive a relation of the type shown in Figure 5-4, difficulties may arise in obtaining core of the required diameter (between 150 mm and 250 mm), especially if a new area is to be mined. An approximate method, based on the UCS test for a 50 mm diameter sample (a height of 100 mm to 150 mm), may allow a good estimation of the critical rock mass strength. The procedure suggested in this section is conceptually similar to that proposed by Ryder and Özbay (1990).

The first step is the upgrading of the UCS strength to that of a sample of w/h = 1. The International Society of Rock Mechanics recommends that UCS tests be performed at w/h = 0,33. UCS tests are sometimes done with w/h = 0,5. Assuming that w/h ≈ 0,4 (i.e. sample height = 125 mm, sample diameter = 50 mm), the difference in w/h is therefore 0,6. Assuming a linear relationship between w/h and strength, the following formula allows the determination of the strength of a w/h = 1 sample (Θ), from a given UCS strength:

$$\Theta = \frac{1}{1-(0{,}6)(1-a)}\,UCS$$

$$= f_{UCS}.UCS \qquad \textit{Equation 5-7}$$

where f_{UCS} = the upgrading factor applied to UCS tests to estimate the strength at w/h = 1

$$= \frac{1}{1-(0{,}6)(1-a)}$$, assuming that the UCS test has w/h = 0,4.

The average value of 1-a of the series of w/h tests of different diameters, tested in GAP334, was 0,28 (see Figure 5-6). The average value of 1-a for the two plotted values from the GAP024 data in Figure 5-7 is 0,25. The average of these two values is 0,27. For this value of 1-a, f_{UCS} = 1,19.

The second step is the downgrading of the w/h = 1 strength for the 50 mm size, to the strength at the critical size. The average strength of the 50 mm samples shown in Figure 5-4 is 148 MPa. The critical rock mass strength is 110 MPa. The downgrading factor, f_c, from the strength at w/h = 1, to the critical rock mass strength, is therefore 110/148 = 0,74. Referring to Figure 5-2b), for norite, the ratio of the strengths at two inches (approximately 50 mm) and the critical rock mass strength is approximately 0,8.

Therefore the critical rock mass strength, Θ_c, can be written as:

$$\Theta_c = f_{UCS} \times f_c \times UCS \qquad \textit{Equation 5-8}$$

For the Merensky Reef test data,

Θ_c = f_{UCS} x f_c x UCS
= 1,19 x 0,74 x UCS
= 0,88 x UCS.

In the above procedure, two factors must be determined, f_{UCS} and f_c. Of the two factors, f_{UCS} is the easier to determine. This is simply the ratio between the strength of a w/h = 1 sample and the UCS strength. As such, it is suggested that when UCS tests are performed, w/h = 1 tests also be performed, until representative values of f_{UCS} are established for each rock type or geotechnical area. This will not involve significant extra cost, because the core is already obtained for the UCS testing. Less core is required for a w/h =1 test than for a UCS test.

The factor f_c is more difficult to determine. The value of approximately 0,70 to 0,80 may be valid for hard rocks. However, this has only been established experimentally for Merensky Reef from Amandelbult Platinum Mine, and norite (see Figure 5-2). The value of f_c for softer rocks, such as chromitite, may well be lower. These values should be determined experimentally, at least for each major reef, if not for each mine or geotechnical area.

5.4.5 The effect of jointing on pillar strength

This section reports the results obtained by Esterhuizen (1997). The numerical modelling tool used was UDEC (ITASCA, 1991), to allow convenient modelling of joints. The modelling parameters are detailed in Table 5-5. The details of the model geometry and boundary conditions are shown in Figure 5-12. No *in situ* stresses were modelled.

Table 5-5 Details of the modelling parameters used by Esterhuizen (1997).

Model element	Values / details
coal material	strain softening: • bulk modulus = 2,67 GPa • shear modulus = 1,6 GPa • strain softening • friction = 20° = constant • cohesion dropped linearly from 2,51 MPa to 0,1 MPa in 0,08 plastic strain
joints	friction = 20°; cohesion = 0; dilation = 5°
roof and floor	elastic: bulk modulus = 8,0 GPa; shear modulus 4,8 GPa
pillar contacts	friction = 20°, cohesion = 0

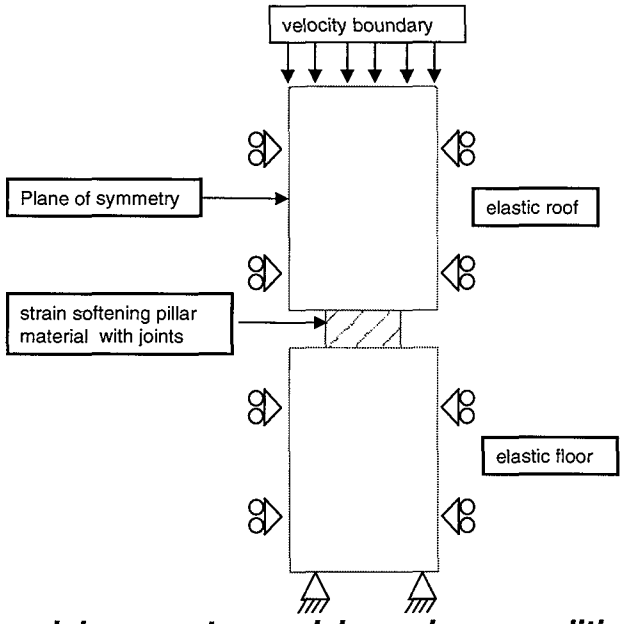

Figure 5-12 UDEC model geometry and boundary conditions to determine the effect of jointing on coal pillar strength (after Esterhuizen, 1997).

The results for pillar w/h's of 2, 3, 4, and 6 are shown in Appendix B. If an orthogonal joint set intersects the pillar in an orthogonal pillar side, then the factors obtained from each joint set are multiplied, to determine the overall pillar strength reduction factor.

Esterhuizen (1997) back analysed the numerical modelling results to coal pillar collapse cases, with success. These results have not been back analysed to hard rock pillar case studies. This is an area that should be investigated in the future. However, it is considered that the results provide a good first approximation of the effect of joint dips and pillar joint frequency on hard rock pillar strength.

5.5 A methodology for the design of pillars

Many factors influencing the strength of pillars are listed in the introduction of this chapter. Not all of these factors could be addressed in the scope of this project. The flowchart in Figure 5-13 addresses those issues in pillar design that were considered to be most influential in pillar

strength determination, and could be reasonably addressed in the scope of SIMRAC project GAP334.

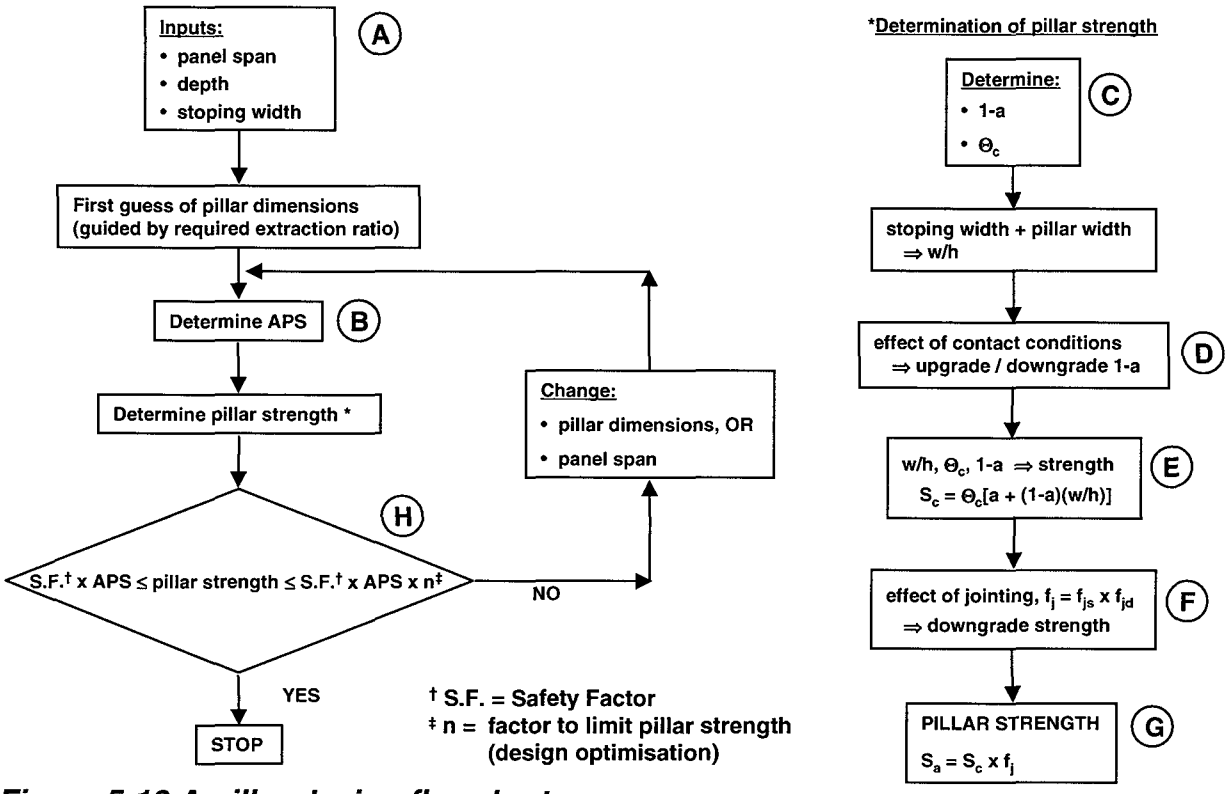

Figure 5-13 A pillar design flowchart.

To explain the rationale of the methodology, selected blocks in the flowchart are discussed in detail below.

Block A: The panel span may be obtained by empirical experience, or by the use of the methods described in Chapter 3 and Chapter 4.

Block B: The average pillar stress (APS) may be obtained by numerical modelling, according to the suggestions in Section 2.5. If numerical modelling is not practical, and tributary area theory loading is assumed, then it is suggested that the APS so obtained be adjusted to account for the loading system behaviour discussed in Chapter 2.

Block C: Θ_c may be obtained according to Section 5.4.1.1 or Section 5.4.4. The value of 1-a is obtained as follows:

1) fit a linear function to laboratory tests of w/h ≤ 6 (Equation 5-1), and
2) normalise the linear function according to Equation 5-5.

Block D: The contact friction angle between Merensky Reef and steel platens is of the order of 15°. The value of the w/h strengthening parameter 1-a is proportional to the contact friction angle (Figure 5-11). Therefore, if the *in situ* contact conditions are such that the effective pillar / hanging- or footwall contact friction angle is greater than 15°, it is suggested that 1-a be increased, according to the relationship shown in Figure 5-11. This may be the case for gradational pillar contacts at the hangingwall and footwall ("gradational" implies that the rock type changes gradually between the reef rock type and the hangingwall rock type).

The effect of contact friction has not yet been back analysed to *in situ* pillars. This is an area that requires future work. Due to this, if the value of 1-a is upgraded, it is suggested that the upgrade is limited to a maximum value of 0,50 (corresponding to a contact friction angle of approximately 30°). If the value of 1-a derived from laboratory testing is greater than 0,50, then this should be used. Values of 1-a = 0,6 have been measured for chromitite in laboratory testing.

Block E: Once a trial value of w/h has been selected, and suitable values of Θ_c and 1-a have been derived, Equation 5-6 may be used to determine the pillar strength (S_c) taking contact conditions and the critical rock mass strength into account.

Block F: To determine the total effect of the jointing in both directions (f_j), the charts in Appendix B should be used for each of the orthogonal faces of the pillar, in turn (i.e. one dip face and one strike face). If a face is intersected by more than one joint set, the most persistent, or dominant, joint set should be selected. The pillar strength reduction factor for each direction is obtained as a function of the dip and frequency of the joint set. The strength reduction factor for the strike joint set is termed f_{js} and the dip joint set, f_{jd}.

To account for joint sets intersecting each of the orthogonal faces, the factors for each direction are multiplied. This method was used with success by Esterhuizen (1997) in back analysis of coal pillar collapses.

Block G: The pillar strength (S_a) taking all the quantified pillar system factors into account.

$$S_a = S_c \times f_j \qquad \textit{Equation 5-9}$$

Block H: This is the check against the safety factor. If the pillar strength is larger than the safety factor times the APS, the optimisation parameter, n, ensures that the pillar is not over-designed. If, for example, the tolerance for over-design is 20 per cent, then n = 1,20.

The effect of variability of design parameters has not been explicitly taken into account in this design process. Examples of variables that vary are UCS, joint set frequency, and joint set dip. Esterhuizen (1993) provides a methodology for taking variability into account. It is assumed that the safety factor of 1,6 takes uncertainty and variability adequately into account. The correct value of safety factor for different geotechnical areas required further work.

5.6 A preliminary methodology for the design of crush pillars

Currently, there is little information with respect to the design of crush pillars. Some theoretical and practical considerations have been provided by Özbay and Roberts (1988). They introduced the concept of a "transition zone", a range of depths in which crush pillars can be introduced. Özbay and Roberts defined the transition zone in terms of two criteria:

1) an assumed pillar strength (an input parameter for crush pillar design)
2) the theoretical elastic average face abutment stress.

Özbay and Roberts stated that crush pillars may be used at the depth that the average face abutment stress is equal to the pillar strength. The transition zone was defined as a range, rather than a single depth, to account for uncertainties in load and pillar strength, and practical difficulties in cutting pillars of the correct dimensions.

If a crush pillar is defined as a pillar that is loaded beyond its peak strength as it is formed, then it is crucial that the face stresses are high enough to cause crushing at the face. This depends on:

1) the mining depth
2) the mining geometry
3) the regional spans
4) the pillar w/h
5) other factors that affect pillar strength (material strength, contact conditions, jointing, etc).

The latter two factors mentioned above define the peak load that must be applied to the pillar to crush the pillar. It is commonly accepted that pillars of w/h between about 3 and 5 potentially fail in a violent manner. Therefore, it is usually recommended that crush pillars be designed with w/h < 3. The lower limit of w/h is usually defined by practical mining considerations, and is usually defined as about w/h=2, for stoping widths of up to about 1,5 m.

As has been seen in Chapter 2, the first three factors above interact in an extremely complex way. The pillar width is also a part of the second factor mentioned. The results from Chapter 2 indicated that, in general, pillar loads are less than is assumed by tributary area theory. In the presence of regional support, narrow pillars are relatively less stiff than wider pillars. This results in pillars of low w/h receiving less load than pillars of higher w/h. Crush pillars, due to the need to be of low w/h, will be relatively narrow, and therefore will receive less load than comparatively wider, elastic pillars.

Due to the potential for violent failure if pillars are not crushed at the face, it is crucial that the load on the pillar be determined as accurately as possible. This ensures stable and safe crush pillar failure. Therefore, the theoretical, elastic, average face abutment stress is not a good enough measure to determine the loads on a crush pillar. Numerical modelling is required to determine the load on the pillar, if the first three above-mentioned factors are to be taken into account properly.

In many areas of the Bushveld Complex, the bearing capacity of the footwall is lower than the strength of the crush pillars (as they are currently designed). The footwall therefore yields, and the pillars do not crush. This also occurs in other mining areas. The crush pillar design could be optimised in such cases.

A preliminary methodology for the design of crush pillars is shown in Figure 5-14. As discussed above, the load is a crucial parameter. In the derivation of the curves in the left portion of the Figure, the following parameters were kept constant:

- number of pillars = 9
- panel span = 30 m, which is a span typically found in shallow to intermediate depth mines.

The modelled pillar widths were 2 m, 3 m and 4 m. The depth was allowed to vary. The surface was explicitly modelled. The Young's modulus was 70 GPa, and Poisson's ratio was 0,2.

In the transition zone, the rock mass and the rock face can be considered to be in an elastic state. A pillar would only crush as it is formed as a result of its geometry. Therefore, the use of elastic modelling to obtain the load under the given depth and geometry assumptions is considered to be reasonable.

For the reasons discussed above, the chart (Figure 5-14) caters for pillars of $2 \leq w/h \leq 4$. The left half of the chart shows the APS as a function of depth and pillar width. The pillar load curves have been drawn taking the loading system into account (see Chapter 2). The APS curve for the 2 m pillar, assuming tributary area theory load is shown as a comparison to the 2 m pillar curve taking the surface and loading system into account.

A pillar strength curve is drawn on the right hand side as a function of w/h. Any relevant pillar strength curve could be drawn, based on the particular conditions in the design problem. It is envisaged that each mine would develop curves for their particular geotechnical areas, according to the pillar design flowchart shown in Figure 5-13. This provides flexibility to the methodology. The pillar strength curve plotted in Figure 5-14 is an example of such a curve. The critical rock mass strength is assumed to be 100 MPa. The normalised slope of the curve (1-a) is 0,31. A constant pillar joint reduction factor of 0,85 has been assumed for all values of w/h. In practice this is not the case, as the effect of jointing reduces with increasing w/h.

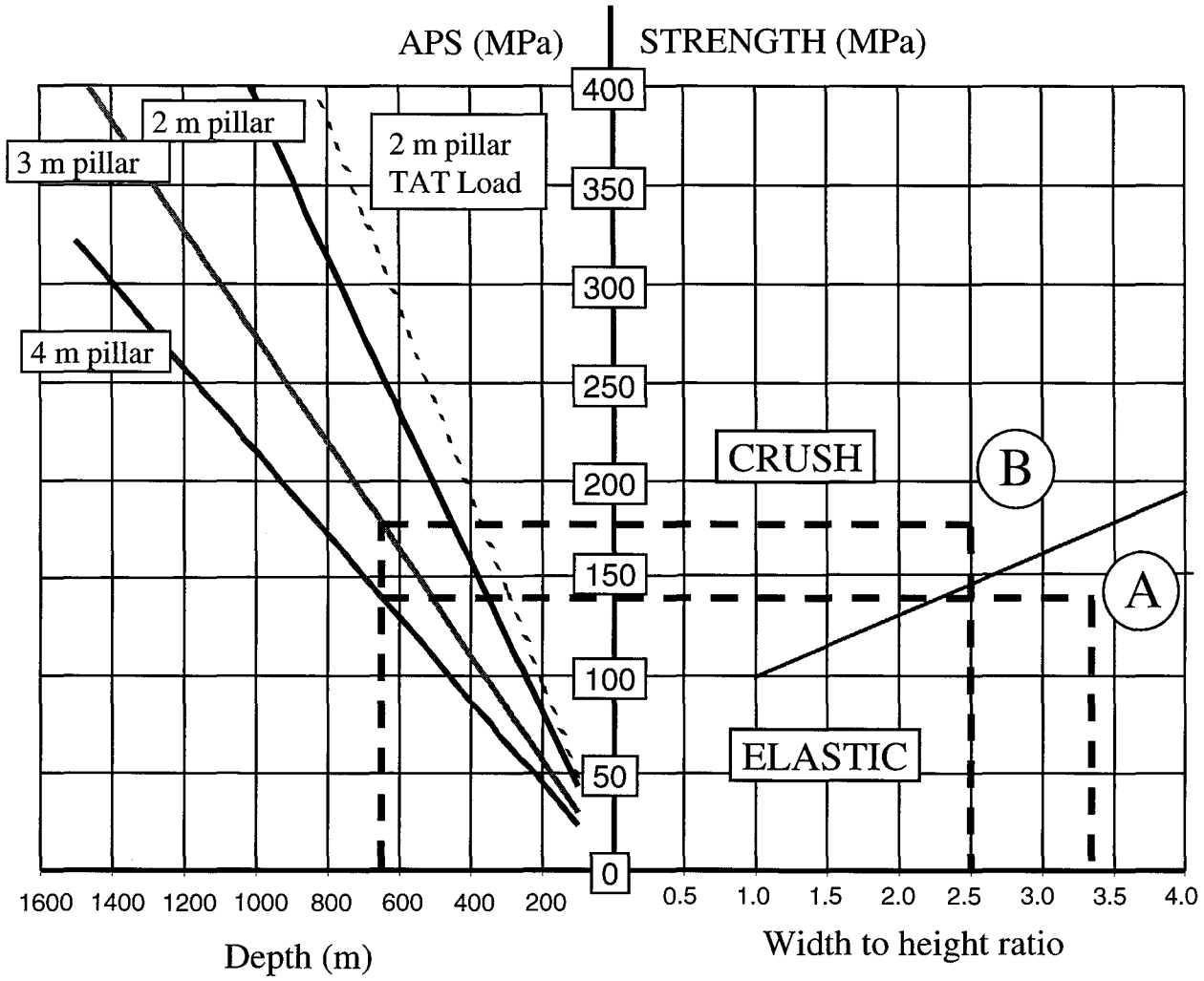

Figure 5-14 Preliminary chart for the design of crush pillars.

5.7 *In situ* crush pillar monitoring

5.7.1 Introduction

A 5 m x 3 m "crush" pillar was instrumented below the 10/26W/4W panel at Amandelbult Platinum mine (the site) to assess the validity of the current strength formulae used on the Platinum mines and to provide a better understanding of "crush" pillar behaviour.

The site was situated well ahead of the lower panel, in an advanced strike gully. The instrumentation, used for measuring stress, included: permanent doorstoppers, vibrating wire load cells, a hard inclusion load cell (Zafer load cell), flat jacks and a Glotzl cell. Some of these instruments were installed in the centre of the pillar to measure the effect of cutting a 0,01 m x 1,36 m x 1 m sub-horizontal slot immediately below these instruments to enable flat jacks installed in the slot to be pumped to the original stress of the pillar. Three separate jacks were installed from the back of the slot outwards in order to determine the stress distribution within the pillar as loading increased. An extensometer and several borehole camera holes were also installed in the pillar to correlate deformation and fracturing with stress during subsequent mining in adjacent panels.

5.7.2 Site description and mining sequence

The breast, westward mining face of the panel above the instrumented "crush" pillar (the pillar), was stopped to form a temporary up-dip protection pillar (between 5 and 6 in Figure 5-15) at the start of the project. At the beginning of the experiment, the face of the panel immediately down dip of the pillar was 30 m behind the up-dip panel and was advanced during the installation of the instruments. A 3 m x 3 m cubby was blasted on the up-dip side of the gully opposite the pillar as shown in Figure 5-15 and Figure 5-16. Cubbies 2 m wide and 3 m deep were blasted on either side of the proposed pillar, which would eventually become holings.

The mining sequence (step) was unusual, as shown in Figure 5-15. Most of the steps were performed separately, i.e. one step at a time. All the instruments were installed well ahead of the face during the mining of step 2.

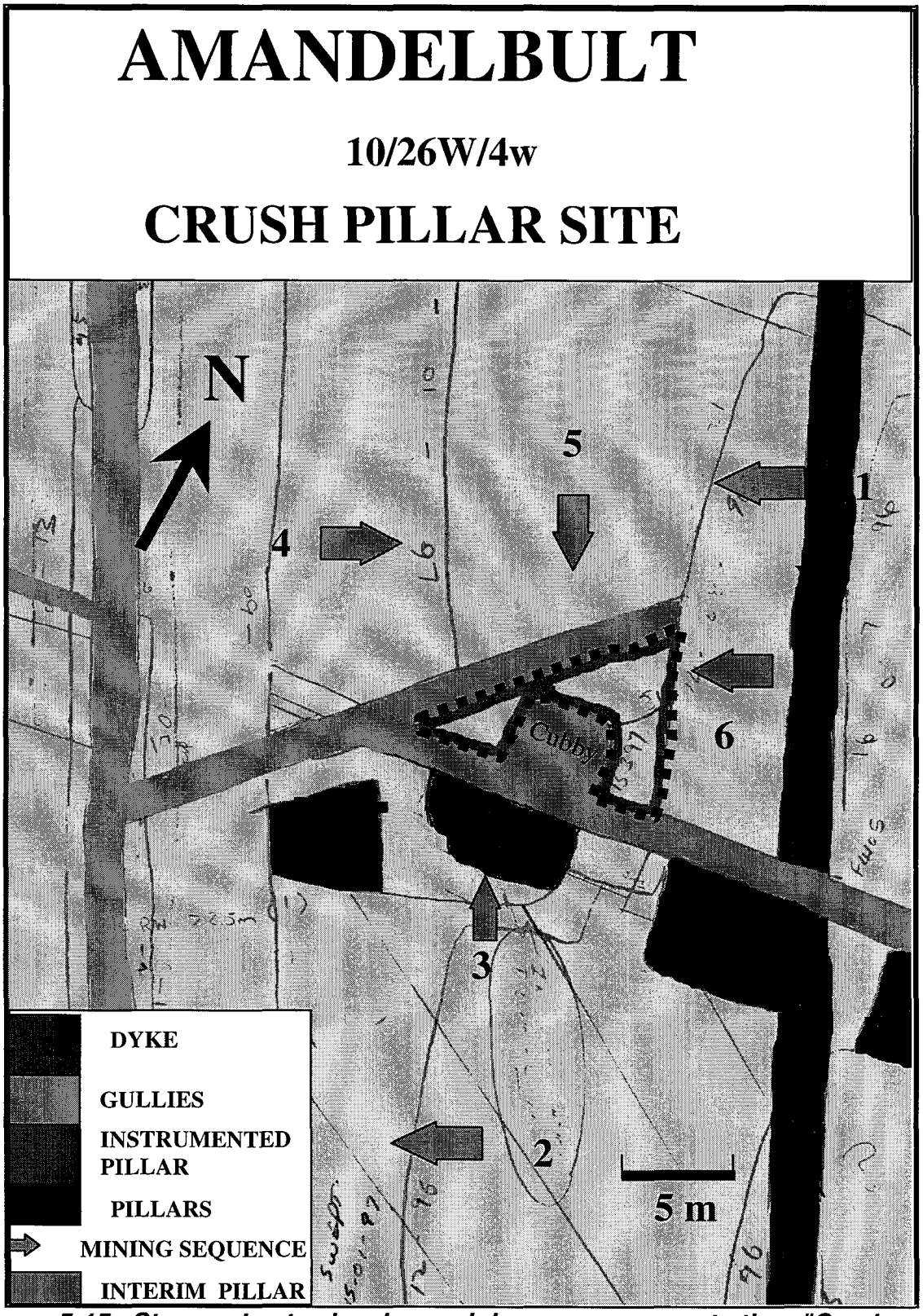

Figure 5-15 Stope sheet showing mining sequence at the "Crush pillar instrumentation site".

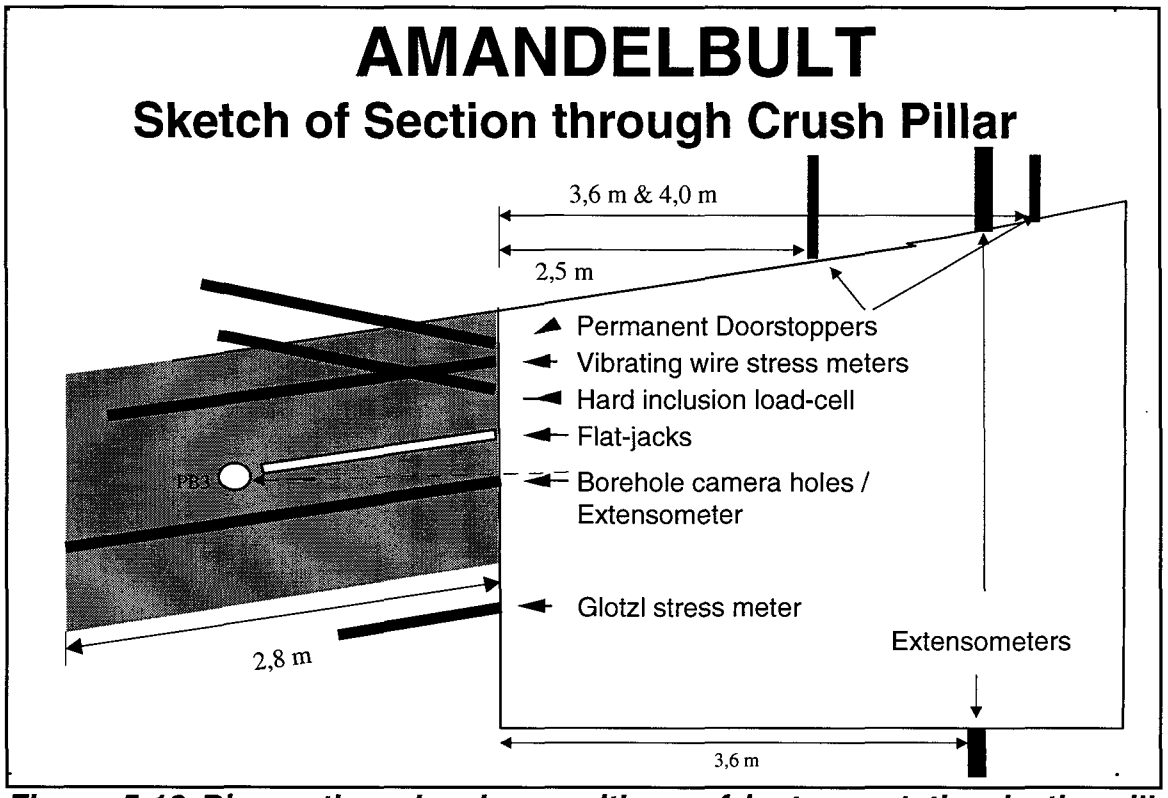

Figure 5-16 Dip section showing positions of instrumentation in the pillar and cubby.

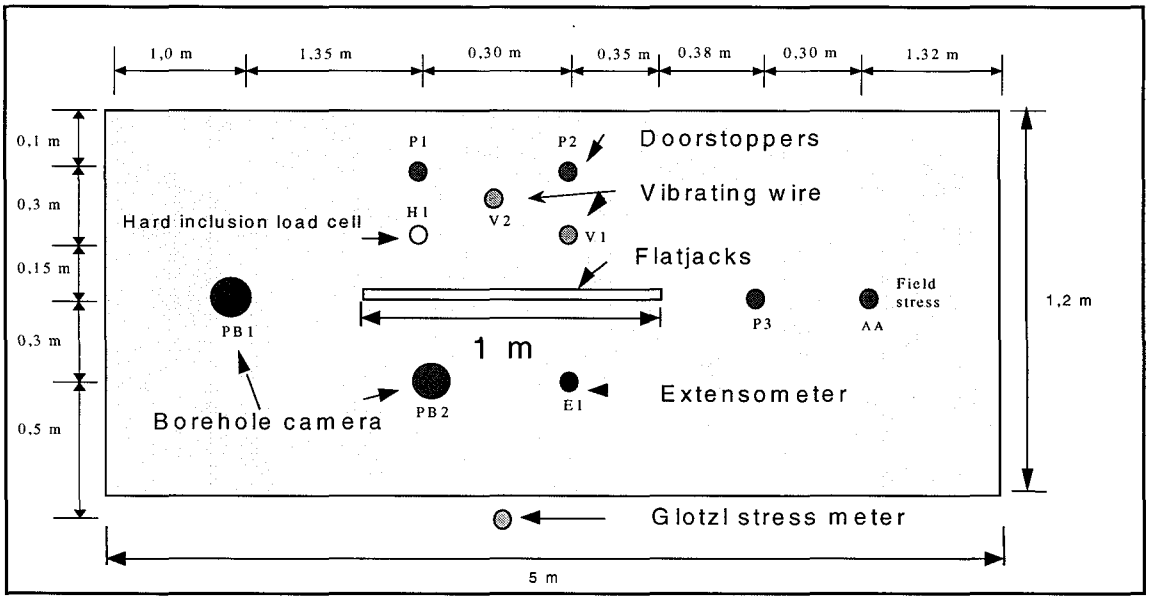

Figure 5-17 View of pillar from gully showing positions of instrumentation.

5.7.3 Results

5.7.3.1 Underground instrumentation

A list of the instruments installed at the site is shown in Table 5-6. Table 5-7 summarises the major events that were recorded during the formation of the pillar and Figure 5-18 to Figure 5-21 are examples of the results of the instrumentation. A complete diary of the events, and graphs reflecting the results of each instrument, have been included in CSIR Miningtek Technical Report 98/0440.

Problems were experienced during the pumping of the flat-jacks, which caused the outer jack to fail before any measurements were taken. The other two jacks could not be pumped to the original stress of the pillar and therefore created a stress shadow, affecting the results obtained from some of the other instruments installed close to the slot. During the time when the pillar became highly stressed, a large slab of rock broke away from the front of the pillar, shearing through the pipes connecting the pressure gauges to the flat-jacks and destroying some of the other instrumentation connections. Unfortunately, this occurred before the pillar failed and therefore these results have not been included in the analysis but the graphs up to the time of this incident have been included in the technical document.

Table 5-6 Instrumentation installed at the site.

Type	Installed
Permanent door stoppers	7
Over-cored door stoppers	4
Vibrating wire strain meters	5
Hard inclusion load cell	1
Glotzl load cell	1
Flat jacks	3
Extensometers	3
Borehole camera surveys	8
Geological logging	1
Geomechanical testing	1
Displacement cantilevers	2

Figure 5-18 shows the results of doorstopper P2, which was installed in the hangingwall at a depth of 0,77 m above the pillar (see Figure 5-16 and Figure 5-17). The position was close to the axis that is perpendicular to the centre of the pillar and the results were therefore assumed to be a fair reflection of the average stress at the centre of the pillar. The results of the vibrating wire stress cells were a factor of four lower than the doorstoppers, an example of which is shown in Figure 5-19, but the trends were similar. Earlier work performed by Spencer (1997) with vibrating wire stress cells on the Merensky Reef also showed that the stress was underestimated by about the same factor. The position of V1 (Figure 5-19) was 0,17 m above the centre axis of the pillar (see Figure 5-16 and Figure 5-17). The results of the Zafer load cell were completely different to any of the other instruments i.e. failure was recorded at an earlier time and there was an increase in stress when the other instruments recorded a failure, see Figure 5-20. This instrument was installed near the toe of the borehole at a depth of 0,36 m above the centre axis of the pillar, Figure 5-16 and Figure 5-17. Figure 5-21 shows the pillar dilation results, measured through the width of the pillar as shown in Figure 5-16 and Figure 5-17.

Table 5-7 Diary of major events recorded around the pillar.

DATE	Event
3rd November 96	Spalling started on the east corner of pillar (0,05 m slab)
13th January 97	Large scale spalling of the up-dip protection pillar, slight dog-earing (dipping towards the east) in hole PB1 but nothing in hole PB2 or hole PB3, Figure 5-16 and Figure 5-17.
14th January 97	Shearing, to a depth of 0,15 m, and dog-earing started in hole PB2. Further deterioration of hole PB1. No dog-earing in hole AA. Only open joints to a depth of 0,2 m in hole PB3.
17th January 97	Holing blasted through on right side; pillar is 4,9 m long. Hole AA has started dog-earing (also dipping towards the left but at a shallower angle than the other holes). Pillar started spalling on the west side.
30th January 97	Seismic event caused a rock which was attached to the pillar to be flung a distance of 1,5 m. Dog-earing in hole PB1 appears to be increasing between 1,42 m to 2,5 m and in hole PB2 between 1,3 m and 2,9 m.
5th February 97	Pillar failed violently. A large portion of the pillar has broken away with about 0,5 m of hangingwall. Up to 2m from the pillar, slabs were hanging from the hangingwall, which appeared to be the result of horizontal fracturing. PB1 and PB2 were sheared throughout the length of the hole. The cracking had stopped on the pillar but was heard on the protection pillar.

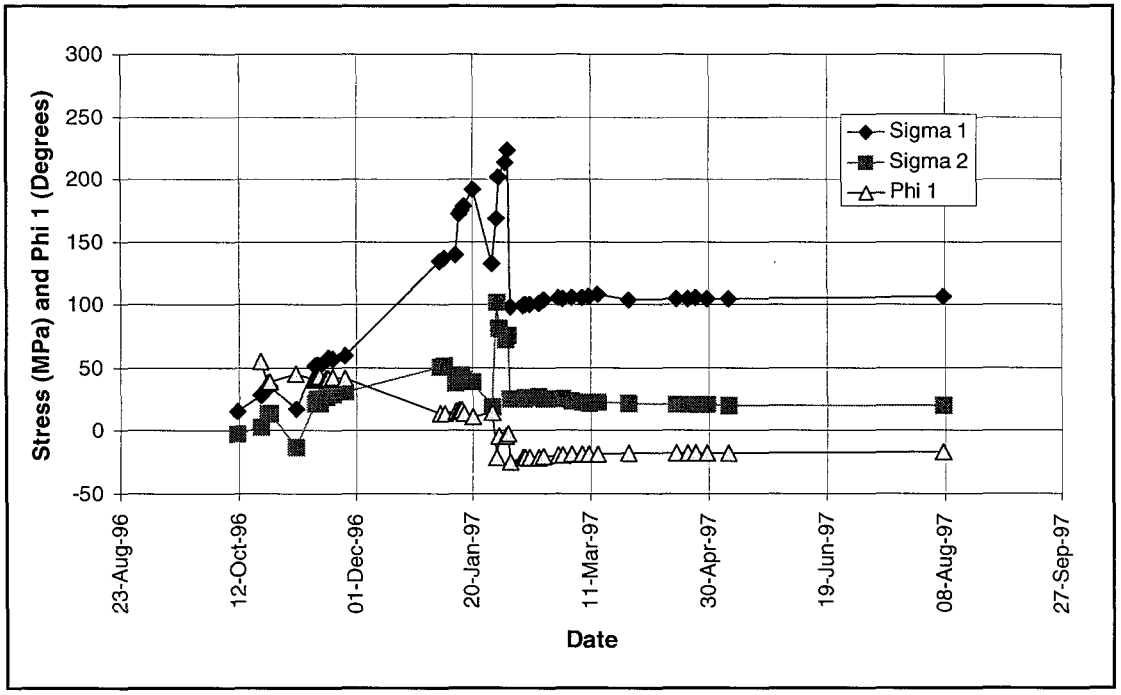

Figure 5-18 Total field stress measured by doorstopper P2 at 0,77 m above the pillar.

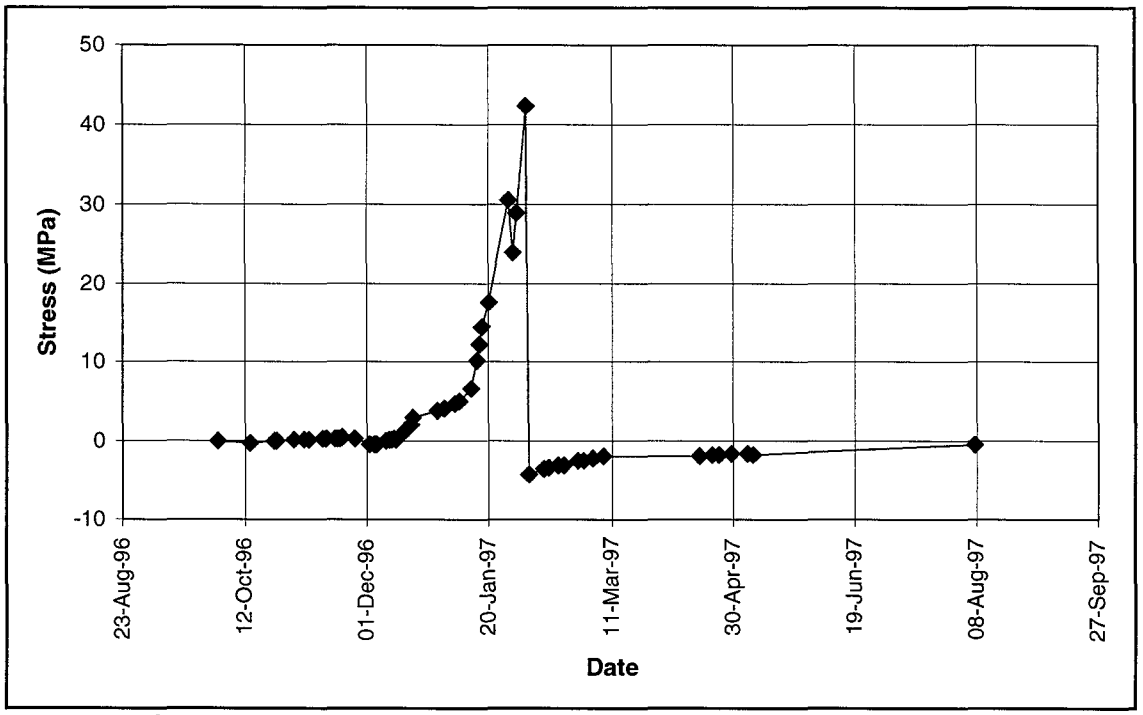

Figure 5-19 Stress change measured by vibrating wire stress cells at 0,17 m above the pillar.

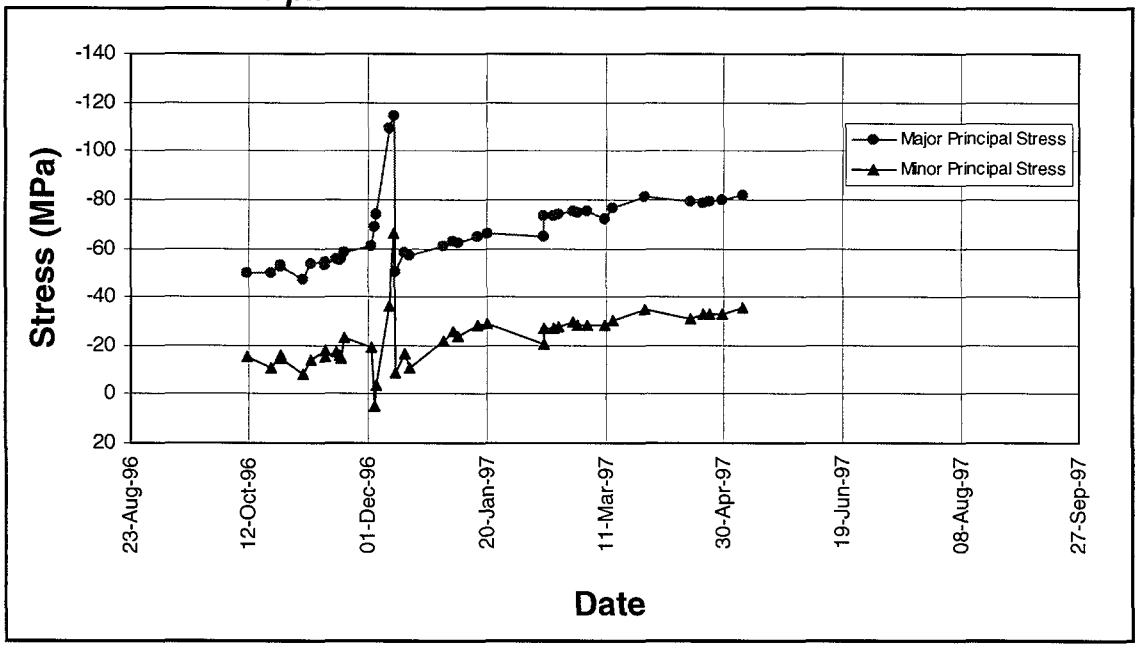

Figure 5-20 Vertical field stress measured by the Zafer load cell at 0,36 m above the pillar.

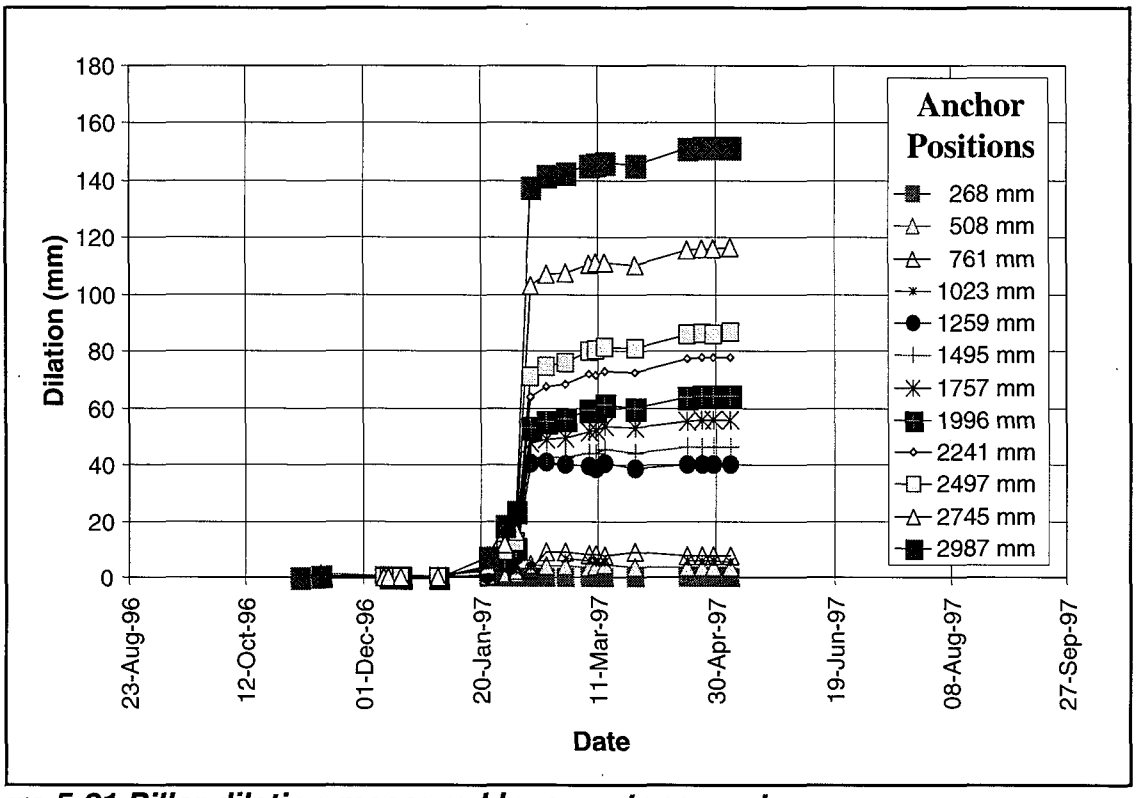

Figure 5-21 Pillar dilation measured by an extensometer.

5.7.3.2 Laboratory rock test results

Core from one of the doorstopper holes in the pillar was used to perform a geomechanical test. The results were used to interpret the instrumentation results.

Table 5-8 Results of the geomechanical test.

Strength (MPa)	Young's Modulus (GPa)	Poisson's Ratio	Density (kg/m^2)
276,2	151	0,250	3700

5.7.4 Discussion

The geologists log, Figure 5-22, shows that the pyroxenite hangingwall of the Merensky Reef had been altered in this area to an iron rich pegmatoid. Observations confirmed that the pillar had also been replaced with the same material. The laboratory result confirmed that the rock was different, being much stronger than typical pyroxenite, with an extremely high Young's modulus. The pillars to the east of the site shown in Figure 5-15 did not appear to have been replaced to the same degree, if at all. To the west of the site, only one relatively small, iron rich pegmatoid pillar was left and behind this pillar was the ledge and centre-raise. The nearest pillars on the other side of the raise were more than 20 m from the site. It would therefore appear that the pillar was stronger than the adjacent pillars and the higher modulus would have attracted a higher stress. Observations indicated that before the instrumented pillar failed, the adjacent pillars were shielded. It was only after failure of the instrumented pillar that the others showed a significant increase in stress fracturing.

"Crush" pillars in that area were normally cut at dimensions of 4 m on dip and strike. The instrumented pillar was 5 m on strike and 3 m on dip. The reason for this unusual configuration was that the machinery used to install some of the instrumentation was unable to extend more than 1,5 m to install at the centre of the pillar.

The Zafer load cell appears to have recorded a failure well before the other instruments, see Figure 5-20 and Figure 5-18. On exactly the same day that this failure occurred, the vibrating wire stress cell, shown in Figure 5-19, started to record a stress change. Other instruments, including the flat jacks, also recorded a stress change on that date, the results of which have been included in the technical document. It appears that a section of the pillar where this instrument was located failed on that date, transferring the stress to other parts of the pillar. A similar event appears to have occurred on 30 January 1997, see Table 5-7 and Figure 5-19, indicating that sections of the pillar failed at different times. These findings, as well as the variation in stress measurements and observations made during drilling, indicate that there was a variation of strength within the pillar. However, the measured stress drops could also have been the result of progressive failure due to uneven loading.

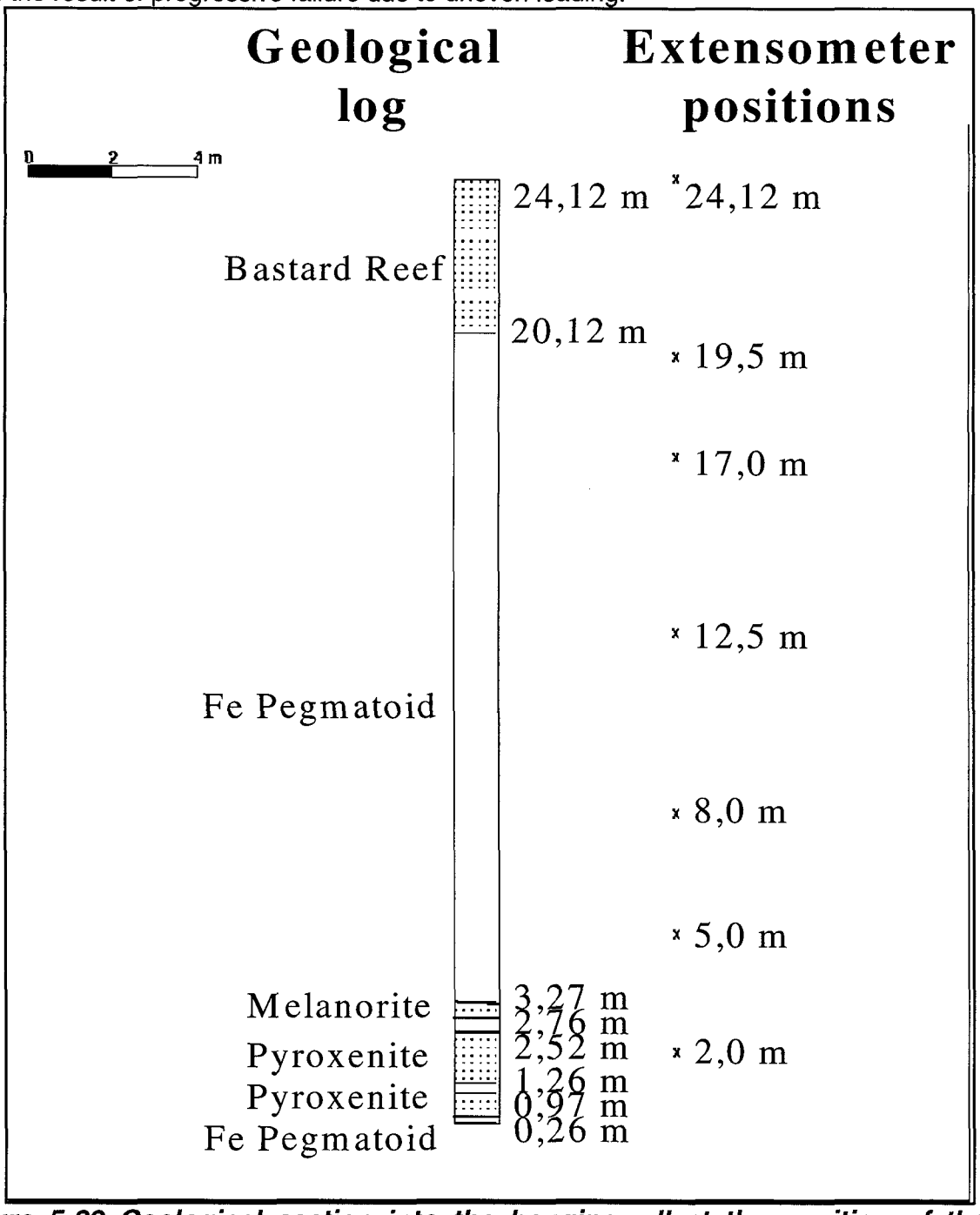

Figure 5-22 Geological section into the hangingwall at the position of the E2 extensometer.

The final failure of the pillar on 5 February 1997 was recorded by all the instruments that were operating, including the Zafer load cell, which showed a slight stress increase, Figure 5-20. The phenomenon of stress decrease measured by some instruments while other instruments record an increase indicates that stress was transferred from one part of the pillar to another. Stress transfer would have occurred if the region to where the transfer was taking place was at a lower stress, validating the earlier recorded pillar failure in that region of the pillar by the Zafer cell, Figure 5-20. These findings have promoted confidence in the instrumentation results. After the failure, the P2 doorstopper (Figure 5-18) recorded a slight increase in stress, which quickly levelled out to 107 MPa.

Doorstopper P3, which was installed near to and in-line with the flat jacks, appears to have been affected by the slot. The recorded stresses, which are shown in the technical document, were very much higher and the readings became unstable just before the pillar failed, indicating that the end of the hole had fractured and perhaps the instrument was detached. Drilling speeds indicated that there was a variation in rock properties near the slot, which could have resulted in highly stressed zones affecting the P3 results. The drilling appears to have confirmed the variation of rock properties within the pillar.

The vibrating wire stress cell, Figure 5-19, dropped back to the original field stress after the pillar failure, indicating that it had stopped functioning properly. These instruments measure deformation of a borehole and it could be expected, therefore, that, if shearing occurred on either side of the cell, the section of hole where the cell was installed might not have been affected by any changes. Most of the instruments measured a gradual stress increase between May 1997 and August 1997, and this was also reflected by P2 (Figure 5-18) but to a much smaller degree. It is assumed that certain zones within the pillar may have re-compacted sufficiently to allow stress regeneration in those zones. This view was substantiated by the observed corresponding increase in confinement, measured by some of these instruments.

The results of P2, Figure 5-18, are assumed to be most representative of the stress at the centre of the pillar, because of the following reasons:

1) location of installation,
2) agreement with the residual stress recorded by the Zafer load cell,
3) agreement with observations (Table 5-7), and
4) consistent, good correlation between the gauges on the instrument.

Observations of fracturing in boreholes PB1, PB2 and PB3 were used in conjunction with the pillar extensometer results to determine the size of the intact core of the pillar at various stages of loading. The area of the intact core was divided by the total area of the pillar and the result used to reduce the recorded stress of P2 to reflect the average pillar stress up to failure, as shown in Figure 5-23. The pillar extensometer showed a slightly smaller intact core than was estimated from the observations. Figure 5-24 records strains of 23 mε between 1,023 m and 1,259 m, and 13,5 mε between 2,494 m and 2,745 m into the pillar at failure. These large strains indicate that failure had occurred between those anchors. The intact core could therefore have been between 1,24 m and 1,76 m, which reduced the average pillar strength (APS) to between 85 MPa and 121 MPa. The pillar strength, estimated by using the observed stress fracturing (recorded in Table 5-7), was slightly higher. After failure, stress fracturing was observed to have progressed right through the pillar, which was confirmed by the extensometer (Figure 5-21). Therefore, it was difficult to determine the stress distribution and to analyse the residual stress. The post failure values recorded in Figure 5-23 and in the text below were modified by the same factor used to determine the failure stress. The residual strength was calculated to be between 41 MPa and 58 MPa. The APS and post failure strength values should be used with caution for designing crush pillars, bearing in mind that the instrumented pillar was atypical.

Observations made in the borehole camera holes indicated that most of the fracturing developed in a direction parallel to the length of the pillar. Even after the pillar had failed, fracturing was only observed to a depth of 0,15 m in PB3, whereas the other holes showed

fracturing throughout the pillar. This indicates that a two-dimensional computer model could be used to simulate the conditions.

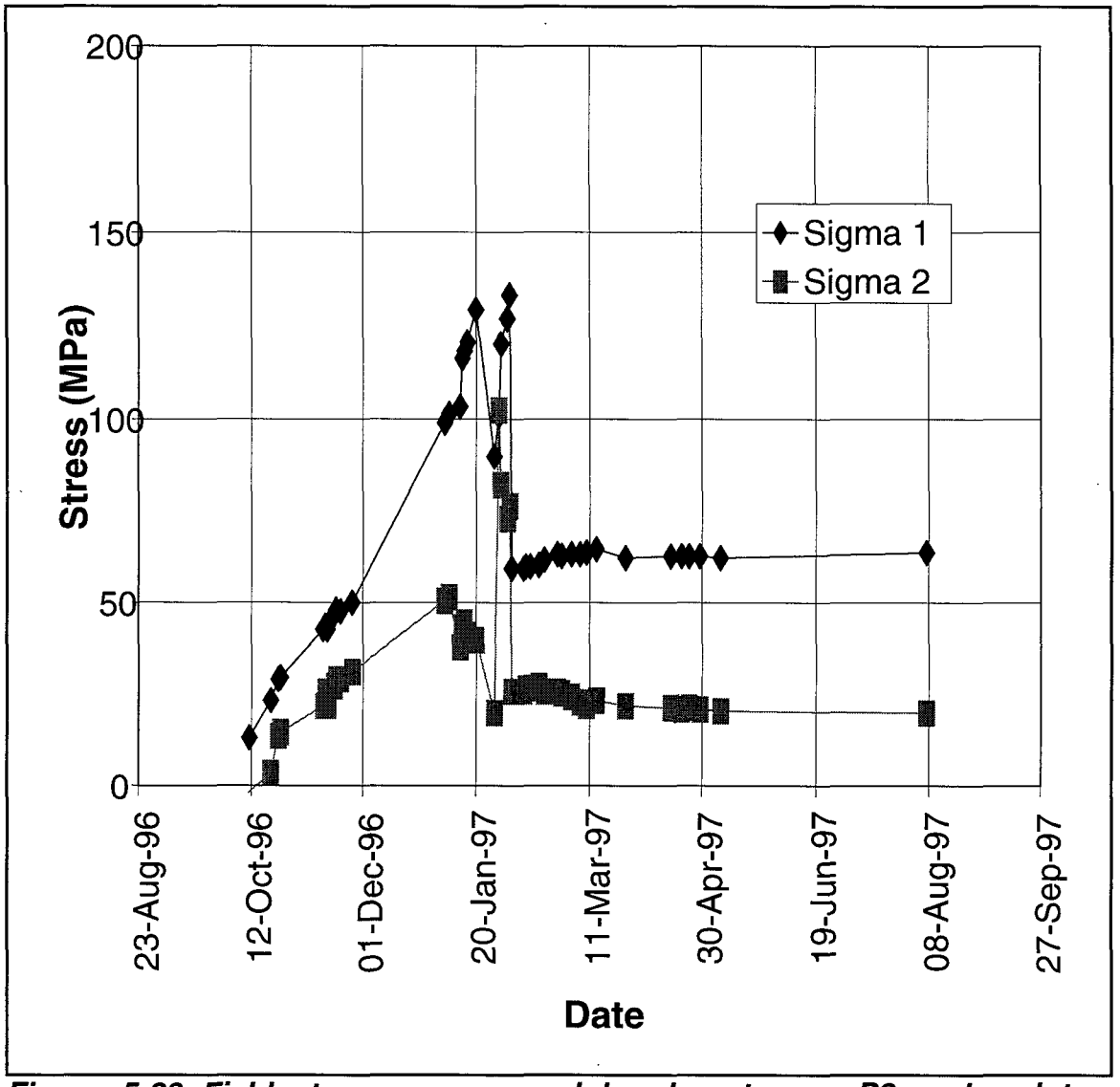

Figure 5-23 Field stresses measured by doorstopper P2, reduced to reflect average pillar stress.

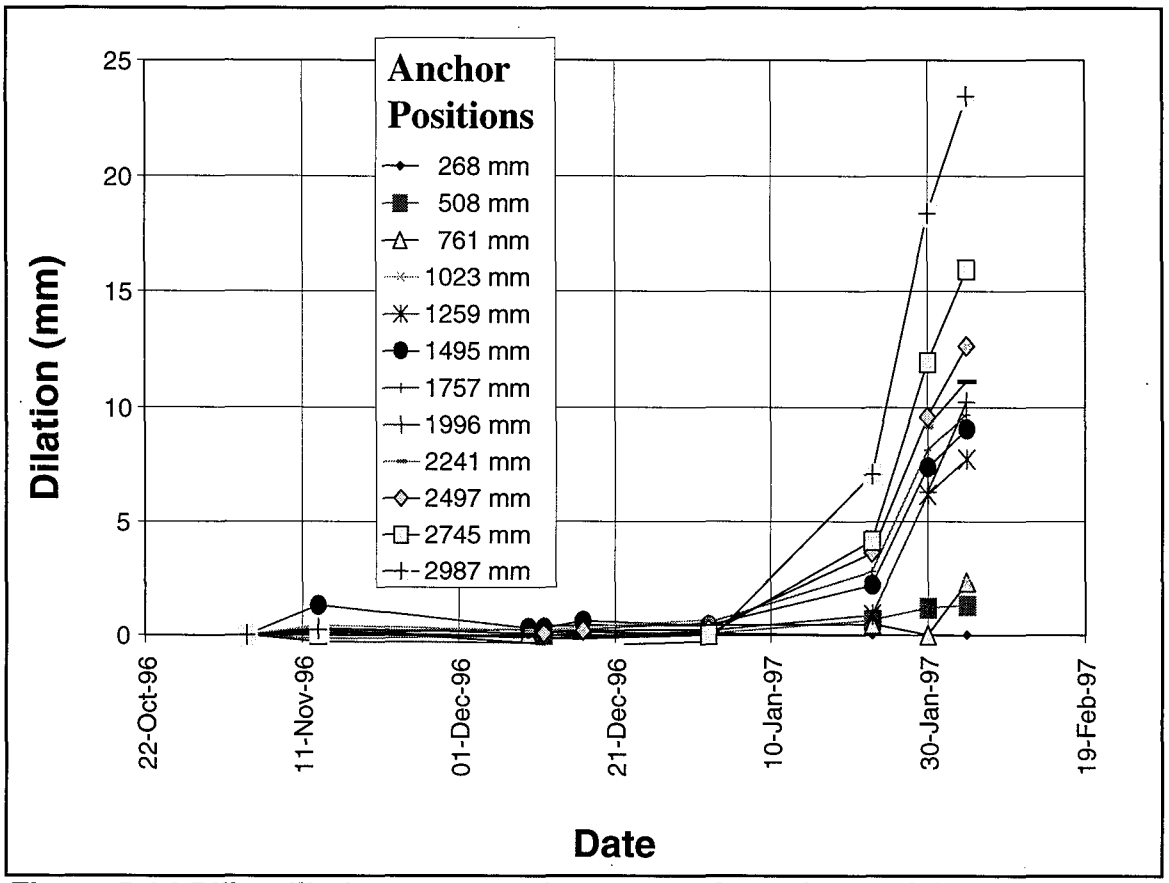

Figure 5-24 Pillar dilation measured up to the date of pillar failure.

5.7.5 Conclusions

The results of the experiment were atypical because the pillar dimensions and rock type were unusual and therefore the APS and post failure strength should only be used as a guide for designing crush pillars.

The APS was based on evidence regarding the size of the intact core, and was calculated to be between 85 MPa and 121 MPa. Criteria for determining the stress distribution through the pillar after failure was difficult to ascertain and therefore the same factor used to reduce the failure strength was also used on the residual strength. Based on this analysis the residual strength was between 41 MPa and 58 MPa.

Stress fracturing within the pillar appears to have developed in a direction parallel to the long axis of the pillar. Very little fracturing was observed across the short axis of the pillar, indicating that a two-dimensional computer model could be used to simulate conditions.

5.8 Back analysis of pillar performance at Impala Platinum Mine

The Merensky Reef pillar system, with pillars measuring 3 metres wide by 6 metres long, has a peak strength of 150 MPa at a strain of 5.4 millistrains. This was based on the back analysis of underground measurements using the MINSIM-W and FLAC computer programmes. In addition to the pillar strength, Mohr Coulomb and strain softening parameters were determined for use in FLAC, thus enabling the pillar performance curve to be generated up to the peak strength of 150 MPa.

The hangingwall (pyroxenite) of the Merensky Reef is stronger than the footwall (anorthositic norite). This was confirmed by underground observations where fracturing of the footwall occurred but not the hangingwall.

A majority of the stope closure occurred as footwall lifting. This occurred because loading of the pillars induced higher horizontal stress in the footwall between the pillars. This stress caused the footwall to move upwards into the stope. The footwall 4 contact, being a cohesionless mud parting, provided the boundary along which opening occurred allowing an upward buckling of the footwall into the stope.

Contrary to conventional wisdom, load shedding can occur in these rock types at a width to height ratio of 5:1. This was also reported by Spencer and Kotze (1990), based on the violent failure of pillars having width to height ratios of 5:1.

Pillar failure occurs as a yielding process into the footwall. The opening up of the footwall 4 contact occurs at a point on the pillar performance curve when the stress and strain values are 132 MPa and 1.6 millistrains respectively.
A large difference in the amount of footwall heave was noticed between two locations in the same panel, that were approximately 35 m apart in the strike direction. This was attributed to the variable joint conditions. Localities of greatest footwall lifting corresponded to areas of increased intensity of jointing.

However, in spite of this progress two uncertainties remain:
1) Why the discrepancy between the calculated strengths for 3 metre pillars of 150 MPa and 200 MPa (Lougher 1994) and a weaker strength of 100 MPa reported for five metre wide pillars (Kotze, 1974)?
2) As pillar failure did not occur, what form does the post failure curve take and what is the residual strength?

Full details of this work are supplied in Appendix D.

5.9 Examples

Example 5-1 Elastic pillar design – good rock mass conditions

Problem

It is required to design an elastic pillar system at a depth of 250 m. The parameters for the pillar design are provided in Table 5-9.

Table 5-9 Input data for pillar design problem – good rock mass condition

Parameter	Value	Parameter	Value
Young's modulus, E	70 GPa	UCS	145 MPa
Poisson's ratio	0,2	assumed f_c	0,7
geometry	9 pillars, 10 panels	joints striking on reef strike	0,5 jts/m dip = 80°
depth	250 m	joints striking on reef dip	1 jt/m dip = 80°

stoping width	1,4 m	panel span (from Chapter 3 or Chapter 4, or from other mining constraints)	30 m
contact friction angle (see Section 4.11)	25°	Safety Factor	1,6
(1-a) determined in the laboratory	0,35	rock mass density, ρ	3000 kg/m^3

Solution

First guess of pillar dimensions:
It is required that the extraction ratio be greater than 90 per cent. The first guess pillar dimensions are 6 m on strike by 3 m on dip. Holings will be 2 m wide.

The next step is to determine the average pillar stress (Block B in Figure 5-13).

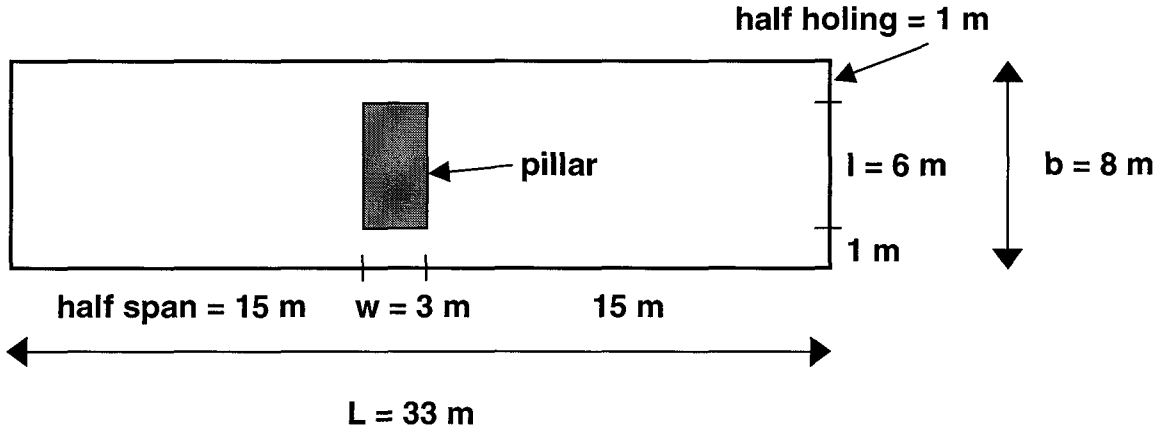

Figure 5-25 The basis of the calculation of tributary area theory load.

For the dimensions of pillar length (l), pillar width (w), and panel span, a representative pillar unit area is as shown in Figure 5-25. The given dimensions are shown in the diagram. Using the symbols in Figure 5-25, the extraction ratio (e) is thus:

$$e = \frac{Lb - wl}{Lb}$$ ***Equation 5-10***

and, 1-e is:

$$1 - e = \frac{wl}{Lb}$$ ***Equation 5-11***

The average pillar stress (APS) is calculated as follows:

$$APS = \frac{\sigma_v}{1-e} = \frac{\rho g D}{wl/Lb}$$ ***Equation 5-12***

where σ_v = the vertical component of the virgin stress field,
ρ = the assumed rock mass density,
g = acceleration due to gravity, and
D = depth of mining.

Substituting into Equation 5-12, $APS = \frac{3000.10.250}{3.6/33.8}$ = 110 MPa.

This figure should be adjusted for the loading system characteristics discussed in Chapter 2. For nine pillars, pillar width = 3 m, span = 30 m, and D=200 m (Figure 2-13), the APS is 87 per cent of the tributary area theory load . The change in percentage of the tributary area theory load with depth is shown in Figure 2-14 for the 5 m width pillars. The change from a

depth of 200 m to 250 m for the span = 30 m curve involves a change of about 1 per cent. Thus the more accurate APS = 110 x 0,87 x 0,99 = 95 MPa.

Alternatively, detailed numerical modelling may be performed. Section 2.5 contains useful information that should be considered when performing numerical modelling of shallow to intermediate depth mine layouts.

Next, the pillar strength is determined.

The value of 1-a was determined to be 0,35 in the laboratory (Block C in Figure 5-13).

To determine Θ_c (Block C in Figure 5-13):

From Equation 5-7, $f_{UCS} = 1/[1-(0,6)(1-a)] = 1/[1-(0,6)(0,35)] = 1,27$.

From Equation 5-8, $\Theta_c = f_{UCS} \times f_c \times UCS = (1,27)(0,7)(145) = 129$ MPa.

w/h = 3 ÷ 1.4 = 2,1.

Effect of contact conditions (Block D in Figure 5-13):

Good contacts; contact friction angle was determined as 25° (by means of the methodology presented in Section 4.11.

From the relation shown in Figure 5-11, the value of 1-a for the underground contacts is 0,41.

Pillar strength, taking contact friction and critical rock mass strength into account (Block E in Figure 5-13):

From Equation 5-6, $S_c = \Theta_c[a + (1-a)(w/h)]$

$= 129[0,59 + (0,41)(2,1)]$

$= 187$ MPa.

Determine joint reduction factor, f_j (Block F in Figure 5-13):

For the strike joint set (strike of joint set coincides with strike of reef):

w/h 2,1 ≈ 2; frequency = 0,5 joints / m; dip = 80°

from Figure B-1 in Appendix B, $f_{js} = 0,93$ (by interpolation)

For the dip joint set (strike of joint set coincides with dip of reef):

w/h = 6 ÷ 1.4 ≈ 4; frequency = 1 joint / m; dip = 80°

from Figure B-3 in Appendix B, $f_{js} = 0,90$ (by interpolation)

Total effect of jointing, $f_j = f_{js} \times f_{jd} = 0,93 \times 0,90 = 0,84$.

Pillar strength (Block G):

$S_a = S_c \times f_j$

$= 187 \times 0,84$

$= 157$ MPa.

Check safety factor (Block G in Figure 5-13):

S.F. x APS = 1,6 x 95 = 152 MPa.

pillar strength ≥ S.F. x APS → criterion in Block H in Figure 5-13 is satisfied.

PILLAR DESIGN IS SATISFACTORY

STOP

Example 5-2 Elastic pillar design – poor rock mass conditions

Problem

The input data is the same as in Table 5-9, as used in the previous example, except that the rock mass conditions differ. The strike joint set has a frequency of 2 joints / m, dipping at 70°. The dip joint set has a frequency of 3 joints / m, dipping at 75°.

Solution

First guess pillar width:

The pillar width is now revised to 4 m (compared to 3 m in the previous example).

Pillar APS (Block B in Figure 5-13):

The increase in pillar width results in L = 34 m, w = 4 m (see Figure 5-25).

Substituting into Equation 5-12, $APS = \frac{3000.10.250}{4.6/34.8}$ = 85 MPa.

Referring to Figure 2-13, the proportion of tributary area theory loading for 3 m pillars is 87 per cent, and for 5 m pillars 91 per cent. By interpolation, the proportion of tributary area theory loading carried by the 4 m wide pillar is 89 per cent. Figure 2-14 results in a further decrease of about 1 per cent. Thus the more accurate APS = 85 x 0,89 x 0,99 = 75 MPa. Alternatively, detailed numerical modelling may be performed. Section 2.5 contains useful information that should be considered when performing numerical modelling of shallow to intermediate depth mine layouts.

Pillar Strength:

Θ_c and 1-a (Block C in Figure 5-13):

these are unchanged from the previous example

Θ_c = 129 MPa

1-a = 0,35

w/h = 4 ÷ 1,4 = 2,9

Θ_c and in situ *1-a are the same as in the previous example (Block C in Figure 5-13):*

1-a = 0,41

Θc = 129 MPa

Pillar strength, taking contact friction and the critical rock mass strength into account (Block E in Figure 5-13):

From Equation 5-6, $S_c = \Theta_c[a + (1-a)(w/h)]$

$= 129[0,59 + (0,41)(2,9)]$

$= 229$ MPa.

Determine joint reduction factor, f_j (Block F in Figure 5-13):

For the strike joint set:

w/h 2,9 ≈ 3; frequency = 2 joints / m; dip = 70°

from Figure B-2 in Appendix B, $f_{js} = 0,72$

For the dip joint set (strike of joint set coincides with dip of reef):

w/h = 6 ÷ 1.4 ≈ 4; frequency = 3 joints / m; dip = 75°

from Figure B-3 in Appendix B, $f_{js} = 0,73$

Total effect of jointing, $f_j = f_{js} \times f_{jd} = 0,72 \times 0,73 = 0,53$.

Pillar strength (Block G):

$S_a = S_c \times f_j$

$= 229 \times 0,53$

$= 121$ MPa.

Check safety factor (Block G in Figure 5-13):

S.F. x APS = 1,6 x 75 = 120 MPa.

pillar strength ≥ S.F. x APS → criterion in Block H in Figure 5-13 is satisfied.

PILLAR DESIGN IS SATISFACTORY

STOP

Example 5-3 Crush pillar design

Problem

Mining is to be at a depth of 650 m. The panel spans are set at 30 m. The stoping width is 1,2 m. Determine the pillar width that would allow crushing of the pillar, assuming the pillar strength curve provided in Figure 5-14.

Solution

First guess: a pillar width of 4 m. This implies w/h = 3,3. Starting at the Depth axis in Figure 5-14, going up to the 4 m pillar width line, and reading across to w/h = 3,3, it can be seen that this pillar is predicted to be in an elastic state (point A).

Second guess: pillar width = 3 m. In this case, w/h = 2,5, and point B is arrived at. This pillar is predicted to crush.

5.10 Conclusions

A new pillar design rationale has been produced, that depends on an engineering understanding of the primary factors that influence pillar strength. This understanding has enabled the definition of design charts for each influencing factor. These charts have been incorporated into a pillar design flowchart, to aid in the simple and practical application of the design charts (see Figure 5-13).

The main influences on pillar strength, and the factors that have been investigated are:
1) w/h
2) the effect of the contact conditions
3) strength of the pillar material
4) the effect of jointing.

Design charts have been produced, or methodologies described, for each of the above factors. The methodologies are general, and are suited to hard rock pillar design in any geotechnical area. Laboratory testing is an important component of the first three factors mentioned above.

The downgrading factor (f_c) to account for the reduction of strength with increasing volume from laboratory scale (50 mm) to *in situ* scale is of the order of 70 per cent, for Merensky Reef. It is likely to be similar for other hard rock reefs. An approximate methodology has been provided to determine this value (the critical rock mass strength). Once the critical rock mass strength been obtained, no volume effects need to be catered for in design. In this case, the linear function has been shown to perform as well as the power formula, to account for the effect of w/h.

Laboratory testing of model pillars may underestimate the effect of w/h on *in situ* pillars, due to the "weak" contact conditions at the sample / platen interface in the laboratory. To account for *in situ* contacts, an *upgrade* of strength will, in most cases, be required.

An initial crush pillar design methodology has been produced, in the form of a simple flowchart (see Figure 5-14). The load portion of the flowchart takes account of the loading system. The strength curve may be drawn by the designer on the basis of pillar strengths at his / her particular mine, according to the methodology presented in Figure 5-13.

The results of the back analysis of the Impala data showed that the Merensky Reef pillar system, with pillars measuring 3 metres wide by 6 metres long, has a peak strength of 150 MPa at a strain of 5.4 millistrains. This was based on the back analysis of underground measurements using the MINSIM-W and FLAC computer programmes. The pillar system yielded as a result of the footwall heave.

Worked examples have been included to show the use of the design charts and the design flowchart in practical examples.

5.11 References

Bieniawski, Z.T. 1968a. *In situ* large scale tests on square coal specimens measuring 2 meters in width. *CSIR report MEG 694.*

Bieniawski, Z.T. 1968b. The compressive strength of hard rock. *Tydskrif vir Natuurwetenskappe*, vol. 8, no 3/4:163-182.

Esterhuizen, G. S. 1993. Variability considerations in hard rock pillar design. *Proc. SANGORM Symp.: Rock Engineering Problems Related to Hard Rock Mining at Shallow to Intermediate Depth*, Rustenburg.

Esterhuizen, G.S. 1997. The effect of discontinuities on the strength of pillars in coal mines. *Ph.D. Thesis.* Pretoria: University of Pretoria.

Galvin, J.M. Hebblewhite, B.K. Salamon, M.D.G. 1996. Australian coal pillar performance. *International Society of Rock Mechanics News Journal*, Vol. 4 No. 1.

Hedley, D.G.F. and Grant, F. 1972. Stope-and-pillar design for the Elliot Lake Uranium Mines. *CIM Bulletin*, July.

Hoek, E. and Brown, E.T. 1988. The Hoek-Brown failure criterion-a 1988 update. *Proc. 15th Canadian Rock Mech. Symp.,* University of Toronto.

ITASCA Consulting Group, Inc. 1991. UDEC Universal Distinct Element Code, Version 1.7.

Kotze, T.J. 1974. A report on the collapse that took place in the 4 shaft area of Bafokeng South. Impala Platinum Internal Report.

Lougher, D.R. 1994. An in situ investigation into the behaviour of the surrounding rock mass in a hard rock pillar mining environment. *M.Sc Dissertation.* University of the Witwatersrand, Johannesburg.

Mark, C. and Barton, T. 1996. The uniaxial strength of coal : should it be used to design pillars? *15'th Int. Conf. On Ground Control in Mining*, Ozdemar *et al* (eds.), Golden, Colorado.

Özbay M.U. and Roberts M.K.C. 1988. Yield pillars in stope support. *Rock Mechanics in Africa*, Sangorm Congress, Swaziland.

Ryder, J.A. and Özbay, M.U. 1990. A methodology for designing pillar layouts for shallow mining. *ISRM Symp. : Static and Dynamic Considerations in Rock Engineering*, Swaziland.

Salamon, M.D.G. and Munro, A.H. 1967. A study of the strength of coal pillars. *J. South Afr. Inst. Min. Metall.,* September.

Spencer, D. 1997. April progress report on SIMRAC. *GAP 024*, 6

York G. and Canbulat I. 1998. The scale effect, critical rock mass strength and pillar system design. *J. South Afr. Inst. Min. Metall.,* vol. 98, no. 1 Jan/Feb.

6 A design methodology for the bearing capacity and the yielding of foundations of hard rock pillar systems

6.1 Introduction

This chapter addresses Enabling Output number 8 (see page 13).

It has been acknowledged that the behaviour of a pillar system depends on the strength of the pillar material as well as of its surrounding rock mass. The design of a pillar support system requires therefore a good understanding of the pillar foundation system behaviour.

In a study of the mechanisms that lead to the failure of the foundation system in a planar ore-body type of mining environment, the following parameters, which are believed to be the most influential, were investigated:

- the mining geometry
- the stress environment
- the profile of vertical stress distribution at the contact between the pillar and the foundation
- the depth and frictional properties of major parting planes.

This chapter presents an investigation into the stability of the foundation system using FLAC analysis (Cundall, 1995). The stability is captured in three key parameters: the yield stress, the closure at yield stress and the maximum closure at full load. The study describes principal failure mechanisms, and then presents design charts, which underpin the suggested design methodology. Examples on the usage of the design charts are presented.

6.2 Literature review

The bearing capacity failure of foundations as described by Özbay and Ryder (1989) can take place in many ways depending on the strength, thickness and location of any weak strata within the roof or the floor.
In practice, different modes of failure can be encountered:

- Pillar failure due to foundation deformation: this occurs when a brittle pillar rests on a plastic foundation. The pillar can be weakened due to the induced horizontal shear -tensile traction or loss of width to height confinement due to slip on weak parting planes.
- Stable pillar punching into the foundations: this is the second mode of failure whereby the weaker part of the foundation fails due to the pillar foundation loading. The footwall heave and some movement of the gully sidewalls often accompany this failure mechanism.
- Unstable pillar punching into the footwall: this failure mode is usually associated with seismic events and involves the shearing of the pillar into brittle foundation material accompanied by large hangingwall collapses.

This study concentrates on the second mode of pillar failure, which commonly occurs in mines in the Bushveld Complex.

The literature reveals that few studies aimed at a fundamental, theoretical or experimental understanding of the bearing capacity of the foundation in mining structures have been conducted in the past. After completing many compression tests on quartzite material using a steel punch in the laboratory, Wagner and Schümann (1971) presented a stamp-load bearing

strength theory which states that the foundation fails when the average pillar stress is four times the uniaxial compressive stress (UCS) value of the rock material. However, Özbay and Ryder (1989) showed that the failure of the footwall foundation occurs at a lower average pillar stress (APS) of about three times the value of the UCS. Before failure, a phase of inelastic deformation is observed at an APS value about equal to the UCS of the footwall.

Wagner and Schümann suggested the use of the stamp-load bearing tests to study the strength of rock under triaxial conditions that appear to be similar to the foundation bearing capacity problem in hard rocks. According to the qualitative model, they depicted the mechanism of failure of rock under stamp loads schematically as shown in Figure 6-1.

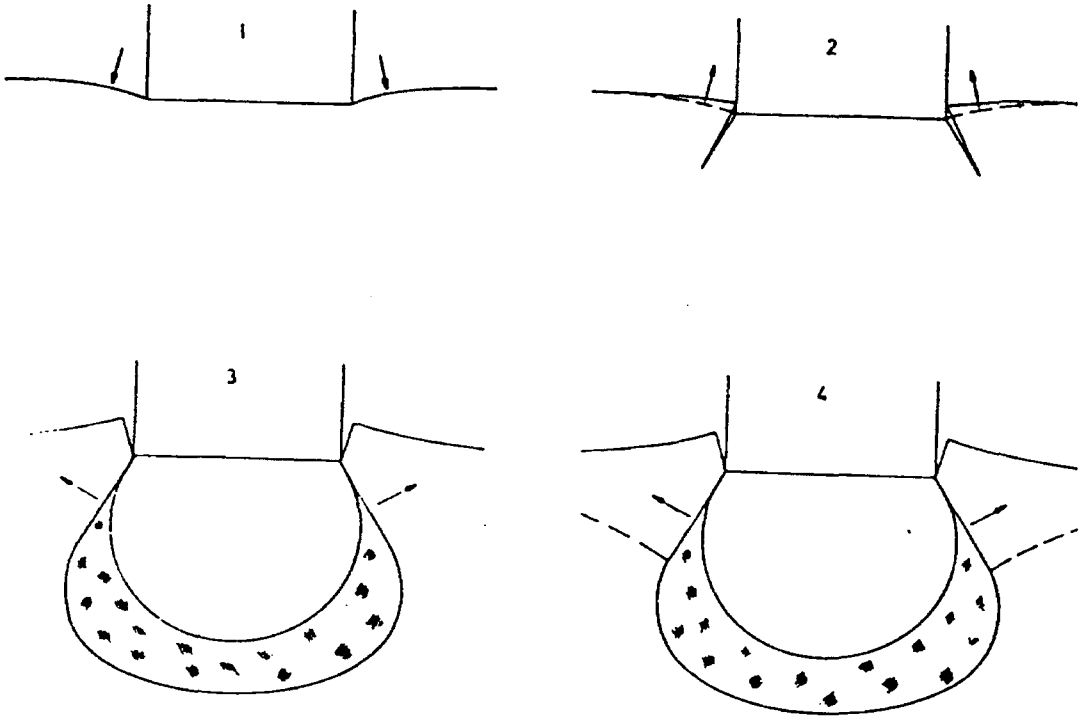

Figure 6-1 Failure mechanism of rock under stamp load (after Wagner and Schümann, 1971).

The initial loading in step 1 shows the elastic behaviour of the foundation. Step 2 shows a tensile ring crack starting at the edge of the stamp. As the load increases, the surface moves slightly upwards and becomes destressed. This phenomenon is known as elastic rebound of the surface. With further increase in load, step 3 starts with the failure of the foundation under compression followed by a volumetric expansion in the direction of the minimum principal stress. Due to this lateral expansion, the surface moves upwards and the surface strain changes from tensile to compressive. In step 4, a rapid increase in volumetric expansion is witnessed and failure of the rock specimen is observed.

It is noteworthy that the well-known civil engineering method of Terzhaghi is sometimes used in mining engineering for the calculation of the bearing capacity of underground structures. There are three main problems associated with the use of this method:

- The first is the loading of pillars, which is much more complex than the loading of a footing.
- The second problem is that the method assumes a homogeneous foundation.
- The third is that the method assumes associated plasticity, while rock exhibits non-associated plastic flow.

Because of these differences in foundation behaviour and properties, it was decided to examine the problem using numerical modelling.

6.3 Research Methodology

6.3.1 Pillar foundation geometry

The behaviour of the pillar foundation system has been investigated using the numerical modelling approach as a result of many and interacting variables, which have to be taken into account. The yield stress, which is reported as bearing capacity, the closure at the yield stress and the maximum closure were the three outputs. To simulate the entire behaviour of the pillar foundation system, 1600 FLAC runs were performed.

The mining layout modelled consisted of excavations in a tabular ore body repeatedly supported by a pillar system, as shown in Figure 6-2.

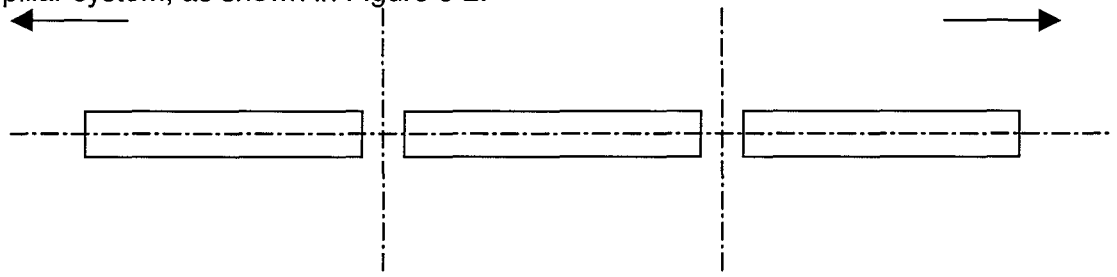

Figure 6-2 Tabular excavation ore body.

Assuming planes of symmetry along the stope horizontal centre line and the pillar vertical centre line, the geometry of the model can be reduced to a quarter of the pillar foundation system, as presented in Figure 6-3. The model representing the above-described situation, and yielding the best representation of the theoretical load and convergence distribution, was fixed in the x direction at both sides and a stress boundary was applied in the y direction at the bottom boundary, with the relative dimensions as shown in Figure 6-3. The height of the model was set to about double the width as suggested by Özbay and Ryder (1990) and Cook *et al* (1984). A stress boundary condition was applied in the y direction at the bottom of the model to take into consideration the initial stress conditions.

By increasing the span and keeping the width of the pillar constant, four different ratios of s/w namely 6,7, 14, 25,5 and 35,4 were generated, giving rise to four different geometries. This range of ratios allows the analysis of pillar foundation systems in steps with spans ranging from about 11,8 m to 59,4 m for a four m pillar. The parting was assumed to be horizontal, with no cohesion. Only one parting was modelled at a time, but this was positioned at three different depths into the footwall. Table 6-1 summarises the input parameters.

Table 6-1 Input parameters.

Variable	*Symbol*	*Values*			
ratio of span to pillar width	s/w	6,7	14	25,5	35,4
depth of parting (m)	h	1 (parting1)	2 (parting2)	3 (parting3)	s*
k-ratio	k	0	0,5	1	1,5
depth of mining (m)	D	400	600	800	1000
parting friction angle (º)	N, Phi	0	15	30	45

s* = standard case without parting.

The type of pillar stress profile was the last variable to be investigated to assess its impact on the bearing capacity and closure. Elastic and inelastic pillars were therefore studied.

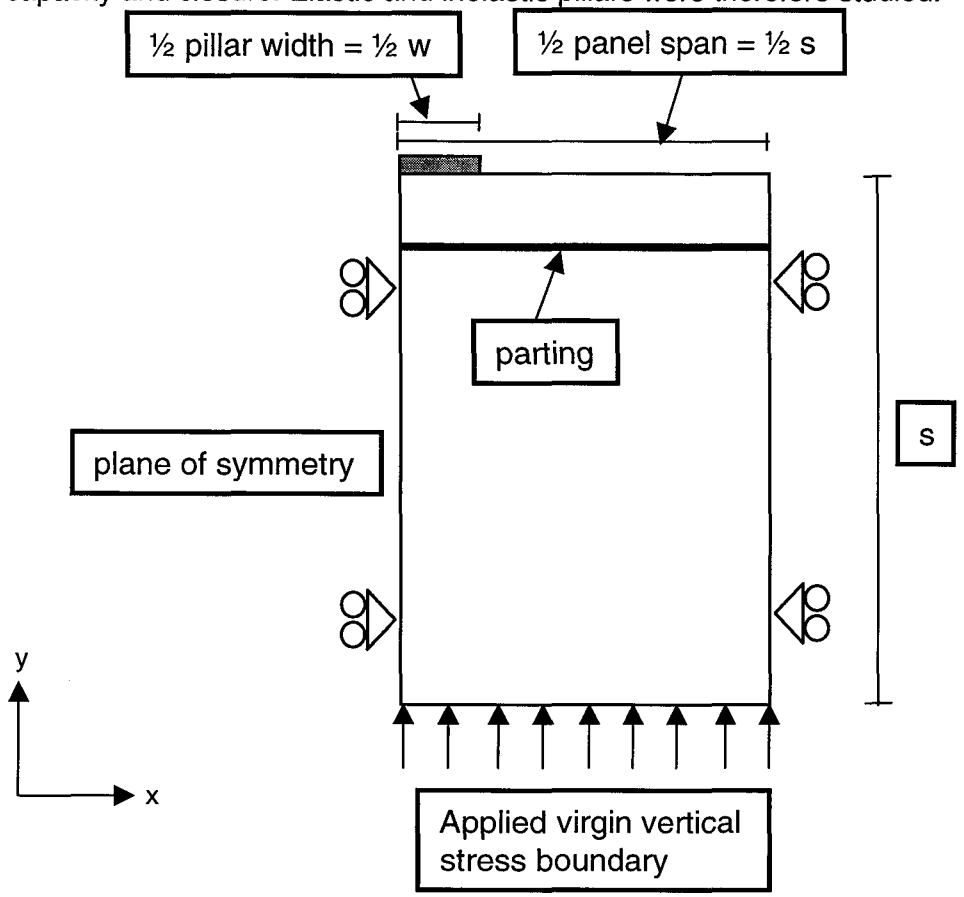

Figure 6-3 Model geometry: two dimensional cross section of pillar and panel geometry (after Kabeya* et al, *1997).

6.3.2 Bearing capacity determination

The bearing capacity assessment is based on the failure mechanism of rock under a stamp-load test that assumes four distinct steps, as suggested by Wagner and Schümann (1971). During the third step in Figure 6-1, there is a substantial growth of fractures from the edges of the stamp towards the centre line which leads to an increase in volume of the rock. In the stress-displacement curve sketched in Figure 6-4, the contact of these fractures at the centre line coincides with the yield point, for which its earliest localisation appears to be very important.

The analysis of the pillar foundation system was based on the above conceptual stress-displacement curve. The yield stress was defined as the stress at which the developing fractures contact with the vertical centre line of the pillar foundation system. The yield stress is determined at the end of the third step in the failure process in Figure 6-1.

The yield stress value will always be less than the value corresponding to the ultimate bearing capacity which in fact would bring the entire system to complete failure. It is acknowledged that the yield stress, which is reported as bearing capacity, is conservative.

The Mohr-Coulomb failure criterion was used for the FLAC analysis, and the material properties in the first row in Table 6-2 were used during the numerical modelling.

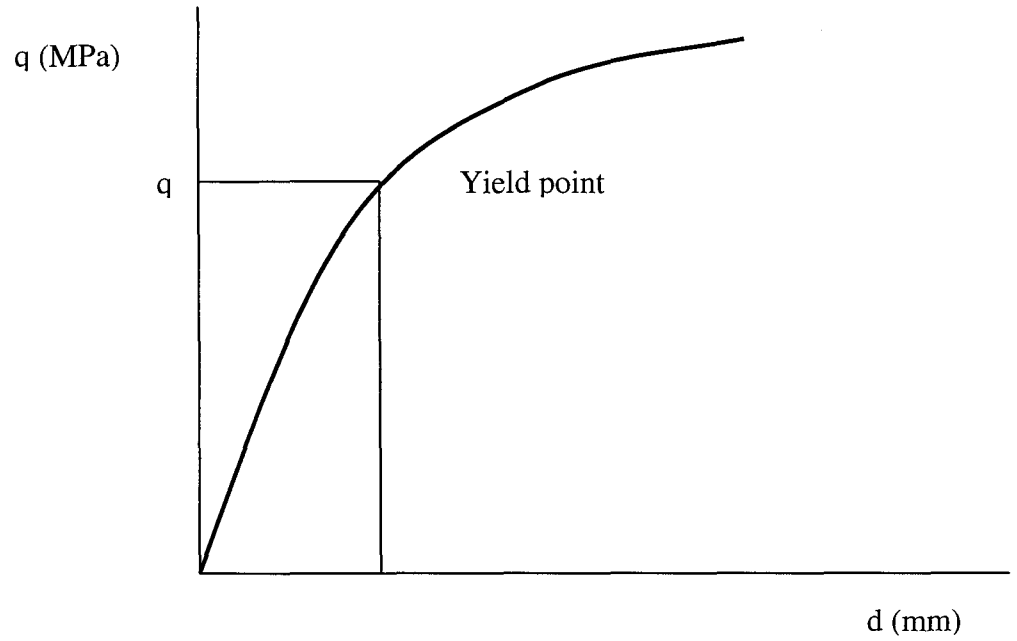

Figure 6-4 Stress-displacement curve.

Table 6-2 Material properties.

Bulk modulus (GPa)	*Shear modulus (GPa)*	*Cohesion (MPa)*	*Friction angle*	*Tensile strength (MPa)*
34,4	25,8	38 MPa	41º	10
34,3	29,1	35 MPa	51º	-

The material properties were chosen to model the pillar foundation system in the Bushveld Complex platinum mines, and therefore they may not be appropriate for other hard rock mining situations. However, a slight difference in the closure behaviour may be expected to be observed for a typical 200 MPa UCS quartzite, for which material properties are given in the second row in Table 6-2.

6.4 Results

6.4.1 Discussion of failure mechanisms

Four modes of failure were identified during the investigation. Weak partings parallel to the stope are the major contributing factor to the failure mechanism as sketched in Figure 6-5.

The compressive load on the pillar results in a buckling of the whole pillar foundation system, which depends on the stiffness of the system. The stiffness of the system is influenced by factors such as the span to pillar width ratio (s/w) and depth of parting (h).

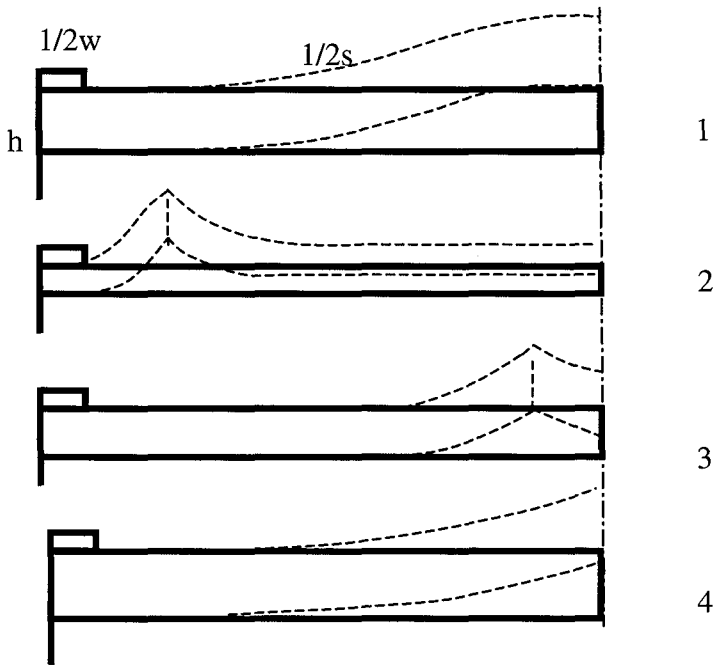

Figure 6-5 Failure mechanisms.

Mechanism 1: The buckling has two distinct curvatures and the maximum deformation is reached at the mid-span. The stiffness of the system appears to be less influenced by the ratio s/w than the depth of parting, which results in a high rigidity in the vicinity of the pillar. This mode of failure is dominant for pillar foundation systems with greater parting depths, including the standard case where there is no parting.

Mechanism 2: The buckling results in maximum deformation in the vicinity of the pillar. In this case the rigidity of the pillar foundation system in the vicinity of the pillar is much softer and is unable to transmit the load to the parting. This mechanism has been mostly observed for closer partings such as parting 1,1 m into the footwall.

Mechanism 3: The buckled parting has its maximum deformation in the middle third of the span. The rigidity of the pillar foundation system in the vicinity of the pillar is higher than in Mechanism 2, allowing the transmission of the load to the parting. This is the case where the s/w and h parameters are both in the middle of their ranges. Most of this type of failure was observed for the case where the parting was modelled 2 m into the footwall.

Mechanism 4: Similar to the first mechanism in terms of stiffness of the system, this mode of failure is characterised by a single curvature of the beam plate. The maximum deformation is much larger than in Mechanism 1, and is also reached at mid span. Parting 3 has displayed this type of failure and thicker partings are expected to behave this way, especially over 1000 m depth.

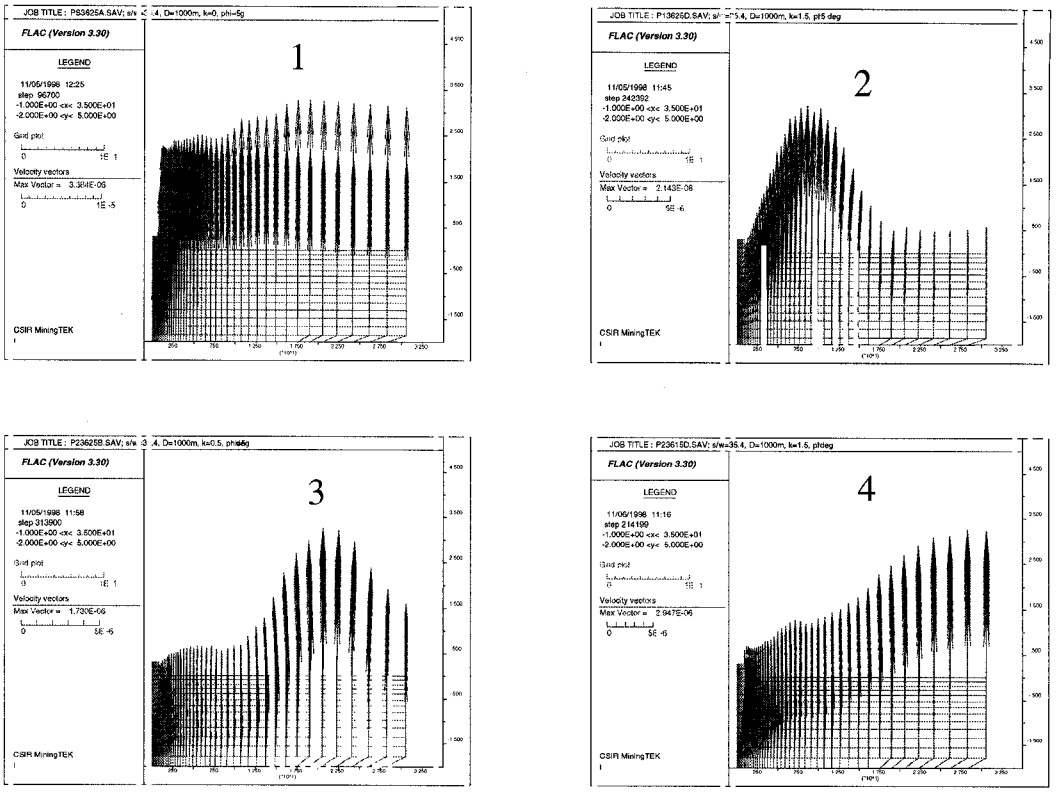

Figure 6-6 Failure mechanisms as shown by FLAC plots of velocity vectors.

Although the geometry of the pillar foundation system (defined by s/w and h) are the most influential parameters in determining the mode of failure, the other defined parameters also play a role. As a result, different failure mechanisms to those described above may occur, for the same geometry when there is a change in k-ratio, depth or friction angle.

6.4.2 Pillar foundation design methodology

6.4.2.1 Implications of closure for support design

The presentation of the closure design charts in two steps, namely the closure when the yield stress is reached and the maximum closure after full load transfer, has been very useful in terms of providing simple criteria for support design.

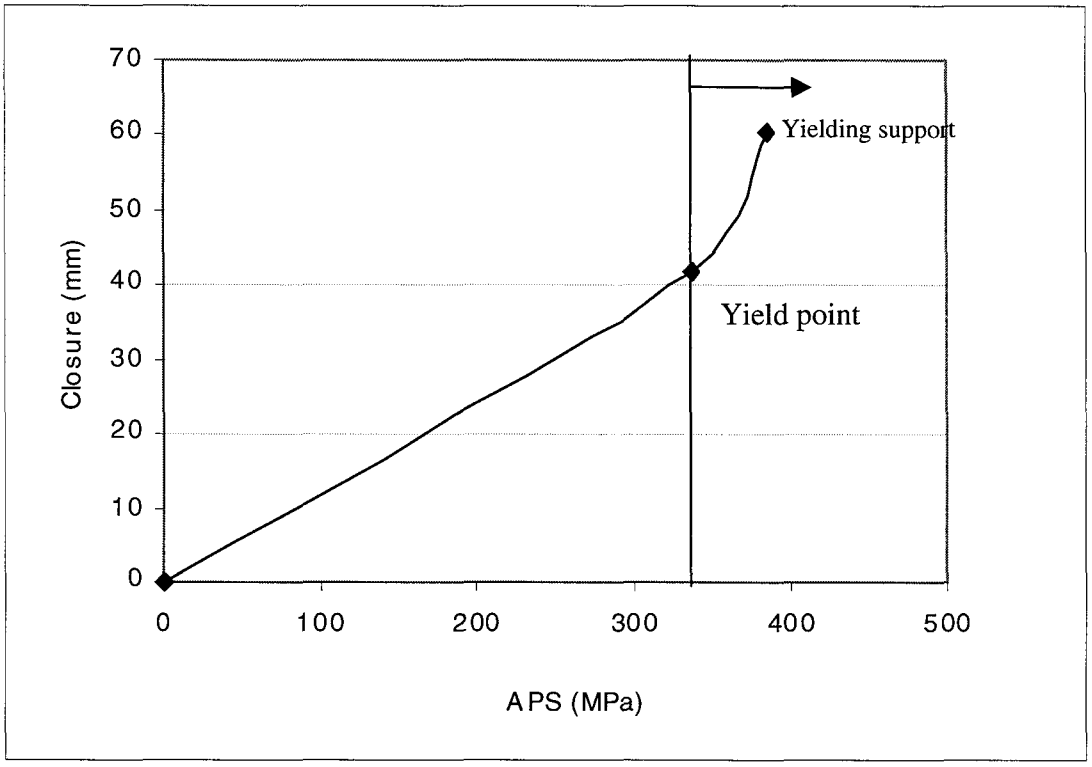

Figure 6-7 APS versus closure: yield point.

From the APS versus closure curve given in Figure 6-7, the yield point can be easily determined. In this case, the yield stress is 347 MPa for a closure of 42 mm at mid-span. The yield point is defined by the acceleration of closure due to the increase of load. Before this yield point, the deformation increases in a linear manner with an increase of the load. For the purposes of this report, the yield point has been termed the bearing capacity.

The determination of the yield point has an advantage in terms of defining the zone where only the yielding support must be used as shown in Figure 6-7. Before the yield point, the use of stiff support and yielding support is possible, depending on the allowable closure that the support element is able to carry. This then leads to the use of the charts, shown in the following section, as design tools.

6.4.2.2 Bearing capacity and closure design charts

The rock mechanics practitioner can choose between one of three design outputs:

- the foundation bearing capacity,
- the closure at the yield point of the foundation,
- the closure at full load that the foundation will bear (a function of geometry and depth).

It has been found that the radar chart was the most efficient way of representing the large number of input variables. A radar chart can be defined as a circular chart where each variable has its own value axis radiating from the centre point. Lines are then used to connect all the values in the same series. A typical example is given in Figure 6-8. On this chart, the bearing capacity is represented as a function of k-ratio (k) depth of mining (D), ratio of panel span to pillar width (stoping width), depth of parting (h) and friction angle (phi, or N).

The axis of reference is vertical. This axis is used to scale the output variable, which in this case is the bearing capacity. In Figure 6-8, the bearing capacity varies from 0, at the centre of the chart, to a maximum of 900 MPa at the outer circle of the chart. Each concentric circle corresponds to a value of the bearing capacity. In the case where the output is the closure, the values represent the total closure for the hangingwall and footwall because of the symmetry.

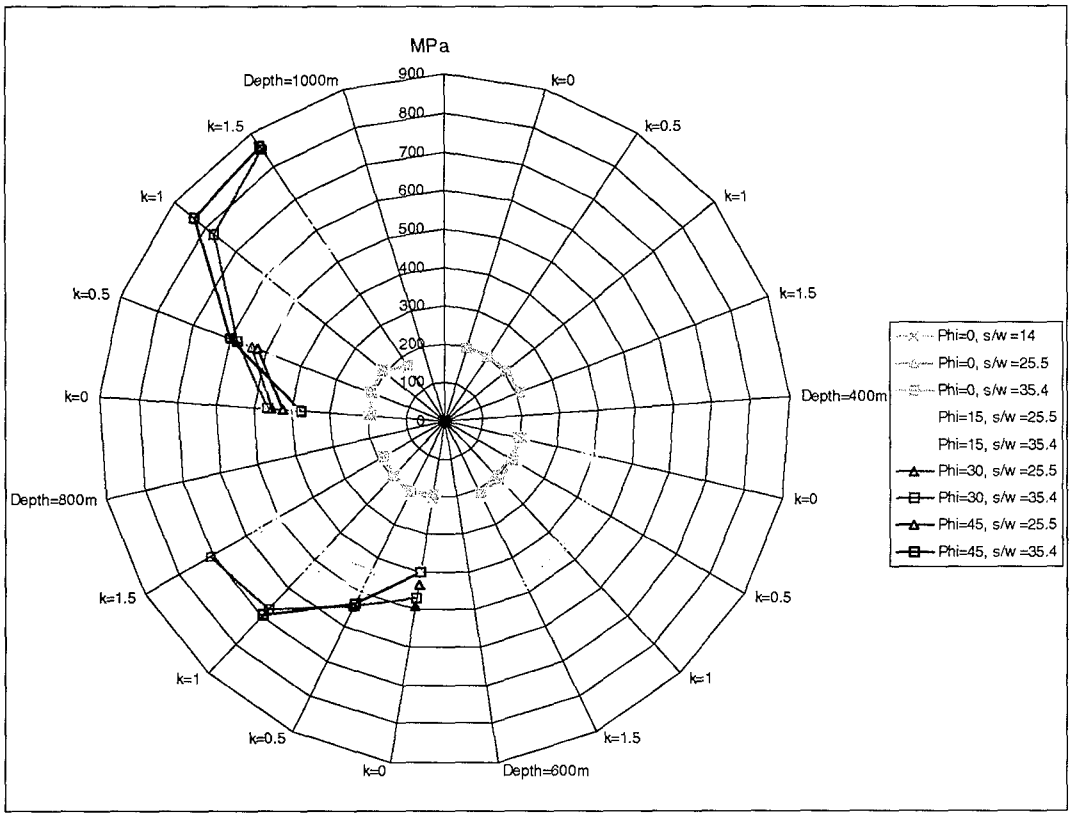

Figure 6-8 Typical bearing capacity design chart (h=1).

Each of the four sectors represents a depth, starting clockwise from the axis of reference. Four different radii, k=0, k=0,5, k=1 and k=1,5, indicate the change in k-ratio for each specific depth of mining. For clarity, a radius "Depth=400m" on the chart separates the first and second mining depth. Another parameter is the friction angle of the interface N, which is read off directly on the chart using different colour curves. Lastly, different point symbols represent the parameter s/w. The colour-point marker scheme is defined as described in Table 6-3.

For instance, a blue line marked with squares in the fourth quadrant would signify the following parameters: D=1000 m, s/w=35,4, N=45º, while the squared purple line in the first quadrant refers to the same s/w=35,4 but for a different friction angle and depth: N=0º, D=400 m respectively.

Table 6-3 Design chart colour – point marker scheme.

			s/w (Marker)			
			Diamond	Cross	Triangle	Square
Friction angle phi (colour)	0	Purple	6,7	14	25,5	35,4
	15	Red	6,7	14	25,5	35,4
	30	Green	6,7	14	25,5	35,4
	45	Blue	6,7	14	25,5	35,4

Many of the combinations of variables did not result in the yielding of the foundation. These are therefore not plotted. About 35 percent of the combinations yielded.

The influence of k-ratio on the bearing capacity is well depicted in Figure 6-8. The bearing capacity increases with k-ratio at all depths.

For the same depth, the bearing capacity increases with the interface friction angle, N. The bearing capacity generally increases with s/w but a decreasing trend was noticed for the lowest friction angle, N=0°. Tables of bearing capacity values for different partings are given in the Internal Note 98-0411. The bearing capacity varies between 1 to 5,2 times the UCS value.

The foundation design charts are presented in Figure 6-9 and Figure 6-10 where the output parameter is the closure corresponding to the bearing capacity and the maximum closure after the complete load transfer to the pillar respectively. Similarly to the bearing capacity chart, the closure chart provides the closure value as a function of known input parameters. The colour–marker scheme is the same. In Figure 6-9, the closure generally increases with the k-ratio, the depth of mining and the interface friction angle. For any parting depth, the investigation involves 256 runs.

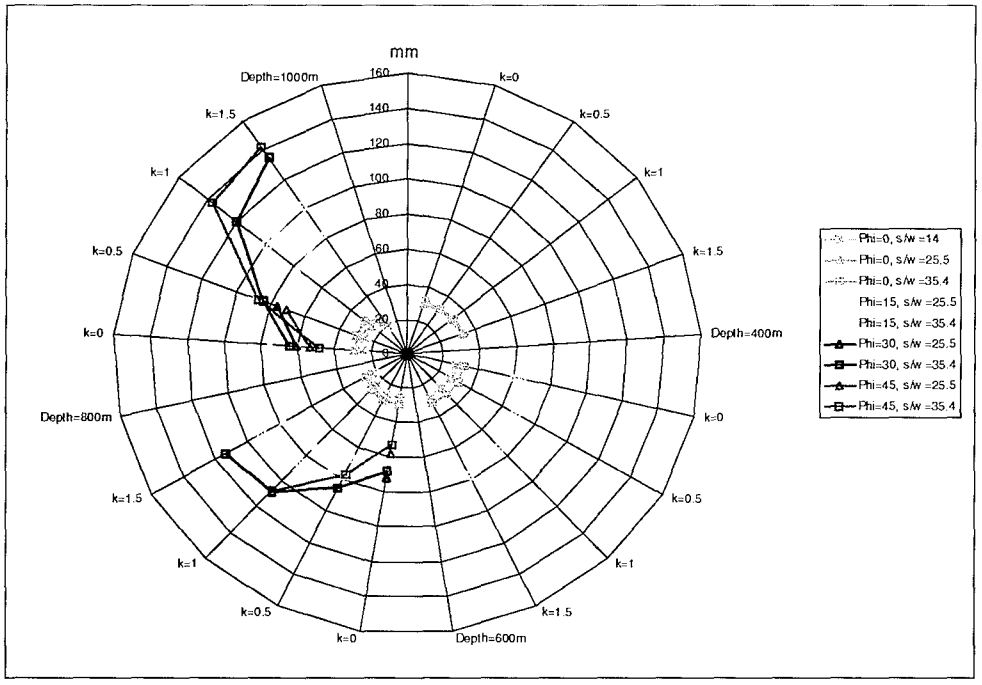

Figure 6-9 Typical closure chart (h=1) at foundation yield point.

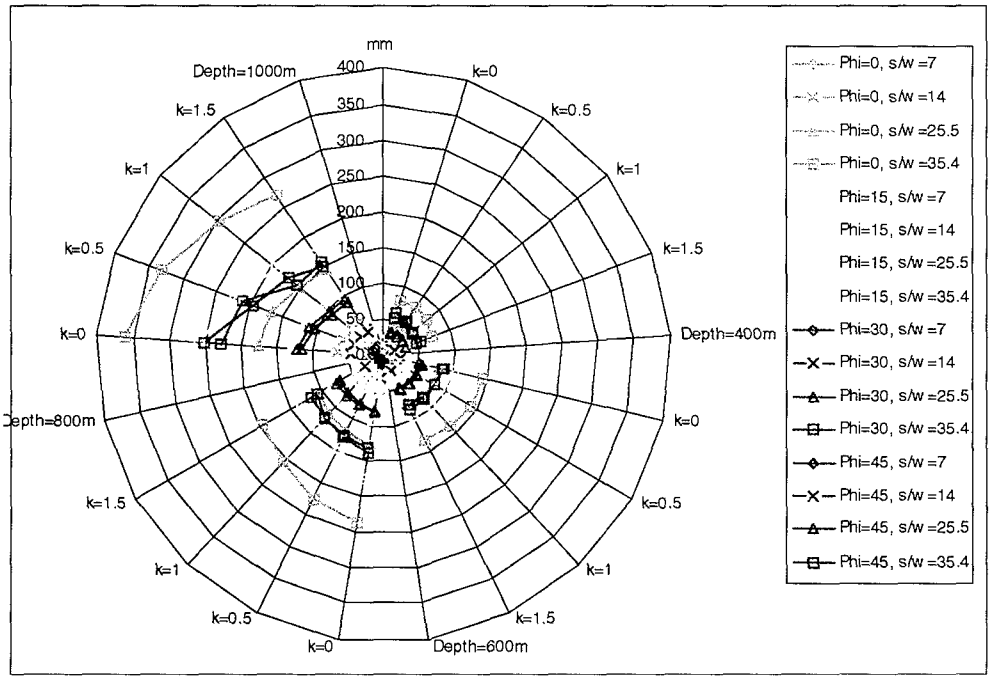

Figure 6-10: Typical maximum closure chart A (h=1) at full load.

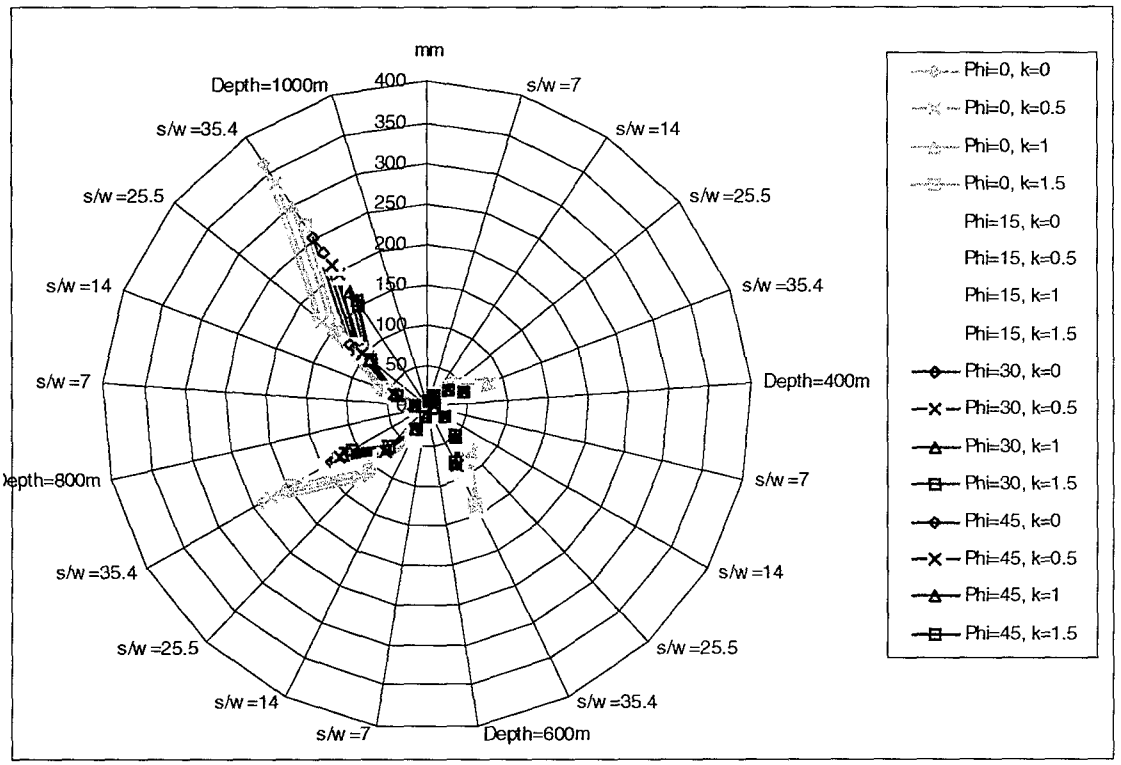

Figure 6-11: Typical maximum closure chart B (h=1) at full load.

An example of another form of the design charts, where s/w is represented on the radii, is presented in Figure 6-11. The colour–point marker scheme is similar with only one difference. The different symbol represents different k-ratio values in the following sequence: diamond is equivalent to k=0, cross represents k=0,5, triangle relates to k=1 and square shows k=1,5.

It can easily be read on the chart in Figure 6-11 that the maximum closure increases with the depth of mining and decreases with an increase in the interface friction angle. The full set of closure charts is presented in Appendix C. In order to facilitate the reading of charts for closures less than 150 mm, such as in Figure 6-10 and Figure 6-11, a few zoomed versions are provided in Appendix C.

6.4.2.3 Influence of the pillar vertical stress profile

It is well established that the pillar stress profile for a pillar behaving elastically shows a stress increase from the centre line to the edge of the pillar where the stress concentration is at its maximum. In the case of inelastic failure of pillars, this profile changes because of the inelastic behaviour of the fractured periphery of the pillar.

An assessment of the effect of the type of stress profiles on the bearing capacity and closure, by comparing the elastic and inelastic pillars, has shown that elastic pillars fail at a higher bearing capacity than inelastic pillars. The range of variation varies from 0 to a maximum of 40 percent. The closure at the yield stress increases from 0 to a maximum of 50 percent from elastic to inelastic pillars. The maximum closure has shown the same trend as the closure at yield stress, but a higher range of variation from 0 to more than 100 percent has been witnessed, especially at a higher s/w.

6.4.2.4 Examples: bearing capacity and closure

Example 6-1 Footwall stability: decision on the requirement for yielding support

Problem

Mining conditions in a particular mine are as follows: depth of mining, D=800 m; k-ratio, k=1,0; ratio s/w=25,5; parting friction angle. N=15º; parting depth, h 1 m. The pillar is known to deform elastically.
Choose the suitable type of support element.

Solution

With the above conditions, the APS is calculated as follows:
APS = Φ_v / 1-e = Δ g D / 1-e = 3000* 10 * 800 / (1-24,5/25,5) = 612 MPa
Using the chart in Figure 6-8, the yield stress q is about 460 MPa.
As the APS > q, the APS point on a graph similar to Figure 6-7 would be in the right portion of the curve. Therefore, a yielding support is recommended.

6.5 Case Study

An underground instrumentation programme was conducted at Impala Platinum mines in order to improve pillar design by monitoring pillar behaviour. The final SIMRAC report of the project GAP 024 issued in November 1995 contains the details of the entire study, from which some data relating to closure have been extracted. The project site was located at 12 shaft, Bafokeng North Mine at depths between 593 m and 644 m below surface. The mining layout consisted of 27 m to 30 m long panels with a system of 3 m wide by 6 m long pillars running parallel to strike gullies. In one case, the closure measured next to a pillar was 53 mm, while 40 mm was recorded at mid span in a nearby panel. This has confirmed the pillar punching effect resulting in the footwall lifting.

Referring to the mode of failure described in this report in Figure 6-5, mechanism 2 (see Section 6.4.1) appears to be the most likely to have occurred. However, the mud parting had the following properties: D=600 m, h=3 m, s/w = 10, c=0 MPa, N=0º. Assuming that k=1, the maximum closure, using the relevant design chart, at mid span gives a value of 30 mm (s/w=14). This is lower than the 40 mm measured, but the small difference could be accounted for by movement on inclined joints which is not accounted for in the current modelling.

6.6 Optimisation of the design methodology using closure for the design of yielding elongate support

The design methodology that is described below presupposes that the mining layout consists of tabular excavations repeatedly supported by a pillar system, such as previously shown in Figure 6-2. The additional input parameter is the allowable closure Y_a^* . This is determined by the type of yielding support available in the market and other considerations, such as design philosophy, which differs from mine to mine, and cost issues.

6.6.1 Design methodology

The aim is to design the foundation system in such way that the maximum stope closure (Y_m), controlled by the pillar foundation system, is between 90 to 100 percent of the allowable closure (Y_a^*) for the support element. The optimised value of foundation closure assumed here is 90 percent of the yield capacity of the support. This is subject to the discretion of the rock

mechanics practitioners at each mine. If, for example, a particular yielding support unit has a high variability of yield capacity, then the rock mechanics engineer may decide that 85 percent is a better optimal value. Another option is to design for a range in which the maximum of the range is less than the yield of the support, for example, design the foundation such that the closure falls between 75 percent to 90 percent of the yield capacity of the support. This provides a safety factor. An iterative process is used to determine the optimal value of s/w for the given allowable support deformation (Y_a^*), by following the design flow chart in Figure 6-12

Figure 6-12 is a flow chart depicting the design methodology. The starting point is the choice of the smallest s/w and the best estimate of k-ratio. The first test separates the flow chart into two legs: parting and no parting cases. Following the "no parting" leg, the first reading of the maximum closure, Y_m, using the design chart for the standard case, is made and checked against the allowable closure, Y_a^*. If the maximum closure is greater than the allowable closure, s/w must be decreased and the process must be repeated, or a different type of yielding support is chosen which can accommodate the closure. If not, the test of optimisation is processed, whereby the maximum closure must be between 90 and 100 percent of the allowable closure.

From the outcome of this second test, the design can be stopped in the case where the answer is yes, or alternatively s/w can be increased to a new value for a second iteration of the process.

In the case where there is a parting, h and N must be determined. Thereafter another reading of a new maximum closure, Y_m', using the appropriate design chart, will be made. Similarly to the first leg, the two tests are processed and the decision taken as shown in Figure 6-12.

The design process can then be summarised as follows:
1) Determine the supportable span and the width of the pillar in order to define s/w.
2) Determine the bearing capacity and check if the foundation can sustain it.
3) Determine the stope closure using the appropriate chart.
4) Check if the support unit can tolerate the closure. If this is verified, the design stops. If not, the support unit is changed or, as a last resort the pillar design modified.

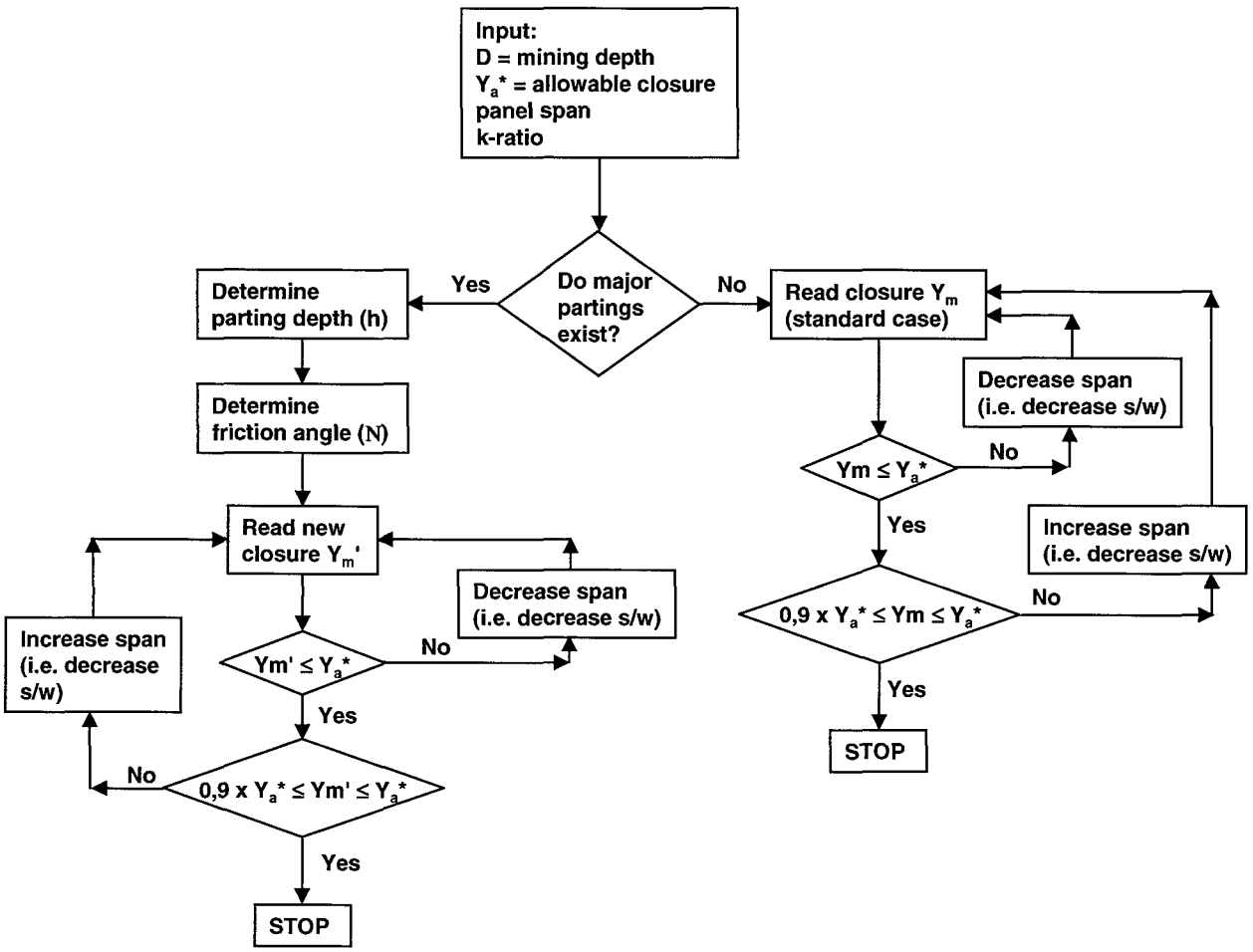

Figure 6-12 Optimisation design flow chart for closure of the footwall to aid in the design of yielding support.

6.6.2 Examples: Optimisation of foundation design to account for elongate support yield capacity

Example 6-2 Footwall design optimisation to cater for yielding support capacities: footwall with no partings

Problem

Determine the geometry of the pillar foundation system knowing that the mining depth is 1000 m. The yielding support allows a closure of 40 mm (Timber pole support).

Solution

A. Assuming that the rock mass does not have parting
First choice of s/w = 6,7, using the design chart for the standard case in Figure 6-13, the maximum closure for k=0,5 at 1000 m is 15 mm (Y_m = 15 mm).
The allowable closure (Y_a^* = 40 mm) is greater than the maximum closure (Y_m = 15 mm).

As (0,9 x Y_a^* = 36 mm) > (Y_m = 15 mm), the foundation design is not optimised. The ratio s/w must be increased.

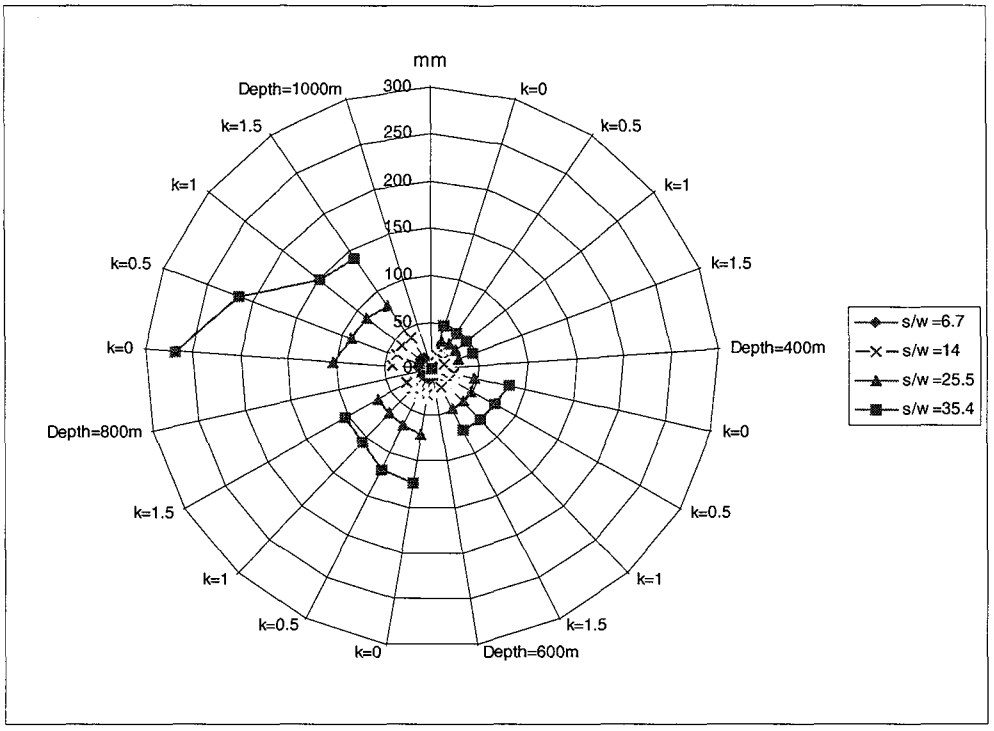

Figure 6-13 Closure: standard case (no parting).

For the second choice of s/w=14, the design chart gives 39 mm. The optimal allowable closure (0,9 * Y_a), is still less than the new maximum closure (Y_m = 39 mm), therefore this ratio can be accepted for this case.

Example 6-3 Footwall design optimisation to cater for yielding support capacities: footwall with a major parting

Problem

Assume that there is a parting at 1 m depth, (h = 1 m), k=0.5, and N=0º. The pillar deforms elastically.

Solution

First choice of s/w=25,5, from the design chart in Figure 6-10, the maximum closure, Y_m, for k=0,5 and D=1000 m, is 170 mm. The optimal allowable closure (0,9 * Y_a^* = 270 mm) is greater than the maximum closure, Y_m = 170 mm. The value of s/w must be increased.

For the second choice of s/w=35,4, the maximum closure, Y_m, is then about 340 mm. In this case, $Y_m > Y_a^*$, and therefore s/w must be decreased. A linear interpolation between the two s/w values, namely 25,5 and 35,4, gives the correct s/w of 31,3.

6.7 Laboratory testing of foundation yielding

In this chapter, the bearing capacity has been defined as the *yield point* of the foundation. At Western Deep Levels, back area stabilising pillar foundation seismic activity occurred at an average APS of 1,2 times the UCS of the foundation material. York (1998) demonstrated that this level of seismicity was associated with the yield of the foundation, rather than the ultimate failure of the foundation.

York (1998) also showed that the boundary conditions of laboratory tests can profoundly affect the ultimate bearing capacity, by means of numerical modelling. The ultimate bearing capacity

of foundations was shown to be potentially about ten times the UCS, in the case of stiff boundaries.

The ultimate bearing capacity of foundations is assumed to be about 2,5 times the UCS of the foundation material. Dede (1996) tested samples of Elsburg quartzite in a biaxial frame, with the loading sample geometry shown in Figure 6-14. Dede obtained strengths of about 2,5 times the UCS. The lateral confinement was applied by means of a pressure boundary. If the foundation begins to yield (by the formation of a Prandtl wedge), lateral dilation is expected to occur. A pure pressure boundary will offer little resistance to such lateral deformation, as the pressure pump will attempt to maintain a constant pressure. If the confining flat jack is sealed off during the course of the test (as was the case in the testing performed by Dede), then lateral pressure can build up. However, the jacks and hydraulic equipment would allow fairly non-rigid boundaries.

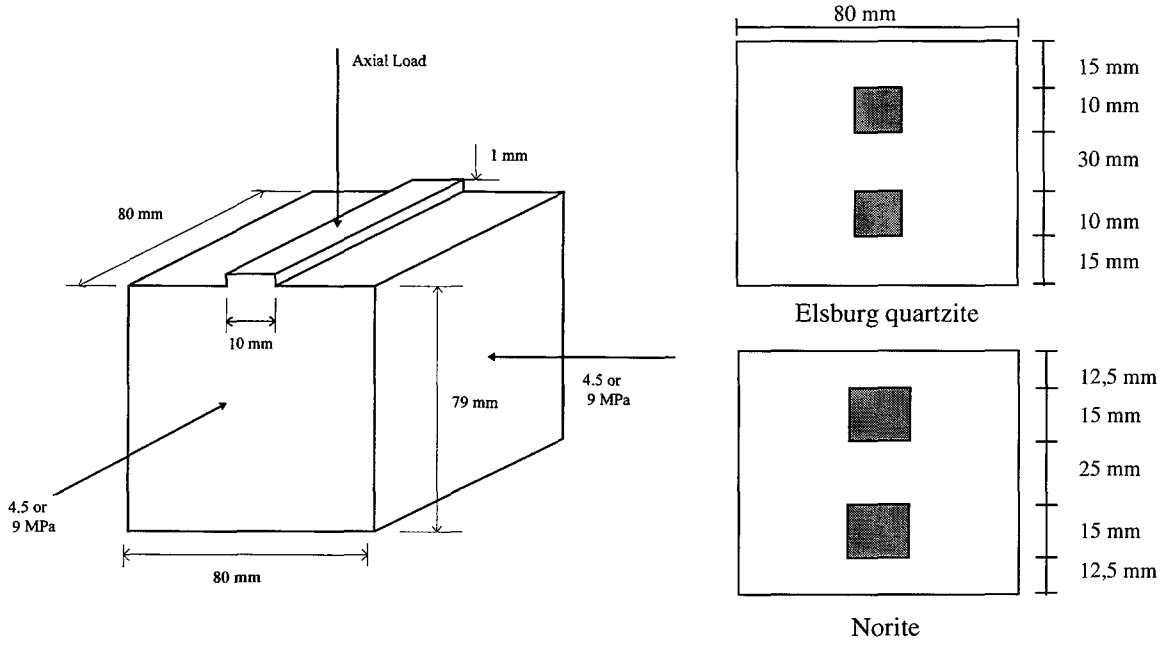

Figure 6-14 Geometry of sample (shown on left), with plan views of the square pillar geometry on the right.

In attempt to improve the boundary conditions, the hydraulic pressure system was replaced with a system whereby bolts were set into the circular frame that surrounds the sample. Lateral pressure was applied to the sample by tightening the bolts. In this way, the stiffness, compared to the hydraulic system, increased by a factor of about 10.

The increased stiffness led to dramatic increases in the ultimate bearing capacity of the Elsburg quartzite. The strength of the quartzite strip pillar geometry was almost doubled, to an average of 1108 MPa. This is about five to six times the UCS of the material.

However, the point of interest for design purposes is the yield point of the foundation, termed the bearing capacity. The bearing capacity is important, because this value will correspond to:
1) seismic activity in deep level gold mines with stabilizing pillars and deeper platinum mines
2) footwall heave in more shallow mines
3) a general worsening of conditions due an increase in regional closure.
The increase in regional closure could be understood in terms of a softening of the system. The rest of this section will focus on the yield point of the tests.

The square pillar geometry is shown on the right of Figure 6-14. A friction reducer, stearic acid, was applied to all four sides of the sample. Thus planes of symmetry were effectively constructed. Therefore, the geometries as sketched on the right of Figure 6-14 represent a

typical shallow mining layout with in-panel pillars. The gap between the pillars represents the holing between pillars, while the distance to the side represents a half panel span. The width of the quartzite pillars was 10 mm, while the width of the norite pillars was 15 mm (both strip and square pillars for both quartzite and norite).

The yield stress and corresponding axial displacement are shown Table 6-4. As may be seen, some of the tests were not repeatable.

Table 6-4 The scope and results of the tests in the testing programme

Details	Test no.	axial displ. (mm)	APS (MPa)
		Bearing capacity (yield point)	
Elsburg qtz.- 1 pillar	2004-100	0.92	700
	2004-200	0.88	744
	2004-300	0.92	675
	2004-401	1.16	765
	2004-501	1.08	748
	average	**0.99**	**726**
Elsburg qtz. - 1 pillar - parting 6.8mm	2001-502	1.35	828
	2001-503	1.20	628
	2001-700	1.08	778
	average	**1.21**	**745**
Elsburg qtz. - 2 pillars	2004-101	1.00	1175
	2004-201	1.25	1135
	average	**1.13**	**1155**
Norite - 1 pillar	201n101	0.84	703
	201n103	1.04	583
	average	**0.94**	**643**
Norite - 1 pillar - parting 7.2 mm	201n301	0.96	555
	201n302	0.80	560
	201n303	0.76	600
	average	**0.84**	**572**
Norite - 2 pillar (20*15)	201n401	0.84	945
	201n402	0.92	946
	201n403	0.88	880
	average	**0.88**	**924**
Norite - 2 pillar (20*15) - parting 7 mm	201n502	1.06	888
	201n503	0.86	688
	average	**0.96**	**788**
Norite - 2 pillar (20*15) - parting 10 mm	201n601	0.86	880
	201n602	0.80	800
	average	**0.83**	**840**

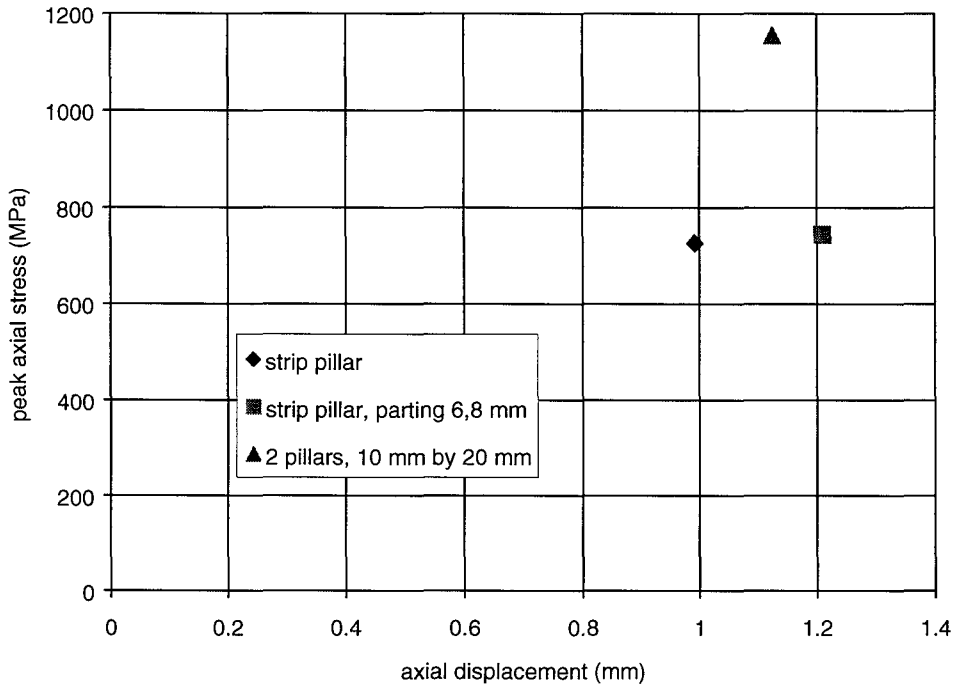

Figure 6-15 The APS and axial displacement at the yield stress for the quartzite samples.

The averages for the quartzite tests are shown in Figure 6-15. A number of observations may be made regarding Figure 6-15:

1) the bearing capacity of the square pillar geometry is significantly higher than that of the strip pillar geometry
2) the bearing capacity of the strip pillar with a parting is almost the same as that of a strip pillar with no parting, this with the parting depth about two-thirds of the pillar width
3) while the bearing capacities are similar for the strip pillar with and without a parting, the displacements are not, and the displacement increases by about 20 per cent in the presence of the partings.

The averages for the norite tests are shown in Figure 6-16. A number of observations may be made regarding Figure 6-16:

1) the bearing capacities of all three of the square pillar geometries are significantly higher than those of the strip pillar geometries, as is the case for the quartzite tests
2) the bearing capacity of the strip pillar with a parting shows a decrease compared to the strip pillar with no parting; however, as may be seen in Table 6-4, the results of the strip pillar with no parting were not repeatable, making this result inconclusive
3) in the square pillar geometries, the presence of a parting reduced the bearing capacity
4) a decrease in parting depth from 10 mm to 7.2 mm (ratio of parting depth:pillar width from two-thirds to about ½ respectively), results in a decrease in the bearing capacity.

The greater bearing capacity in the case of the square pillars is probably due to the three dimensional nature of the fracture patterns (a 2D strip pillar need only open two fracture "planes", while a square pillar must open four "planes" to cause failure of the foundation).

Both rock types show a relatively small difference between the bearing capacity for the cases of no parting and the case of a parting at a depth of about two-thirds of the pillar width. This agrees with the modelling results presented earlier in this chapter (for h = 3 m, corresponding to a depth = ¾ pillar width). A significant difference is seen (except in the case of the quartzite strip pillar) when the parting depth decreases to about ½ the pillar width.

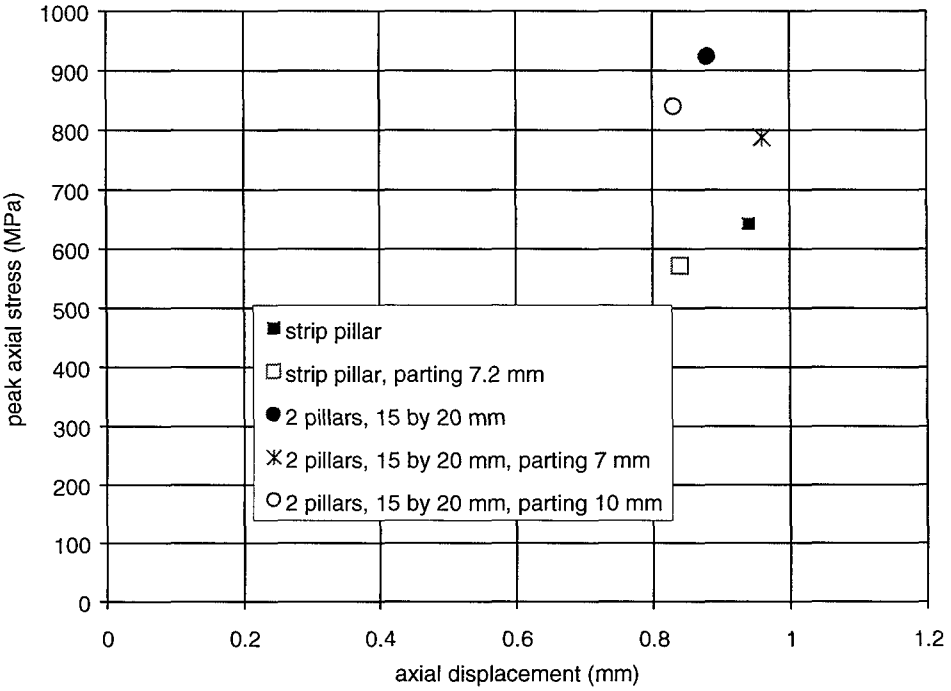

Figure 6-16 The APS and axial displacement at the yield stress for the norite samples.

6.8 Summary and conclusions

An investigation to determine a design methodology for the bearing capacity and the yielding of pillar foundation systems in hard rock was conducted for a wide variety of conditions, with the following results:

- The failure mechanisms of footwall foundations were determined, and deformation in the presence of partings was defined. Four potential mechanisms of stope footwall closure (heave) have been identified.
- Design were produced charts describing the bearing capacity, the closure at yield stress and the maximum closure at full load as functions of span to pillar width ratio, k-ratio , depth of mining, parting depth, and the friction angle.
- A design methodology for the pillar foundation system using the bearing capacity and closure design charts was discussed and the implication of the foundation closure on support design highlighted.
- An optimisation methodology to determine the yield requirements of support under pillar foundation failure conditions has been developed.

The results of the laboratory tests were highly significant:

- the ultimate bearing capacity and the bearing capacity (yield point) of foundation systems are affected by the boundary conditions
- the bearing capacity of strip pillar foundations is lower than that of square pillar foundations
- the bearing capacity of foundations decreases as the parting depth decreases.

6.9 References

Cook N. G., Hood M. and Tsai F. 1984. Observations of crack growth in hard rock loaded by an indenter. *International Journal Rock Mechanics Mining Sciences & Geomechanics Abstracts*, vol. 21 No 2.

Cundall, P. A. 1995. FLAC Manual V3.33.

Dede T. 1996. Investigations into the mechanism of fracture onset and growth in layered rock using physical and numerical modelling. ***M.Sc. Dissertation.*** University of the Witwatersrand.

Kabeya K. K., Botha D. and York G. 1997. Design methodology for yielding foundations of hard rock pillars. *1st Southern African Rock Engineering Symposium*, Sangorm, Johannesburg.

Özbay M.U. and Ryder J.A. 1988. Investigations into foundation failure mechanisms of hard rock squat rib pillars. *International Symposium Rock Mechanics & Rock Physics at depth.* Pau, France.

Spencer D. In situ pillar monitoring at Impala Mines – Appendix 4. 1995. Final report on SIMRAC project GAP 024, Gencor Rock Engineering Consultant.

Wagner H. and Schümann E. H. R. 1971. The stamp load bearing strength of rock. An experimental and theoretical investigation. Rock Mechanics 3/4.

York G. 1998. Numerical modelling of the yielding of a stabilizing pillar/foundation system and a new design consideration for stabilizing pillar foundations. *J. South Afr. Inst. Min. Metall.,* October.

7 Integration of system design components into a pillar system design methodology for shallow to intermediate depth hard rock mines

7.1 Introduction

This chapter addresses Enabling Output number 9 (see page 13).

In each of the previous chapters, design charts have been produced to determine the effect of geotechnical or geometric parameters on the desired output. In some cases, these design charts have been incorporated into design flowcharts, to suggest the use of the design charts in a practical design methodology. The aim of this chapter is to collate all the design flowcharts, to show how they are integrated to produce a *pillar system design methodology*.

This chapter then represents both an integration and a summary of the outputs of this project.

7.2 The pillar system design flowchart

The pillar system design can be defined according to Figure 7-1. The Loading System and Stress Regime inform the entire pillar system design process, and provide inputs into each component of the pillar system design. At each component, it may be found that the inputs, from the previous component, are such that a stable design cannot be performed for the first estimated parameters. For example, in the Pillar Design component, a given panel span, from the Panel Span Design component, may result in the load being too great for the desired pillar dimensions. The panel span could be adjusted, or the pillar dimensions could be adjusted. The backward loops shown in Figure 7-1 indicate this choice.

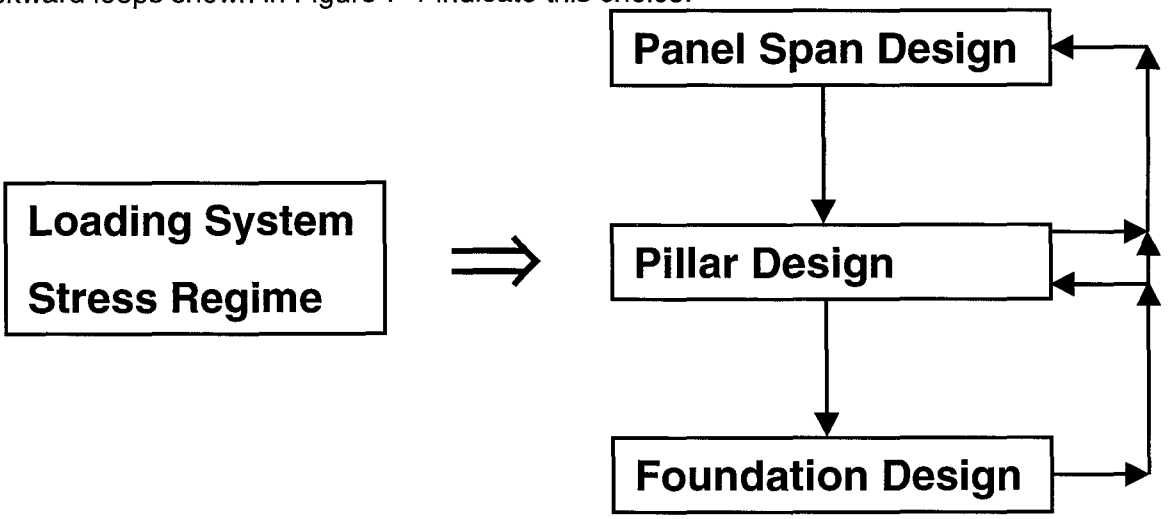

Figure 7-1 The pillar system design flowchart.

7.3 The loading system

This section briefly addresses Enabling Outputs 2 and 3. More complete detail may be found in Chapter 2. Numerical modelling has shown that the theoretical tributary load will most often be an overestimation of the pillar load. This has two consequences:

1) pillar strengths may be overestimated in back analysis
2) inefficient pillar system designs will be performed (with the associated reduction in ore recovery).

The effect of geometry on pillar loading is shown in Figure 7-2, for a depth of 200 m. As may be seen, even for panel spans of 50 m, with nine pillars (10 panels), the average pillar stress (APS) of the middle pillar is below 95 per cent of the theoretical tributary area load. A typical mining scenario, of perhaps five to seven, three m wide, pillars, and stope spans of 30 m, results in pillar loads of between 80 and 85 per cent of tributary area load (see Figure 7-2).

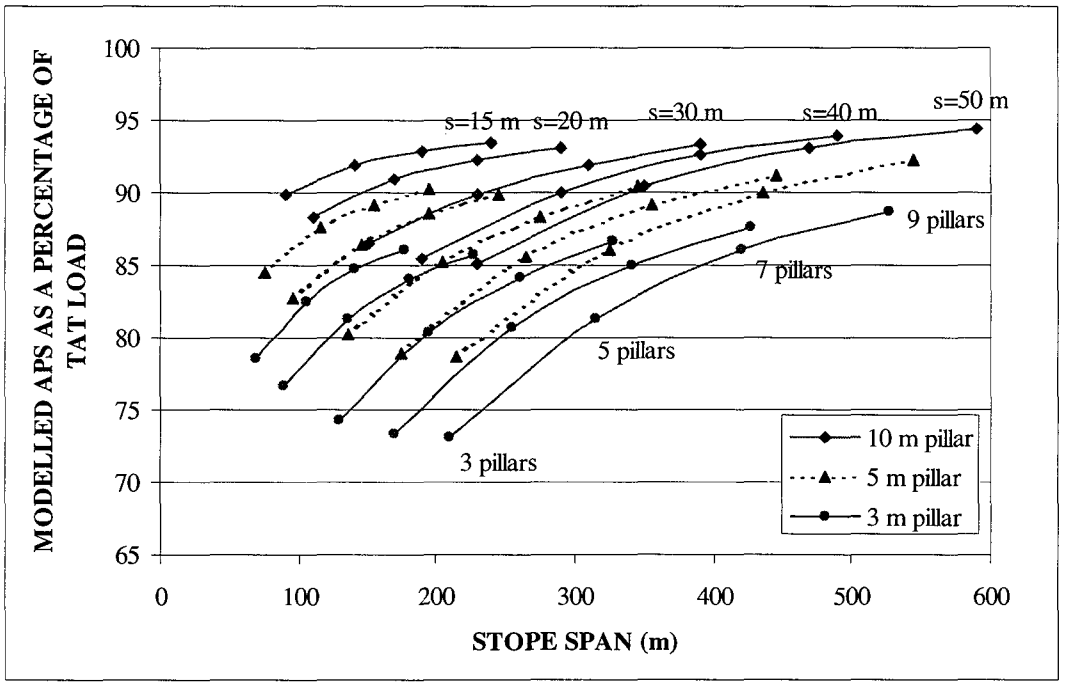

Figure 7-2 The APS as a proportion of the theoretical tributary area load, from numerical modelling of various mining geometries and pillar sizes at 200 m depth.

The effect of depth on pillar load is shown in Figure 7-2. The proportion of tributary area load changes rapidly close to the surface. The curves flatten at greater depths. The depth at which the curves flatten is related to the total stope span, and probably to the stiffness of the pillars. Importantly, beyond this depth, the APS, expressed as a proportion of tributary area load, does not *change.* The curves shown in Figure 7-2 are based in the assumption that regional pillars are present, and that they are wide enough to effectively compartmentalise the mine.

The result shown in Figure 7-4 is for spans with no in-panel pillars. The result shown in Figure 2-2 is for spans with in-panel pillars. A comparison of the two cases implies that the ¼ depth rule need only apply to situations where no in-panel pillars are used. The above results indicate that regional pillars may not be necessary at all in the presence of elastic pillars. However this conclusion is based upon theoretical numerical modelling considerations. In the light of this, it is suggested that regional pillars should be maintained as "barriers", even in the presence of elastic pillars. In the presence of elastic pillars, the ¼ depth rule is conservative. Ratios of span to depths up to ½ are commonly used with no occurrences of backbreaks. This experience, together with the numerical modelling results, suggest that ratios of regional span to depths up to ½ may be safely used.

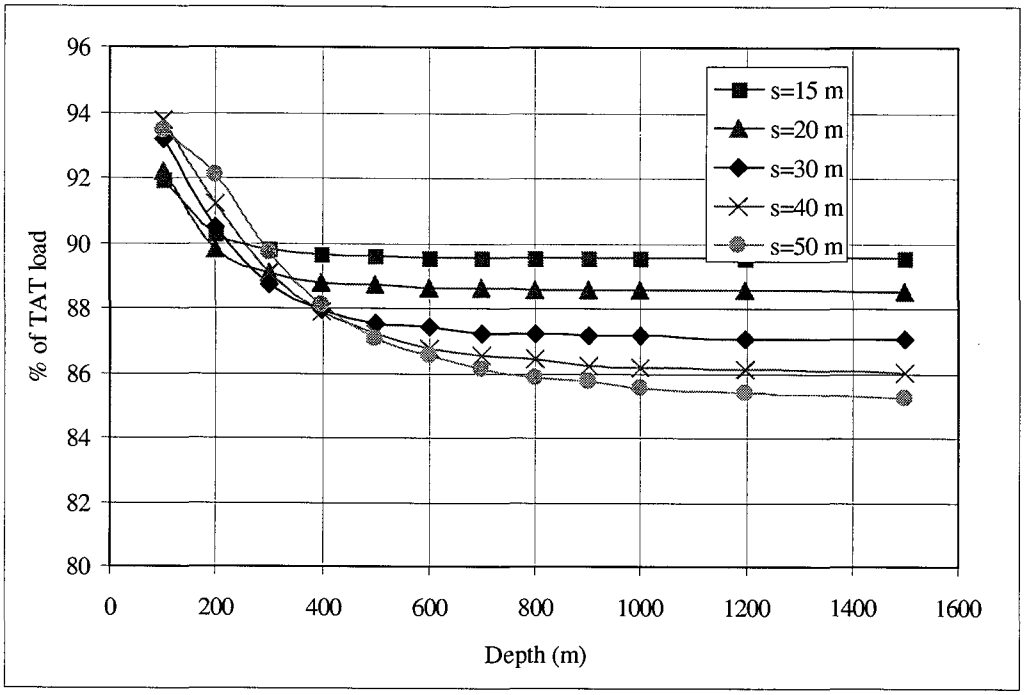

Figure 7-3 The difference in APS as calculated by Tributary Area Theory and from numerical modelling for various depths for 9 in-panel pillars, and varying panel spans.

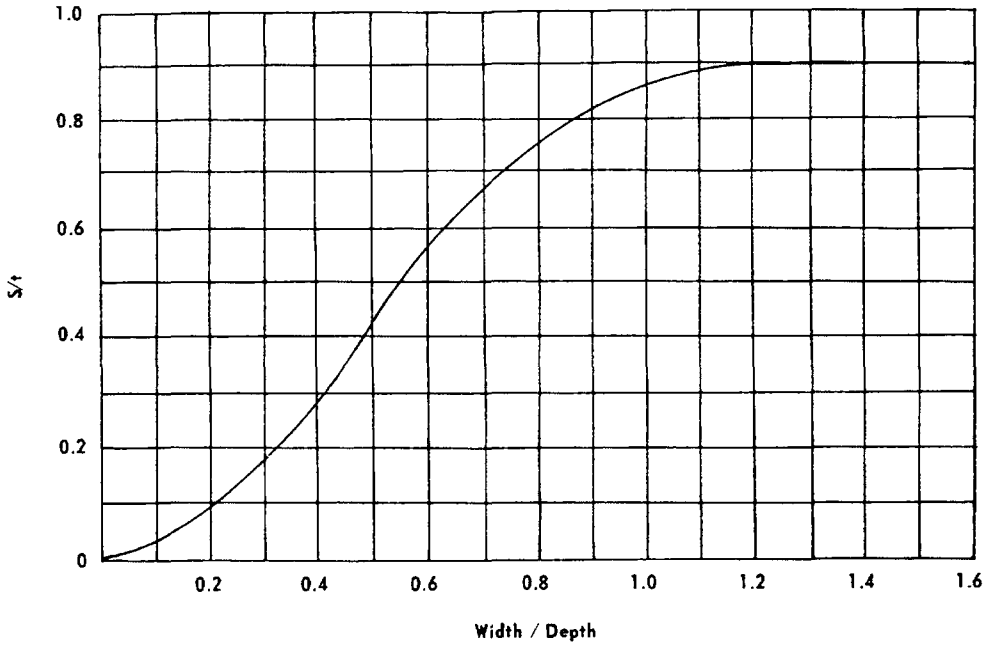

Figure 7-4 Surface subsidence (S) normalised to seam thickness (t), plotted against the ratio of span (Width) to depth (after Cummins and Given, 1973).

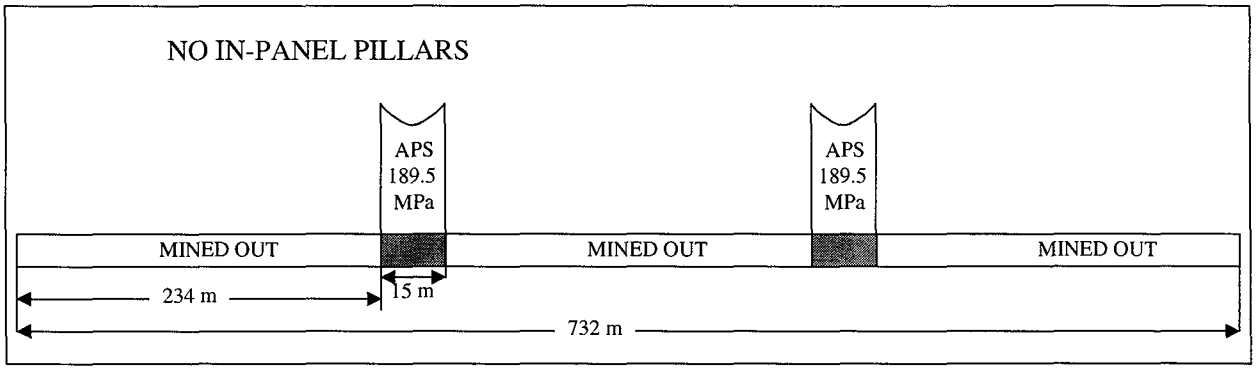

(a)

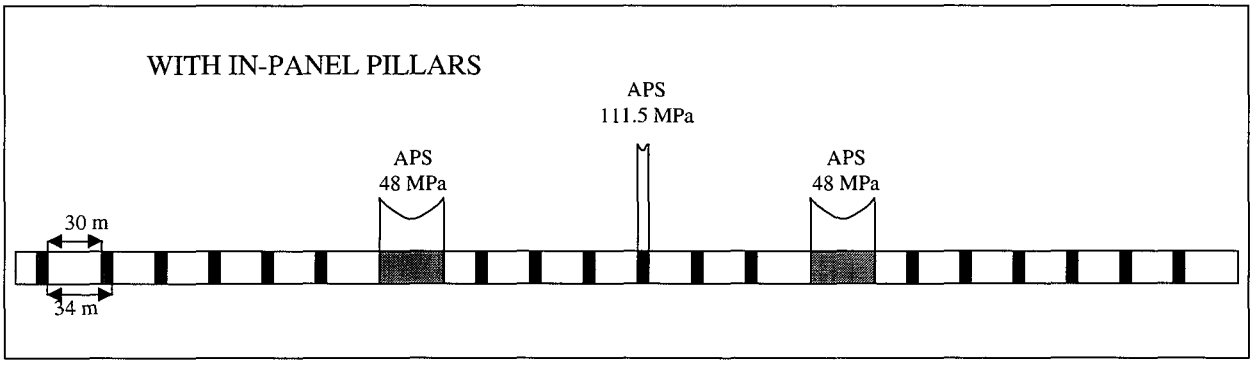

(b)

Figure 7-5 Effect of regional and in-panel pillars on regional pillar loading.

7.4 Panel span design component

7.4.1 The empirical approach

This section briefly addresses Enabling Output 5. More complete detail may be found in Chapter 3. This project has provided two approaches to panel span design. The first is an empirical approach. A Critical Panel Span Design Chart has been produced (Figure 7-6), relating a maximum safe span to a rock mass rating. The rock mass rating is the modified Q system, as developed by Impala Platinum Mine. The data was gathered on the Merensky Reef in the Bushveld Complex. As is the case for all empirical solutions, this Critical Panel Span Design Chart is valid in the range of the empirical data. Therefore this chart should only be used for panels in the Merensky Reef.

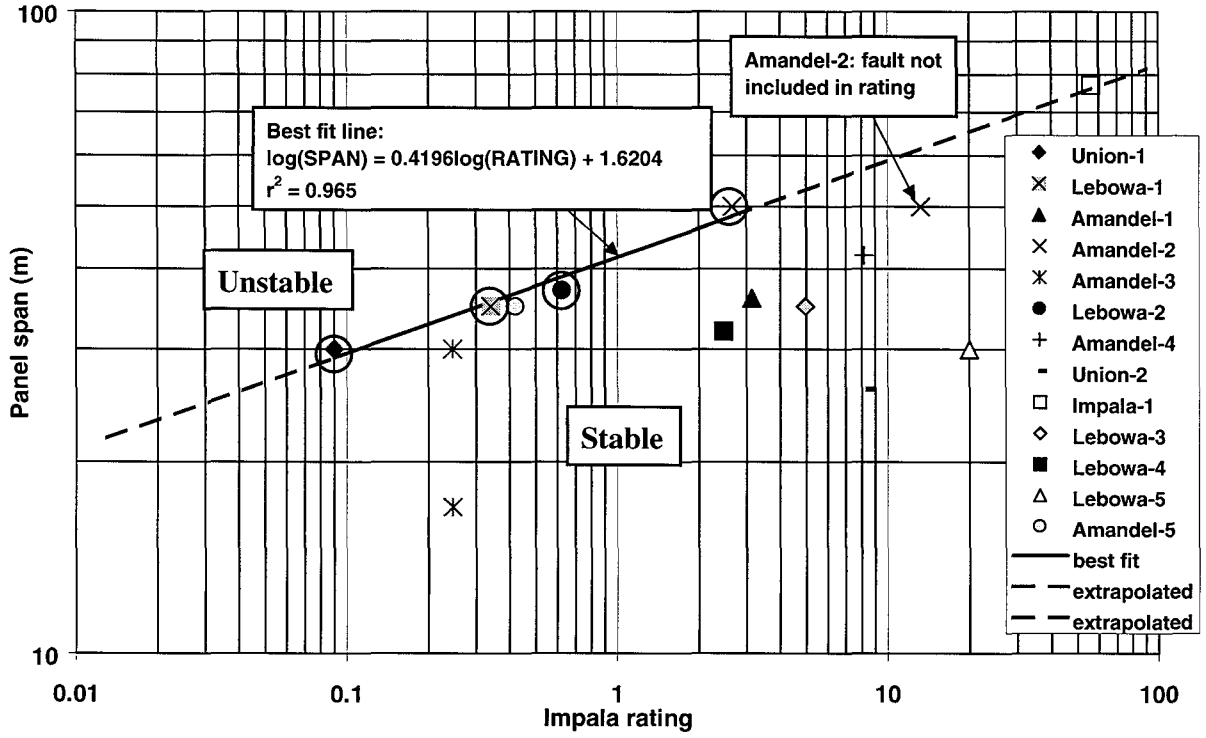

Figure 7-6 The Critical Panel Span Design Chart for the Merensky Reef.

The input parameters for the determination of the Critical Span are those required to determine the Impala modified Q system rock mass rating. These include parameters such as joint frequency, joint alteration and the presence of water. A Stress Reduction Factor is also applied to account for major geological features. Details of this methodology can be found in Chapter 3.

7.4.2 The numerical modelling approach

This section briefly addresses Enabling Outputs 5, 6 and 7. More complete detail may be found in Chapter 4. Alternatively, the definition of stable spans has been determined by means of numerical modelling. A number of assumptions are built into the numerical modelling. The most important assumption is that hangingwall failure is limited to failure of, or along, geological joints. The rock itself is assumed to remain undamaged.

The analysis was done using a two dimensional program. This is a very simplified model of reality. Only two joint sets were used in the model. All joints are assumed to be continuous throughout the model. Joint sets, or the odd joint, in the plane of the model, are not modelled. This is not necessarily a major limitation because the second major joint set is often very non-persistent.

Due to the above-mentioned limitations, the results must only be used for situations where similar conditions prevail in terms of the rock mass structure and properties. The results should not be used if a different failure mode is experienced. Examples of where this methodology is not applicable are:

1) triplets in UG2 reef, which fail in a plate bending mechanism
2) very good rock mass with very few joints
3) dilational movement in the hangingwall due to high stress at the face
4) the rock itself fails in shear or tension
5) two orthogonal major joint sets of very high persistence
6) presence of faults or dykes running parallel to the lines of pillars.

The results presented may be conservative under the following *in situ* conditions:

1) lack of reef parallel planes

2) only one major joint set that is non-persistent (apart from the stratification planes)
3) a second major joint set is present (more or less orthogonal to the modelled inclined joint set) and both joint sets are non-persistent
4) any combination of the above.

The main result of the way the model is set up is that the failure mode is limited to shear failure or cantilever failure. For steep dipping joints (> 75°), failure occurred by tensile splitting near the centre of the panel.

For given joint sets and joint friction angles, any given panel span is defined as self-supporting, supportable, or unsupportable. In these charts, the maximum supportable thickness of hangingwall is deemed to be 1,5 m. These charts can be modified to take into account support systems with higher support resistance capabilities. A simple methodology has been provided that allows the determination of the *in situ* joint friction angles. An example of a panel span design chart is shown in Figure 7-7.

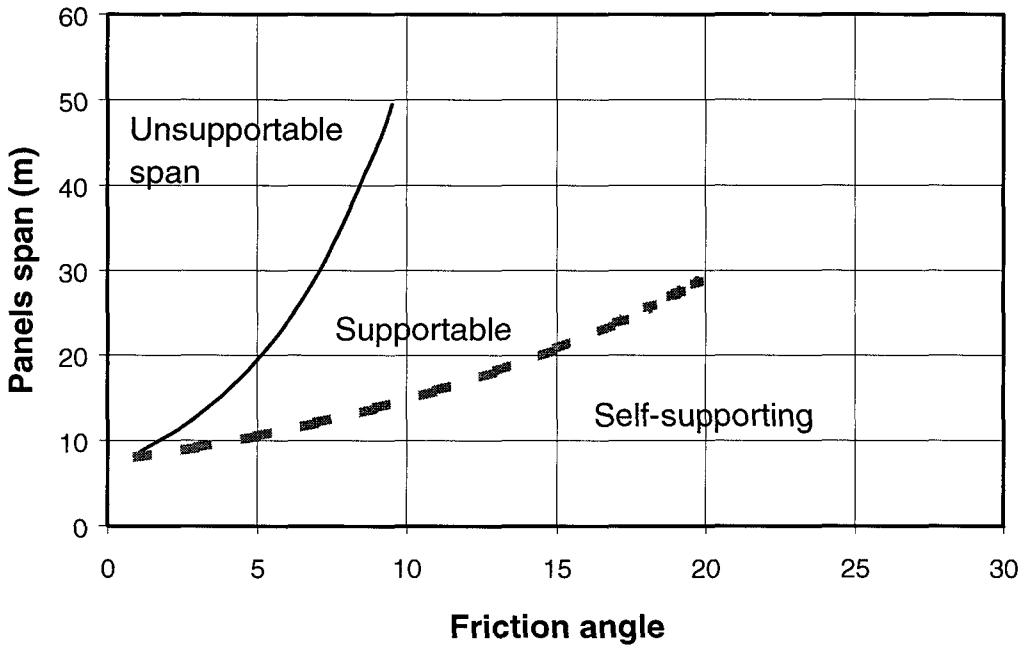

Figure 7-7 An example of a panel span design chart defined by the use of numerical modelling, for joint sets orientated at 0° and 85° to 90°.

Once a panel span has been determined, the design of support may be done with the use of a chart such as shown in Figure 7-8. The modelling was done assuming elongate support. Such a design chart should not replace proper detailed support design, as is shown in the Final Project Report on GAP330, Stope Face Support Systems. back analysis is required to determine what percentage instability is acceptable.

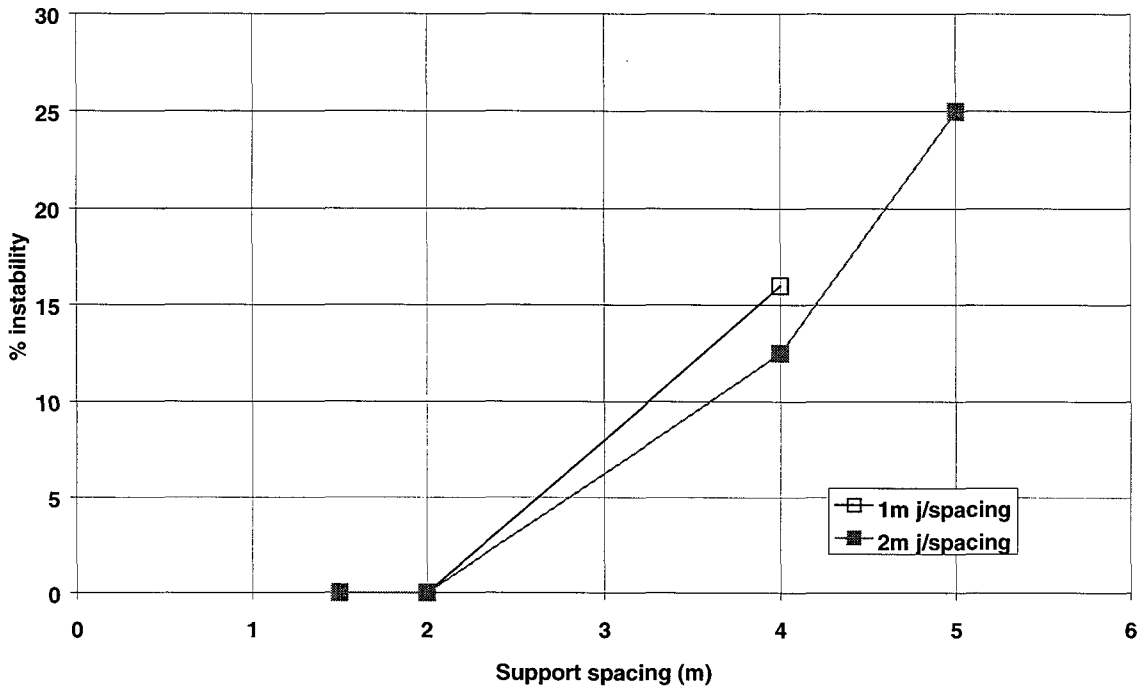

Figure 7-8 Elongate support relative hazard chart for the 0°/(60°-70°) joint sets.

The process of determining the *in situ* friction angle and the use of the design charts is shown in Figure 7-9 and Figure 7-10.

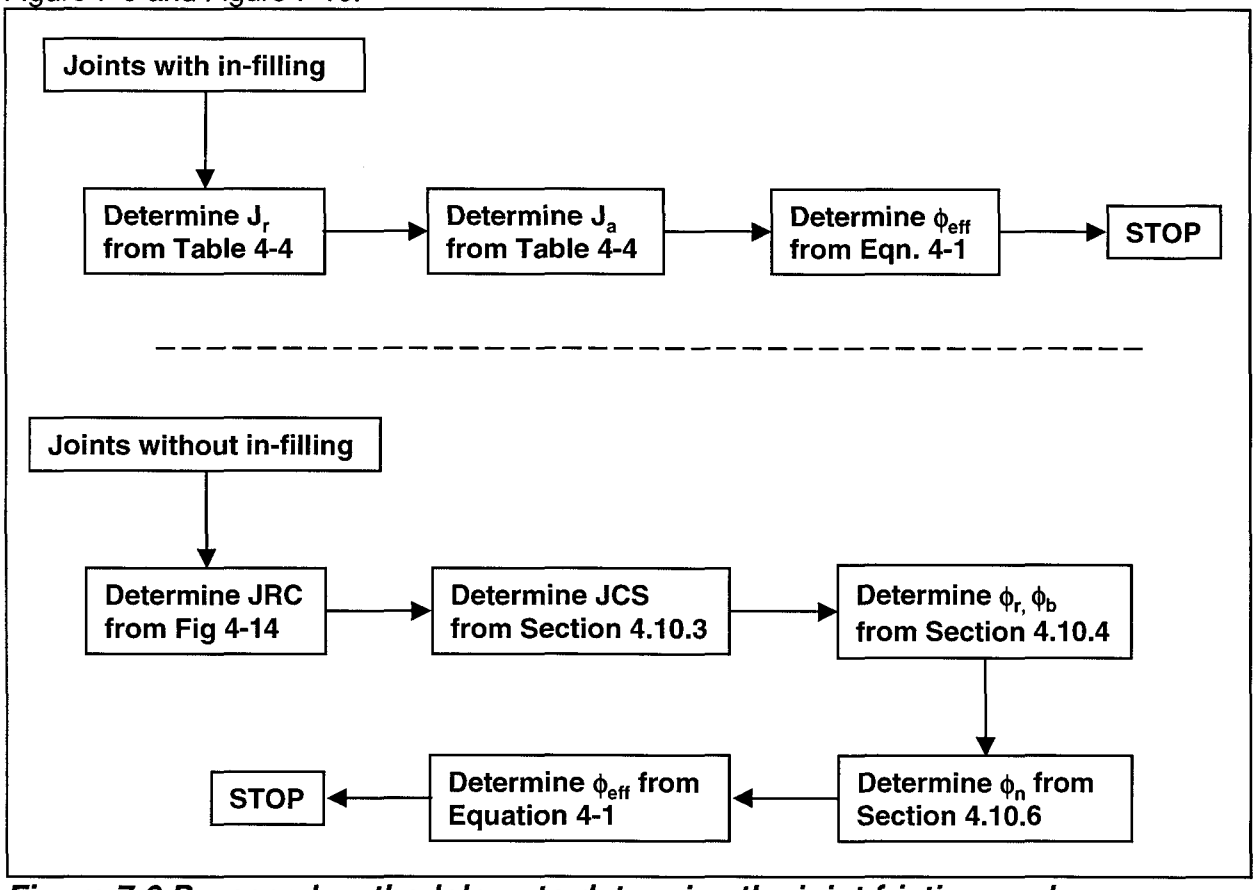

Figure 7-9 Proposed methodology to determine the joint friction angle.

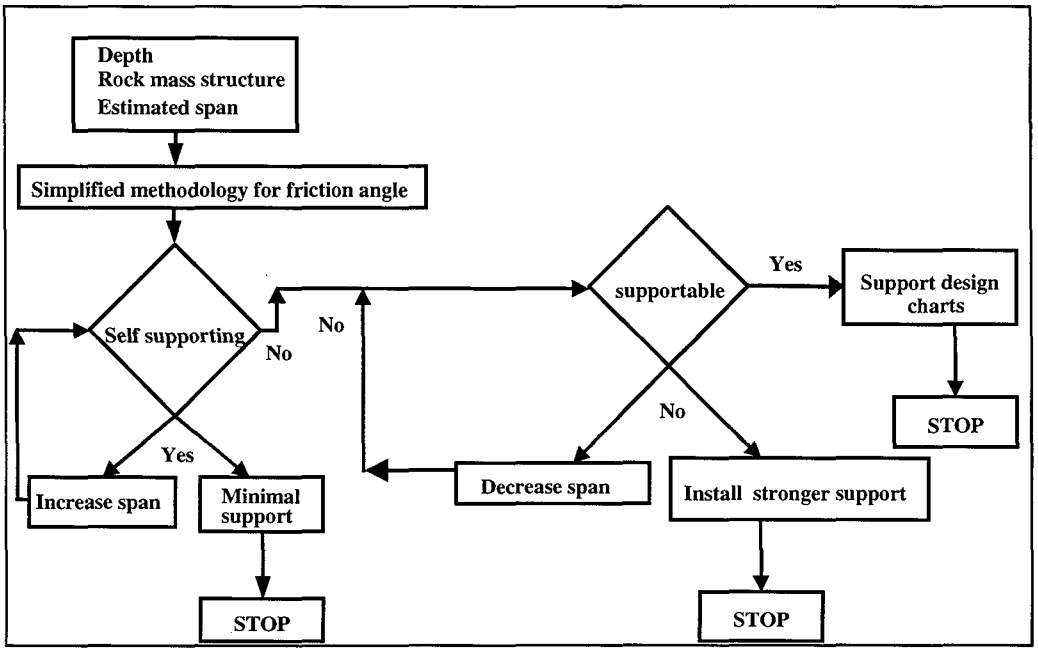

Figure 7-10 Proposed methodology for panel span and support design.

Thus the output of both the empirical and modelling approach is the panel span.

7.5 Influence of internal panel support systems on the stability of the panel hangingwall

This section briefly addresses Enabling Output 6. Enabling Output 6 is also addressed in the preceding section. More complete detail may be found in Chapters 3 and 4. The load reaction generated by the sticks that were instrumented appears to have been sufficient to delay inelastic deformation for at least 1 m into the hangingwall. Inelastic deformation occurred from the first blast, indicating the need to install support as close to the face as possible. The effective stress trajectory from the face abutment into the hangingwall sufficient to prevent horizontal stress fracturing was at an angle of 60^0 - 75^0, indicating that face support design should not take the face capacity into account. It appears that the packs started to generate sufficient reaction to support the fractured zone, of 4,5 m, after about 84 mm of closure had occurred. A support resistance of 712 kN/m^2 could have been generated to stabilise the fracture zone, where the weight of the material would have generated a load of 140 kN/m^2. This finding indicates that there was a horizontal driving force enabling the observed inelastic deformation to occur.

Timber props increase their capacity to deform if the closure rate reduces, but are less stiff, therefore, the engineer should design using the timber characteristics best suited to the closure rates on his mine.

7.6 Pillar design

This section briefly addresses Enabling Output 4. More complete detail may be found in Chapter 5. Pillar design is done by firstly determining the critical rock mass strength. The critical rock mass strength is defined as the asymptotic strength as volume increases, for mine pillar scale problems. This value is then adjusted for the three main factors which influence pillar strength:

1) the ratio of pillar width to pillar height (w/h)
2) the effect of the contact conditions on the w/h ratio strengthening effect (1-a)

3) the effect of jointing.

Details on the derivation of these are described in Chapter 5. The design charts that show the effect of these factors are given in the following three figures.

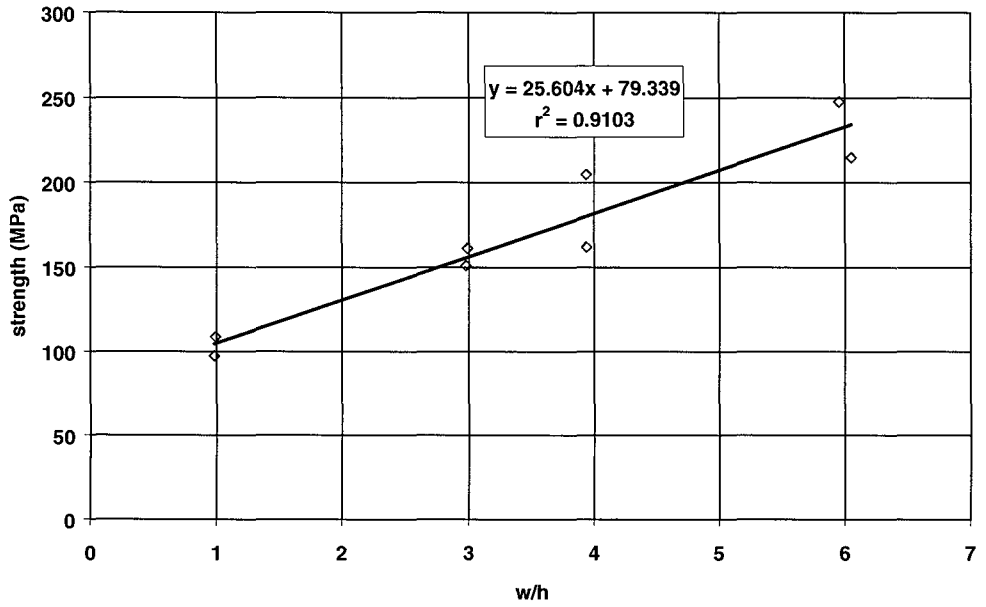

Figure 7-11 The effect of w/h on pillar strength. Laboratory samples are Merensky Reef of diameter = 248 mm.

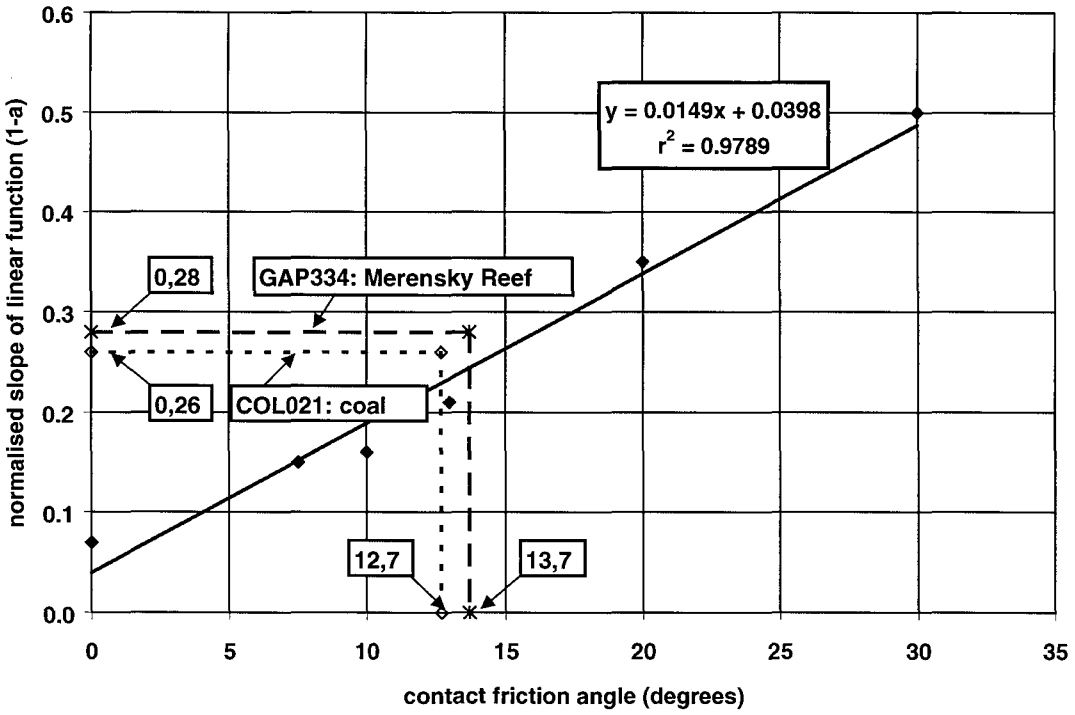

Figure 7-12 The w/h strengthening parameter, 1-a, as a function of the contact friction angle, according to numerical modelling. The values derived from laboratory testing on coal and Merensky Reef are also shown.

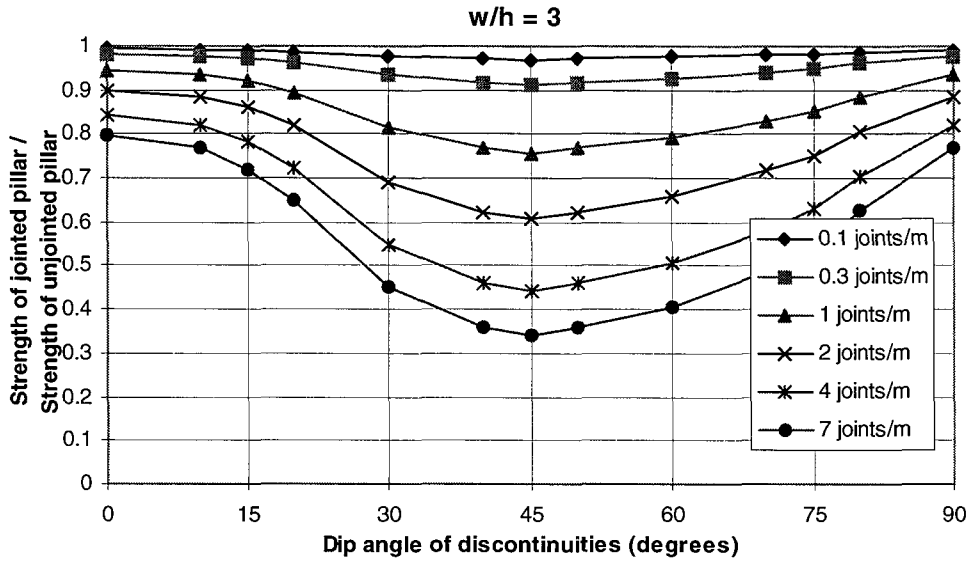

Figure 7-13 The effect of jointing on pillar strength as a function of the joint set dip angle, for a pillar of w/h = 3. A different curve is drawn for different joint frequencies.

Charts showing the effect of jointing for pillar w/h = 2, 4 and 6 are shown in Appendix B.

Figure 7-14 is the pillar design flowchart which shows the simple and practical application of the design charts illustrated in the previous three figures.

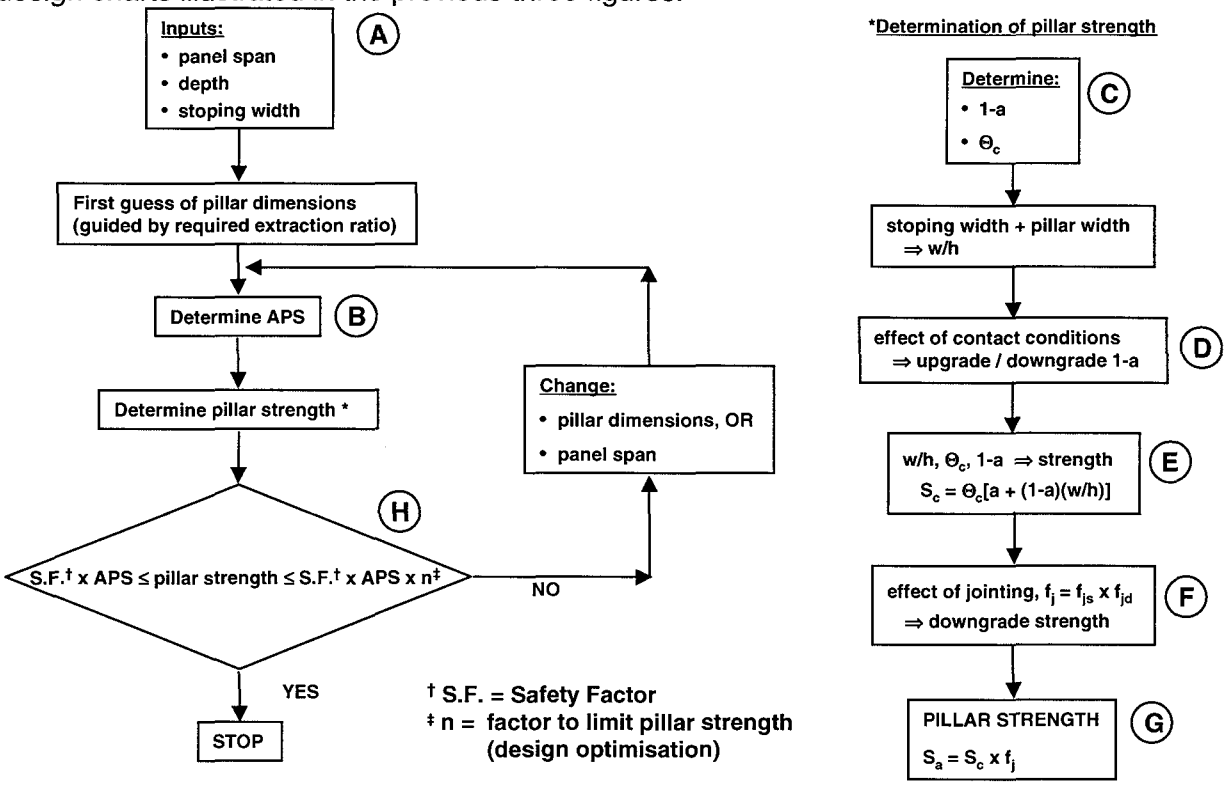

Figure 7-14 A pillar design flowchart.

A feature of the new pillar design methodology is that it accounts for the fundamental engineering influences on pillar strength.

7.7 Stability of the pillar foundation and panel footwall

This section briefly addresses Enabling Output 8. More complete detail may be found in Chapter 6. The bearing capacity (yield point) and the footwall heave at the yield point of the foundation were obtained by means of numerical modelling. These have been depicted in design charts. In many cases, the yield point occurred at values lower than the ultimate load on the pillar. In these cases, the heave at final load has also been depicted in design charts. The parameters and the range of values modelled are shown in Table 7-1.

Table 7-1 The parameters modelled and the range covered in the parametric study.

Variable	*Symbol*	*Values*			
Ratio of span to pillar width	stoping width	6,7	14	25,5	35,4
Depth of parting (m)	h	1(parting1)	2 (parting2)	3 (parting3)	s*
k-ratio	k	0	0,5	1	1,5
Depth of mining (m)	D	400	600	800	1000
Interface friction angle (/)	N, Phi	0	15	30	45

s* = standard case without parting.

The material properties of the rock were representative of typical footwall rock found in platinum mines in the Bushveld Complex. The dominant factor in most cases was not so much the material strengths, but the geometry (ratio of panel span to pillar width) and the depths and properties of the parting planes.

The following two figures provide examples of design charts. Figure 7-15 shows the bearing capacity of the system with a parting 1 m below the stope, while Figure 7-16 shows the footwall heave after full load has been transferred to the pillar / foundation system (also a parting 1 m below the stope). It is difficult to differentiate between the curves for closures less than 200 mm in Figure 7-16. In such cases, the charts have been re-plotted with different scales to allow the use of the charts for closures less than 200 mm, for example. These are shown in Appendix C.

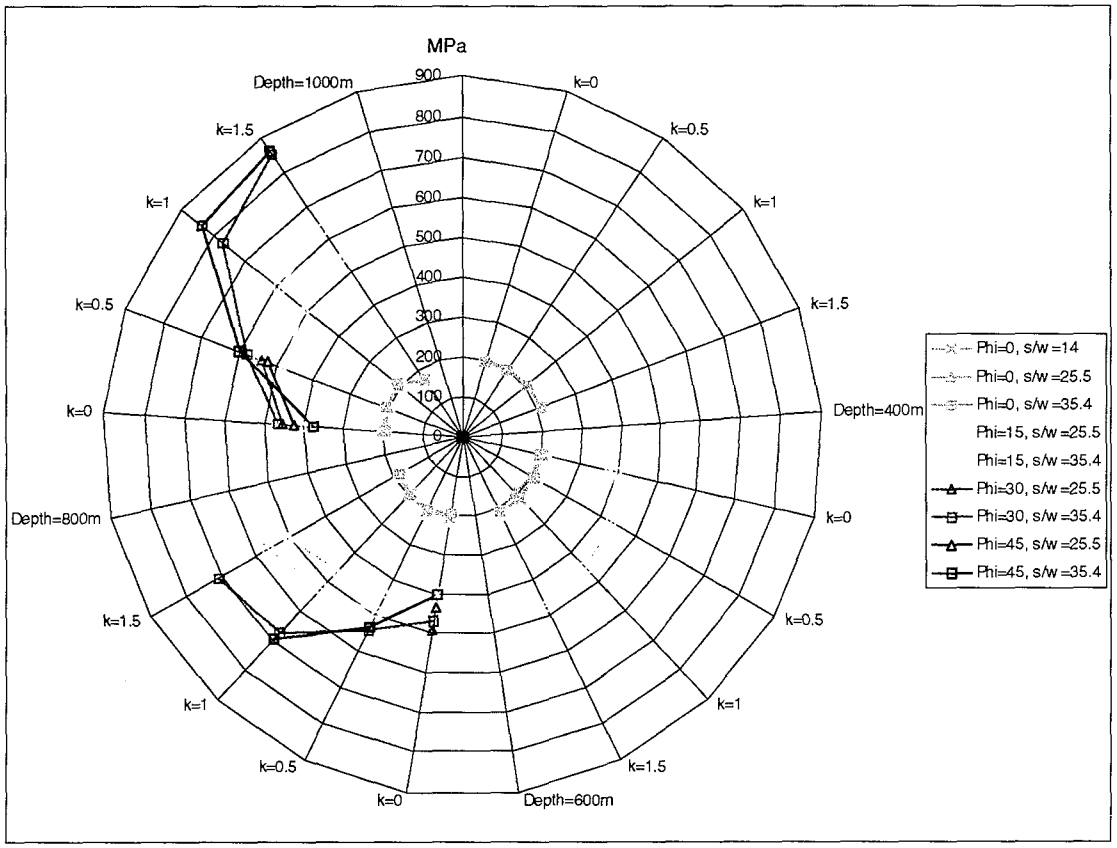

Figure 7-15 Design chart for the bearing capacity of foundations, for a 1 m deep parting in the footwall.

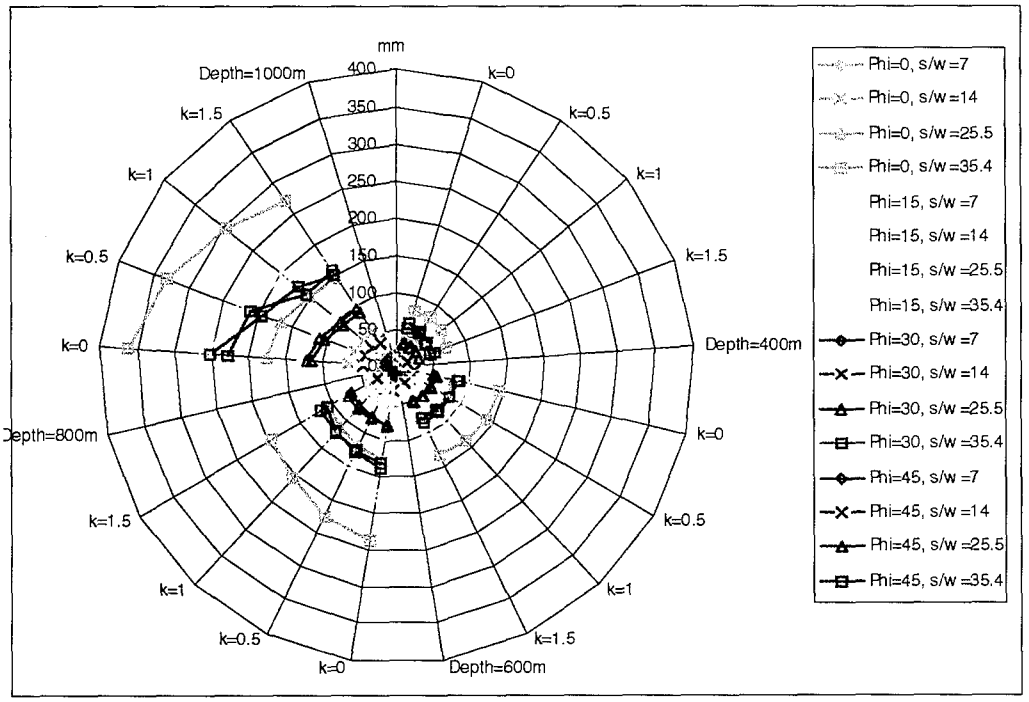

Figure 7-16 Design chart for the maximum heave (after full load transfer to the pillar / foundation system), for a 1 m deep parting in the footwall.

Elongate support is often compromised by footwall heave. The design charts have been incorporated into a flowchart for the optimum design of yielding support, taking footwall heave into account. The flow design chart is shown in Figure 7-17.

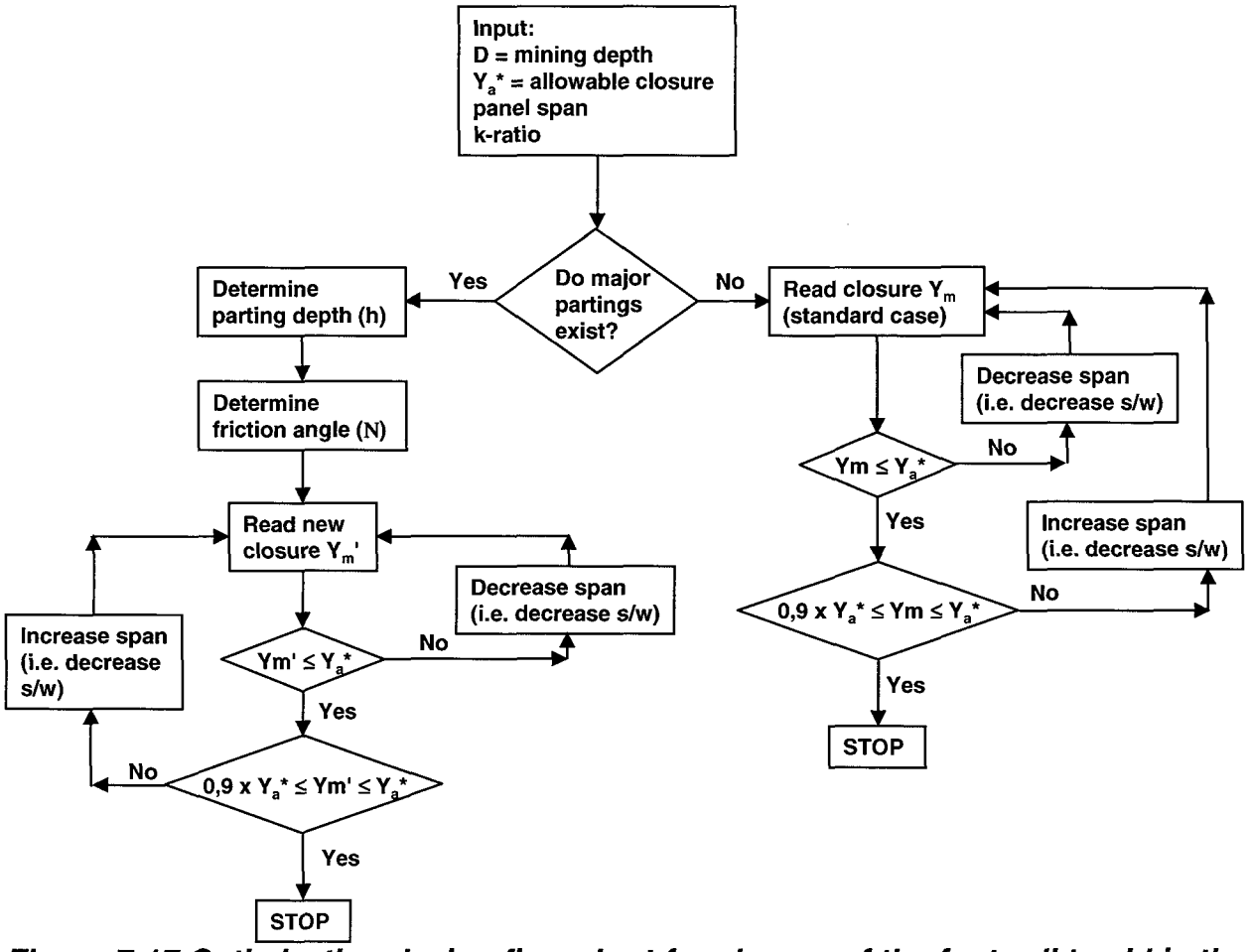

Figure 7-17 Optimisation design flow chart for closure of the footwall to aid in the design of yielding support.

7.8 Development of Windows™ based software for implementation of results and recommendations to industry

A computer programme has been prepared that encapsulates the design charts and the flowcharts of the various components. The programme is user-friendly. To use the programme, the user opens the supplied spreadsheet file, with the use of the Microsoft spreadsheet programme Excel. The programmes have been embedded in the file, such that the user can follow the design methodologies easily. The programme has been submitted to SIMRAC.

7.9 Conclusions

This chapter has provided the design flowcharts for each component of the pillar system, and some of the design considerations, to enable a pillar system design methodology. The design flowcharts follow each other logically, with outputs from each design flowchart leading to inputs to the next.

For shallow to intermediate depth mines with pillar layouts, It is proposed that safer mine layouts can be designed, based on the rational design methodologies presented in this report.